Université de Toulouse

THÈSE

En vue de l'obtention du

DOCTORAT DE L'UNIVERSITÉ DE TOULOUSE

Délivré par :

Université Toulouse 3 Paul Sabatier (UT3 Paul Sabatier)

Présentée et soutenue par :
Carlos Mario QUINTERO PINZÓN
le 25 septembre 2012

Titre :

Luminescent Spin Crossover Nanomaterials: Physical Properties and Applications

---

École doctorale et discipline ou spécialité :
ED SDM : Nano-physique, nano-composants, nano-mesures - COP 00

Unité de recherche :
Laboratoire de Chimie de Coordination - CNRS - UPR 8241

Directeur(s) de Thèse :

Gábor MOLNÁR

Jury :
Mme. Montserrat GOMEZ SIMON, Professeur à l'Université de Toulouse, Présidente
M. John MCGARVEY, Professeur à Queen's University of Belfast, Rapporteur
M. Mario RUBEN, Professeur à l'Université de Strasbourg, Rapporteur
M. Sylvestre BONNET, Professeur à l'Université de Leiden, Examinateur
M. Azzedine BOUSSEKSOU, Directeur de recherche au CNRS, Toulouse, Membre Invité

A mi abuelita Maria Gilmita quien nos dejó a principios de este año (2012).

Acknowledgements

I would like to thank the Switchable Molecular Materials Team (equipe P), the Laboratoire de Chimie de Coordination (LCC) and the Ministère de l'Enseignement Superior et de la Recherche for hosting me and funding this thesis.

I thank Azzedine Bousseksou and Gábor Molnár for choosing me and believing that I had what was necessary to get this thesis done. In particular, I am very grateful of having Gábor as my thesis director: his advices, his constant support and his quality not only as a researcher but also as a person were priceless for my professional and personal growth during this thesis. Also, I would like to thank Lionel Salmon for his help while solving my doubts in chemistry, a field unfamiliar to me. I thank Lionel Rechignat for being always there to help me with everything I needed inside and outside the laboratory. I thank William Nicolazzi for his theoretical support in this thesis and also for his constant efforts to give me interesting facts about the French culture.

I would like also to thank: Carlos B, Manuel, Helena, Illia, Amalita, Salma, Gautier, Khaldoun, Edna, Olena, Simon and Gaëlle for their friendship and encouragement during these years in LCC. I will always remember all those precious moments that we spent together.

Additionally, I would like to thank our collaborators from LAAS: the Nanobiosystems group, Nadia, Aline, Jonathan and Crystophe Thibault. In particular, I would like to thank Christian Bergaud, without him this thesis could have never happened. I thank also the technical support team of the clean room in LAAS (TEAM), especially Franck Carcenac and our colaborators from the University of Groningën: Wesley Browne and Lily Hou.

Last but not least, I would like to thank my family and the friends that I have met here in France for their unconditional and vital support during these three years of thesis.

Contents

Acronyms

AFM	Atomic force microscopy
AO	Acridine orange
CCD	Charge-coupled device
CCR	Crosscorrelation
EBL	Electron beam lithography
ϵ	Molar absorptivity
FRET	Förster resonance energy transfer
FWHM	Full width at half maximum
γ	Molar fraction
hptrz	4-heptyl-1,2,4-triazole
HS	High spin state
IPA	Isopropanol
J(λ)	Overlap integral
k_b	Boltzmann constant
LS	Low spin state
MIBK	Methyl isobutyl ketone
NA	Numerical aperture
NaAOT	Sodium bis(2-etsodium bis(2-ethylhexyl) sulfosuccinate
OTs	Tosylate
OTS	Octadecyltrichlorosilane
PCB	Printed circuit board
PDMS	Polydimethylsiloxane
PMMA	Poly(methyl-methacrylate)
Q	Quantum yield
r_{SA}	Separation distance between a sensitizer-acceptor pair
R_0	Förster Distance
Rh110	Rhodamine 110
ROI	Region of interest
SAMIM	Solvent-assisted micromolding
SCO	Spin Crossover
SEM	Scanning electron microscopy
TCSPC	Time-Correlated Single-Photon Counting

General Introduction

The singular size-dependent physical and chemical properties of nano-materials make them ideal building blocks for the advancement of the emerging nano-technologies that their bulk counter parts cannot provide. Nonetheless, contrary to semiconductors and metallic materials, molecule-based nanomaterials have been less studied. Our comprehension of matter starting from single molecules to bulk macroscopic materials may be extended while studying nano-objects of such type. In addition to their unique properties observed at the nano-scale, research into molecule-based nano-objects has opened different pathways to process them as colloidal suspensions, thin-films and other types of nano-scale assemblies. The continuous increase of sophistication in the synthetic chemistry is playing a key role in the field of material science-based technologies. As a result, nanoparticles of molecule-based materials are expected to be used as novel elements in display devices, sensors, drugs, cosmetics, active pigments, etc [1].

In this context, the recent emergence of spin crossover (SCO) nano-materials offers an excellent platform to investigate size reduction effects in molecular solids owing to the extreme sensitivity of the SCO phenomenon to minute changes in the crystal lattice. The switching between the two spin states is accompanied by a significant change of molecular shape and volume, leading to strong elastic interactions between the molecules in most bulk solids. These cooperative intermolecular interactions associated with the small energy gap between the HS and LS states are expected to give rise to significant size reduction effects on the SCO phenomenon. From a very simple point of view, size reduction effects in these molecular materials are expected to occur mainly due to the decrease in the number of interacting metallic centers, resulting in a cooperativity loss of the material. Nevertheless, other parameters and material properties should be considered in order to successfully understand the experimental observations obtained for SCO nano-materials. Up to now, these observations have been limited to the measurement of the optical absorption or magnetization as a function of temperature in a huge ensemble of nanoparticles with different degrees of size dispersion [1]. There is a clear need to develop novel methods sensitive enough to probe extremely small quantities of SCO material.

The main objective of this thesis is to provide a new protocol that permits the detection of the SCO in a single nano-object. To accomplish this, we propose luminescence as a highly sensitive technique that may be employed at scales where other conventional methods are no longer effective. *We aimed to develop SCO nano-materials with luminescence properties in order to isolate these objects, address them and then probe*

their properties via luminescent detection.

In the past few years, a few multifunctional materials combining luminescence and spin crossover (SCO) properties have been reported in the literature with the aim of achieving luminescence signal modulation resulting from the spin state switching phenomenon. These efforts have been motivated by a variety of different goals. First, the change of the energy transfer mechanism between the SCO complex and the luminophore upon the spin state change is a conceptually interesting phenomenon in its own right. Perhaps more importantly, a luminophore may also be used to report upon the spin state of SCO materials. Indeed, in many cases the detection of a luminescence signal is more efficient or easier to implement than other techniques commonly used in the spin crossover field (magnetometry, optical absorption and so on). In particular, SCO nano detection opens up very exciting perspectives for luminescent SCO nanomaterials. In general, luminescence can provide superior contrast and sensitivity for non-contact (remote) signal detection with fairly high spatial and temporal resolution. These assets can be used advantageously in various photonic applications. The combination with SCO will add the possibility of tuning the luminescence signal or detecting physicochemical changes in the environment of the SCO centre. Examples include photonic switches, thermometers, gas sensors, etc.

For the scope of this thesis, we have chosen a luminescent doping approach for SCO materials. This concept aimed to supply a characterization technique generic enough for studying various (even all) members of a given family of SCO complexes (rather than a particular derivative) from bulk down to the nano-scale in an isolated object without changing neither the probe nor the experimental setup.

Chapter I is centered on the background theories and developments necessary to begin the quest of combining two physical phenomena - luminescence and spin crossover - within a single material. In order to understand how the spin crossover may modulate the luminescent response of a luminophore, it is crucial to learn the mechanisms that govern both processes. Thus, this chapter starts with a general introduction to luminescent materials and then highlights the luminescence energy transfer as the key concept for the design of luminescent SCO materials. Then, a brief overview of the SCO phenomenon is provided. It begins with a description of the SCO with a crystal field theory approach. It mentions the entropic origin of the thermal SCO, illustrates the different spin transition curves and also introduces the notions of cooperativity in SCO materials. Then, the electronic transitions and the optical properties of SCO complexes are discussed as well as some relevant examples of these materials. Finally, the classical detection methods of SCO are depicted and the emerging tendencies with new methods are described.

Hybrid materials with combined spin crossover and luminescent functionalities are treated in chapter II. First, literature examples - aimed to be exhaustive - are discussed. We have divided the synthetic strategies into two parts, one dealing with luminescent spin crossover complexes and the other using luminescent doping. Then, the development of luminescent doped SCO materials is discussed. In the course of this thesis, triazole based systems produced by three different synthetic strategies were characterized. Systems ranging from bulk materials to nanoparticle powder in

the solid state and also in the form of colloidal suspension were studied as a function of temperature. Attempts with diverse luminophores as the doping agent and different characterization techniques such as reflectivity microscopy, UV-visible absorption and fluorescence spectroscopy were employed. Additionally, an epifluorescence microscopy set up was particularly useful to develop a proper methodology for characterizing this type of systems at a small scale. It was necessary to find the appropriate parameters for acquiring the maximum of the luminescence signal coming from the samples as well as a critical view for examining the behavior of the luminophores as a function of temperature when combined with SCO materials. Without the optimization of these parameters, the goal of the luminescent detection in a single nano-object would not have been possible.

The detection of the SCO down to a single nano-object may be a difficult task, but the isolation of the object could be an even more challenging mission. Hence, chapter III deals with the organization of SCO nano-materials and the detection of the SCO phenomenon at the nano-scale. It is shown that the luminescent detection of the SCO is a promising characterization technique even for a single nano-object. First, a concise review of thin films fabrication and the organization/patterning in the nano-scale of SCO materials is provided. In the second part, an intermediate phase of luminescent detection at small scales for observing the most interesting luminescent systems developed in chapter II for spin coated thin films is reported. Additionally, a new system developed in chloroform solution is introduced; it serves not only for spin coating SCO thin films of good quality on different surfaces and to follow successfully the SCO via fluorescent detection, but also to elucidate energy transfer mechanisms with luminescence lifetime and photobleaching rate measurements. The last part explains the diverse attempts adopted for isolating SCO nano-objects. Methods ranging from random to directed microcappilary assembly of SCO nanoparticles and also *in situ* synthesis of isolated luminescent SCO objects based on soft lithographic techniques are explored. At the same time, their respective characterization in fluorescence microscopy is shown and the experimental challenges that this task imposed are discussed.

In chapter IV, the temperature measurement on systems with characteristic lengths at the micro and nanoscale is put into context; to achieve this goal, a brief review of the current microthermometry methods is given. Contact and non-contact methods are examined including an analysis of their advantages and limitations for making temperature measurements with high spatial resolution with a particular emphasis on fluorescence as an optimal choice for thermal imaging nanostructures. Then, the most popular fluorescence thermometry techniques are described and the potential of luminescent SCO nano-materials as versatile two element systems in these type of applications is highlighted. Subsequently, the use of metallic nanowires as localized heat sources for the development of high speed temperature controlled on-chip devices is explained. Here, as a proof of concept, thin films of luminescent SCO systems are employed to obtain thermal profiles of gold micro - nanowires heated by Joule effect. The development of the setup and data treatment together with some perspectives is also discussed.

Finally, this manuscript ends with a general conclusion as well as some perspectives for future directions in this burgeoning area of research.

Chapter 1

Luminescence and Spin Crossover Phenomena

1.1 Introduction

This chapter deals with the basic knowledge necessary to understand the resulting combination of two physical properties - *luminescence* and *spin crossover* - within a single material. The aim is to modulate the luminescence properties *via* the change of spin state of the transition metal complexes in the material. The spin state switching by different external stimuli will then lead to the switching of the luminescence, which may be a useful asset for many applications. Conversely, the luminescence signal can be used to detect the spin state changes in the material when other detection methods are not suitable, as is often the case in nanometric sized spin crossover materials for example. We begin this chapter with a general introduction to luminescent materials with a particular emphasis on *luminescence energy transfer* and then an overview of the spin crossover phenomenon is provided. It should be noted that several detailed reviews are available on both topics [2–8]. Here we tried to bring together only those ingredients, which are the most important for the design and application of multifunctional luminescent SCO entities that will be described in Chapters II, III and IV.

1.2 Luminescent Materials and Luminescence Energy - Transfer

From lasers, lamps, computer displays, biological markers and security inks to even basic things such as the piece of paper that we use to write on, or a glow in the dark sticker, photoluminescent materials are ubiquitous in our everyday life. All of these materials absorb electromagnetic radiation (light) and then re-emit a part of it at a different wavelength. Photoluminescence is a particular case of luminescence. In general, luminescence leads to the conversion of specific types of energy into radiation over and

above thermal radiation [2]. It is currently defined as: "Spontaneous emission of radiation from an electronically excited species or from a vibrationally excited species not in thermal equilibrium with its environment" [9]. Depending on the excitation source, additional types of luminescence can be considered: cathodoluminescence (where the excitation source is a beam of electrons rather than light), electroluminescence (electrical current) chemiluminescence (chemical energy), triboluminescence (mechanical energy), and so on. Photoluminescence processes can be divided in two main steps that are typically represented in a *Jablonski diagram* as shown in Figure 1.1. The first is excitation, where energy is absorbed by an absorbing centre or 'sensitizer' (S) that is initially in its ground state S_0 and it is promoted to an excited state S_1^*. The second step is the return to the ground state. Here, the excited centre can either emit a photon (fluorescence, phosphorescence, delayed fluorescence) following - in some cases - internal conversion or intersystem crossing(s) processes, it can dissipate the energy in the form of heat, or it can transfer the energy to an 'Acceptor' (A) nearby. These steps are considered in more detail in the following sections.

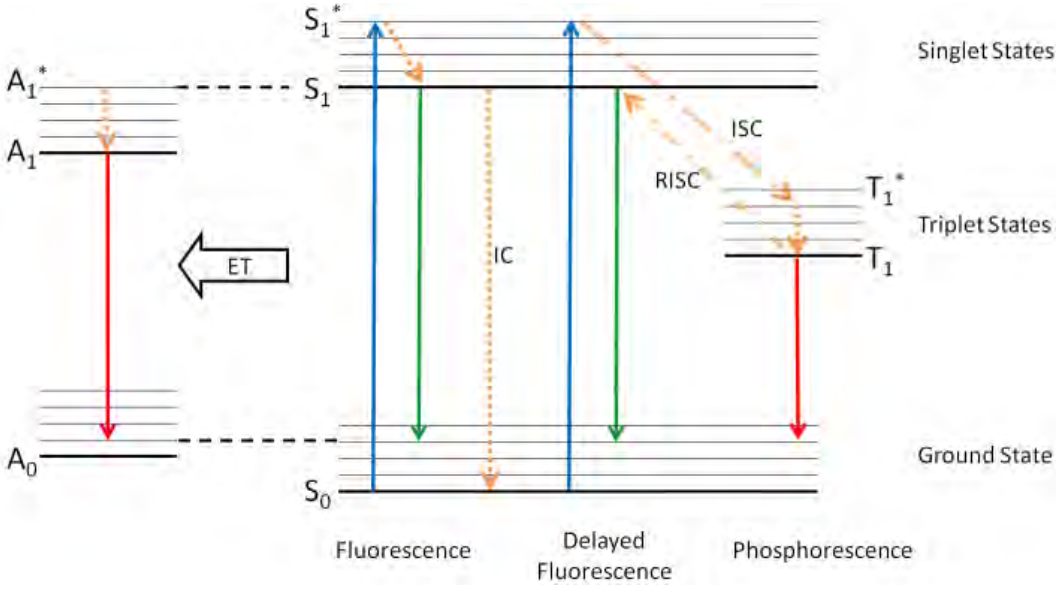

Figure 1.1: Jablonski diagram showing excitation, internal conversion (IC), fluorescence, intersystem crossing (ISC), reverse intersystem crossing (RISC), phosphorescence, delayed fluorescence and energy transfer processes (ET).

1.2.1 Photoexcitation of Luminescent Materials

To observe a luminescent response, it is necessary to consider which conditions are the appropriate for elevating the system into an excited state, *i.e.* how to give energy to the system efficiently. In the particular case of photoluminescence, it is important to consider the optical absorption spectrum of the material under study. The *configurational coordinate model* is often employed to explain optical properties of a material. This model recreates the potential energy curves of an absorbing centre as a function of a configurational coordinate [2, 3]. In the simplest case, an absorbing centre in

its ground state, $\boldsymbol{g}$, and its surrounding ligands are oscillating around an equilibrium distance R_0 in the so called 'breathing mode' (see Figure 1.2). This system can be modelled as a harmonic oscillator and as a result, its energy can be resolved in the form of a parabolic potential well as a function of the centre - ligand distance, R. Here, the potential well is composed of several discrete energy or vibrational levels, each of them with a characteristic wave function. It is important to note that in the lowest vibrational level, the highest probability of finding the system is at R_{g0}. By contrast, for the other levels the highest probability is located at the intersections with the parabola that describes the well. Once the centre has absorbed light, it passes from its ground state $\boldsymbol{g}$ to an excited state $\boldsymbol{e}$. Excited states can also be described as parabolic wells in the configurational coordinate diagram. However, the excited chemical bond between the absorbing centre and the ligand is altered (usually becoming weaker); as a result, the shape of the parabola and the equilibrium distance R_{e0} might be different from those of the ground state (Figure 1.2a).

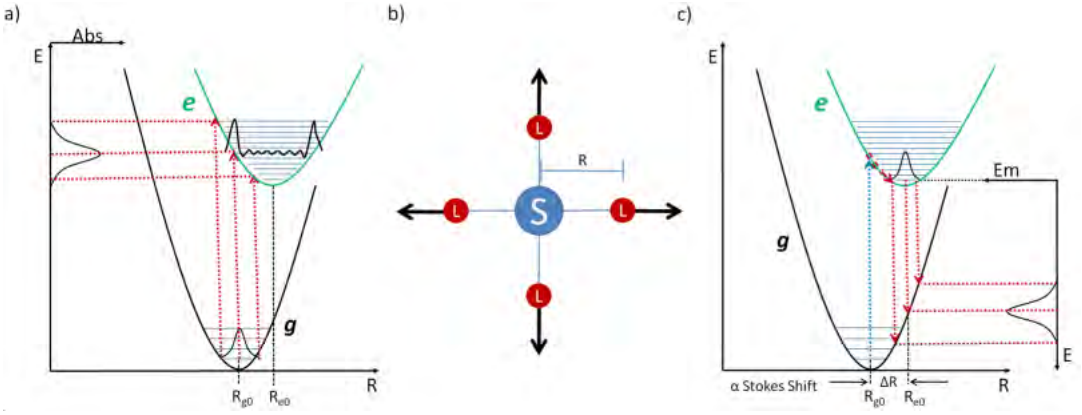

Figure 1.2: **a)** Configurational coordinate diagrams for the ground state and an excited state displaying the potential energy as a function of the parameter R for the system shown in b. The difference between the minimum of the parabolas ($\Delta R \neq 0$) gives rise to a broad absorption band. The ground state $\boldsymbol{g}$ and the excited state $\boldsymbol{e}$ have an equilibrium distance at R_{g0} and R_{e0}, respectively. The probability density functions for the lowest vibrational level of $\boldsymbol{g}$ and the level corresponding to the transition of maximum absorption in $\boldsymbol{e}$ are also displayed. **b)** Diagram illustrating an adsorbing centre and its four ligands oscillating in the symmetrical stretching or "breathing" mode. **c)** Once the system is excited, it relaxes by internal conversion to the lowest vibrational level of the excited state. The overlap of the wave function at this point with those functions of the vibronic levels of the ground state produces an emission band or ray depending on the difference of the equilibrium distances (ΔR) of the two potential wells

In an optical absorption event, an electron is promoted into a higher energetic level and as a result, the configuration of the system will correspond to a higher vibrational level in the excited state, $\boldsymbol{e}_n$. According to the *Franck-Condon principle*, an electronic transition happens without changes in the position of the absorbing centre or its surroundings. In fact, the promotion of an electron to an excited state can take around 10^{-15} s; this is too fast for rearrangement of the heavy nuclei of the atoms involved in the process [6]. Thus, the absorption of a photon is represented as a vertical transition in the configurational coordinate diagram. Assuming that the absorbing centre is initially at the lowest vibrational level of $\boldsymbol{g}$ and taking into account the overlap between its probability density function with those of the vibrational levels in $\boldsymbol{e}$, the optical absorption transition is more likely to happen at R_{g0}, towards the border

of the parabolic well of $\boldsymbol{e}$ (Figure 1.2a). It is precisely at this point that the maximum of the absorption band can be found (maximum overlap of both wave functions) [3]. However, it is also possible (although less likely), that the initial transition begins at $R > R_{g0}$ or $R < R_{g0}$. This situation will lead to transitions that will need a little more or a little less energy and, as a result, these variations give rise to a certain width of the absorption band. This configurational coordinate model allows us to explain the different features of band or line structure in the absorption and emission (*vide infra*) spectra of various materials and also their temperature and pressure dependence.

So far, we have described the origins of the optical absorption transitions and their width. Another feature that we will have to consider is the intensity of these transitions. Not every possible transition observed in the configurational coordinate diagram from $\boldsymbol{g}$ to $\boldsymbol{e}$ can happen as an optical transition. There are selection rules that make some of the transitions highly probable or *allowed* and very intense, some others less probable or *forbidden* and very weak in intensity. The principal selection rules are:

- *Laporte* or *parity selection rule*: Transitions that do not involve a change in parity (such as *d*-*d* and *f*-*f*) are forbidden ($\Delta l = \pm 1$).
- *Spin selection rule*: Transitions involving a change in spin multiplicity are forbidden ($\Delta S = 0$).

It should be stressed that these rules should not be considered as absolute. They can be relaxed due to wavefunction admixtures. For example, phenomena such as spin-orbit coupling, electron-vibration coupling and uneven crystal-field terms can partially allow forbidden transitions [3, 4]. An important consequence is that the absorption spectrum of a luminescent centre often differs depending on whether it is a free ion/molecule or embedded in a lattice surrounded by different types of ligands. One parameter often employed to compare the intensities of the absorption bands of a given material is the molar absorptivity (ϵ). This quantity reflects the ability of its active centres to absorb light at a given wavelength. It is usually expressed in units of $L \cdot mol^{-1} \cdot cm^{-1}$. Additionally, a quantity known as the oscillator strength (f) is also used for expressing the strength of a given transition. This dimensionless parameter can be calculated as shown in equation 1.1 (where n is the refractive index) from the area under the absorption band when its extinction coefficient is plotted as a function of the frequency ($\tilde{\nu}$, expressed in cm^{-1}) and not of the wavelength [6, 10].

$$f = \frac{4.32 \times 10^{-9}}{n} \int \epsilon(\tilde{\nu}) d\tilde{\nu}. \tag{1.1}$$

Table 1.1 gives approximate orders of magnitude for the extinction coefficients and the oscillator strengths of different absorption bands depending on their nature and the extent to which they are allowed for various transition metal complexes.

Finally, one should not forget that in addition to the transition probability, the absorption of a given material is also governed by other factors, such as the population

Type of Transition	Approximate f	Approximate ϵ
Spin-forbidden, Laporte forbidden	10^{-7}	0.1
Spin-allowed, Laporte forbidden	10^{-5}	10
Spin-allowed, Laporte allowed	10^{-1}	10000

Table 1.1: Typical orders of magnitude for oscillator strengths and extinction coefficients for different absorption bands present in various transition metal complexes [10]

of states, the path length (l) and the molar concentration of the active centres (c). This dependence is condensed in the *Lambert-Beer law* which states that the transmission (T) of light through a material is an exponential function of the product of ϵ, c, and l as it is shown in equation 1.2.

$$T = \frac{I}{I_0} = e^{-\epsilon lc}, \tag{1.2}$$

where I and I_0 are the transmitted and incident light intensities, respectively. Usually, equation 1.2 is employed in an alternative form in terms of optical density (OD) (or absorbance, A) instead of transmission as displayed in equation 1.3 [6].

$$OD = -log_{10}\frac{I}{I_0} = 0.434\epsilon lc = 0.434A. \tag{1.3}$$

1.2.2 Return to the Ground State

Once a luminescent system has absorbed energy, it has different options for returning to the ground state. These include radiative return to the ground state (emission), non-radiative return to the ground state and energy transfer between active sites. Obviously, this latter process is of central interest for the design of luminescent SCO materials.

1.2.2.1 Radiative Return

Once the system is promoted into a higher vibrational level of the excited state $\boldsymbol{e_n}$, it will rapidly relax to the lowest vibrational level of $\boldsymbol{e}$ by returning the excess energy to the surroundings. This can also be interpreted in the configurational coordinate diagram as the rearrangement of the positions between the optical centre and its ligands so that the new centre-ligand distance (R) is equal to the equilibrium distance R_{e0} of the excited state (see Figure 1.2). This process of disipating energy in the form of vibrations or heat is known as internal conversion and it is a significantly slower process ($\approx 10^{-13}$s - 10^{-12}s) than the electronic transitions [2, 3]. As soon as the system is at $\boldsymbol{e_0}$, it will be capable of returning to the ground state *via* spontaneous emission

of a photon with an energy that matches the energy gap between $\boldsymbol{e_0}$ and the energetic level of the ground state to which the system is restored, $\boldsymbol{g_n}$. The maximum of the emission will be found at the vertical transition obtained when the system is at R_{e0} and the crossing point with the ground state. Similarly to the absorption processes, an offset between the centres of the two potential wells will cause the overlap of the wave function associated with $\boldsymbol{e_0}$, with energy levels of the ground state at different values of R. As a result, when $\Delta R \neq 0$ the emission will be a band composed of several wavelengths and if $\Delta R \approx 0$ the emission will be close to a monochromatic ray [3]. After emission, the system will be in the ground state, but not necessarily in the lowest vibrational level. Thus, another process of internal conversion will take place in order to return the system once again to R_{g0}. From Figure 1.2c, we can infer that due to these non radiative relaxations, the emitted photons will be of the same or lower energy than the excitation, the difference being the so-called *Stokes shift*. The Stokes shift gives us direct information about the separation (ΔR) between $\boldsymbol{g}$ and $\boldsymbol{e}$. From the configurational coordinate diagram we are able to observe that the larger the Stokes shift is, the bigger ΔR will be and therefore the broader the emission band of the system. The significant consequence is that, the emission of a luminescent centre will be sensitive to the rigidity of its environment and the interactions with surrounding species. Additionally, it is also possible to confirm that the wavelengths where emission is observed (although due to different non radiative transitions not necessarily their intensities) will be virtually independent of the excitation energy, provided it is sufficient to populate the excited state.

In contrast to the absorption, where the key parameters for studying the phenomenon are the extinction coefficient and the oscillator strength, for luminescence the factors for characterizing the emission of a given system are the *luminescence lifetime* and the *quantum yield*. The former yields kinetic information about the emission events and the latter, the efficiency of the process. So far, the energy diagrams used to describe the luminescence have not taken into account the duration of the excited states or their possible decay and, as a result, the concept of lifetime is necessary. We can define the lifetime as the average duration of time a luminophore remains in the excited state following excitation [6]. A luminescent centre in its lowest excited state ($\boldsymbol{e_0}$) can relax to the ground state essentially in two ways: luminescent (radiative) pathways (L) and non-luminescent (non-radiative) pathways (NL). Depending on the amount of available deactivation options, the system will be prone to rapidly emit a photon (very high number of L's and low number of NL's), rapidly return to the ground state without emission (very low number of L's and high number of NL's) or remain at the excited state due to lack of options (very low number of L's and NL's). In other words, the higher the number of exit paths of a particular type (L or NL), the more likely the system is to take it. In this case it is possible to infer that there will be a certain probability per unit of time (rate) that the system will *exit the excited state via* either an emissive or a non-emissive transition derived from the number of relaxation pathways. Hence, the time 'T' at which the system leaves the excited state $\boldsymbol{e_0}$ is a continuous random variable with a *probability density function* (p.d.f) $p_T(t)$.

We are interested in characterizing T, where T is the random variable that describes the time after the excitation (at a time $t_0 = 0$) when the event "*leaving the excited*

state" happens to a luminophore. In order to do this, we can record the system as a function of time at fixed Δt intervals until the system relaxes at $T + \Delta t$. (The system will be still at the excited state at T.) With the knowledge that the ground state is the only state with an infinite lifetime, it is assured that the system will eventually relax to the ground state ($P(T > t_0) = 1$). Hence, the probability of leaving the excited state after the first time interval of observation at $t = t_0 + \Delta t$ (or remaining at the excited state during that interval) can be written as:

$$P(T > t_0 + \Delta t) = P(T > \Delta t) = (1 - (k_L + k_{NL}) \cdot \Delta t), \tag{1.4}$$

where k_L is the time independent probability per unit of time (rate) for spontaneous emission of a photon (Einstein's A coefficient) and k_{NL} is the time independent rate for leaving the excited state through a non-luminescent pathway [11]. These two rates are completely independent and their sum gives the total exit rate from the excited state.

It is worth noting that the system has no memory. If it has not yet left the excited state during a particular Δt interval, the probability of leaving the excited state after the following interval will still be the same as for the first one (*i.e.* $P(T > (n+1) \cdot \Delta t | T > n \cdot \Delta t) = P(T > \Delta t + t_0) = (1 - (k_L + k_{NL})\Delta t)$). Thus the probability of the system leaving the excited state after a time t (where $t = D \cdot \Delta t$), yields a series of dependent observations, in which the probability for all of them to happen is:

$$P(T > D \cdot \Delta t) = (1 - (k_L + k_{NL}) \cdot \Delta t)^D \quad \text{or} \tag{1.5}$$

$$P(T > t) = (1 - (k_L + k_{NL}) \cdot \Delta t/_D)^D. \tag{1.6}$$

If we make the time intervals very small ($\Delta t \to 0$), then the amount of observations for covering the same amount of time will increase in a manner such that $D \to \infty$; then we will obtain:

$$P(T > t) = lim_{D \to \infty}(1 - (k_L + k_{NL}) \cdot \Delta t/_D)^D, \tag{1.7}$$

$$P(T > t) = e^{-(k_L + k_{NL})t} \tag{1.8}$$

From equation 1.8 it is apparent that the random variable T is distributed exponentially and as a result, it has a *probability density function* as:

$$p_T(t) = \begin{cases} (k_L + k_{NL})e^{-(k_L + k_{NL})t} & , t \geq 0 \\ 0 & , t < 0 \end{cases} \tag{1.9}$$

The expected value of this random variable is also known as its lifetime (τ); this is the weighted average of all the possible values that the random variable (T) can take. Thus, the expected value of T will be:

$$< T > \; = \int_0^\infty t \cdot p_T(t) = \frac{1}{k_L + k_{NL}} \; . \tag{1.10}$$

Hence the expected value for the time at which a luminophore leaves the excited state or the lifetime of the excited state $\boldsymbol{e}$ (τ_e), is the inverse of the sum of its spontaneous emission rate (k_L) and non-luminescent decay rate (k_{NL}). If we think of a

material with a number, N_0, of identical excited centres that behave in the same manner, the population of the excited state of a material becomes:

$$N(t) = N_0 \cdot P(T > t) = N_0 e^{-(k_L + k_{NL})t} = N_0 e^{-t/\tau_e}, \tag{1.11}$$

where $P(T > t)$ is the probability of leaving the excited state after a given time t.

In order to estimate the efficiency of the luminescence for a given system, we can define the *quantum yield* (Q) as the ratio between the spontaneous emission rate of the active centre and its total exit rate from the excited state (Equation 1.12). Here, we will be able to measure how often the system will relax via a radiative pathway compared to its total relaxation processes to the ground state.

$$Q = \frac{k_{_L}}{k_{_L} + k_{_{NL}}} \tag{1.12}$$

The selection rules for absorption transitions also apply for emission processes. Even though populating an excited level that has different multiplicity to that of the ground state is unlikely to happen (spin selection rule), electrons in the excited state are susceptible to undergoing spin conversion and passing to a lower excited level with different multiplicity. This process is known as *intersystem crossing* (ISC). As a result, those electrons will be trapped in an excited state with a forbidden transition for returning to the ground state. As a consequence, there are two main emission processes that can be distinguished:

- *Fluorescence*: Luminescence obtained from the radiative return to the ground state without a change of the initial spin state of the system. Due to the allowed nature of the transition, it is a fast process and its lifetime is $\approx 10^{-7} - 10^{-5}$ s. This type of emission is usually illustrated by employing the particular case of an organic luminophore emitting a photon from an excited singlet state, S_1, to a singlet ground state, S_0.

- *Phosphorescence*: Luminescence obtained from the radiative return to the ground state from an excited energetic level of different spin multiplicity. Due to the forbidden nature of the transition (spin selection rule), it is a much slower process than fluorescence and its lifetime goes from $\approx 10^{-3}$ to 10^{0} s and more [2, 3]. Additionally, since the levels involved in the emission process are closer than in the case of fluorescence, the emitted photons are of lower energy (see Figure 1.1). Phosphorescence is often exemplified in the literature with molecules that emit a photon from an excited triplet state, T_1, to a singlet ground state, S_0. It is worth stating that due to the low emission rates of this process, phosphorescence can be mistaken with another emission mechanism denominated *delayed fluorescence*. In this case, following ISC, it is possible to return to the original excited state by thermal activation or by collision with another excited molecule (in solution) (*reverse intersystem crossing*, RISC) and then emit a photon in the same manner as in conventional fluorescence [8].

1.2.2.2 Non-Radiative Return

In a luminescent material, all energy that has been absorbed and has not been emitted in the form of radiation, must be dissipated in the form of heat to the surroundings via internal conversion. So far, we have seen that after the absorption event, the system relaxes to the lowest available excited state ($\boldsymbol{e}_0$). However, if we consider two potential wells with $\Delta R \neq 0$ and an excited state with sufficiently high energy, it is possible for the system to pass through a crossing point of the two potential wells and so transit non-radiatively to the ground state (Figure 1.3a). With this model is possible to explain the typical quenching of the luminescence with temperature or so called *thermal quenching*. At higher temperatures, higher energetic excited levels can be reached and the probability of finding a crossing point with the ground state (or another excited state) increases. It is also possible to observe that the greater the offset between the two parabolas, the more non-radiative transitions can be obtained. Conversely, if the two potential wells are centred and their shapes are alike (as often observed for strongly forbidden transitions), non-radiative transitions are unlikely to happen. As a result, luminescent centres with stiff surroundings that restrict expansion after optical excitation (ΔR), usually present less non-radiative processes, higher quantum yields and low thermal quenching [3].

It appears that non-radiative transitions are the primary competing processes for luminescence. However, we should also consider all those non-radiative transitions that may serve to feed an emitting level, as shown in Figure 1.3b. Supposing a strongly forbidden transition occurs between $\boldsymbol{g}$ and $\boldsymbol{e}$, the excited level will be difficult to populate. However, if there is also an additional excited level $\boldsymbol{e'}$ above $\boldsymbol{e}$ with an allowed optical transition from $\boldsymbol{g}$, it is possible for the system to find a crossing point between $\boldsymbol{e'}$ and $\boldsymbol{e}$ during the internal conversion. Thus, we will be able to effectively populate the excited state $\boldsymbol{e}$, circumventing its forbidden transition from the ground state [3]. From this point of view, it is clear that some sections of the bands observed in the absorption spectrum of a material may not display a luminescent response as the energy may be dissipated through non-radiative transitions. For this reason, while considering the luminescent response of a material, the *excitation spectrum* provides more information. In contrast to the absorption spectrum, where one observes how much light of a particular wavelength is absorbed by the material, in the excitation spectrum one measures the emission of the material at a fixed wavelength while varying the excitation source wavelength. In this way, the excitation spectrum will take into account not only where the system absorbs energy, but also which wavelengths produce an efficient luminescent response.

An additional phenomenon to consider within the context of non-radiative pathways for returning to the ground state is the photodesctruction of the system during the excited state or *photobleaching*. Usually in the case of molecular luminophores, each time they enter into an excited state, there is a probability per unit of time to be destroyed *via* a photochemical process (very often photo-oxidation) [12]. As a result, the luminophore may change irreversibly to a different molecular form that does not absorb or emit light. The photobleaching processes happen usually on a timescale of seconds or minutes (depending on the power of the excitation), making them practi-

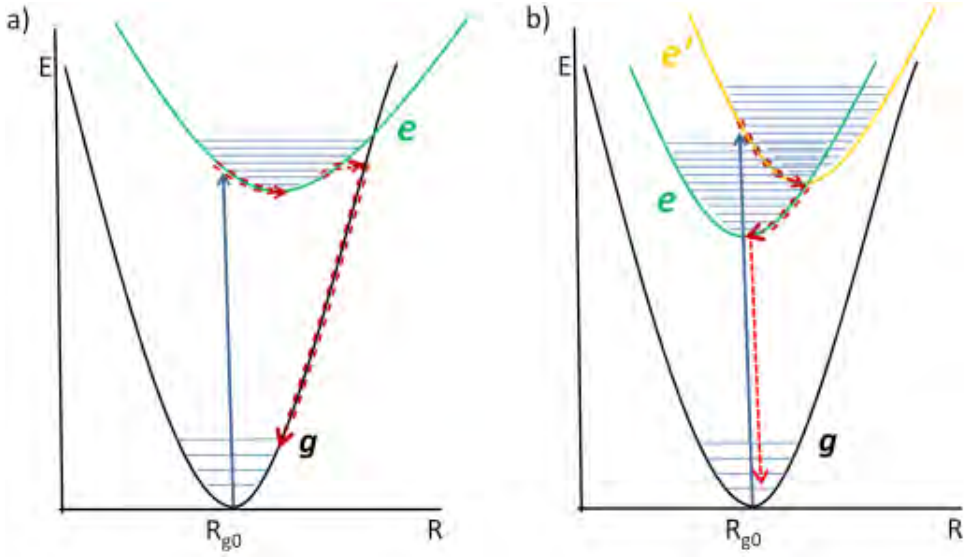

Figure 1.3: Configurational coordinate diagram of non-radiative processes: **a)** Non-radiative return from the excited state e to the ground state e via a crossing point of the two potential wells. **b)** Non-radiative transition from e' to e that effectively populates the emitting excited state e.

cally 10 orders of magnitude slower than fluorescence. Consequently, careful interpretation of the emission spectrum as a function of time is required, particularly in the case of experiments with long exposure times and/or high power excitation.

1.2.3 Energy Transfer

In the previous discussions of an excited state returning to the ground state by either radiative or non-radiative transitions, the excitation energy was dissipated to the surroundings by the same entity that absorbed it. However, it is important to also consider how the energy can flow from one place to another inside a given medium and the aspects that influence these processes. Indeed, these processes will actually constitute the mechanism by which a luminescent SCO material will function. In an energy transfer scheme, there are two entities: a sensitizer (S) responsible for absorbing the excitation energy and an acceptor (A) that will receive the energy of the excited sensitizer. The interaction between the two is described below.

1.2.3.1 Radiative Energy Transfer

Radiative energy transfer, also known as *emission - reabsorption* process is the "trivial" case where the sensitizer (S) absorbs energy, emits a photon and then the acceptor (A) reabsorbs the emitted photon. If the excited acceptor is a luminophore, it will emit a second photon and we will have cascade luminescence [3]. However, if the acceptor dissipates the energy a quenching effect (suppression of luminescence) will be observed. In a radiative energy transfer, both entities (sensitizer and acceptor) are independent of each other and do not interact directly. As a result, their excited state lifetimes will not be affected by the presence of the other.

The primary condition for radiative energy transfer to occur is that there should be a spectral overlap between the emission of S and the absorption of A; only photons emitted within this spectral window will participate in the transfer. The efficiency of the process (starting from the excitation event) will be influenced by the quantum yield of S (Q_s), and by the oscillator strength of A at the spectral overlap.

For radiative energy transfer, the distance that separates the sensitizer and the acceptor does not influence the event of absorbing the emitted photon. However, this regime will be ruled by the *Lambert-Beer law*. Even if the above mentioned criteria for the efficiency of the process are fulfilled, the emission of S will be absorbed by an A (there could be more than one acceptor) depending on the concentration of A and also on the geometry of the sample in consideration. In order to have reabsorption, it is necessary to have an acceptor in the pathway of the emitted photon. For example, at a fixed concentration, if the size of the sample is very small, there will be little chance for the emitted photon to find and acceptor.

1.2.3.2 Non-Radiative Energy Transfer

We consider a sensitizer-acceptor pair fixed in a material, separated by a distance, r_{SA}. If r_{SA} is sufficiently small that there is a non-vanishing interaction between them (such as a wave function overlap or an electric or magnetic multipolar interaction) and there is a spectral overlap between the two (resonance condition), there is a probability per unit of time that the energy is transferred from the sensitizer to the acceptor by a non-radiative process, *i.e.* without an emission and reabsorption of a photon [3]. In 1946, Theodor Förster introduced for the first time his theory of non-radiative resonant energy transfer between two interacting dipoles [13–15]. Later Dexter expanded the theory for higher order electromagnetic as well as for exchange interactions [16, 17]. One shall note that the energy transfer can be also non-resonant (phonon-assisted) and multi-step process (energy migration). In the following we will consider only the case of a single-step, Förster-type (dipolar) resonant energy transfer process and for further details on this topic we recommend the excellent review of Powell and Blasse [7].

In contrast to a radiative energy transfer, in a FRET (Förster resonance energy transfer) scheme the sensitizer and the acceptor are interacting with each other and they behave as if they were one whole system (See Figure 1.4). In the case of an electric dipole-dipole interaction, equation 1.13 defines the transfer rate (probability per unit of time) k_T for a given sensitizer-acceptor pair separated by a distance r_{SA} as:

$$k_T = \left(\frac{1}{\tau_S}\right)\left(\frac{R_0}{r_{SA}}\right)^6 , \tag{1.13}$$

where R_0 is the so-called Förster distance characteristic of the sensitizer-acceptor pair under consideration [6, 7, 11]. It represents the separation of the pair at which k_T equals the exit rate (k_S) from the excited state for S in absence of A; typical values for this distance range between 0.5 and 10 nm [11]. The rate k_S is the inverse of the lifetime of S (τ_S) and it includes all deactivation pathways of S other than the energy

transfer. The value of R_0 for a pair S-A is given by equation 1.14 [6]:

$$(R_0)^6 = \frac{9000(ln10)k^2Q_s}{N_A 128\pi^5 n^4}\left[\frac{\int_0^\infty \epsilon_A(\lambda)F_S(\lambda)\lambda^4 d\lambda}{\int_0^\infty F_S(\lambda)d\lambda}\right] . \tag{1.14}$$

Here, ϵ_A is the extinction coefficient of A expressed in units of $L \cdot mol^{-1} \cdot$ cm^{-1}, F_S is the luminescence intensity of S in arbitrary units, λ is the wavelength expressed in cm, n is the refractive index of the medium, Q_s is the quantum yield of S, N_A is Avogadro's number and k is a factor that describes the spatial orientation of the electric fields of the interacting dipoles of S and A. The value of k ranges between 0 and 4; however, if the orientation between the sensitizers and the acceptors in a given material is assumed to be random, its value is usually set to $^2/_3$ [11]. The ratio of the integrals inside the brackets is known as the overlap integral ($J(\lambda)$) and employing the units mentioned above, it will be expressed in $L \cdot mol^{-1} \cdot$ cm^3.

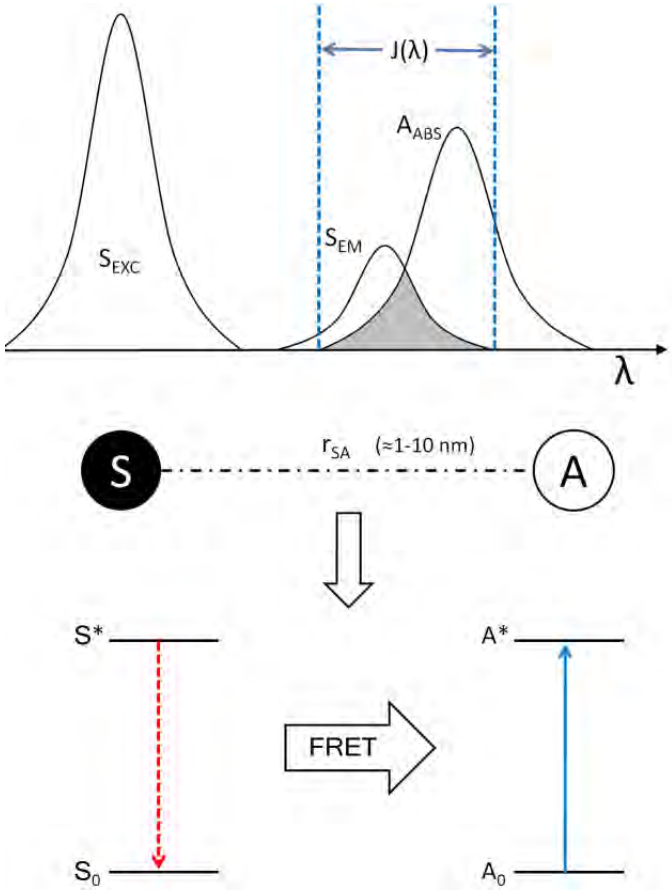

Figure 1.4: Schematic illustration of resonant energy transfer between the centres S and A

If a non-radiative energy transfer can take place between a given S-A pair, by exciting exclusively S and approaching A, the luminescence intensity and lifetime of the first decreases. The energy transfer towards A without an emission can be understood as an energy leak for S. It constitutes a relaxation pathway for the excited state of S, in addition to those which are inherent to it (luminescent and non-luminescent)

and under no circumstance it does modify them. As a result, whenever A is close enough, the lifetime of the excited state for S will be reduced and also its radiative response, not because the intrinsic radiative rate of S has been modified, but due to the additional exit from the excited state that FRET introduces. In presence of FRET the modified life time τ'_S of the sensitizer will be:

$$\tau'_S = (k_S + k_T)^{-1} = \left(\left(k_{L_S} + k_{NL_S}\right) + k_T \right)^{-1} , \tag{1.15}$$

$$\tau'_S = \left(\frac{1}{\tau_S} + k_T \right)^{-1} . \tag{1.16}$$

As seen in equation 1.13, the Förster resonance energy transfer is a phenomenon extremely sensitive to the distance between the sensitizer and the activator ($\alpha \cdot 1/R^6$). As a result, it is often used to measure distances between two moieties at particular places within a molecule before and after a configurational change. It may constitute a powerful tool for inferring spatial information below the diffraction limit by employing visible light. Additionally, if both the sensitizer and the acceptor are luminescent, the luminescence of A due to FRET can be employed as a marker to indicate the specific points where the two luminescent species, which were independently spread into a medium, come into contact. Another interesting application of FRET is the analysis of the local environment of the S-A pair. The non-radiative energy transfer is sensitive to fluctuations of the optical properties of the S-A pair; any change to their local environment could lead to a change of the orientation of the dipoles, emission and absorption spectra or quantum yields involved in the process and as a result, a drastic variation of k_T.

1.2.3.3 Self-Quenching

So far energy transfer has been considered only for different active centres. However, it is possible to have an energy transfer (radiative and/or non-radiative) between identical centres and this should be taken into consideration while characterizing the luminescent response of a particular system. This phenomenon is observed when the concentration of luminescent centres is very high and it is termed *inner filter*, *self-quenching* or *concentration quenching* by different authors [3, 6]. *A priori*, if the active centre has a large Stokes shift; it is unlikely to have an energy transfer (radiative or non-radiative) with another centre of the same type. However, if we consider luminophores with smaller Stokes shift, its excitation and emission bands can be broad enough to overlap. In a highly concentrated system, the separation between centres is small and the chance of having energy transfer increases dramatically. As a consequence, the excitation energy might be displaced more than once between different centres and travel long distances without an emission (energy migration). Thus, the probability of finding a quenching moiety, a defect in the material or a non-radiative transition increases; accordingly, the luminescent response measured under such saturated conditions will be of lower intensity than the response obtained from

a diluted sample. Furthermore, this quenching effect will be restricted only to the wavelengths involved in the spectral overlap of the excitation and emission spectra, and as a result, the measured emission spectrum will be deformed [6].

1.3 Introduction to the Spin Crossover

Certain $3d^4$ - $3d^7$ transition metal complexes display a change of electronic configuration between two states one with minimum spin or low spin state (LS) and another of maximum spin or high spin (HS) state after the application of an external stimulus; this phenomenon has been denominated spin crossover (SCO), spin transition or spin equilibrium [18]. The SCO triggered by temperature perturbation was first reported in 1931 by Camby *et al.*[19] on iron(III) dithiocarbamate complexes almost simultaneously to the publication of the ligand field theory by Bethe [20]; this theory made possible to describe these observations as a temperature dependent thermal equilibrium between the two possible ground states predicted for an octahedrally coordinated metal ion with a d^5 configuration. Besides the temperature, different perturbations can be employed to change the spin state of SCO systems: pressure, light irradiation, strong external magnetic fields or the inclusion of guest species in the environment of these complexes. The switching between the two spin states is accompanied by a significant change of molecular shape and volume due to the alteration of the characteristic metal-ligand distances in each state; hence, variations of the magnetic, optical, mechanical and electrical properties are expected upon the crossover [18, 21, 22].

The following sections provide a brief overview of the SCO phenomenon with a particular emphasis on iron (II) (d^6 electronic configuration) since it is the metallic center of the largest number of spin crossover compounds and also the one employed in this thesis.

1.3.1 SCO description with a Crystal Field Theory approach

The spin crossover phenomenon can be explained from a molecular point of view in a first attempt with a simplified version of the ligand field theory, the crystal field theory. This approach is an electrostatic model that describes the electron distribution in the d or f orbitals of a metallic ion under different symmetries [23]. In this model the interactions between a positively charged metal ion and a set of negatively charged ligands are considered purely electrostatic, cause of the coordination bonds and key factor for the stability of the complex. Additionally, the ligands are considered as punctual charges that determine the symmetry of the external electrostatic field affecting the metal ion and also, the electronic configuration of the metal ion is taken into account explicitly.

In general, if we consider a metal ion with a d^4 to d^7 electronic configuration in a perfect octahedral coordination, its electrons will experience a repulsive force coming from the ligands. This force is more or less intense depending on the orientation of

the orbital occupied by the electrons of the metal. Thus, the electrons are prone to occupy the d orbitals that are as far as possible from the direction of the ligands (*i.e.* the x, y and z axes) in order to minimize electrostatic repulsion. In fact, (see Figure 1.5) the orbitals $d_{x^2-y^2}$ and d_{z^2} (which have the lobes oriented along the coordinated axes) are destabilized by the presence of the negative charges of the ligands and hence, its energetic level will be raised; these two orbitals are anti-bonding and represent the basis of the irreducible representation e_g of the octahedral symmetry group (O_h). In contrast, the orbitals d_{xy}, d_{yz} and d_{xz} (which have their lobes oriented towards the bisectors of the axes) are less destabilized and consequently, their energetic level will be lower to that of the e_g orbitals. These three folded orbitals are basically non-bonding and represent the basis of the irreducible representation t_{2g} of the symmetry group O_h. As a result, a lift of the degeneracy of the valence orbitals d is observed under the influence of an octahedral electrostatic field. The splitting between these two sets of orbitals is represented by the parameter of the ligand field strength or crystal field splitting noted as 10Dq. The ligand field strength depends on both, the set of ligands and the coordinated metal ion; its value is a function of the metal ligand distance as $(1/r)^n$, with n=5-6 [23].

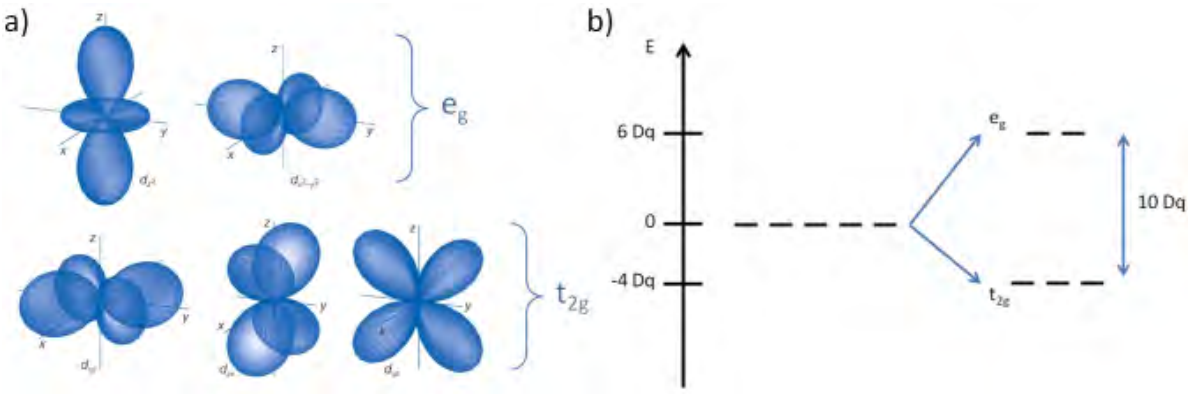

Figure 1.5: **a)**Representation of the 3d orbitals. **b)** Separation of the d orbitals in an octahedral ligand field induced by the ligand field strength 10Dq.

Additionally to the repulsive force coming from the ligand field described above, the electron-electron repulsion (or spin pairing energy Π) has to be taken into account while considering the Russell-Sounders coupling scheme and a metal ion with more than one d electron; this energy can be calculated as a function of the Racah parameters B and C for the electronic repulsion [23]. With these two factors in mind, two competing effects are observed. In one hand, a part of the d electrons tends to form a complete sub-shell (giving preference to those orbitals of lower energy and thus avoiding the repulsion of the ligand field) and on the other, the tendency of the d electrons to occupy the d orbitals according to Hund's rule (filling the orbitals with a maximum number of unpaired electrons). For the particular case of iron(II), it is possible to define two ground states with different distributions for the six d electrons depending on the magnitudes of 10Dq and Π (See Figure 1.6a):

- If Π > 10Dq, the six electrons will be distributed into the five d orbitals according

to Hund's rule with maximum spin multiplicity (2S+1=5). This paramagnetic ground state is denominated high spin state (HS).

- If $\Pi < 10Dq$, the six electrons will pair up in the t_2g orbitals with minimum spin multiplicity (2S+1=1). This diamagnetic ground state is denominated low spin state (LS).
- If $\Pi \approx 10Dq$, the SCO phenomenon can occur.

The origin of these two ground states can be observed in the Tanabe-Sugano diagram for the electron configuration d^6. This diagram plots the evolution of the separation between the electronic states relative to the ground state of a free metal d^6 ion under the influence of an octahedral ligand field as a function of the ligand field strength in units of the Racah parameter B (See Figure 1.6b). In fact, the origin of the term "spin crossover" lies in the crossover of the energy vs field strength curves for the possible ground state terms for ions of a particular d^n configuration in the Tanabe-Sugano and related diagrams [24, 25].

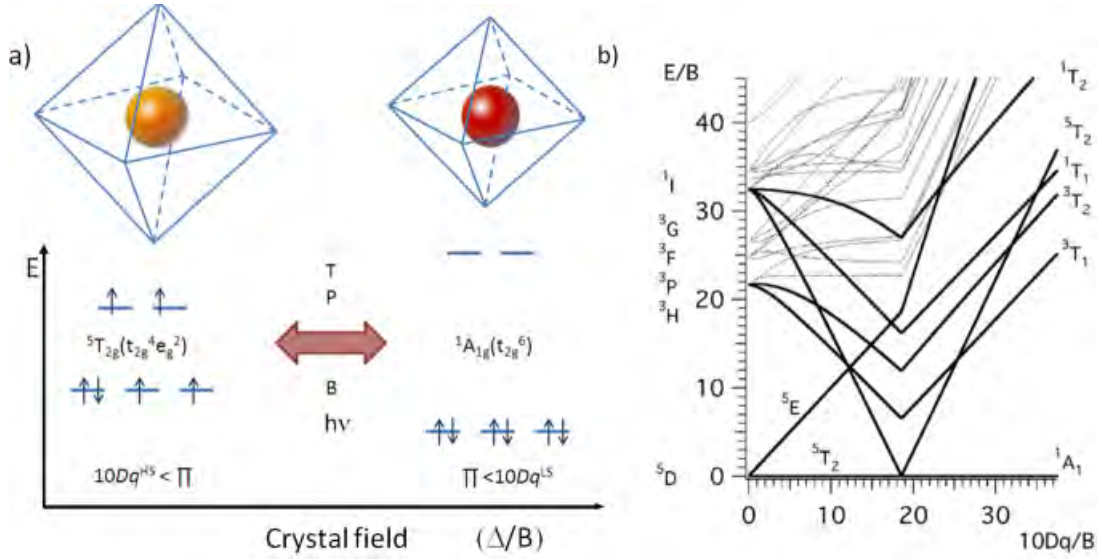

Figure 1.6: **a)** High spin (weak ligand field) and low spin (strong ligand field) electronic configurations of a $3d^6$ ion (Fe(II), Co(III)) in an octahedral complex. **b)** Tanabe-Sugano diagram for a transition metal ion with six d electrons.

In the Tanabe-Sugano diagram, the free ion ground state ^5D splits into the $^5T_{2g}$ high spin state described before as the ligand field increases (Π >10Dq). However, when the ligand field surpasses the critical value where it matches the electron-electron repulsion energy (Π=10Dq), the $^1A_{1g}$ state becomes the new electronic ground state. It is worth to note that for a given Fe-ligand pair their characteristic metal-ligand distance R in the LS state is shorter than in the HS state. This comes from the fact that in the high spin state, two electrons occupy the anti-bonding orbitals and in the low spin state, all of them are restricted to the non-bonding orbitals. In the particular case of Fe(II)-N coordination, R_{LS} is found to be between 1.95 and 2 Å; conversely, R_{HS} has typical values between 2.12 and 2.18Å ($\Delta R \approx 0.2$Å).

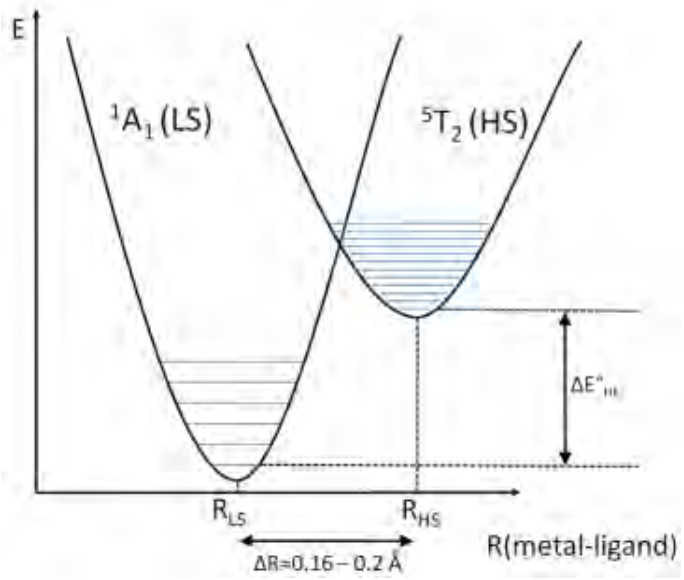

Figure 1.7: Potential energy of the high spin ($^5T_{2g}$) and low spin ($^1A_{1g}$) states along the totally symmetric metal - ligand stretching coordinate in the harmonic approximation.

The potential energy of the high spin ($^5T_{2g}$) and low spin ($^1A_{1g}$) states along the totally symmetric metal - ligand stretching coordinate in the harmonic approximation can be condensed as two parabolic potential wells, vertically and horizontally displaced relative to each other (See figure1.7). The vibrational energy (E^{vibr}) for the different levels can be calculated as:

$$E_i^{vibr}(n) = \left(n + \frac{1}{2}\right) h\nu_i \ , \tag{1.17}$$

$$\nu_i = \frac{1}{2\pi}\left(\frac{f_i}{\mu}\right)^{\frac{1}{2}} \ , \tag{1.18}$$

where μ is the reduced mass of the system and f_i is the bonding force constant characteristic of the state i (HS or LS). Since the chemical bond between the iron center and the ligands becomes weaker when their separation increases, $f_{LS} > f_{HS}$; thus, the number of vibrational level per energy unit will be higher in the high spin state than in the low spin state (*i.e.* the separation of the energy levels in LS is more important than in HS). The energy difference between the lowest vibrational modes ($n = 0$) of the LS and HS potential wells is denominated zero-point energy difference ($\Delta E^0 = E^0_{HS} - E^0_{LS}$). From Figure 1.7 it is possible to observe that the condition for having a thermal spin transition is that ΔE^0 has to be of the order of thermally accessible energies k_BT. This way, complexes at low temperatures are in the low spin state and as the temperature increases, an entropy-driven population of the high-spin state will be observed. There are essentially two reasons for the entropy difference between the two spin states: the higher spin degeneracy of the HS state compared to the LS state and the higher density of vibrational states of the HS state. Even though the low spin state is the quantum mechanical ground state at all temperatures, at high temperatures it is the high spin state the thermodynamically stable ground state.

During the transition, the metal-ligand distance changes abruptly and as a result, the ligand field strength will change as well. It is possible to estimate the ratio between the strengths in the two spin states as [23]:

$$\frac{10Dq^{LS}}{10Dq^{HS}} = \left(\frac{R_{HS}}{R_{LS}}\right)^{n} \tag{1.19}$$

with n=5-6. Considering average values for R_{HS}=2.2Å and R_{LS}=2.0Å for the case of Fe-N coordination and n=6, the ratio is ≈ 1.7. With the knowledge of the metal-ligand distance dependence of 10Dq and the fact that the electron-electron repulsion (II) changes very little between the two spin states, ΔE^0 can be calculated as a function of $10Dq^{LS}$ or $10Dq^{HS}$ from the Tanabe-Sugano diagram as it is illustrated in Figure 1.8. From this diagram it is possible to deduce 3 relevant intervals for the thermal spin transition [23]:

- If $10Dq^{HS} < 10000$ cm^{-1}, $\Delta E^0 < 0$ and as a result HS will be the thermodynamically stable ground state at all temperatures.
- If $10Dq^{LS} > 23000$ cm^{-1}, $\Delta E^0 > 2000$ cm^{-1} and as a result the LS state will be the ground state even at very high temperatures.
- If 11000 cm^{-1} $< 10Dq^{HS} <$ 12500 cm^{-1} and 19000 cm^{-1} $< 10Dq^{LS} <$ 22000 cm^{-1}, then $0 < \Delta E^0 <$ 2000 cm^{-1} and the thermal spin crossover can be expected.

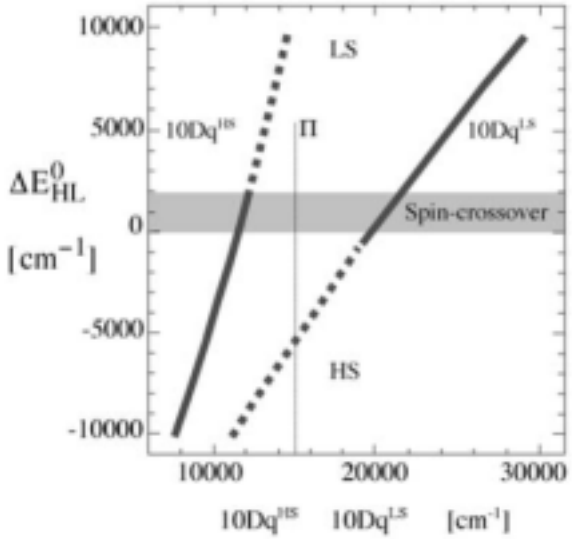

Figure 1.8: Regions of stability of either one or the other spin state as a function of the ligand field strength. The region of spin crossover compounds is indicated by the shaded area. This plot corresponds to a typical Fe(II)N_6 coordination compound under consideration [23].

1.3.2 Entropic Origin of the Thermal Spin Crossover

In the simplest scenario, it is possible to describe the SCO phenomenon as the equilibrium between two phases in a system constituted by an assembly of isolated SCO molecules without interaction with each other. Under common experimental conditions (T *isothermal*, P *isobaric*, N ensemble), the thermodynamical function for this particular system is the Gibbs free energy variation $\Delta G = \Delta G_{HS} - \Delta G_{LS}$ between the HS and LS phases:

$$\Delta G = \Delta H - T\Delta S \ , \tag{1.20}$$

where ΔH and ΔS correspond to the enthalpy and entropy variations during the transition $LS \rightarrow HS$, respectively. Equation 1.20 shows that at low temperatures, the system is dominated by the term of the enthalpy; conversely, at high temperatures is the term of the entropy that becomes the dominant factor privileging the *statistical disorder*. ΔH can be divided into two contributions, an electronic part ΔH_{el} estimated in 0 - 1000 cm^{-1} (0 - 12000 $J{\cdot}mol^{-1}$) and a vibrational part ΔH_{vibr} estimated in 100 cm^{-1} (1200 $J{\cdot}mol^{-1}$)[26, 27]. Hence, we can assume that the main contribution to ΔH is in most cases electronic ($\Delta H \approx \Delta H_{el}$) and its sign is always positive during a $LS \rightarrow HS$ transition.

The entropy variation ΔS has also two different parts. First, there is an electronic contribution ΔS_{el} that is attributed to the change of the total spin momentum S (ΔS_{el}^{spin}) and the change of the angular orbital momentum L (ΔS_{el}^{orb}) when a $LS \rightarrow HS$ transition takes place. These two quantities can be written as a function of the ratio of the spin and orbital multiplicities in the two molecular states:

$$\Delta S_{el}^{spin} = N_a k_b ln\left(\frac{2S_{HS}+1}{2S_{LS}+1}\right) \ , \tag{1.21}$$

$$\Delta S_{el}^{orb} = N_a k_b ln\left(\frac{2L_{HS}+1}{2L_{LS}+1}\right) \ , \tag{1.22}$$

where N_a and k_b are the Avogadro's number and the Boltzmann constant, respectively. However, the orbital degeneracy is taken only in the case of a perfect octahedral symmetry which is unusual for the complexes of molecular systems. In consequence, most of the times the approximation $\Delta S \approx S_{el}^{spin}$ and in the case of a spin transition between $^1A_1$ and $^5T_2$, $\Delta S_{el}^{spin} = 13.38$ $J{\cdot}K^{-1}{\cdot}mol^{-1}$ [26, 27].

Heat capacity measurements in Fe(II) based SCO complexes have demonstrated that the ΔS_{Total} during the spin crossover has typical values between 40 $J{\cdot}K^{-1}{\cdot}mol^{-1}$ and 80 $J{\cdot}K^{-1}{\cdot}mol^{-1}$[28]. Since these values are considerably higher to that of a simple change of spin multiplicity during the transition, an additional contribution of vibrational origin ΔS_{vib} has to be considered. This contribution comes mainly from the stretching mode of the elongating distance Fe-N and also from the distortional modes of the octahedron FeN_6 (15 vibrational modes). Additionally, it is worth noting that the degeneracy of vibrational origin is higher in the HS state than that of the LS state (See section 1.3.1), then during a $LS \rightarrow HS$ SCO there will be a large increase of the statistical disorder.

As a result, it is possible to conclude that at low temperature ΔH_{el} is the dominant term and the LS state is stable; in the contrary, as the temperature increases the entropic term $T\Delta S_{Total}$ becomes more important and the state with higher degeneracy becomes stable, *i.e.* the HS state. Furthermore, there is a temperature of equilibrium (T_{eq}) at which $G_{HS} = G_{LS}$. It is obtained when the quantity of molecules in the HS and LS state are the same; from equation 1.20 we can infer that $T_{eq} = \Delta H_{el}/\Delta S$. Hence, the thermal SCO is governed by entropic phenomena of mainly vibrational origin ($\approx 70\%$) [29].

1.3.3 Characteristics of the Thermal SCO and Notions about the Cooperativity in SCO solids

The thermal spin transition curve is usually obtained by plotting the high spin fraction (γ_{HS}, it is an order parameter that defines the mean number of molecules in the HS state) as a function of temperature. One parameter deduced from this type of curves for characterizing the response of a particular SCO system is the transition (or equilibrium) temperature (T_{eq})[18].

Even though the origin of the spin crossover is purely molecular, the macroscopic manifestation of the phenomenon is the result of the cooperative interactions of the molecules that compose the bulk material. The cooperativity comes mainly from the different volume that a SCO molecule ocupies in each spin state; thus the lattice properties of the material determine how the changes in the metal-donor atom distances propagate through a given SCO solid. From this point of view, the cooperativity has mainly an elastic origin that gives place to a combination of complex short and long range interactions. In a first approximation, these interactions can be understood as an internal stress that increments as the LS fraction increases and it influences all the molecules of a crystal with the same "intensity" and independently of the distances [30].

It is possible to model the continuous, discontinuous (or abrupt) and the hysteresis character or even the equilibrium temperature T_{eq} employing the thermodynamic of phase transitions according to Slichter and Drickamer[31]. If a number N of molecules that can undergo SCO is considered, each of these molecules could exist in the HS or in the LS state; hence, it is possible to define the molar fraction (γ) of the molecules HS as γ_{HS} and the LS molar fraction as $\gamma_{LS} = 1 - \gamma_{HS}$. In absence of intermolecular interactions, it is possible to introduce in the Gibbs free energy expression (G) a mixture entropy term (S_{mix}) that represents the different distribution possibilities for the HS and LS population of N molecules. This term is expressed as:

$$S_{mix} = -R\left[\gamma_{HS} ln(\gamma_{HS}) - (1-\gamma_{HS}) ln(1-\gamma_{HS})\right], \tag{1.23}$$

where R is the the gas constant. S_{mix} is maximum for $\gamma_{HS} = 0.5$ and it will disappear for $\gamma_{HS} = 0$ or $\gamma_{HS} = 1$. By taking into account the S_{mix} term, the Gibbs free energy becomes:

$$G = \gamma_{HS} G_{HS} + (1-\gamma_{HS}) G_{LS} - TS_{mix}, \tag{1.24}$$

with G_{HS} and G_{LS} corresponding to the Gibbs free energies for the electronic states HS and LS, respectively. The partial derivate of G as a function of γ_{HS} is:

$$\left(\frac{\partial G}{\partial \gamma_{HS}}\right) = \Delta G + RTln\left(\frac{\gamma_{HS}}{1-\gamma_{HS}}\right). \tag{1.25}$$

The condition for having a thermodynamical equilibrium in the SCO at constant temperatures and pressures is:

$$\left(\frac{\partial G}{\partial \gamma_{HS}}\right)_{T,P} = 0 \ , \tag{1.26}$$

in consequence:

$$ln\left(\frac{1-\gamma_{HS}}{\gamma_{HS}}\right) = \frac{\Delta G}{RT} = \frac{\Delta H}{RT} - \frac{\Delta S}{R} \ . \tag{1.27}$$

Then, by taking into account that $\Delta G = 0$ when $\gamma_{HS} = \gamma_{LS} = 0.5$ and consequently that $T_{eq} = \Delta H/\Delta S$ we obtain:

$$\gamma_{HS} = \frac{1}{1 + e^{\left[\frac{\Delta H}{R}\left(\frac{1}{T} - \frac{1}{T_{eq}}\right)\right]}} \tag{1.28}$$

When the SCO molecules are in the solid state, the molecular interactions play an important role in the SCO properties present in the material. These were introduced in the model of Slichter and Drickamer with an interaction term, G_{int}:

$$G_{int} = \Gamma\gamma_{HS}(1-\gamma_{HS}) \ , \tag{1.29}$$

where Γ is an effective cooperativity parameter [31]. It represents the tendency for a molecule or an active center in a given spin state to be surrounded by molecules or active centers with the same spin state. Indeed, Γ reflects the transmission efficiency of the structural changes associated to the SCO through the crystal *via* the molecular interactions. This efficiency is responsible of the manifestation of the cooperative phenomenon in physical properties of the system. The free enthalpy of the system including the interaction term G_{int} is written as:

$$G = \gamma_{HS}G_{HS} + (1-n_{HS})G_{BS} - TS_{mix} + \Gamma\gamma_{HS}(1-\gamma_{HS}) \ . \tag{1.30}$$

If G_{BS} is considered the origin of energies, it is possible to write:

$$G = \gamma_{HS}\Delta H + \Gamma\gamma_{HS}(1-\gamma_{HS}) - RT\left[(1-\gamma_{HS})ln(1-\gamma_{HS}) + \gamma_{HS}ln(\gamma_{HS}) + \gamma_{HS}\Delta S/R\right] \ . \tag{1.31}$$

Considering again the equilibrum condition for the system (equation 1.26), it is possible to determine the temperature of the system as a function of γ_{HS}:

$$T(\gamma_{HS}) = \frac{\Delta H + \Gamma(1-2\gamma_{HS})}{Rln\left(\frac{1-\gamma_{HS}}{\gamma_{HS}}\right) + \Delta S}. \tag{1.32}$$

Equation 1.32 allows us to describe various types of SCO (see Figure 1.9):

- $\Gamma = 0$: There are not molecular interactions and it is possible to express γ_{HS} as a function of T:

$$\gamma_{HS} = \frac{e^{\frac{\Delta S}{R}}}{e^{\frac{\Delta S}{R}} + e^{\frac{\Delta H}{RT}}}; \tag{1.33}$$

  as a result, the thermal population of the spin states is done following a Boltzmann type distribution, characteristic of a gradual conversion, called spin conversion.

- $\Gamma < 2RT_{eq}$: Describes also a gradual conversion, typical of weak molecular interactions. In this range, $\frac{dT}{d\gamma_{HS}}$ is positive for $0 < \gamma_{HS} < 1$; thus, the crossover is gradual and without hysteresis.

- $\Gamma \approx 2RT_{eq}$: Case of systems where the molecular interactions are strong. Here, $\frac{dT}{d\gamma_{HS}}$ is positive but it becomes zero for $\gamma_{HS} = 0.5$; thus, the transition is sharp and without hysteresis.

- $\Gamma > 2RT_{eq}$: Systems where the molecular interactions are very strong. Under these conditions, the equation 1.32 presents a local minimum and a local maximum that indicates the presence of a thermal hysteresis.

The most important types of thermal SCO curves are summarized in Figure 1.10. The gradual conversion also known as spin equilibrium is displayed in Figure 1.10a and it is possibly the most commonly observed. As we have already seen, in the solid state and in presence of strong cooperativity, the observed transition may be abrupt (discontinuous or first-order) (Figure 1.10b) and when the cooperativity is high enough, the system may display a response with hysteresis (Figure 1.10c). This type of transitions are defined by two "transition temperatures", one for decreasing "overcooling" ($T_{1/2}\downarrow$), and one for increasing temperature "overheating"($T_{1/2}\uparrow$). Two main factors are responsible of the hysteresis in the SCO phenomenon: first, the transition may be accompanied by a structural phase change in the lattice and second, the intramolecular structural changes than take place upon the transition may be propagated to the surrounding molecules due to strong elastic interactions between them. Furthermore, it is worth to note that this bistability feature allows the observation of the system in two different spin states within a certain range of external stimulus (memory effect)[18]. This hysteresis is associated with a phase separation process that takes place usually by nucleation and growth [32].

It is also possible to find two step transitions due to different factors (Figure 1.10 d). Crystals with two different lattice sites for the SCO molecules [33] or binuclear systems can also display this type of response [34]. In the latter case, even though the surroundings of each metallic ion are similar (even identical), the spin transition of one metal center may interfere with the transition of a second one. Furthermore, systems that present only a single lattice site may transit in two steps with spontaneous symmetry breaking [35]; this observation has been assimilated as short "antiferro-like" range interactions that generate a preferential formation of HS/LS pairs upon the crossover[36].

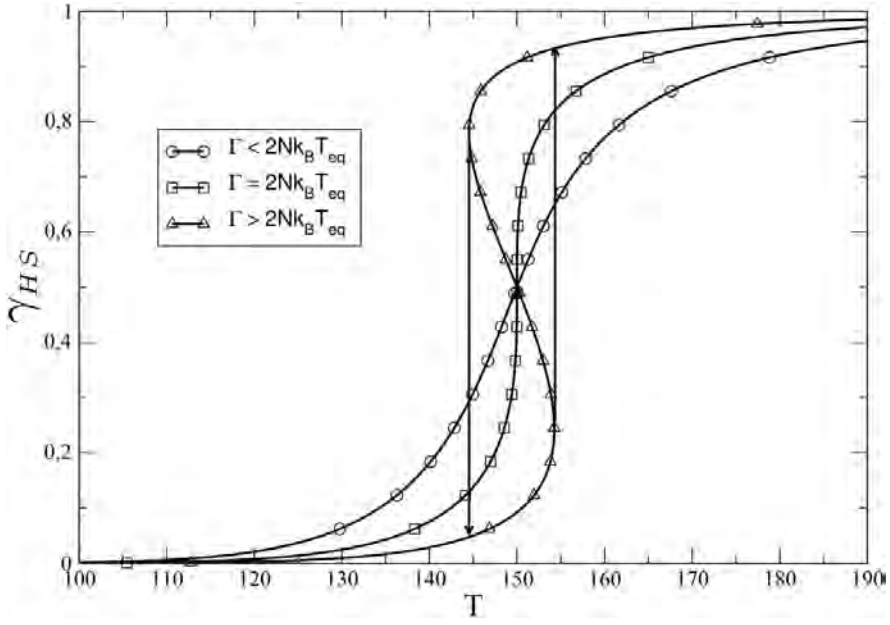

Figure 1.9: Slichter and Drickamer Model: evolution of the γ_{HS} as a function of the temperature T for three different values of Γ, $\Gamma = 1500\ J \cdot mol^{-1} < 2Nk_bT_{eq}$, $\Gamma = 2500\ J \cdot mol^{-1} = 2Nk_bT_{eq}$, $\Gamma = 3000\ J \cdot mol^{-1} > 2Nk_bT_{eq}$ that reproduce the state change observed for complexes weakly cooperative, cooperative and strongly cooperative, respectively. The values of the parameters are $T_{eq} = \Delta H/\Delta S = 150\ K$ with $\Delta H = 12000\ J \cdot mol^{-1}$ and $\Delta S = 80\ J \cdot K^{-1} \cdot mol^{-1}$.

Besides the transition temperature and key information about the degree of cooperativity associated with the transition, the high spin fraction plot as a function of temperature may provide other valuable informations such as the completeness of the transition by judging the remaining "residual HS fraction" at low temperatures and/or "LS fraction" at high temperatures (Figure 1.10e). The observations of such fractions in the limits of the transition may have diverse origins. For example, a few SCO molecules could be located in a different lattice site where the crystal field is strong enough or weak enough in order to prevent the formation of high spin species (LS fraction) or low spin species (HS fraction). Also, it can be that the structural change or local disorders that accompany the SCO may not occur in particular zones of the crystal. Additionally, kinetics effects at very low temperatures can produce also residual HS species; if the rate of high spin to low spin transition is small enough, it is possible under specific experimental conditions to "freeze" an important amount of HS molecules by decreasing the temperature of the sample abruptly [5].

1.3.4 Electronic Transitions and Optical Properties of Spin Crossover Complexes

The change of the spin state of the molecule naturally leads to a complete change of its electronic absorption spectrum. For example, in the case of an octahedral complex with $3d^6$ electronic configuration (Fe(II) , Co(III)), we have seen that the ground state of the molecule may change from the singlet ($^1A_{1g}$) LS to the quintet ($^5T_{2g}$) HS electronic configuration (Figure 1.11). According to the Franck-Condon principle, the geometry

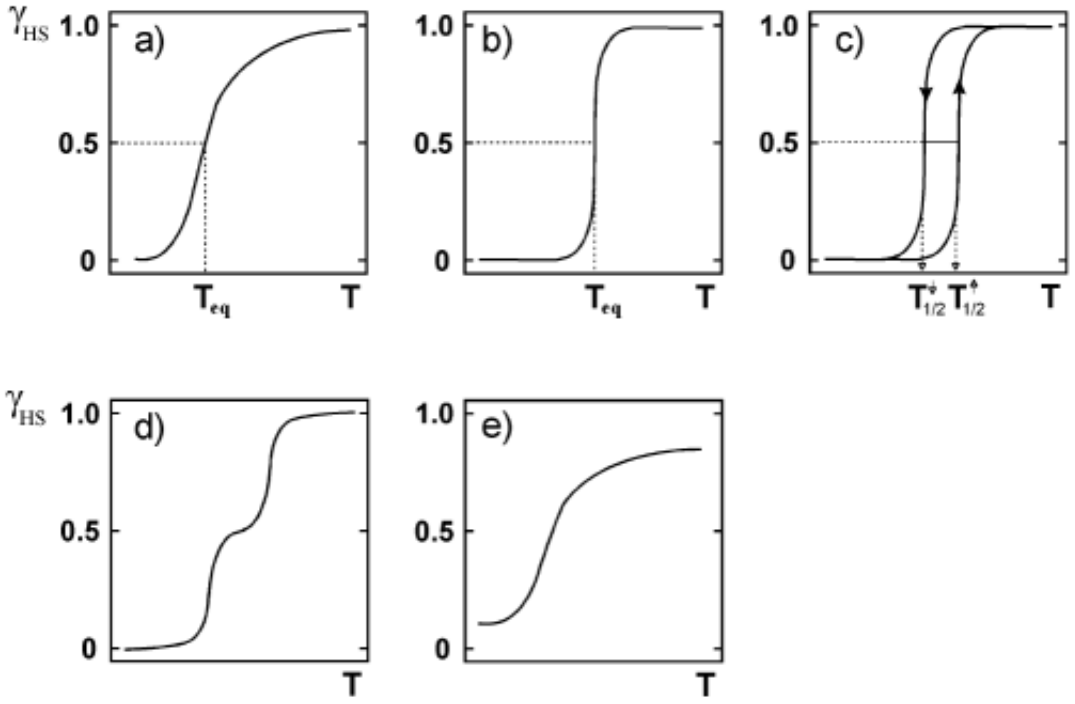

Figure 1.10: Principal types of thermal SCO responses plotting the high spin fraction (γ_{HS}) as a function of temperature. **a)** gradual, **b)** abrupt, **c)** with hysteresis, **d)** two steps and **e)** incomplete.

of a molecule does not change within the 10^{-15} s of an optical absorption process. Thus during the absorption of a photon in a SCO molecule, the metal-ligand distance will not change and hence, the optical transitions of such molecule can be represented as vertical transitions in the Tanabe-Sugano diagram (Figure 1.6b). From this, it is clear that in the HS state there is only one spin-allowed metal-centred *d-d* transition ($^5T_2 \rightarrow {}^5E$), while in the LS state there are two transitions of this type ($^1A_1 \rightarrow {}^1T_1$,$^1A_1 \rightarrow {}^1T_2$). In addition, weak spin-forbidden transitions ($^1A_1 \rightarrow {}^3T_1$,$^1A_1 \rightarrow {}^3T_2$) can be also detected in the LS spectra.

The SCO phenomenon is always accompanied by a color change (thermo/ piezo / vapor /photo -chromism). Due to the fact that the spin crossover phenomenon occurs for a relatively narrow range of ligand field strengths, the visible absorption spectra of different SCO complexes with the same metal ion and the same donor atoms (*e.g.* $Fe(II)N_6$) are expected to be fairly similar. In reality, however, the colour of the compounds can be rather different due to the occurrence of various charge transfer transitions in the visible range. In particular, metal-ligand charge transfer (MLCT) bands are often observed for ligands with extended π electron systems [18]. Charge transfer transitions involving molecular orbitals located primarily on the metal ion will be inevitably altered by its spin state. Since these transitions are usually very intense when compared to the relatively weak (Laporte forbidden) *d-d* ligand-field transitions they can completely dominate the perceptible colour of the sample.

As an example, Figure 1.11 shows the single crystal optical absorption spectra of the SCO complex $[Fe(bbtr)_3](ClO_4)_2$ (where bbtr stands for 1,4-di(1,2,3-triazol-1-yl)) in the visible and near-infrared (NIR) wavelength ranges [37]. In the high temperature

(HS) state the sample is nearly transparent and only a weak, broad absorption is observed in the NIR around 830 nm, which can be assigned to the $^5T_2 \rightarrow {}^5E$ transition. On the other hand, in the low temperature (LS) state the sample displays a purple colour due to an absorption band centred at $\approx$ 590 nm, which can be assigned to the $^1A_1 \rightarrow {}^1T_1$ transition. The molar extinction coefficients for these metal-centred transitions are rather low: they span from a few to a few tens of $dm^3 \cdot mol^{-1} \cdot cm^{-1}$. In the LS state, however, one can also observe the onset of a very strong absorption below ca. 430 nm, which is an indication of the possible occurrence of intense singlet charge transfer transition(s) in the UV region.

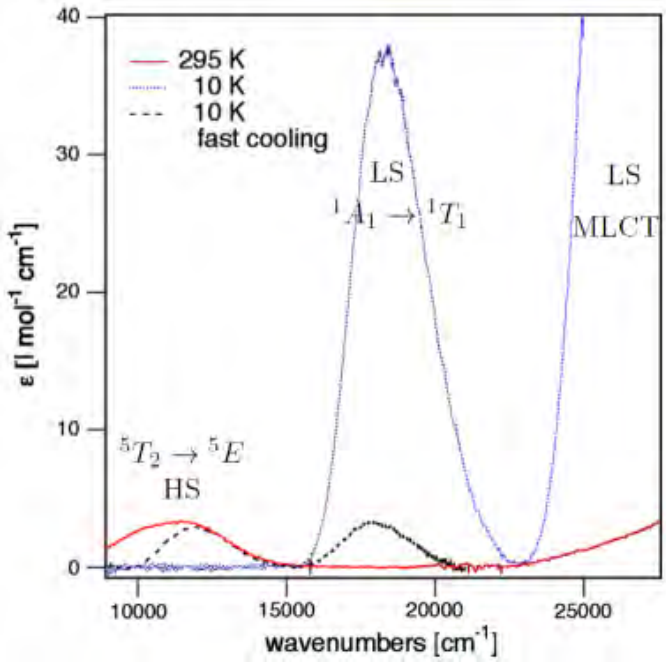

Figure 1.11: Single crystal absorption spectrum of $[Fe(bbtr)_3](ClO_4)_2$ at 295 K (red) and at 10 K on slow cooling (blue) and after temperature quenching (black) [37].

SCO materials exhibit also important changes of the refractive index through the whole UV - VIS -NIR spectral ranges due primarily to the important density change accompanying the spin state change. This strong electron - lattice coupling arises from the different population of anti-bonding *eg* and non-bonding t_{2g} orbitals of the Fe(II) ion in the two spin states (Figure 1.6a). The volume of the octahedron defined by the six bonding nitrogen atoms around the Fe(II) ion is typically 25-30% higher in the HS state leading to a unit cell expansion $\Delta V_{HL}/V$ typically between 1 and 10%, depending on the nature of the compound. As a consequence of this significant density change, one should expect a change of the real part of the refractive index upon SCO in the range between $\Delta n_{HL} = n_{HS} - n_{LS} = 0.01 - 0.1$ (In the case of $Fe(II)(hptrz)_3(OTs)_2$ (where *hptrz*=4-heptyl-1,2,4-triazole), our team has found a decrease of the real part of the refractive index $\Delta n_{HL} = -0.01$ accompanying the $^1A \rightarrow {}^5T$ spin transition[38]). In addition to this material density change, one shall consider also the change of the electronic polarizability of the complex [21]. This effect will be particularly important for wavelengths in the vicinity of intense charge transfer transitions.

1.3.5 Examples of SCO materials

Although there are many different families of SCO complexes, we will focus this section on two in particular: Fe-triazoles and Hofmann clathrates. Since 2005, our team has devoted its efforts into the synthesis and physico-chemical characterization for various members of these two families. One of the main motivations for working with these types of compounds is their characteristic transition around room temperature. It is precisely this feature that has allowed the team to create promising research axes towards the development of SCO based photonic devices for gas and temperature sensing applications employing diverse techniques such as surface plasmon resonance (SPR), diffraction gratings and in the frame of this thesis, luminescence.

1.3.5.1 Fe-Triazoles

There is a limited number of SCO complexes with the form of polymer chains with the ligand 1,2,4-triazole (trz) [39]. This type of coordination polymers are composed of 1D "polymeric" chains of triazole-bridged metal ions with counter anions and water molecules situated between the chains in a non coordinated manner [40, 41]. This family of systems presents abrupt spin transitions and even hysteresis that can be as large as 50 K (for example, See Figure 1.12). This high cooperativity can be due to the short Fe-Fe distances and also the rigidity of the triazole ligands and its covalent connectivity.

The SCO behavior of these compounds can be influenced by different factors:

- Substitutions in the position N4 of the triazole ligand (Symbolized by the letter R in Figure 1.12a): the force of the donor at this position when modified has a direct influence on the ligand field around the SCO center and as a result, T_{eq} will be shifted [42, 43]. Also, the substitutes in position 4 of the triazole ligand can also have a strong influence on the size of the chain and, by the same token, on the cooperativity of the system [41].

- Type of counter anions: the nature of the anion has also an effect on T_{eq} depending on its size and its ability to form intermolecular bonds. In fact, it has been reported that the transition temperature can be shifted by 150 K by changing the counter anion of the complex in a series of the triazole derivative [Fe(4-amyl-trz)$_3$](A$_2$) A = ClO_4^-, BF_4^-, triflate, p-toluenesulfonate (See Figure 1.13)[41]. Furthermore, it has also been demonstrated that there is a correlation between the radius of the counter anion and T_{eq} for the polynuclear triazole compounds [Fe(hyetrz)$_3$](X)$_2$·H$_2$O (hyetrz=4-(2'-hyroxyethyl)-1,2,4-triazole, X = Cl^-, NO_3^-, Br^-, I^-, BF_4^-, ClO_4^-, PF_6^-)[44]. The compounds containing the more voluminous counter anion display the lower transition temperatures [45].

- Type and concentration of molecules inserted between chains: for example, reference [44] also showed that the presence of non-coordinated water molecules play a crucial role in the stabilization of the LS state; conversely the presence

of methanol or DMF (dimethylformamide) molecules instead stabilizes the HS state.

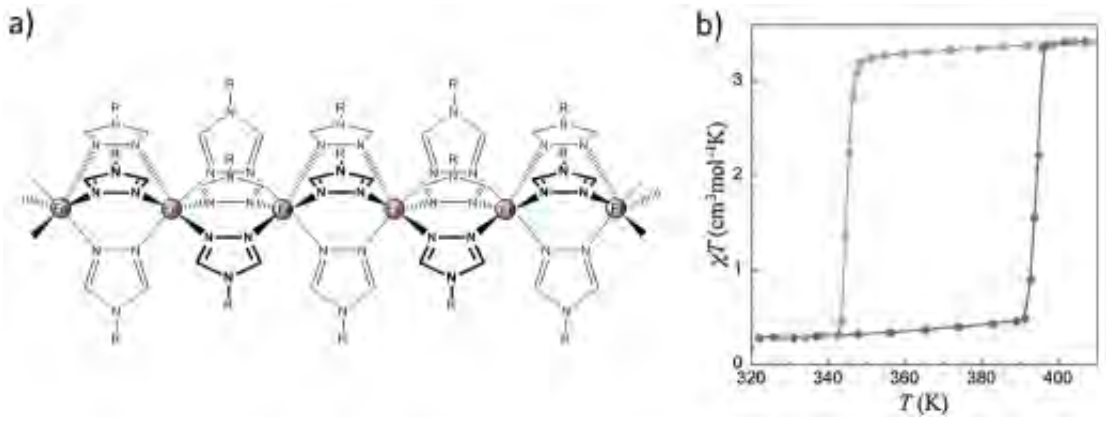

Figure 1.12: **a)** Fragment of a 1D polymer $[Fe(R\text{-}trz)_3)]_n^{2+}$ [46]. **b)** Magnetic susceptibility measurement of the compound $[Fe(Htrz)_2(trz)](BF_4)$ [37].

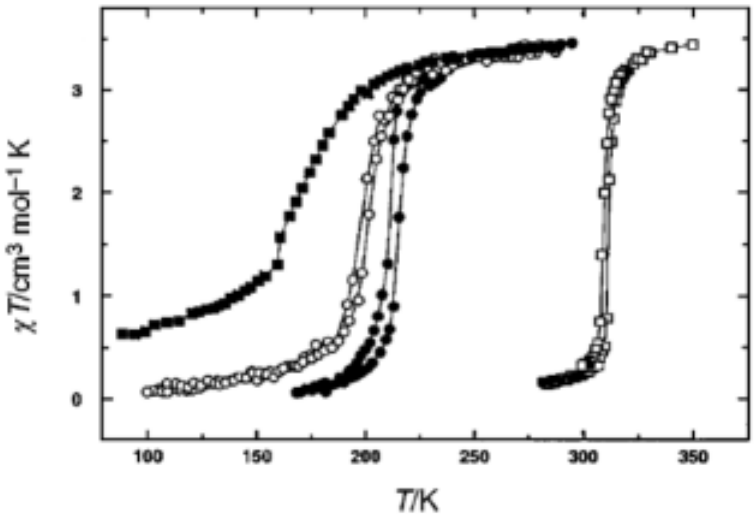

Figure 1.13: Magnetic susceptibility curves for the compounds $[Fe(4\text{-amyl-trz})_3](A_2)$ A = ClO_4^- (closed squares), BF_4^- (open circles), triflate (closed circles), p-toluenesulfonate (open squares) [41].

1.3.5.2 Hofmann Clathrates

The quest for improving the "communication" between the SCO centres has led to the search of new compounds that allow not only more rigid frameworks, but also more versatile systems from a chemical and structural point of view. For these reasons, heteronuclear systems with an architecture of Hofmann clathrate type $((M1(L)_x[M2(CN)_y])$ ·G, where L is an organic ligand, M1 is the SCO center, M2 is a metal such as Ni(II), Pd(II), Pt(II), Ag(I), etc and G is a guest molecule, are of particular interest.

This family of compounds can be two or three dimensional depending on the type of ligands[42]. The first SCO compound of this family was the 2D complex

(Fe(II)(pyridine)$_2$[Ni(CN)$_4$]) and it was synthesized by Kitazawa [47]. A few years later, Real *et al.* changed the ligand of the same compound to pyrazine and obtained a SCO compound with a 3D framework (Fe(II)(pyrazine)[M(CN)$_4$])·2H$_2$O (with M = Ni, Pd, Pt) [48]. These 3D compounds are characterized by a strong cooperativity. It was found that the 3D compounds (pyrazine based) presented a SCO response more cooperative than their 2D analogs (pyridine based) with wide hysteresis (from 20K to 40K width) and at higher temperatures. This fact was attributed to the internal pressure induced by the more rigid 3D structure that tends to stabilize the LS state in the case of the pyrazine complex.

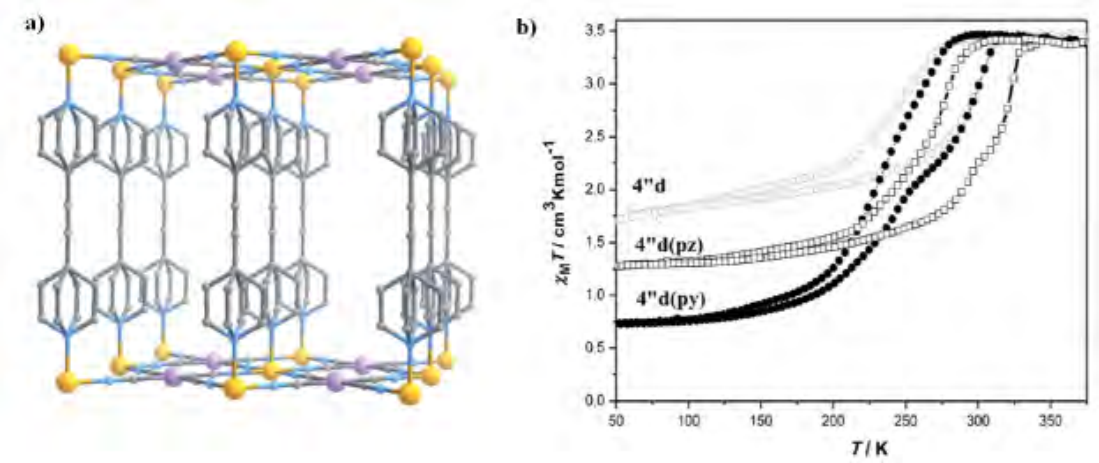

Figure 1.14: **a)**Perspective of a fragment of (Fe(bpac)[Pt(CN)$_4$]) 3D coordination polymer (bpac = bis(4-pyridyl)acetylene)). (Color code: Fe, yellow; Pt, blue-pink; N, blue; C, gray) [49]. **b)** Temperature dependence of $\chi_M \cdot T$ for (Fe(bpac)[Pt(CN)$_4$]) powder sample in the dehydrated form (4"d), with pyridine (4"d(py)) or pyrazine (4"d(pz)) inside its molecular framework [50]

The SCO 3D coordination polymers (See Figure 1.14a) are currently an active research field due to their characteristic cavities at the nanometric scale; these have the potential for hosting guest molecules inside the molecular frameworks that could eventually modulate the SCO response of the system (See Figure 1.14) [50–53]. As a result, applications of storage, filtration and sensors can be imagined.

1.3.6 Detection of the Spin Crossover

Regardless the stimulus employed for triggering the spin crossover phenomenon (temperature change, pressure, magnetic field, or light), it can be monitored employing diverse experimental techniques that may directly or indirectly reveal the electronic state of the SCO centre. Among these techniques we have:

1.3.6.1 Classical Methods

- **Magnetic Susceptibility Measurements**: the most popular characterization technique for SCO materials. The change from the HS state to a the LS state (or *vice versa*) as a function of temperature is reflected in a variation of the magnetic

susceptibility ($\chi_m(T)$) of the material. Taking into account the temperature dependent susceptibilities of the material and the fraction of centers at each spin state (*i.e.* χ_{HS} and χ_{LS}, γ_{HS} and γ_{LS}, respectively), the magnetic susceptibility can be expressed as:

$$\chi_m(T) = \gamma_{HS} \cdot \chi_{HS} + (1 - \gamma_{HS}) \cdot \chi_{LS} \tag{1.34}$$

According to the law of Curie, the product $\chi_m \cdot T$ for a paramagnetic material is constant for all values of T. Hence, if the magnetic susceptibilities at each spin state are not accurately known, the product $\chi_m \cdot T$ vs T is often plotted. This way any variation of the product will be due the SCO phenomenon in the material.

- **Mössbauer Spectroscopy**: it is the spectroscopic method of choice for the study of the SCO in Fe based complexes. This type of spectroscopy allows to distinguish the molar fractions of Fe(II) or Fe(III) centers at each spin state. By the same token, this technique provides valuable insights of the local structure of the material around the iron centers and lattice dynamics information.

- **Crystallography**: X-ray diffraction techniques can be employed to deduce the structural evolution of the compounds upon the SCO by measuring metal-ligand distances and also the deformations of the angles between bonds. Additionally, elastic properties such as the bulk moduli can be inferred. In general, this type of observations are widely used in the SCO field in order to establish structure-property correlations. Hence, the rationalization of cooperative interactions occurring in the materials can be performed and with this knowledge, the "design" of novel SCO materials may become easier. Both single crystal and powder X- ray diffraction technique can yield detailed structural insights into the SCO phenomenon and have been extensively exploited within the field. However, in the typically low symmetry molecular systems which characterize SCO materials, the former method provides easier access to such details and thus often the preferred method for structural analysis when single crystals are available.

- **Heat Capacity Measurements**: thermodynamical parameters such as changes of enthalpy and entropy can be estimated.

- **Vibrational Spectroscopy**: infrared absorption or Raman spectroscopies are actively used since the bond strength between the SCO center and its ligands change significantly from one spin state to the other; hence, there will be vibrational modes characteristic to each spin state. Currently, these techniques have been extended and coupled to optical microscopes in order to perform localized micro-Raman and micro-IR spectroscopies.

- **Optical Spectra Measurements**: it has already been shown that the SCO phenomenon is accompanied by a color change (usually pronounced) due to the change of the electronic configuration of the SCO centers. As a result, it is possible to monitor the SCO phenomenon by means of optical reflectivity and

absorption spectroscopies. Since the absorbance is closely proportional to the concentration of the colour centres, when normalized appropriately, these absorption spectra directly yield the temperature dependence of the molar fraction of the metal ions in the LS or HS states.

- **Other techniques**: in this category it is possible to mention Extended X-ray Absorption Fine Structure (EXAFS) that is used to obtain structural information of SCO systems, particularly when is not possible to obtain appropriate crystals for X-ray diffraction. Also, X-ray absorption near edge structure (XANES) is employed to infer geometry and oxidation states of SCO samples. X-ray emission spectroscopy (XES) provides a detailed element-specific picture of the local electronic structure around a given atomic site. The emitted radiation is dominated by the decay of valence electrons of the excited atomic center; in the case of highly oriented systems, angular- dependent XES enables the separation of states of different symmetry of the involved orbitals. Nuclear Forward Sacttering (NFS) is a powerful technique that is capable of assessing hyperfine interactions in condensed matter. Inelastic Neutron Scatering (INS) is used to study atomic and molecular motion as well as magnetic and crystal field excitations. It distinguishes itself from other neutron scattering techniques by resolving the change in kinetic energy that occurs when the collision between neutrons and the sample is inelastic.

1.3.6.2 Emerging Methods

It is worth to realize that the recent trends for developing detection methods of the SCO phenomenon are centered in two main research axes: size reduction and time resolved studies or the combination of them (spatio-temporal). For this reason, new approaches have been considered to reach more sensitive set ups that seek to monitor the SCO at smaller scales and without the need to probe an important amount of material. In this manner, certain properties characteristic of the nanometer scale and dependent on size, shape and crystalline phase may be revealed. On the other hand, but still with a similar purpose, the research of the transition processes during and after thermal and optical excitation resolved in space and time can provide also valuable information about the size effect and non linear phenomena in the dynamics of such systems after a perturbation [1].

- **Refractive Index Change**: spin crossover thin films can be used to modulate the propagation of electromagnetic waves in plasmonic or other type of guided wave devices. Our team has developed this idea in ref. [54] on the example of a surface plasmon polariton (SPP) wave. Figure 1.15 shows the conventional attenuated total reflectance setup we used to excite SPPs at the interface of a gold layer and a thin film of a SCO complex. For an appropriate combination of the wavelength, polarization and incidence angle of the exciting light beam a resonance is observed in the reflectance spectra. This is the so-called “simultaneous wave vector and frequency matching condition”. The corresponding minimum

in the angular reflectance curve of the Au/SCO multilayer is clearly observed in Figure 3.7a. When the temperature of the multilayer is increased the spin state of the SCO layer changes from HS to LS and the associated increase of the refractive index leads to a shift of the resonance to lower angles. This temperature dependent behavior occurs due to both ordinary thermal expansion of the material as well as due to the SCO phenomenon. However, these two phenomena can be differentiated due to the observed discontinuity of the shift of the minimum of the angular reflectance around the transition temperature of the film (Figure 1.15b). A very similar result was obtained with a diffraction grating device made of the same compound (Figure 1.16) [38]. As shown in Figure 3.8c the diffraction efficiency of the surface relief grating varies in a linear manner far from the spin transition, but this latter leads to an abrupt change in the diffracted light intensity. Using transmittance theory (diffraction gratings) or the Fresnel equations (SPP device), the variation of the photonic signal can be traced back quantitatively in each case to the refractive index change accompanying the SCO [38, 54].

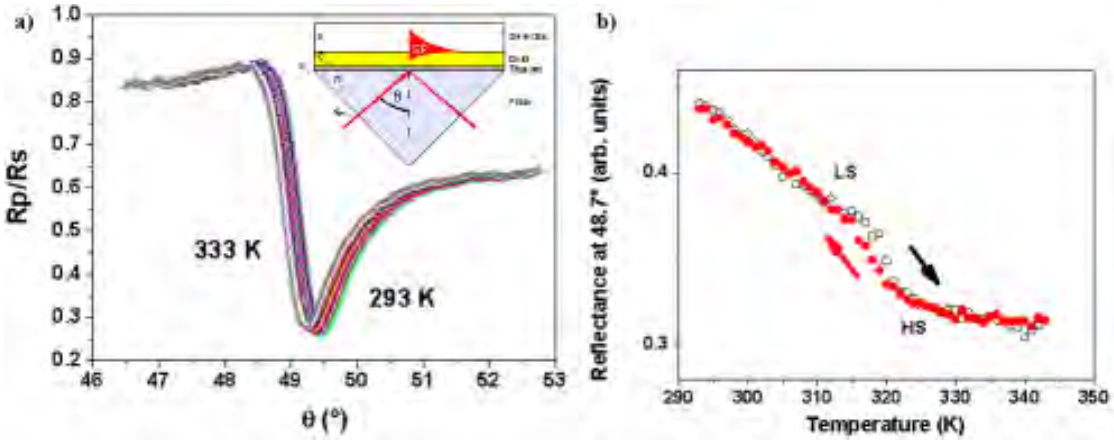

Figure 1.15: **a)** Angle-dependent reflectance spectra of a glass / Ti (5 nm) / Au (45 nm) / [Fe(*hptrz*)$_3$](OTs)$_2$ (30 nm) multilayer as a function of the temperature (λ = 660 nm). The inset depicts the schema of the conventional Kretchmann configuration used in the measurements. **b)** Temperature dependence of the reflectance intensity (at $\theta = 48.7°$) of the multilayer in the heating and cooling modes (dT/dt = 2 K/min) [54].

- **Electrical Measurements**: A number of recent papers have been devoted to the study of the transport properties of SCO materials from the single molecule or nanoparticle [1, 55–58] to the macroscopic level [21, 22] with promising perspectives in nanoelectronics and spintronics. In particular, the characterization of a single object placed in a "nano-gap" has been extremely difficult. There is always a considerable uncertainty for assessing the real origin of the variations in the electrical current changes measured on the samples as a function of a bias voltage; these could be due to the SCO or other unrelated phenomena. Furthermore, it is not trivial to extrapolate the different physical properties observed on a macroscopic ensemble of (nano) objects to those observed in the single object measurements. There are theoretical calculations in early stages of development

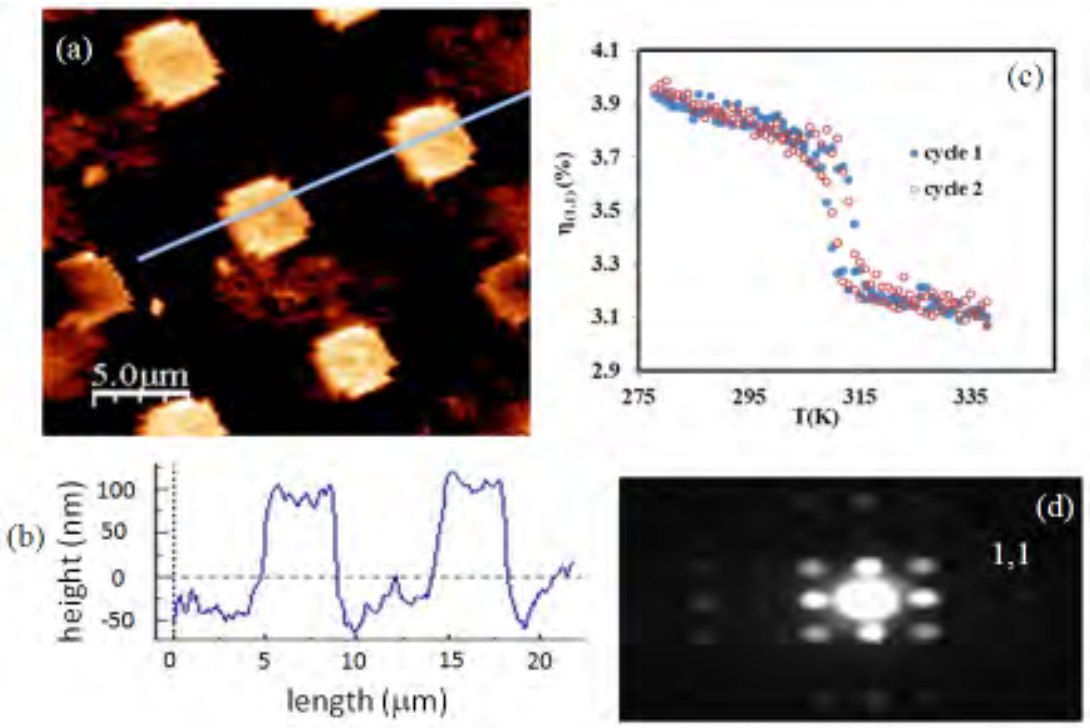

Figure 1.16: **a)** AFM topography image and **b)** height cross-section of a surface relief grating of the spin crossover compound $[Fe(hptrz)_3](OTs)_2$. **c)** Variation of the diffraction efficiency (λ= 650 nm) for the diffracted spot (1,1) as a function of the temperature through two heating - cooling cycles (dT/dt = 2 K/min). The diffraction image of the grating is shown in **d)** [38].

for the description of the electrical transport in SCO materials that will surely provide useful help. For example, our team has observed a thermal hysteresis loop in the dc electrical conductivity of the compound $[Fe(Htrz)_2(trz)](BF_4)$ clearly associated to the SCO phenomenon (Figure 1.17) [22]. Different versions of the powder of this compound were placed between two steel electrodes and the conductivity of the ensemble was measured as a function of temperature. It was observed that the LS phase of the compound is more conductive than the HS phase due to a lower activation barrier of the LS form. It was shown that the possibility to observe a spin state dependence of the conductivity in the highly insulating SCO materials is very dependent on the interplay between the spin transition temperature and the activation parameters of the compound. Additionally, it was also demonstrated that by modifying the conditions of the synthesis, it is possible to modify drastically the charge transport behavior of the sample without affecting the SCO properties of the material. In consequence, small variations in the morphology or composition of the measured objects can lead to dramatic changes in the conductance behavior. All these studies reveal the electrical measurements as a promising characterization tool for performing size effect studies of SCO materials.

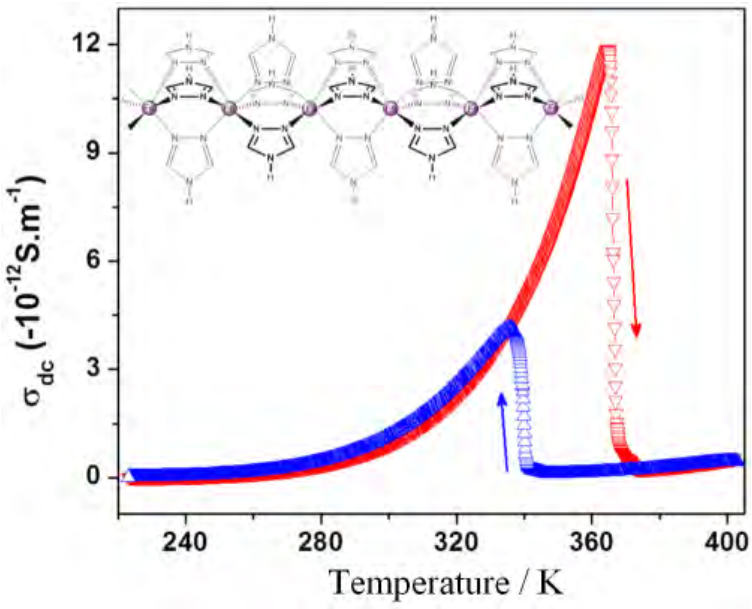

Figure 1.17: Temperature dependence of the dc electrical conductivity of the compound $[Fe(Htrz)_2(trz)](BF_4)$ [22]. (Heating (red) and cooling (blue) modes.)

Alternatively to the existing methods for SCO detection at the macro- and nano-scales, this thesis work proposes the fluorescence detection as a novel powerful tool to perform characterization of the SCO materials, valid down to the limit of a single molecule detection.

Chapter 2

Materials with combined spin crossover and luminescent functionalities

2.1 Introduction

Transition metal ions such as Fe(III), Fe(II), Co(II) and Ni(II) are reputed luminescence "killers" and consequently, the desire to combine luminescence and spin crossover materials may at first sight appear rather counterintuitive. However, the spin crossover phenomenon involves such drastic changes in the electronic and crystal structure of the material that a change in spin state may perturb the environment of the luminophore enough to allow a luminescent response upon the SCO. While of course both electronic and structural effects are intrinsically linked in SCO materials, their respective impact on the interaction between SCO and luminescent materials is subtly different.

The luminescence signal may be modulated by the structural changes that occur on SCO, for example changes in the density (and hence rigidity) of the lattice can affect both the wavelength and intensity of the light emitted by the luminophore. In this way the probe could detect the elastic changes due to the spin transition propagating through the material, independently of the spectral properties of the SCO centres. Alternatively, the luminescence can be modulated directly due to the change in the electronic configuration of the SCO material during the transition. If the separation between a pair of energy levels associated with the luminophore matches closely an energy level spacing of the SCO centre (in a given spin state) the excited state energy can be transferred to the latter. For example, if the emission and/or excitation bands of the luminophore show significant overlap with the absorption bands of the SCO material, the luminescent response can be quenched via different energy transfer processes. Hence, through the judicious choice of a luminophore with suitable spectral overlap, it should be possible to modulate the luminescent response as a function of spin state of the SCO centres through changes in the optical absorption of the latter material. Key factors in rationalising and optimising the energy transfer

mechanisms in these mixed materials include the nature (radiative or non-radiative) of the quenching process, the relative proportion of luminophores with respect to the spin-active centres as well as their separation. However, if the two entities are too close, non-radiative energy transfer mechanisms might result in severe quenching at all temperatures and loss of the luminescent signal. It is important to remember also that when combining SCO and luminescent systems, there is no guarantee that both properties will be preserved in a single hybrid material. This stems largely from the very high sensitivity of both the luminescent and SCO materials to minor chemical and structural changes caused simply by the presence of the other constituent. In addition, it is important that the luminophore is itself not sensitive to the stimulus used to switch the spin state. For example, if one considers the most usual thermal spin state switching, it is preferable to choose a luminophore which exhibits negligible thermal quenching in the temperature range of interest.

This chapter will be centered on the development of materials that have both SCO and luminescent functionalities. The first part will provide a critical state of the art review about the topic and it will highlight the principal elements necessary for a rational design of this type of novel materials. The second part will deal with the macroscopic characterization of the different luminescent SCO complexes that were synthesized and studied during this thesis and a description of the fluorescence setup and measurements protocols employed to perform the characterization of the samples in the solid state.

2.2 State of the Art

For efficient coupling between luminescence and SCO properties, the *spectral overlap* of the two functional entities and its consequences for quenching must be considered. As stated previously, the quenching energy transfer mechanisms depend also strongly on the *relative proximity of the two centres*. Different synthetic strategies have been employed to combine the two properties. In this section we will divide them into two families:

The first type of synthetic strategy aims *to combine the luminophore and SCO centres into a single entity*, *e.g.* through the use of luminescent ligands or counterions to form luminescent SCO complexes and compounds. In these cases the relative location of each component is usually observable, often through structural analysis techniques and hence energy transfer mechanisms may be rationalised. Furthermore, in these cases the distance between the centres may be to some extent rationally controlled through varying the length of the chemical bridging unit. It is though important to state that chemically changing the SCO molecule to include a luminescent moiety risks changing, or indeed losing, one or both properties in an unpredictable manner. Using such an approach there should be a stoichiometric proportion of luminophore and SCO centres, possibly facilitating quantitative analysis of the spin transition process using the fluorescence technique. However, an aspect usually forgotten while analysing this type of compounds is the self-quenching effect. This particular approach may lead to

materials that have a high concentration of luminescent centres (*i.e.* comparable quantity of SCO centres and luminophores) that can permanently quench the luminescent response of the system at all temperatures, even if the conditions for obtaining both properties at a molecular level are respected. Even though the concept of having one luminophore that probes one SCO centre is an ideal situation for monitoring the spin transition in a material, in the solid state this situation may in fact be *detrimental* to the overall luminescent response. For these reasons, attempting to design combined molecules with specific spectral properties from individual components is difficult and is largely of interest only for fundamental mechanistic studies. It seems difficult to consider this type of approach for the development of practical applications.

Other synthetic approaches concern *doping luminescent entities (metal ions, molecules, etc.) into a SCO material*, at various concentrations, into more or less uncertain positions within the lattice. In fact, in this case the luminophore is used as a structural probe, which is a well-known approach in several fields of science. In these materials, a structural description of the interaction between SCO centres and luminophores is more difficult to obtain and therefore the mechanistic elucidation of energy transfer mechanisms may be rather more complex. Also, one should not overlook the fact that due to its relatively small proportion, the luminophore will probe only a part of the system and it is not guaranteed that the results inferred describe the properties of the ensemble of the material. On the other hand, if the dopant is present in sufficiently low concentrations, the risk of adversely interfering with the SCO properties is reduced. This two-component system has the further advantage that each component is usually independent and so individual modification can be possible. For example, one can fine-tune the SCO properties of certain complexes using well-known methods. In many cases, the optical properties of the SCO complex will not change much and therefore it will be possible to work with the same dopant, which is obviously a huge benefit. On the whole, this synthetic strategy appears thus better adapted for practical developments and perhaps less for mechanistic studies.

We must stress that the frontier between these two main approaches is not always well-defined. For example, if one considers a case in which all counterions are luminescent it would constitute the first approach. On the other hand, if a very low percentage of non-luminescent counterions were replaced with an ionic luminophore, it would clearly represent an example of doping. However, at intermediate proportions of luminophore the distinction is not obvious and perhaps may be less helpful.

2.2.1 Examples of luminescent spin crossover compounds (ligands, counterions, co-crystals)

There are several reports of systems in which the luminescent entity and the SCO centre are part of the same molecule, either with the luminophore being a part of the ligand system surrounding the SCO metal centre [59–62], or forming part of a mixed metal *d-f* molecular material [63]. There are also conceptually related complexes in which the luminophore acts as a counterion to the cationic SCO molecule [64].

Fabbrizzi *et al.* [59] reported a system in which a fluorescent fragment (naphthalene) was substituted onto a tetradentate macrocyclic cyclam ligand (cyclam = 1,4,8,11-tetraazacyclotetradecane) to form the neutral ligand L1. This ligand coordinates to Ni^{2+} to form complexes of general formula $[Ni(L1)X_2]$, where X is a monoionic anion. The result is either low-spin square-planar complexes (in the case of weakly coordinating anions) or high-spin octahedral complexes (when anions coordinate to the Ni in the axial positions). In solution the spin state at the Ni^2+ centre changes through the reversible coordination of solvent molecules (S) in axial positions of the molecules according to the following equilibrium:

$$\begin{array}{lcr} [Ni^{II}(L1)S_2]^{2+} & \rightleftharpoons & [Ni^{II}(L1)]^{2+}] + 2S \\ \text{Octahedral} & & \text{Square Planar} \\ \text{Low Temp.} & & \text{High Temp.} \\ \text{High Spin} & & \text{Low Spin} \end{array}$$

The position of this equilibrium is dependent on the temperature of the system, and unlike in most SCO materials (in which the SCO is not accompanied by a change in the coordination number), higher temperatures favour the low-spin, square planar state. Between 300 and 338 K, the fluorescence intensity of the naphthalene molecule increases with increasing LS proportion by a factor of approximately 2.5 (Figure 4.1), a result of greater quenching efficiency in the HS state. The quenching mechanism in this material was proposed to be energy transfer via double electron exchange, which involves redistribution of electrons between the molecular orbitals of the photoexcited fluorophore and the d-orbitals of the metal centre. In this particular system, the temperature-dependence of the spin state equilibrium may be only observed in free molecules in solution where solvent mobility is high and so it is not strictly comparable to more traditional SCO systems. However, from a wider point of view, this study provides an important proof of concept that the spin state of the material can be probed by fluorescent ligands bound to the SCO centre.

During the 1990s, Piguet et al. [65, 66] combined a series of rare earth metals with transition metal complexes, some of which also displayed SCO properties. These works were the first to introduce the prospect of employing iron(II) as a versatile acceptor for modulating the luminescence of lanthanide ions in heterodimetallic d-f complexes via FRET. Due to the distinctive d-d and MLCT absorption bands of iron(II) in the two spin states and its spectral overlap with the emission of Eu(III), it was expected that the resonant energy transfer Eu(III)→Fe(II) would depend strongly on the spin state of the iron centre. As a result, the lanthanide ion could be employed as the 'reporter' of the spin state in iron-based SCO molecules. For example this was attempted using a heterodimetallic complex (HHH)-$[LnFe(L)_3]^{5+}$, which showed SCO around room temperature [63]. However, even at high temperatures, where the highest possible fraction of $Fe(II)_{HS}$ (> 0.5) was observed, an extremely efficient non-radiative energy transfer between Eu(III) and the Fe(II) centres completely quenched the luminescent response of the lanthanide. Thus, in order to study the energy transfer processes between Eu(III) and Fe(II) in the HS state, they attached a sterically hindering methyl group to the ligand so as to prevent the contraction of the Fe-N bonds necessary for the formation of $Fe(II)_{LS}$ species. This was done in such a manner as to avoid affecting

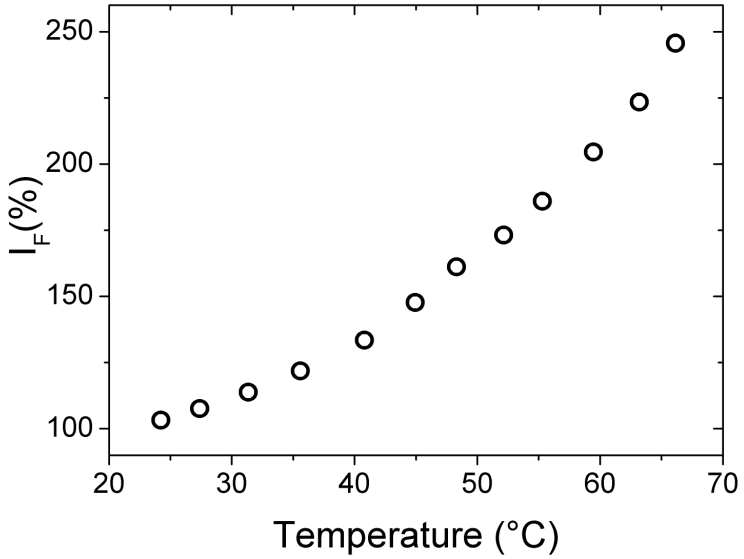

Figure 2.1: Fluorescence intensity for $[Ni^{II}(L1)](ClO_4)_2$ as a function of temperature, as presented in ref. [59] (L1=cyclam framwork with a linked naphthalene fluorescent fragment through a -CH_2- spacer.

the coordination sphere of Eu(III). Even when all iron centres were in the HS state, only a weak luminescence signal could be detected above 580 nm. A drastic decrease of the luminescence lifetime of the Eu(III) ions was observed for the $Fe(II)_{HS}$ complex ($\tau = 0.277$ ms) when compared to the Zn analogue ($\tau = 2.63$ ms). Taking into account the blue shifted MLCT absorption band of the Fe present in both spin configurations (with different oscillator strengths) within that specific coordination environment and the calculated intermetallic distance ≈ 0.9 nm, it was concluded that there was no orbitally mediated interaction (Dexter energy transfer) between the metals. As a result, the energy transfer mechanism was attributed to a Förster resonance type that relies strongly on the spectral overlap of the sensitizer and the acceptor.

Hasegawa et al. [62] reported the temperature-dependant fluorescent behaviour (in methanol/ethanol solution) of two Fe(II) SCO complexes with derivatives of the fluorescent bzp ligand (bzp = 2,6-bis(benzimidazole-2'-yl)pyridine), $[Fe(bzp\text{-}H_2)_2]\cdot(ClO)_4$ and $[Fe(bzp\text{-}H)_2]$. In this study, the electronic absorption spectra of both bzp and $[Fe(bzp\text{-}H)_2]$ were assigned using molecular orbital calculations, while the fluorescent spectra of the two iron complexes were used in the assignment of electronic transitions. The origins of the broad bands observed in the emission spectra of the two metal complexes were also assigned. Both complexes were fluorescent in both the HS and LS states, with emission intensity increasing on cooling. The proportion of HS and LS states was estimated from fluorescence spectra using the Boltzmann equation at various temperatures and was in good agreement with other detection methods. Importantly, they showed that following the fluorescent properties as a function of temperature may be able to provide quantitative information regarding the fraction of each spin state in Fe(II) materials.

Garcia *et al.* [60] substituted a functional moiety at the 4-position of the well-known 1,2,4-triazole ligand system to form N-salicylidene-4-amino-1,2,4-triazole (L2), which shows strong emission in the solid state. Complexation of this ligand to $Fe(NCS)_2$ salt yields the crystalline dinuclear material $[Fe_2(L2)_5(NCS)_4]_3{\cdot}(MeOH)_4$. This system shows a relatively abrupt one-step SCO with $T_c = 150$ K and c.a. 6% residual HS fraction at low temperature. Here, the wavelength of the emission maximum, rather than intensity was followed as a function of temperature, and a striking correlation with the SCO curve determined from SQUID measurements was observed (as shown in Figure 2.2a), demonstrating the high sensitivity of this probe to changes in its environment as a means for monitoring spin state. This approach, however, is limited by the experimental requirement for high resolution spectra, which in turn requires a high signal-to-noise ratio, something that will of course decrease significantly when moving from the bulk crystalline scale of this study towards nanomaterials. Indeed, when the fluorescence intensity rather than λ_{max} is considered, the results become less clear, as demonstrated in Figure 2.2b, which shows the variation in intensity at constant wavelength (414 nm) after excitation $\lambda_{exc} = 350$ nm. While there is an observed discontinuity in the temperature range of the SCO, the significant thermal dependence in the region in which no transition occurs may make analysis of SCO properties difficult in the absence of magnetic data. In this case, the increasing intensity of the luminescence below T_c was attributed by the authors to the stiffening of the lattice.

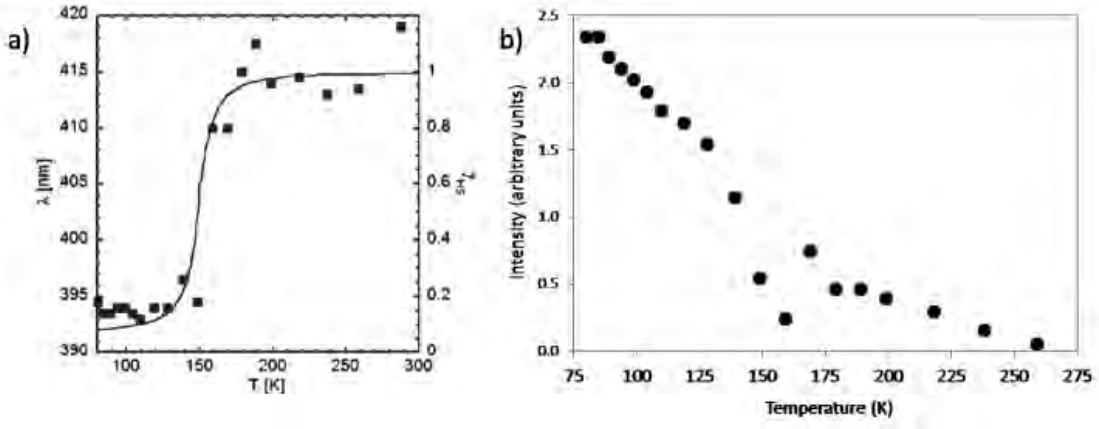

Figure 2.2: **a)** Variation of wavelength of the luminescence emission maximum (λ_{max}) as a function of temperature for $[Fe_2(L2)_5(NCS)_4]_3{\cdot}(MeOH)_4$ as reported in [60]. **a)** Luminescence intensity at 414 nm (350 nm excitation) as a function of temperature for the same compound, estimated from Figure S3a of Ref. [60].

In a study by Ruben *et al.* [61], a fluorescent pyrene moiety was incorporated into the bpp ligand, either separated by a long, flexible organic group (4-(2,6-di(1H-pyrazol-1-yl)pyridin-4-yl)benzyl-4-(pyren-1-yl)butanoate (L3)), or directly attached via an sp^3 C-C bond (2,6-di(1H-pyrazol-1-yl)-4-(pyren-1-yl)pyridine (L4)). Complexation of these ligands to Fe^{II} metal centres afforded materials with very different SCO properties. As a consequence of accommodating the supramolecular $\pi - \pi$ stacking interactions of the pyrene ligands in $[Fe(L4)_2](ClO_4)_2$, the iron coordination sphere is highly distorted and thus does not undergo SCO, remaining in the HS state across the investigated temperature range. By contrast, the two complexes $[Fe(L3)_2](ClO_4)_2$ and

$[Fe(L3)_2](BF_4)_2{\cdot}CH_3CN{\cdot}H_2O$ both show spin crossover behaviour without hysteresis. $[Fe(L3)_2](BF_4)_2{\cdot}CH_3CN{\cdot}H_2O$ is fluorescent across the investigated temperature range (17 - 295 K), and the emission spectrum at 17 K shows features that can be attributed to monomer and excimer pyrene fluorescence. Despite this, no obvious correlation between the SCO and fluorescence properties could be established in this material, with the temperature dependent quenching of the emission being attributed to an intrinsic feature of the pyrene and linker moiety by reference to related non-SCO compounds. As no structural information is available, it is not clear to what extent the pyrene and the SCO centre interact. This study demonstrates the importance of chemical environment and crystal packing effects in determining the luminescent and SCO properties and highlights what may be one of the most significant problems of combining these properties in a single molecule - it is possible that one, or indeed both, of the properties will be lost in the mixed compound. Hence rational design of such hybrid molecules with specific properties (a particular T_c for example) is extremely difficult.

Kimizuka *and co-workers* [64] synthesised linear iron 1,2,4-triazole complexes with a long lipophilic chain substituted at the 4 position of the triazole ligand. The organic chromophores 9,10-dimethoxyanthracene-2-sulphonate (Anth-SO_3^-) and 1-pyrenesulphonate (PY-SO_3^-) are electrostatically accumulated on the surface of the iron triazole chains, acting as counterions in the two different samples. Combining the luminophore and SCO centre through ionic interaction rather than chemically binding them into a single molecule means the components can be replaced individually to tune the properties. In both cases, the complex forms fibrous nanostructures which undergo SCO in toluene solution. While there was no obvious connection between the SCO and luminescence intensity in the case of Anth-SO_3^-, the complex in the LS state quenches the fluorescence of the PY-SO_3^- anion via energy transfer processes. This is attributed to the significant overlap between the emission spectrum of the luminophore and the MLCT band of the SCO molecule in the LS state. Quenching efficiency diminishes in the HS state and hence luminescence intensity increases with the HS proportion. Above 30 °C (in the HS state) the luminescence intensity is again reduced (Figure 2.3), which was attributed to dynamic quenching of the luminophore by the HS Fe centres, occurring as a result of greater contact between the two units on thermal disintegration of the fibrous structures.

2.2.2 Luminescent Doping

We have seen that combining SCO and luminescence entities within a single molecule can result in unpredictable or uncontrollable properties of both processes. A conceptually different approach concerns coupling SCO and luminescence properties not within one molecule, but rather through physical mixing of two chemically separate entities via the doping or decoration of a SCO material with a luminophore. This field includes the co-crystallisation of structurally similar molecules to afford SCO-luminescent bulk materials [67] and the elaboration of nano-particles with a SCO core decorated by a luminescent shell [68]. The benefit of this approach is that the individual components may be more readily replaced and hence it may facilitate tuning of individual

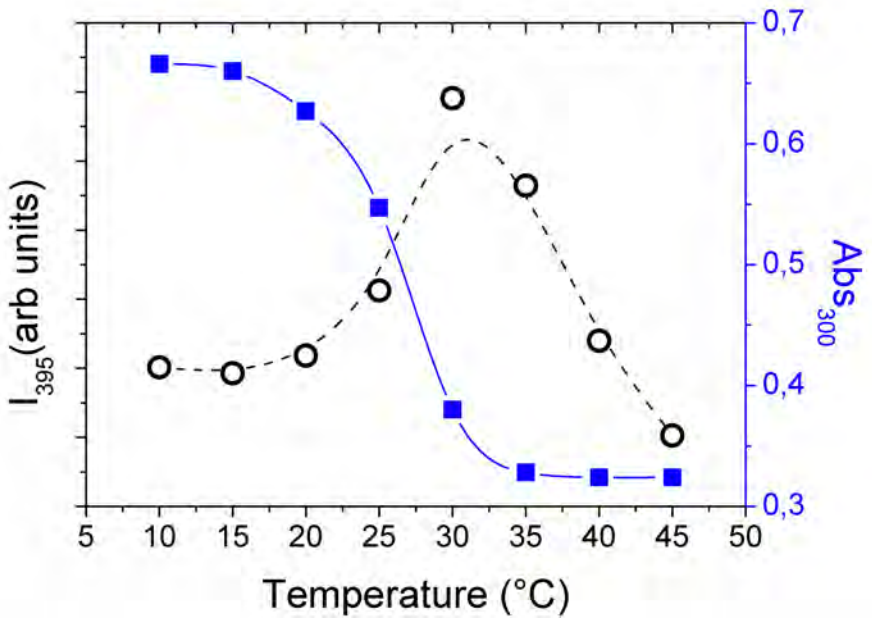

Figure 2.3: Temperature dependence of emission (λ_{ex}=380 nm, open circles) and absorption (at 300 nm, filled squares) intensity for the tris(4-(3-dodecyloxypropyl)-1,2,4-triazole)iron(II) nano-fibres with Py-SO_3^- anions in toluene solution as given in ref.[64].

properties in the hybrid material. However, in such systems, there is not necessarily a stoichiometric proportion of each component, and the relative locations of each are not usually known. Thus the issues of quantitative measurements and elucidation of quenching mechanisms may become rather more complex.

Matsuda et al. [69, 70] developed a simple OLED device, shown schematically in Figure 2.4, in which the electroluminescent emission from a thin film of chlorophyll a was quenched by the LS state of the SCO complex $[Fe(dpp)_2](BF)_4$, allowing for on/off switching of the device output as a function of temperature.

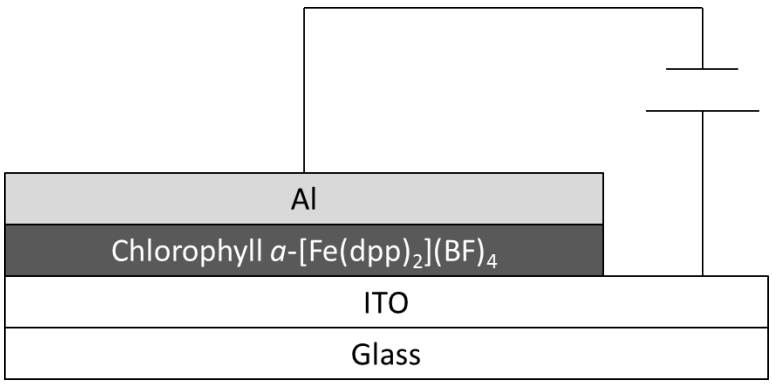

Figure 2.4: Schematic view of the OLED device constructed in [69, 70] (ITO = indium tin oxide).

Electroluminescence differs from the photoluminescence that has been described previously in that it is the result of an electrical input, rather than light. Electron-hole

pairs are generated in OLEDs through a charge injection process, which subsequently recombine producing radiative luminescent emission. The quenching process in this system was reported *not* to be the result of energy transfer from an excited chlorophyll a state to the Fe complex, resulting in radiationless decay. Instead it was speculated that the excited state of the luminophore that is responsible for the electroluminescence above T_c (and in devices without the SCO complex) does not form in the presence of the LS iron complex due to a difference in the efficiency of the charge injection process.

Co-crystallisation was used by Halcrow and co-workers [67] as a tool for doping the SCO material $[Fe(bpp)_2]$ $[BF_4]_2$ (bpp = 2,6-di(pyrazol-1-yl)pyridine) with the structurally related fluorescent complex $[Ru(terpy)_2][BF_4]_2$ (terpy = 2,2':6',2"-terpyridine). The complementary supramolecular interactions shown in the crystal structures of both pure materials - the so-called terpyridine embrace motif - as well as the overall structural similarity allows for the formation of solid solutions of $[Fe(bpp)_2]_x[Ru(terpy)_2]_{1-x}[BF_4]_2$. Virtually complete SCO was observed in all Fe containing complexes, with little change in T_c. An expected result of the reduction in Fe concentration in the lattice is that the small hysteresis shown by the pure Fe complex disappears with 5% Ru complex (x = 0.95), and the SCO becomes much less abrupt as x decreases. Crystalline $[Ru(terpy)_2][BF_4]_2$ has a strong fluorescence emission at 77 K, although this property is much less pronounced in the mixed $[Fe(bpp)_2]_x[Ru(terpy)_2]_{1-x}[BF_4]_2$ species. When x = 0.47 the fluorescence intensity at 77 K is only 7% of that observed in the pure Ru complex, and when x = 0.75 no obvious emission was observed at all. Thus the material of composition $[Fe(bpp)_2]_{0.47}[Ru(terpy)_2]_{0.53}[BF_4]_2$ has been shown to have both SCO and very weak fluorescence properties, albeit within different temperature ranges. One advantage of this approach is that the relative location of the luminophore and SCO elements can be reliably inferred in these co-crystals, which is not necessarily true for other studies involving doping of the luminophore into the SCO lattice. In principle, either of the individual complexes could be exchanged for others with similar structural features, and in this way the properties of either component may be tuned to some extent. It should be noted that directed co-crystallisation of molecular components is far from routine due to the abundance of weak interactions that pervade the lattice and serve to direct the crystal packing in a largely unpredictable manner. However, it is clear from this study that supramolecular complementarity is another useful tool to consider in the development of multifunctional materials.

A different approach to the combination of luminescence with nano-scale SCO materials was presented by Herrera and Colacio *et al.*, [68] in which a core (SCO) - shell (luminescence) nanoparticle architecture was employed. The $[Fe(Htrz)_2(trz)](BF_4)_n$ SCO material was synthesised in a silica nanoparticle (SiO_2NP) matrix using the reverse micelle technique and the luminophore, dansyl (3-(dansylamido)propyltrimethoxysilane), was grafted on the surface of the particles as shown schematically in Figure 2.5. Grafting of the luminophore to the surface of the particles does not significantly affect their morphology or the magnetic properties of an ensemble of particles, but does result in aggregation. This approach may also be considered as a form of doping luminophores into the SCO material, the essential distinction being that the location of the luminophore is known and confined to the surface of the hybrid particles. Metal

dilution effects were also investigated by replacing a proportion of the iron centres with zinc. As expected, as the proportion of Zn(II) ions doped into the SCO material increases, the transition is shifted to lower temperatures, becomes more gradual and the hysteresis width narrows. The thermal luminescent response (intensity monitored at 495 nm with an excitation at 315 nm) of an ensemble of these core-shell particles in which c.a. 50% of the Fe centres have been replaced by Zn closely follows the SCO curve obtained from magnetic studies. In this case, the dansyl luminescence is quenched by the LS form of the Fe complex in the core of the particle via an energy transfer mechanism, resulting from a degree of spectral overlap between the dansyl luminescence and the absorption band of the LS ion. Again, this two component system should allow for the modification of the SCO material so as to tune the sensing properties. However, no fluorescence results are presented concerning the undiluted particles and hence this issue remains to be fully explored.

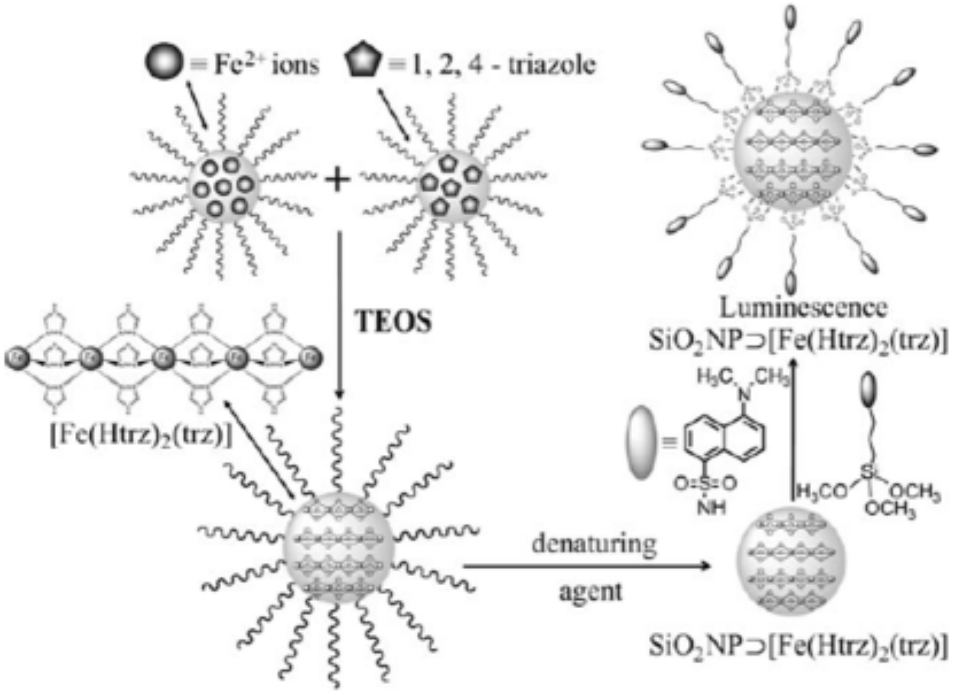

Figure 2.5: Synthetic route and schematic representation of the SCO/luminescence SiO_2 nanoparticles [68].

During this thesis, four additional contributions were made to the literature involving the synthesis of nano-objects and thin films of triazole based SCO complexes doped with trace quantities of organic luminophores [71–74]. These results will be discussed in detail in the following sections and also in chapters III and IV.

2.2.3 Final Remarks

Luminescence detection is a promising alternative to traditional methods for studying the spin crossover phenomenon from materials at the bulk scale to individual nano-

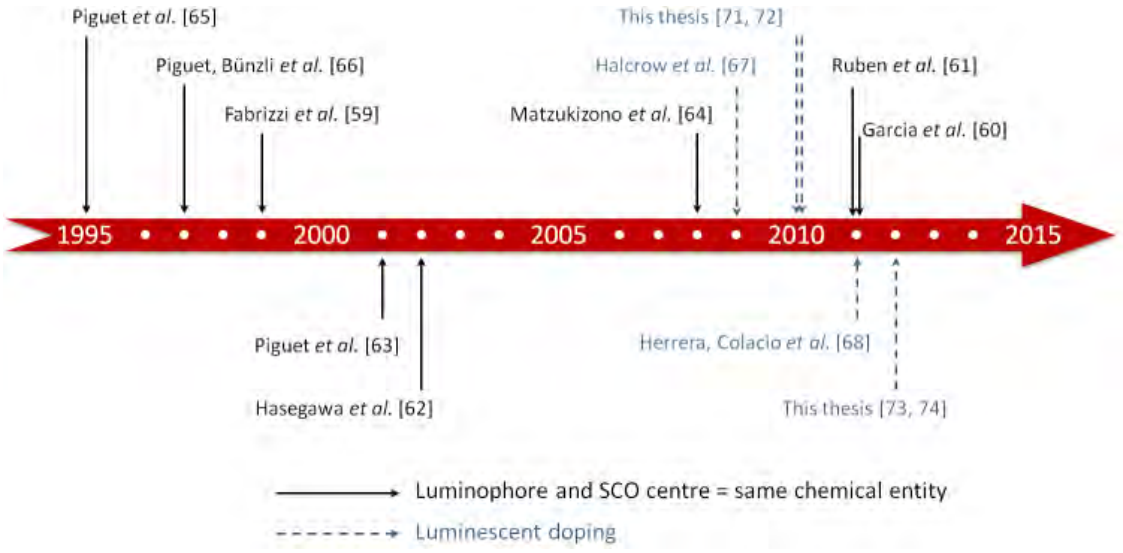

Figure 2.6: List of literature reports related to materials with combined spin crossover and luminescent functionalities. One shall note that before this thesis, there were no reports concerning fluorescent doped SCO materials that successfully modulate the luminescence upon the SCO.

objects and even down to a single molecule. However, due to the high sensitivity to the environment of both SCO and luminescent centers, their combination into one material is a challenging task and may result into the loss of one or even both properties.

During the last 12 years, essentially two different approaches have been adopted to for the design of these novel materials: combination of the SCO center and luminophore into a single molecule and luminescent doping. In the first case, uniting both entities into the same molecule provides clear advantages for rationalizing the structure relationship between the two components. Furthermore, it could allow not only the elucidation, but also the quantification of the interactions between the luminophore and the SCO center. However, this approach may suffer from self-quenching problems. Furthermore, designing each chemical unit may include several compatibility challenges in order to preserve the spin transition and the luminescence, and combining them often requires complex synthetic strategies.

In the second case, the doping of a SCO material with low concentrations of a luminescent agent may have lower risks of deleteriously affecting its original SCO properties. There are fewer constraints for the choice of the luminophore and it will be basically restricted to an appropriate spectral overlap between the emission and the characteristic SCO absorption bands of the material to study. Thus, the characteristics of the spin transition (T_C, cooperativity, etc.) may be tuned independently of the luminophore giving a unique flexibility to the approach. This can be a clear advantage for technological applications and also for the use fluorescence as a SCO probe; this is why we have chosen this strategy for the present work. Nonetheless, the uncertainty of the luminophore location in the lattice introduces additional difficulties in understanding the energy transfer mechanisms involved in these hybrid materials and providing quantitative information regarding the SCO phenomenon.

2.3 Development of Luminescent Doped SCO Materials

This section is dedicated to the development and the characterization of the thermal SCO of luminescent doped systems in the form of colloidal suspensions and nanoparticle powders of different Fe(II) triazole derivates. In particular, polynuclear one-dimensional Fe^{2+}(4-R-1,2,4-triazole)$_3$(anion)$_x$·H_2O SCO compounds have received dedicated attention owing to their favorable characteristics: high transition temperature (around room temperature), the variation of a substituent on the ligand, the anion and the hydration rate allows the modulation of the transition temperature, the width of the hysteresis loop and the abruptness of the spin transition in a wide range. The versatility of the properties of the compounds of this family is thus related to the interaction between the chains via the ligand and trough anions and solvent molecules[75]. Consequently, one can choose almost any member of this family providing a great flexibility in the design of SCO temperature range by maintaining very similar optical properties [45].

As for the doping agent, we have chosen diverse luminescent agents with a strong emission around the green wavelengths (c.a. $\approx$ 550 nm) for having an appropriate spectral overlap with the characteristic the $^1A_1 \rightarrow {}^1T_1$ low spin absorption band of the Fe(II) triazole based SCO complexes that is located in the same spectral range. There are also several additional (general) requirements (or perhaps desired features) for considering a given luminophore a good doping agent; these include *low photobleaching* of the luminophore so as to ensure the system may be cycled repeatedly, sufficiently high intensity of the emission, low sensitivity of the luminophore to the stimuli that are used to change the spin state of the system and mainly, an efficient energy transfer to the complex in one state in order to have an important modulation of the luminescence upon the SCO.

This section is divided in two parts: the first part is devoted to the characterization techniques employed for these SCO systems. A general description of the fluorescence microscopy setup is given and the additional spectroscopic setups employed in this thesis are briefly described. The second part discusses three strategies that were performed to develop luminescent doped SCO materials.

2.3.1 Characterization Techniques

2.3.1.1 Microscopy Setup

A picture of the microscopy set up employed in this thesis and the scheme of the fluorescence microscopy setup employed for the experiments is shown in Figure 2.7a. It is composed by an Olympus BX-51 upright optical microscope equipped with an iKon-M DU934NBV (Andor Technology) back-illuminated charge-coupled device (CCD) image sensor (1024 X 1024 pixels of 13 μm size) and a $X5$ magnification objective (numerical aperture, NA = 0.1 and working distance, WD=15 mm) or a $X50$ mag-

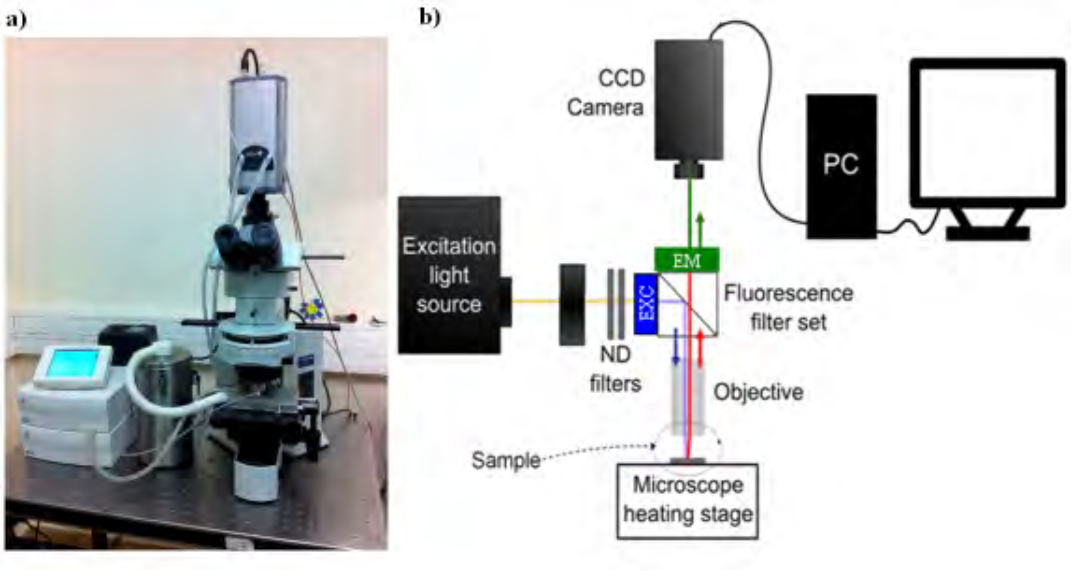

Figure 2.7: **a)** Microscopy set up employed for the thermal characterization of SCO compounds. **b)** Scheme of the fluorescence microscopy configuration.

nification objective (NA = 0.5, WD = 10.6 mm) with long working distances due to the necessity to perform measurements with a temperature controlled chamber. For the fluorescence excitation, depending on the experiment three possible light sources were employed: a halogen lamp, a xenon lamp or a blue LED from ThorLabs with an output centered at 450 nm. Unless otherwise stated, in the fluorescence microscopy measurements the samples were constantly irradiated during the experiments, the excitation and collected light beams were separated by a dichroic mirror (cutting edge at 510 nm) and they were further cleaned with band-pass filters centered at 450 nm (FWHM=45 nm) and at 550 nm (FWHM=50 nm), respectively. For the reflectivity measurements, standard bright field or dark field set up were used. To improve the contrast upon the SCO, the collected light beam was filtered with a band-pass filter centered at 543 nm (FWHM = 23 nm). The temperature control of the sample was carried out with two different platforms according to the experimental specifications: a THMS-600 Linkam cryostat that cools down the sample with liquid nitrogen and also provides a controlled atmosphere with the same gas in a temperature range from 78 K to 873 K. Additionally, a LTS120 Linkam stage with a Peltier (thermoelectrical) heating-cooling system, a semi-controlled atmosphere and embedded electrical inputs in the chamber was also employed; it controls the temperature in a range from 233 K to 393 K. Powder samples were deposited over silicon pieces or thin glass slides to ensure a good thermalization from the temperature stages.

The basic data treatment performed with a CCD image consists on choosing a region of interest (ROI) from the image and then calculating the mean value of the pixels inside. Then, by plotting the value obtained in each acquisition as a function of a given parameter, for example the temperature at which the image was taken, a variation of the luminescence / reflectivity can be monitored. More sophisticated strategies can be employed such as taking a second ROI where there is no sample for performing background subtraction/normalization or also applying different filters for

removing noise of the image and improving contrast of the image (See Chapater IV). It is important to note that while performing observations as a function of temperature, due to thermal dilation of the heating stage and/or the substrate, a drift of the sample and also the focal plane will be observed. Thus, to obtain reliable information of these experiments, it is crucial to place the ROI in the same place (i.e. the same sector of the sample should be analyzed on each image); this aspect will be dealt with in chapter III. However, for the characterization of "macroscopic" samples dealt in this chapter, a high amount of material is available within the field providing strong luminescence signal. Hence, we could use low NA, low magnification ($X5$) objectives for which the thermal drift is no longer critical.

2.3.1.2 Additional Spectroscopic Techniques

2.3.1.2.1 Spectrofluorimeter: A Fluoromax-4 (Horiba-Jobin Yvon) (Figure 2.8a) spectrofluorimeter equipped with a xenon lamp source and a thermostated quartz cuvette with a programmable temperature controller was used to acquire fluorescence excitation and emission spectra as a function of temperature, which were corrected for the instrument response (as implemented in the software).

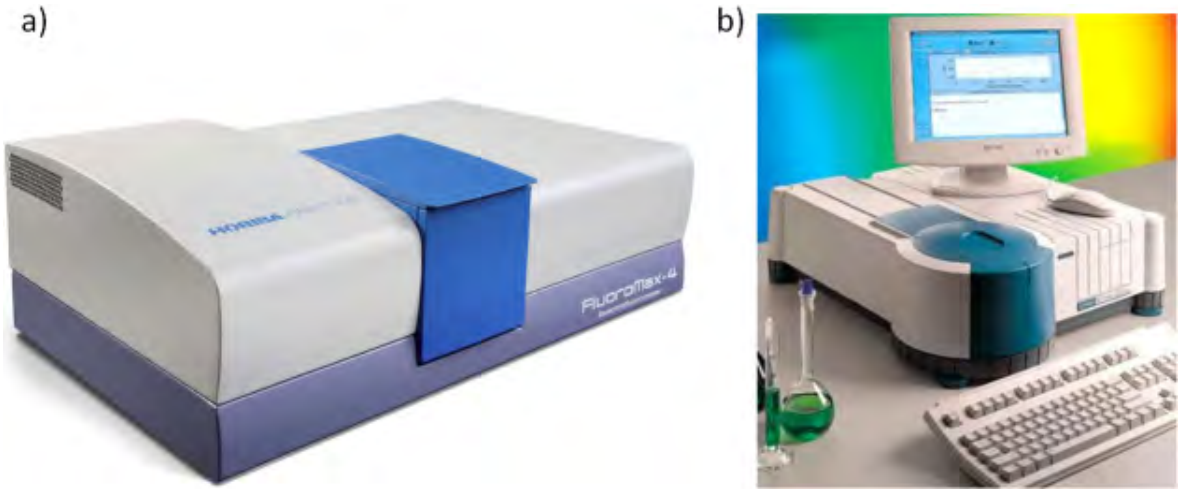

Figure 2.8: **a)** Fluoromax-4 (Horiba-Jobin Yvon) spectrofluorimeter. **b)** Cary-50 (Varian) spectrophotometer.

2.3.1.2.2 UV-Visible Spectrophotometer: Variable temperature UV-vis absorption spectra were recorded on a Cary-50 (Varian) spectrophotometer (Figure 2.8b). Samples in solution were held in a thermostatted quartz cuvette with a programmable temperature controller for performing the measurements. Absorption measurements of SCO thin films deposited on quartz substrates were performed also as a function of temperature with the aid of a LTS120 Linkam stage equipped with a Peltier heating/-cooling plate.

2.3.1.2.3 Spectrographs: Two types of fibered spectrographs were coupled to the optical microscopy setup (Figure 2.9) in order to analyze different signals signal coming from the studied samples in the different microscopy modes (bright field, dark field and luminescence): BWTeK Glacier X (operating wavelengths in the visible range) and a Shamrock SR-303i equipped with an ANDOR iDUS CCD detector (operating wavelengths in the UV-IR range).

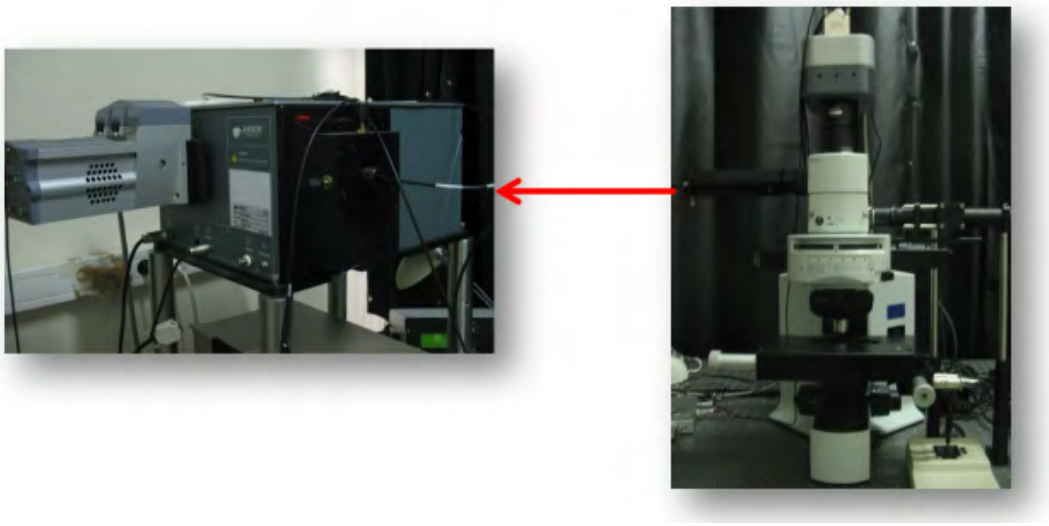

Figure 2.9: Shamrock spectrograph coupled to an Olympus BX-51 microscope.

2.3.2 Luminescent doped SCO materials: The Strategies

The inability for inferring the structural information of doped Fe(II) triazole based materials makes difficult to assess the final location of the luminophore after the doping. As a result, the energy transfer mechanism occurring in such type of systems is not easy to reveal. In spite of this, in order to optimize the energy transfer and in the best case reach an efficient FRET, the distance between the Fe centres of the complex and the luminophores should be small regardless the relative location of the latter; thus the motivation is always to integrate the luminescent agent into the SCO material. With this in mind, we have considered different scenarios depending on the role the luminophore could eventually play in the material: guest, counter anion, coordinating ligand and coordination metal center; these variants have been schematized in Figure 2.10. All these scenarios were considered under the premise of working with low doping levels (*i.e.* less than 1 mol% luminophore per iron atom).

The case of a guest luminophore is possibly the most general scenario. If the luminophore is added during the synthesis, it can be possible for the luminescent agent to end up "trapped" between the triazole chains and the counter anions during the formation of the SCO complex; also it can be weakly attached by van der Waals' forces to the surface of the SCO material. In this case the luminophore does not play any particular role in the structure of the material but instead, it constitutes

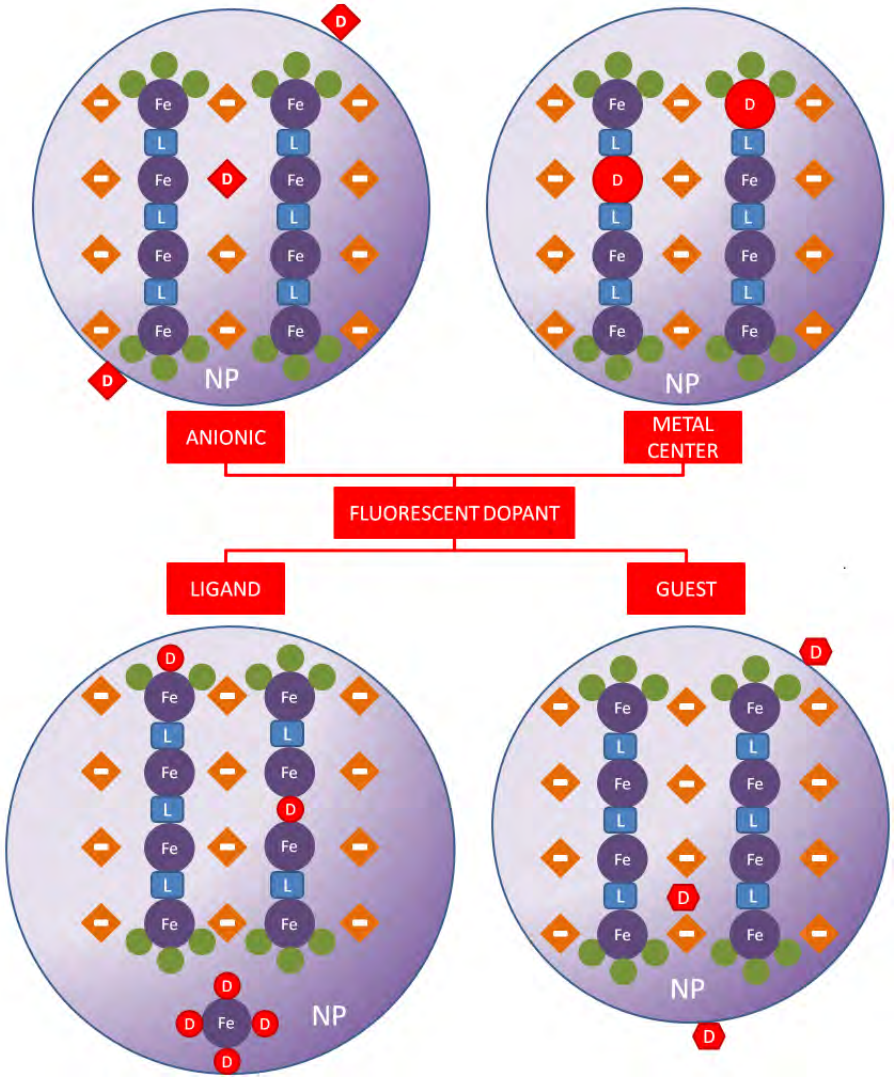

Figure 2.10: Scheme for the possible scenarios for the location of a luminescent doping agent in Fe(II) triazole based nanoparticles. In each situation, the luminescent dopant (D) is represented by the different red symbols.

an anomaly or even a defect that disrupts the "crystalinity" of the material. From this point of view, a positively / negatively charged or a neutral luminescent agent could play the role of a guest in the material. The luminescent doping can also be so thought by means of a counter anion substitution. If a negatively charged luminophore with an appropriate size equivalent to the counter anion employed in the synthesis, there is a chance for the luminophore to occupy a counter anion site in the structure of the material. Additionally, if the grains (or nanoparticles) are positively charged (which from experiences that will be later described it was found to be often the case), the luminophore could be ionic bonded to the surface of the SCO material. With a similar reasoning, a ligand substitution could be rationalized. An adequate ligand with N donor atoms can also act as a bridge to coordinate two iron atoms and be inserted in the middle of a Fe-triazole polymeric chain. Also, such luminescent ligand molecule could coordinate the iron atoms located at the end of the chains to

serve as terminal units that limit their further growth. There is also an "extreme" case where SCO chains are not formed but instead, an Fe(II) atom is coordinated only with luminophore molecules and then, these "monomer -like" species are trapped within a SCO particle. Finally, a luminescent metal centre can also be used as a doping agent. Depending on its coordination number, the metal can act as an Fe(II) substitute in the middle of a chain or act as a terminal coordination metal for the latter.

It is important to note that assuring that any of these scenarios will happen during the synthesis of the SCO material is very difficult. Furthermore, we often do not have an experimental mean to confirm them. However, with the judicious choice of the luminophore we can increase to some extent, the feasibility of one of these to happen upon the formation of the complex. As a result, we have grouped our "attempts" in three different strategies that will be discussed in the following sections. The organic molecules that we have employed as luminescent agents are summarized in Figure 2.11.

- Strategy #1: First attempt towards the development of luminescent SCO nanomaterials. In this strategy nanoparticles of $[Fe(NH_2trz)_3](A)_2$ (A= tosylate (OTs) or nitrate = (NO_3)) were synthesized employing the reverse micelle technique, sodium bis(2-ethylhexyl) sulfosuccinate (NaAOT) as a ionic surfactant and Rhodamine 110 as doping agent (synthesis performed by Lionel Salmon). This was the first attempt of developing luminescent SCO nanomaterials within the frame of this thesis work. It constituted a proof of concept of the fluorescent detection of the SCO. This was a "simple" approach for accomplishing the integration of SCO and luminescence. However, the NaAOT employed during the synthesis presented a double inconvinience: first, its separation from the SCO material was very difficult and second, there was a possible anionic exchange in the particles.

- Strategy #2: Alizarin Red was employed as an alternative doping agent to Rhodamine 110. This organic molecule was employed as a counter anion substitute in the SCO complex with the aim to better integrate the luminophore into the material (closer to the Fe centers). Once again, nanoparticles of $[Fe(NH_2trz)_3](OTs)_2$ were synthesized by means of the reverse micelle technique; however, the secondary alcohol ethoxylate Tergitol 15-S-3 was used as a neutral surfactant to avoid a possible anionic exchange (synthesis performed by Alexei Tokarev). This type of synthesis allowed us to have for the first time, powder of doped SCO nanoparticles with considerably lower quantities of surfactant present in the powder and the posibility of re-disperse them in other solvents.

- Strategy #3: Nanoparticles of $[Fe(hptrz)_3](OTs)_2$ (*hptrz* = 4-heptyl-1,2,4-triazole) were growth in a homogeneous medium employing a stabilizing polymer (PEG-3350). Rhodamine 110, alizarin red and two new doping agents - calcein and acridine orange - were employed as luminophores (synthesis performed by Il'ya A. Gural'skiy). The use of this synthetic approach allowed us to minimize the quantity of additives (polymer-surfactant) during the synthesis leading to more pure materials after the rinsing steps.

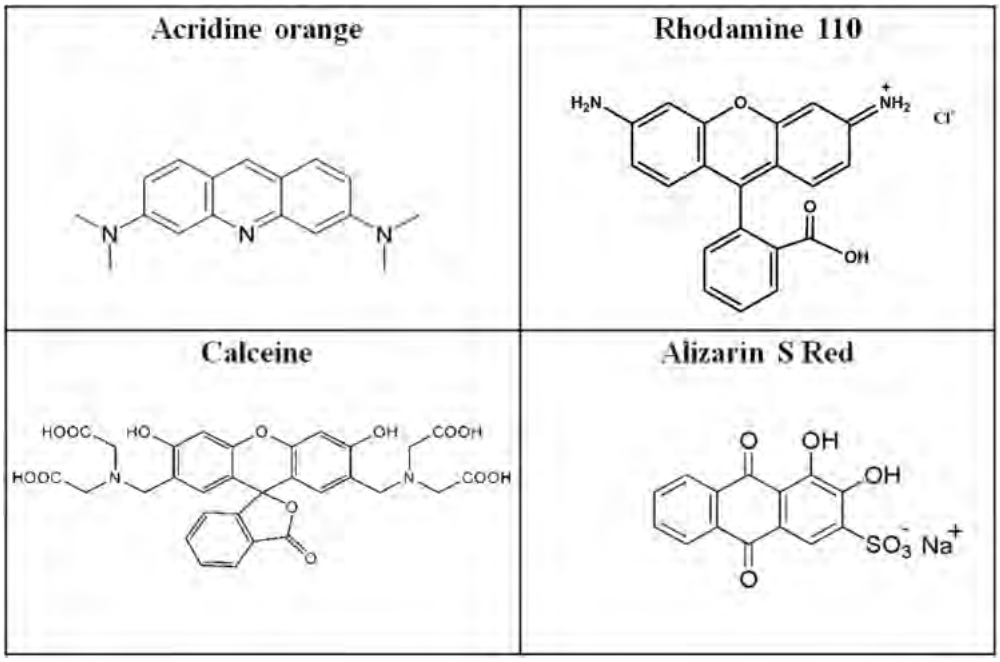

Figure 2.11: Luminescent agents chosen for doping SCO nanoparticles

2.3.2.1 Strategy #1: Organic Luminophore Guest in Reverse Micelles

The first results concerning the synthesis of SCO nanoparticles were reported by Létard et al. [76]. They synthesized nanoparticles of the compound $[Fe(NH_2trz)_3]Br_2$ of *ca.* 70 nm size obtained by the reverse micelle technique (also called water-in-oil microemulsions). The reverse micelles consist of a dispersion of polar liquid droplets stabilized by a surfactant which contains both hydrophobic tail-groups and hydrophilic head-groups in an oil phase. In a typical synthesis for obtaining nanoparticles of a Fe-trizole derivative employing this technique, there is one emulsion that contains the iron salt inside the micelles and a second one that contains a the desired ligand from the triazole family. When these two are put together then mixed vigorously during a few minutes, micellar exchange is produced and it leads to the formation of SCO nanoparticles with a size that depends on the conditions of the reactions: nature of the surfactant, concentration of the precursors, ratio (ω) of the organic/surfactant phase, temperature and time of the reaction. This method has been employed for synthesising SCO nanoparticles not only from derivates of the triazole family [71, 75–87], but also for SCO Hoffmann clathrate like 3D network $[Fe(pz)M(CN)_4]$ (pz = pyrazine, M = Pt or Ni) nanoparticles [88, 89].

As a first attempt for synthesizing luminescent SCO nanomaterials, we have selected the $[Fe(NH_2trz)_3](A)_2$ (A = tosylate or NO_3^-) compounds from the vast family of Fe(II)-triazole complexes[90]. The synthesis of the nanoparticules was realized using the reverse micelle technique - similar to literature reports on other Fe(II)-triazole based nanoparticles [77, 78]. Concerning the luminescent agent, we have retained the rhodamine-110 (Rh110) molecule because (1) it exhibits only a very weak thermal extinction of the luminescence around room temperature (ca. 0.13 $\%.K^{-1}$)[91], (2) its

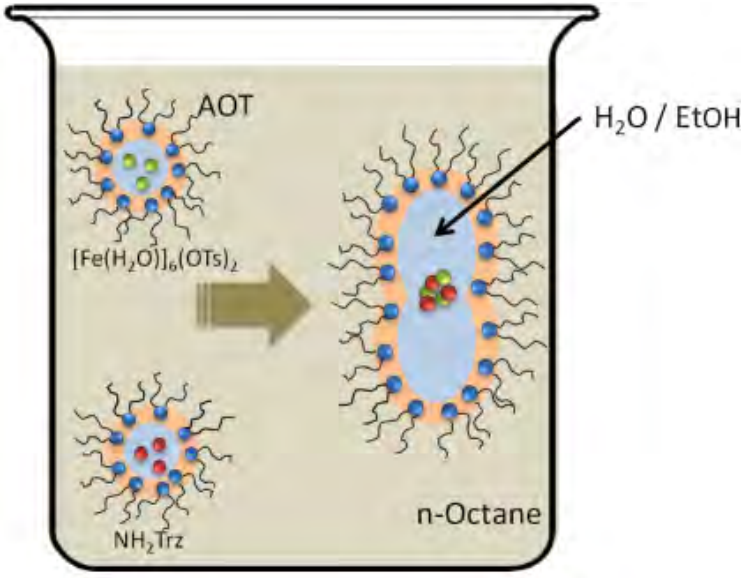

Figure 2.12: Schematic representation of the reverse micelle technique used for the synthesis of $[Fe(NH_2trz)_3](OTs)_2$ nanoparticles in water as the polar solvent for the precursors of the synthesis, bis(2-ethylhexyl) sodium sulphosuccinate (NaAOT) as the stabilizing surfactant and octane as the oil phase.

emission spectrum as well as the low-energy tail of its excitation spectrum overlap the $^1A_1 \rightarrow {}^1T_1$ absorption band of the Fe(II)-triazole complex, (3) it exhibits a relatively weak photobleaching, and (4) its properties within reverse micelles have already been explored [92].

2.3.2.1.1 Synthesis

NH_2trz = 4-amino-1,2,4 triazole, sodium bis(2-ethylhexyl) sulphosuccinate (NaAOT) and octane were purchased from Aldrich and used without further purification. The complex $[Fe(H_2O)_6](OTs)_2$ (OTs = tosylate) was prepared according to the literature [93]. Synthesis of the nanoparticules of $[Fe(NH_2trz)_3](OTs)_2$ was achieved using the reverse micelles (microemulsion) method. Here, the reverse micelles consisted on a dispersion of water/ethanol stabilized by a NaAOT as a surfactant in a phase of octane (Figure 2.12). $[Fe(H_2O)_6](OTs)_2$ (0.380 g, 0.25 M) was dissolved (with a small amount of ascorbic acid) in a demineralised water/ethanol (1+2 mL) mixture, which was added slowly to a solution of 5 g of sodium bis(2-ethylhexyl) sulphosuccinate in 50 mL of octane and the resulting clear solution was stirred for 10 minutes. NH_2trz (0.190 g, 0.75 M) was dissolved in ethanol (3 mL), added to a solution of 5 g of NaAOT in 50 mL of octane and the resulting clear solution was stirred for 10 minutes. The two suspensions were mixed and stirred vigorously for 5 hours at 35 °C. The liquid was left to stand overnight and filtered with a 0.2 μm filter to yield a limpid violet suspension. In the cases of the syntheses with the fluorescent doping agent, the desired amount of rhodamine-110 chloride (Aldrich) was introduced at the same time than the triazole ligand. The dopant concentration (in mol% with respect to the nominal iron salt concentration) was varied between 10^{-4} and 3 %.

2.3.2.1.2 Characterization of the undoped $[Fe(NH_2trz)_3](OTs)_2$

The obtained limpid violet suspension turned colourless when it was heated in an oven to 50 °C and immediately turned back to violet at room temperature confirming the spin crossover properties (Figure 2.14). The size distribution of the nanoparticle suspensions was investigated by dynamic light scattering (DLS) and transmission electron microscopy (TEM). Both a freshly prepared and a one-month-old suspension showed a similar average diameter of 10±(6) nm (see Figure 2.13).

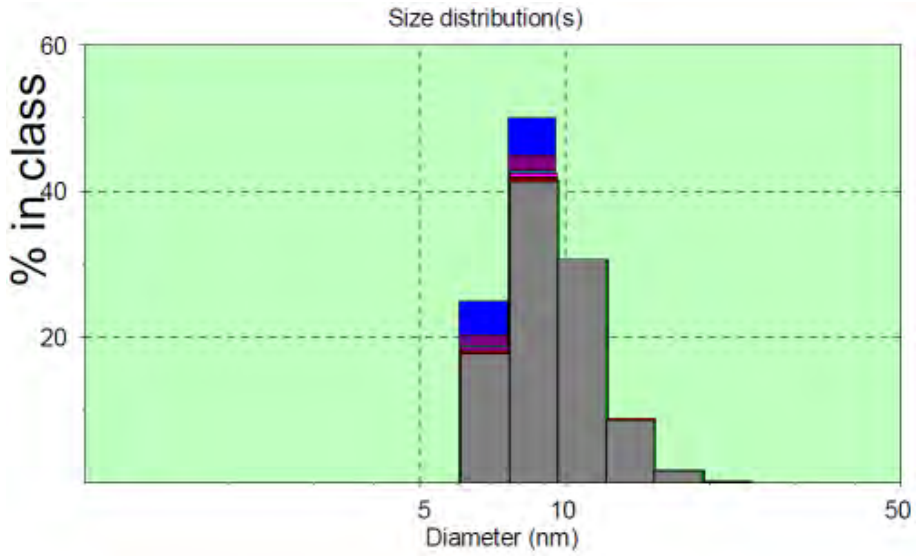

Figure 2.13: Size distribution (analysed by volume) of the $[Fe(NH_2trz)_3](OTs)_2$ nanoparticles measured by DLS.

Figure 2.14a displays the absorption spectra of the non-doped nanoparticle suspension at a few selected temperatures. Two absorption bands appear in the visible (centred at 540 nm) and near-infrared ranges (>660 nm). Since the former bleaches upon heating and the latter upon cooling, we can straightforwardly assign them to the $^1A_1 \rightarrow {}^1T_1$ and $^5T_2 \rightarrow {}^5E$ transitions, respectively. Indeed, in the case of iron(II) SCO complexes there is only one spin-allowed ligand-field transition ($^5T_2 \rightarrow {}^5E$) in the HS state and the corresponding absorption band appears usually in the near-infrared spectral range [23]. On the other hand, in the LS state of these complexes two ligand-field transitions are spin-allowed ($^1A_1 \rightarrow {}^1T_1$ and $^1A_1 \rightarrow {}^1T_2$) and the two absorption bands are observed in the visible and UV spectral ranges, respectively.

If one assumes that the spin transition is complete in both directions (as indicated by the spectra) and the iron ions in the suspension form SCO complexes in a quasi-quantitative manner, one can estimate the molar extinction coefficients as ≈ 65 $dm^3mol^{-1}cm^{-1}$ at 540 nm in the LS state and ≈ 5 $dm^3mol^{-1}cm^{-1}$ at 800 nm in the HS state. These values are in the expected range for spin-allowed d-d transitions. The thermal variation of the maximum absorbance at 540 nm reveals a rather abrupt spin transition with a 9 K wide thermal hysteresis (Figure 2.14b). The transition temperatures (defined as the temperature for which the HS and LS fractions are equal) in the heating and cooling modes are 297 and 306 K, respectively.

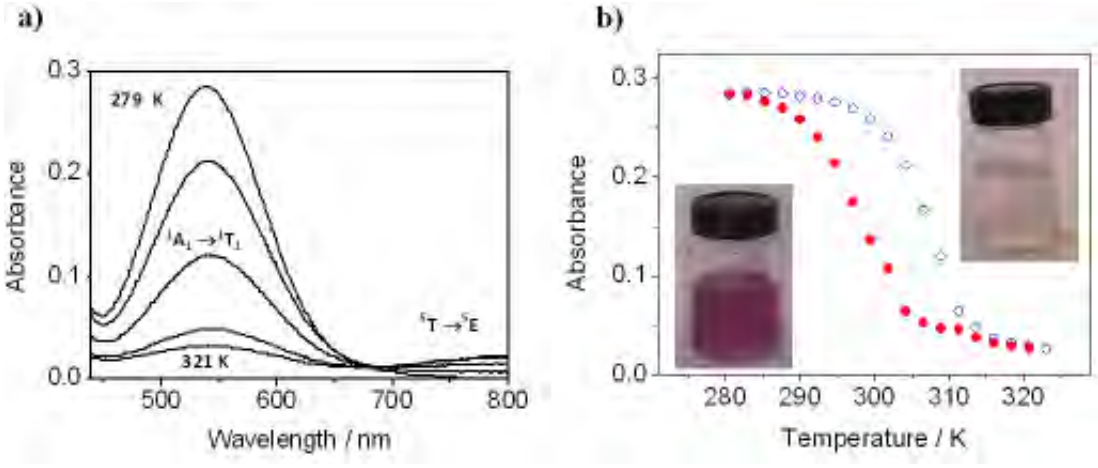

Figure 2.14: Thermochromism of the nanoparticle suspensions. **a)** Absorption spectra of an octane suspension of $Fe(NH_2trz)_3(OTs)_2$ nanoparticles at a few selected temperatures in the cooling mode. **b)** Thermal variation of the absorbance of the suspension at 540 nm in the heating (open symbols) and cooling (closed symbols) modes. The inserts show the photographs of the sample at 295 K (violet) and 320 K (transparent).

2.3.2.1.3 Characterization of Rhodamine 110 doped $[Fe(NH_2trz)_3](OTs)_2$

The room temperature fluorescence excitation and emission spectra of rhodamine 110 (Rh110) doped (3%) nanoparticle suspensions are shown in Figure 2.15a. The maxima of the excitation (475 nm) and the emission (541 nm) bands differ slightly from the literature data for Rh110 [91], which may be related to the fact that the positively charged Rh110 molecules interact with the negatively charged head-groups of the surfactant molecules. Of course, the spectral line shapes are also influenced by the absorbance of the SCO complex, but this effect remains relatively small in our system, evidenced by the shapes of the spectra remaining virtually unchanged between the LS and HS states.

The thermal variation of the fluorescence intensity at 540 nm is depicted in Figure 2.15b. This variation compares well with the changes in absorbance since the fluorescence becomes more intense (by ca. 50 %) in the HS state where the absorbance is bleached. The difference in emission intensity can be well explained by the relevant absorbance changes brought about by the spin crossover phenomenon at the excitation (475 nm) and emission (540 nm) wavelengths: $\Delta A_{540nm} = 0.25$ and $\Delta A_{475nm} = 0.1$ ($e^{0.25+0.1} = 1.42$). As shown in the insert of Figure 2.15b, the change in the emission intensity is also easily observed by eye, which may be a useful feature in various applications. The transition temperatures obtained from the temperature dependence of the fluorescence are 301 and 306 K in the heating and cooling modes, respectively.

It is interesting to note that contrary to the more commonly observed thermal quenching of the luminescence (due to thermal population of non-emitting states), the emission intensity in our system increases with the temperature. The opposite effect could also be achieved, however, if the luminophore displayed a spectral overlap with the HS absorption band in the near-infrared range. In actual fact, the ratiometric use of two emitters (visible and NIR) may be interesting to overcome problems related to

photobleaching or to other sources of signal drift [94]. The details of the mechanism of the luminescence quenching in the LS state and the repartition of the Rh110 molecules within the colloidal suspension have not been studied. We believe, however, that the luminophores must be accumulated within the reverse micelles (either as free molecules or attached to the interface) and quenching occurs via a radiative energy transfer, i.e. the emitted radiation is simply reabsorbed by the nanoparticles in the LS state. Since the emission spectrum lineshape analysis is not helpful in the present case, the energy transfer mechanism may be elucidated by luminescence lifetime or photobleaching measurements.

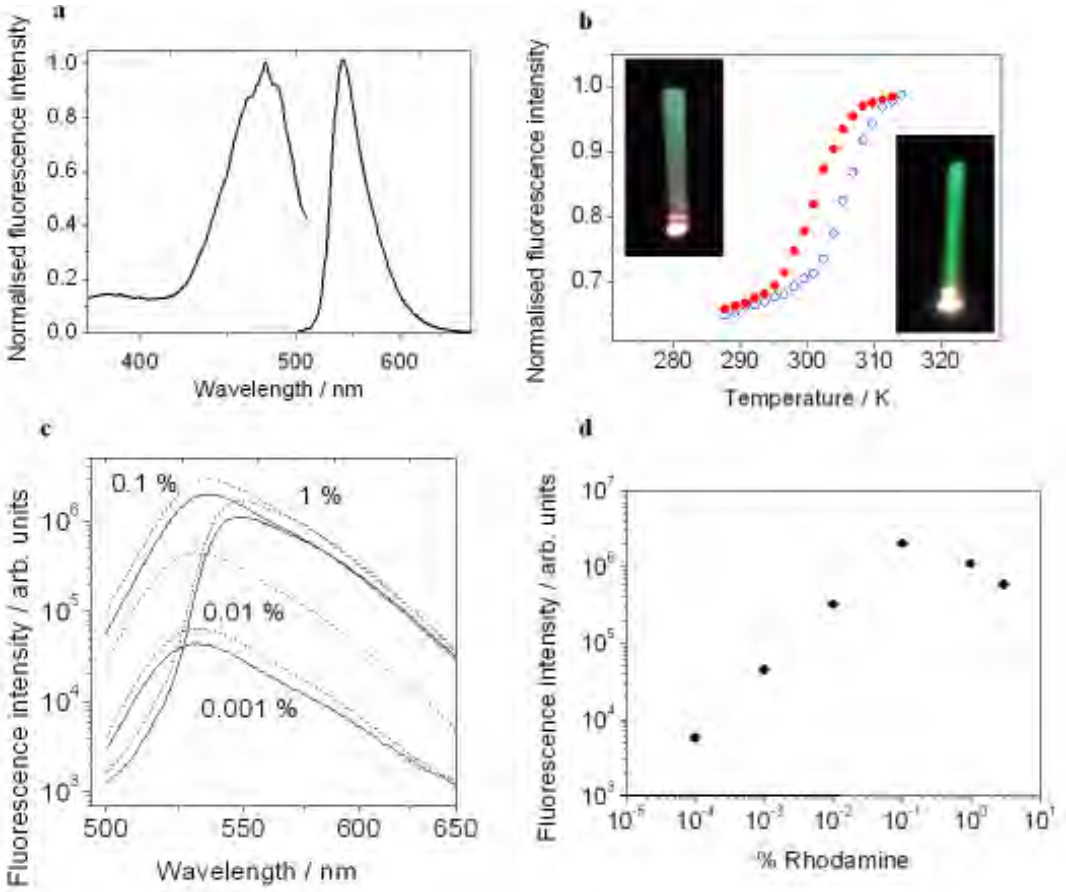

Figure 2.15: Fluorescence of the $[Fe(NH_2trz)_3](OTs)_2$ nanoparticle suspensions. **a)** Fluorescence excitation ($\lambda_{emission}$=540 nm) and emission ($\lambda_{excitation}$=475 nm) spectra of a rhodamine-110 doped (3%) $[Fe(NH_2trz)_3](OTs)_2$ nanoparticle suspension at room temperature. **b)** Thermal variation of the emission intensity at 540 nm in the heating (open symbols) and cooling (closed symbols) modes. The inserts show the photographs of the sample (0.001%) under white light excitation at 295 K and 320 K. **c)** Emission spectra of the suspensions for various rhodamine concentrations. In each case the spectra were recorded successively at 288 K (solid line), 318 K (dashed line) and 288 K (dotted line). **d)** Fluorescence intensity maxima as a function of the rhodamine concentration (288 K).

Another important question concerns the maximum intensity (related to rhodamine concentration) as well as the maximum variation (related to nanoparticle concentration) of the luminescence response with the spin crossover. Unfortunately, the latter concentration cannot be increased significantly due to the destabilisation of the nanoparticle suspensions, thus we have investigated the effect of the Rh110 concen-

tration. As shown in figures 2.15c-d, the luminescence is slightly blue-shifted with decreasing Rh110 concentration and the emission intensity decreases linearly for concentrations below 0.1% Rh110. Above this concentration the shape of the emission spectrum is strongly deformed and its intensity exhibits a concentration-quenching. On the other hand, the variation of the luminescence intensity remains nearly constant (≈50%) for different Rh110 concentrations, as would be expected.

In order to illustrate the potential generality of our approach to detect the SCO in different complexes of the same family without changing the luminescent agent, we have synthesized ultra-small (*ca.* 3 nm) nanoparticles of $[Fe(NH_2trz)_3](NO_3)_2$ by the same method (slightly changing the experimental conditions). This sample showed a modulation of the luminescence that put in evidence a transition around 303 K without any appreciable hysteresis (Figure 2.16).

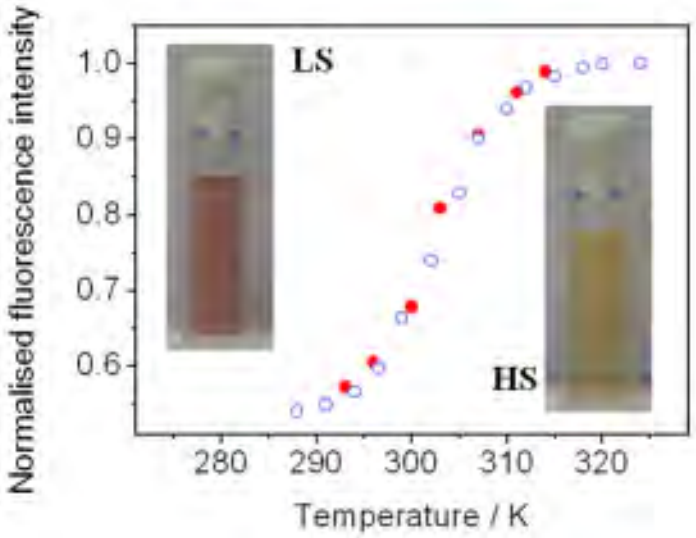

Figure 2.16: Fluorescent thermometry around room temperature. Thermal variation of the fluorescence intensity at 540 nm in the heating (open symbols) and cooling (closed symbols) modes for a rhodamine-110 doped (0.01%) $[Fe(NH_2trz)_3](NO_3)_2$ nanoparticle (3 nm) suspension. The insets display an image of the suspension in the LS (left) and HS (right) state.

2.3.2.2 Strategy #2: Counter Anion Substitution

This strategy will explore the doping of $[Fe(NH_2trz)_3](OTs)_2$ nanoparticles (synthesized with the reverse micelle technique) by the negatively charged alizarin red as a counter anion substitute. In spite of the promising results obtained in the synthesis by reverse micelles employing NaAOT as a surfactant, its ionic nature constituted a risk for modifying the composition of the nanoparticles by possible counter-ionic exchange (revealed by Raman and IR spectroscopy). As a result, the use of the non-ionic surfactant Tergitol as the stabilizer of the micelles was adopted in this strategy.

2.3.2.2.1 Synthesis

The coordination complex was synthesized in reverse micelles. The microemulsion

was prepared by adding the iron precursor in a methanol-water (0.4 ml) solution with ascorbic acid (to prevent the oxydation of the iron centers) and a 4-NH_2-1,2,4-triazole (0.063 g, 0.75 mmol) aqueous solution (0.2 ml) to two equal volumes of the surfractant (5 ml) and stirred. After the synthesis, two forms of samples were obtained. First, the polar phase of the microemulsion was evaporated under reduced pressure and as a result, ultrafine (c.a. 3-4 nm) well dispersed colloids were obtained in the surfactant. Second, we were also able to separate larger nanoparticles (c.a. 100-200 nm) by destabilizing the microemulsion with a nonpolar solvent such as diethyl ether (c.a. 160 ml) and after a centrifugation step, extensive washing with the same solvent and vacuum drying were performed (Figure 2.17).

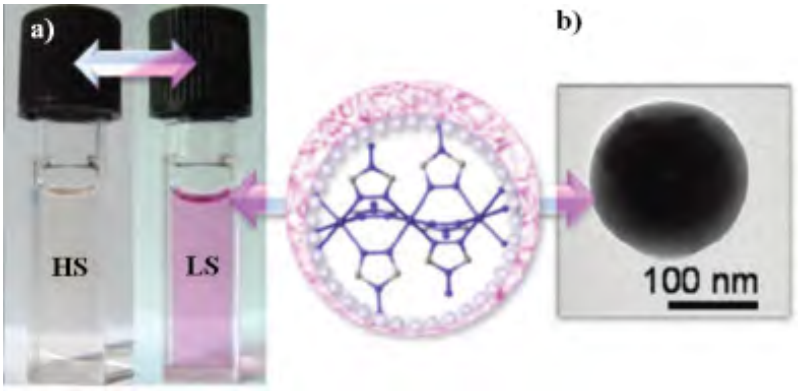

Figure 2.17: Schematic representation of the two possible sample forms of $[[Fe(NH_2trz)_3](OTs)_2$ nanoparticles obtained from strategy #2. **a)** A stable colloidal suspension obtained after vacuum treatment. **b)** Nanoparticle powder obtained after employing solvent precipitation of the reverse micelle microemulsion.

In the case of the doped samples, the alizarin red was added at the same time than the triazole ligand. We would like to stress that in this type of samples it is even less evident to deduce the location of the luminophore; after the evaporation of the polar phase of the micelle, the luminophore could be either integrated into the nanoparticles, onto their surface or solubilized in the surfactant. As for the powder samples, after the precipitation and washing steps, we observed that a part of the luminophore leaves the sample and there is not an evident way to assess how much organic luminophore remains in the final powder (owing to the initially already low concentration).

It is interesting to note that this synthesis provides a powder form of nanoparticles with low surfactant content that can eventually be redispersed in other solvents for further deposition. This would be a very difficult task while working with NaAOT based synthesis; this surfactant is difficult to wash and in the end instead of a powder, we usually obtained a paste.

2.3.2.2.2 Characterization of the undoped $[Fe(NH_2trz)_3](OTs)_2$ (tergitol)

The size and size distribution of the nanoparticles from the colloidal suspension were analyzed by transmission electron microscopy (TEM and HRTEM) using cryo-microtomy techniques (Figure 2.18). TEM images show uniform, spherical, non-aggregated

nanoparticles with a narrow size distribution and a mean particle size of 3.6 nm ± 0.8 nm. The absorption spectrum as a function of temperature was studied for a colloidal suspension containing 2 wt% (27.3 mM) of Fe complex (Figure 2.18b and c). From these measurements an absorption band centered at 540 nm is observed in the low spin state (colored solution) and assigned to the $^1A_1 \rightarrow {}^1T_1$ transition. It bleaches upon the SCO as the sample reaches the high spin state. Also, a second broad absorption band centered at 830 nm can be depicted as the system goes to the high spin state and is assigned to the $^5T_2 \rightarrow {}^5E$ transition of the Fe(II) high spin centers. If it is assumed that the transition is complete in the heating and cooling branches (as suggested by the absoption spectra) and all iron involved in the synthesis formed the SCO complex, it is possible to estimate the molar extinction coefficients for this material ≈ 30 $dm^3mol^{-1}cm^{-1}$ for the LS and ≈ 3 $dm^3mol^{-1}cm^{-1}$ for the HS absorption bands. The measurement indicates that the thermal SCO is reversible and that it has a transition temperature $T_{1/2} = 295$ K (Figure 2.18 c). The suspension was stable within the temperature range of the experiment; however, if the suspension was heated beyond 315 K it began to destabilize and in some cases it tended to decompose (oxidation) by taking a yellowish color; this effect could be partially avoided by purging the cuvette containing the suspension with argon. One shall note that the SCO and optical properties of the final compound varies slightly from that obtained in strategy #1; the difference in the solvent and surfactant during the synthesis, the residual LS/HS fraction of the suspended objects, the different size (objects smaller than in strategy #1 and also the light scattering produced by the particles could explain such disparities.

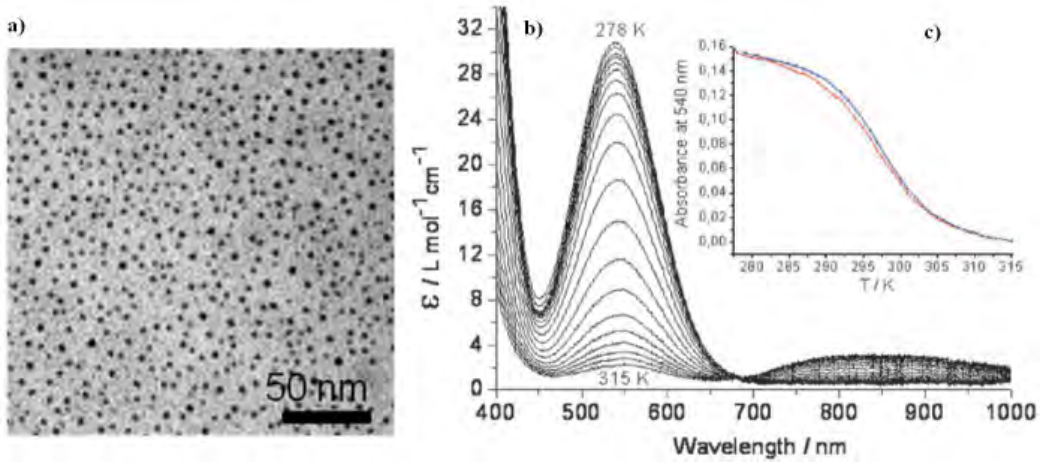

Figure 2.18: **a)** Cryo-microtomy TEM from the colloidal form of $[Fe(NH_2trz)_3](OTs)_2$. **b)** Visible/Near infra-red absorption spectrum of the undoped colloidal suspension as a function of temperature. **c)** Thermal variation of the absorbance at 540 nm.

The morphology of the precipitated powder form of the sample was studied by transmission electron microscopy (TEM) and scanning electron microscopy (SEM). Both types of observations confirmed a spherical morphology of the particles; in general, these types of samples revealed a mixture of several nanoparticle populations of more important sizes than that of the colloidal suspension (50 nm - 300 nm or higher). Furthermore, the faithful size distribution and morphology of the aggregated nanoparticle powder is not always easy to obtain from the electron-microscopy im-

ages. Particularly in SEM, the surfactant remaining on the sample constituted an issue for obtaining proper images of the morphology of the particles from the powder (See Figure 2.19).

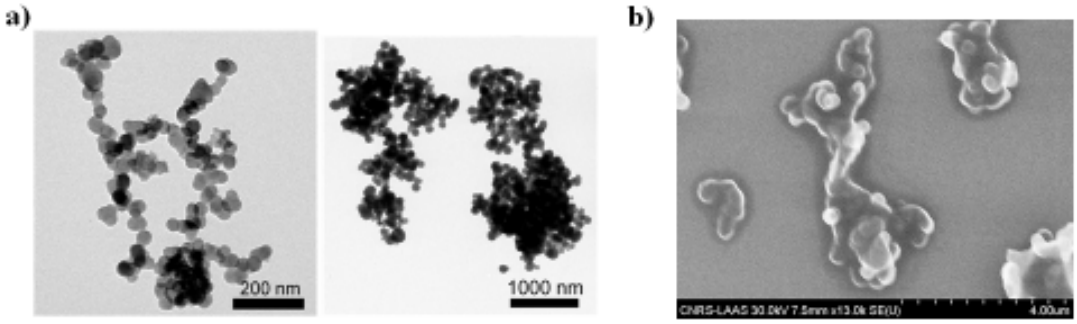

Figure 2.19: **a)** Transmission electron microscopy (TEM) and **b)** Scanning Electron Microscopy (SEM) images of $[Fe(NH_2trz)_3](OTs)_2$ nanoparticle powder obtained by the reverse micelle technique.

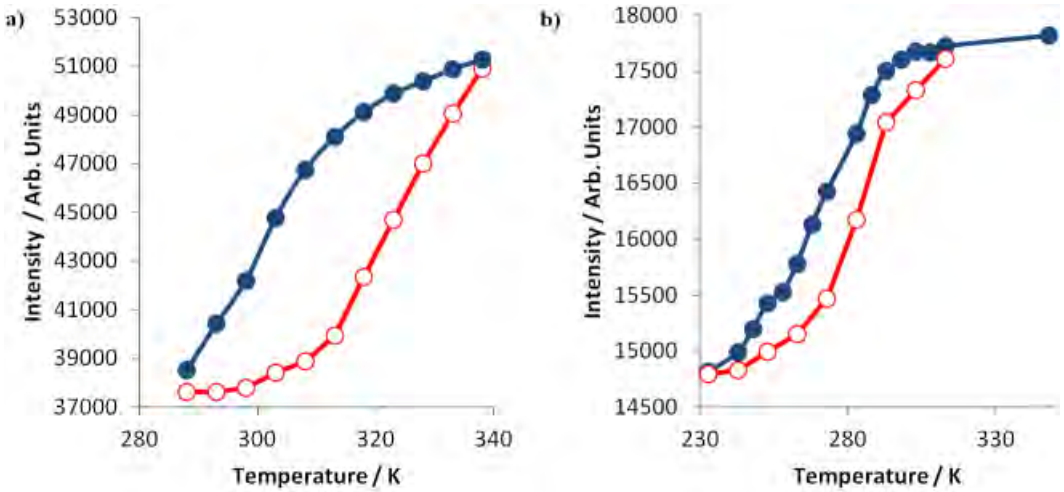

Figure 2.20: Reflectivity measurements at 543 nm (FWHM = 22 nm) of the precipitated nanoparticle powder of undoped $[Fe(NH_2trz)_3](OTs)_2$. **a)** Hydrated form and **b)** dehydrated form (measurement performed under a N_2 atmosphere). (Open and close symbols represent the heating and cooling branches, respectively.)

The SCO displayed by this type of sample was studied with reflectivity measurements at 543 nm as a function of temperature using the microscope set up. The first observations were performed employing the Linkam Peltier based platform in an open atmosphere. Here we observed the dehydration effect in the nanoparticle powder. The sample was heated for 30 minutes at 363 K in order to desolvate of the powder; however, as the sample was cooled down, it gained easily water and as a result, it stayed in its HS state during a wide range of temperatures ($T_{1/2}\uparrow = 322$ K and $T_{1/2}\downarrow = 301$ K, Figure 2.20a). Hence, an artificial enlargement of the hysteresis was observed (width of 20 K) and the cycles were not well reproducible. For this reason we employed the THMS-600 Linkam cryostat. This device allows us to study the sample in a controlled N_2 atmosphere during the whole experiment. After the purge step at 363 K for 30

minutes under a N_2 flow for the same sample, we were able to successfully dehydrate it and observe the behavior of the powder without any water acting as a guest. Figure 2.20b displays the variation of the reflectivity at 543 nm for the dehydrated powder form. In contrast to the hydrated version, the transition is shifted by approximately 26 K to lower temperatures ($T_{1/2} \uparrow = 288$ K and $T_{1/2} \downarrow = 270$ K) and it is accompanied with a narrower hysteresis (width of 16 K). From these measurements we can conclude that the growth of the nanoparticles generated during the precipitation from the reverse micelle leads not only to a morphological change of the particles, but also to the observation of a hysteresis not present in the colloidal suspension, possibly associated to the increase of the particle size or a matrix effect produced by the tergitol.

2.3.2.2.3 Alizarin Red S doping

Alizarin Red S organic molecule was chosen due to its negative charge that, in contrast to the positively charged Rhodamine 110, could serve as a counter anion substitute of the tosylate ion. This way, we expected to increase the possibility of integrating the luminescent agent into the nanoparticle, closer to the Fe(II) centers and as a result, obtaining a higher modulation of the luminescence upon the SCO. The luminescence of the colloidal suspension obtained from a synthesis with 0.5 mol% dopped alizarin red per iron atom was studied as a function of temperature. Figure 2.21 displays the room temperature excitation and emission spectra of the $[Fe(NH_2trz)_3](OTs)_2$ doped nanoparticle suspension and for comparison the 540 nm centered low spin absoprtion band of the complex is ploted. The maxima of the excitation was observed around 450 nm and for the emission at 640 nm. We have found in the literature that the spectra of this organic luminophore varies strongly with to its environment and molecular form and as a result, it has been employed as a sensor in different biochemistry applications [95–99]. Depending on the situation, its excitation maxima can be in the blue or green spectral range; however, its emission is essentially centered in the red around 600 nm. We studied these samples at 540 nm because even though it is not the emission maximum, it is around this wavelength that we should expect the highest modulation of the luminescence.

The thermal variation of the luminescence at 540 nm is shown in Figure 2.22. As the system reaches the HS state, the luminescence triples when compared to the LS state which may constitute an improvement compared to the results obtained with rhodamine 110 in strategy #1. The thermal transition curve reproduces fairly the behaviour obtained by absorption spectroscopy for a similar undoped version of the sample (Figure 2.18b).

The doped powder samples obtained from analog microemulsions were studied with fluorescence microscopy. We would like to stress that for these types of samples the quantity of alizarin red employed in the reverse micelle was the same as for the previous measurements, but as mentioned before, the nanoparticle powder has less alizarin red contents than its original mircoemulsion due to the washing steps. In Figure 2.23 the luminescent response of the dehydrated (30 minutes at 363 K under N_2 flow) doped nanoparticle powder can be observed at 550 nm with a 450 nm excitation. The luminescence of the material increases with the temperature as it transits to

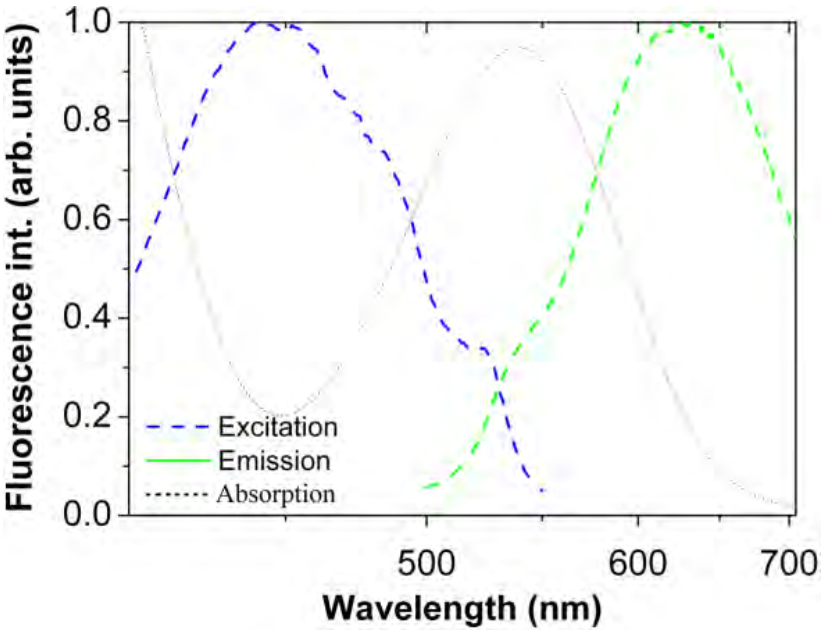

Figure 2.21: Excitation (@540 nm) and emission (@475 nm) spectra of an Alizarin Red doped colloidal suspension of $[Fe(NH_2trz)_3](OTs)_2$ superposed to the characteristic LS *d-d* absorption band of the undoped solution

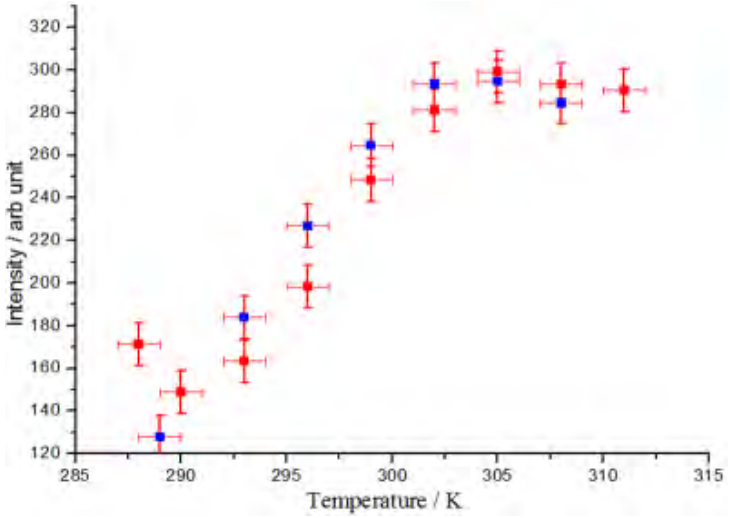

Figure 2.22: Thermal variation of the fluorescence emission intensity at 540 nm in the heating (red) and cooling (blue) modes of an alizarine red (0.5%) doped $[Fe(NH_2trz)_3](OTs)_2$ nanoparticle suspension.

the HS state. Particularly at low temperatures it can be seen that the luminophore displays under these experimental conditions low thermal and photo-bleaching. From the measurement, a 22 K hysteresis is observed with $T_{1/2} \uparrow = 300$ K and $T_{1/2} \downarrow = 278$ K which is centered around the same temperature as the curve obtained for the undoped version in reflectivity. However, one shall note that the comparison of the reflectivity data with the fluorescence measurements is not straightforward since none of these signals is strictly proportional to γ_{HS}.

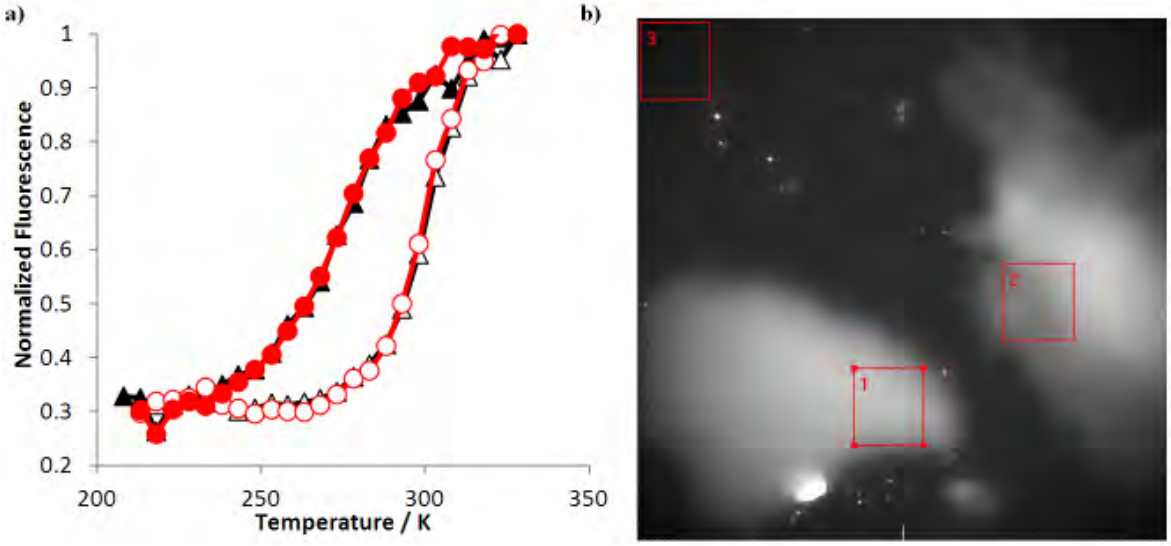

Figure 2.23: **a)** Thermal variation of the luminescence intensity at 550 nm with an excitation at 450 nm of the powder nanoparticles of $[Fe(NH_2trz)_3](OTs)_2$ doped with alizarin red in a controlled N_2 atmosphere. (Open and close symbols represent the heating and cooling branches for ROI1 (circles) and ROI2 (triangles), respectively) b) Fluorescence image of the powder. The ROI employed for obtaining the data are signaled in red.

2.3.2.3 Strategy #3: Synthesis in Homogeneous Medium

In the reverse micelle approach, the most critical issues are the separation of the particles from the surfactant, their resolubilization for future manipulations and also the prevention from aggregation and destruction through oxidation or hydrolysis. Additionally, the presence of an important quantity of surfactant (which is always used in excess to the complex in this method) causes a dilution of the SCO material, decreasing the response of such objects compared to that of a pure SCO object of equivalent size and thus hampering the detection of the SCO at the nanometric level (See Chapter III). From these points of view, it should be stressed that a search of novel approaches towards surfactant free SCO nano-objects with different sizes and new morphologies is an important task.

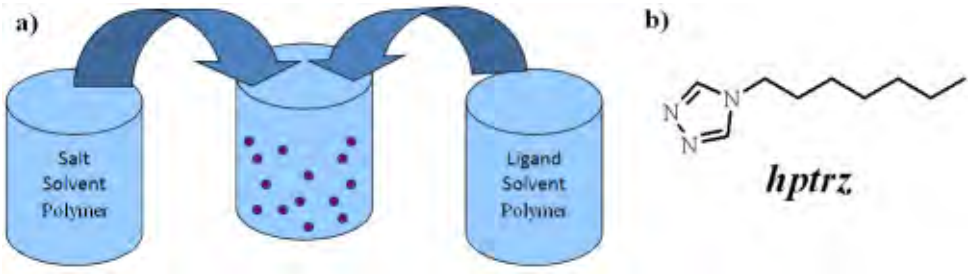

Figure 2.24: **a)** Schematic representation of a homogeneous synthesis in presence of a polymer. **a)** The ligand 4-heptyl-1,2,4-triazole.

One method to limit the growth of complex nanoparticles in solution involves the use of a stabilizing polymer (Figure 2.24). A few essays involving such homogeneous syntheses have been described in literature [100, 101]. In these cases, either

$[Fe(NH_2trz)_3](ClO_4)_2$-PVP regular stripes or nematic liquid crystal gel of $[FeL_3]Cl_2$ (L is 4-(3-dodecyloxy)pro-pyl-1,2,4-triazole) were obtained although no well defined nano- or microobjects were observed. In contrast, various size PVP-protected nanoparticles of Prussian blue [102] and its analogues [103] were synthesized controlling the PVP/metal ratio. More simple approaches for the growth of similar nanoparticles of cyano-bridged molecule-based magnets in organic solvent medium (without polymer or surfactant) were also developed [104, 105].

For this strategy, we explored a homogeneous medium approach for the synthesis of Fe(II)-triazole based particles that consists of the addition of the triazole ligand solution to an iron salt solution containing a polymer. The choice for the latter was made in favor of non-ionic polymeric amphiphilic compounds in order to preclude the exchange between the anionic parts of the polymer with the counter anion of the complex.

We chose as the stabilizing agent polyethylene glycol (PEG-3350) and a water medium to obtain SCO micro- and nano-objects based upon the $[Fe(hptrz)_3](OTs)_2$ complex (*hptrz* = 4-heptyl-1,2,4-triazole, see Figure 2.24b), which is characterized by an abrupt spin transition with a hysteresis loop close to room temperature ($T_{1/2} \uparrow$ = 318 K and $T_{1/2} \downarrow$ = 308 K for the dehydrated bulk powder) higher than that observed for $[Fe(NH_2trz)_3](OTs)_2$ [73]. In the family of the Fe(II) triazole complexes, both the ligand - in particular the nature of the substituent in the fourth position of the heterocycle- and the counter anion influence the polymerization degree and the capability of precipitation of the SCO complexes [41]. Particularly for 4-heptyl-1,2,4-triazole ligand, its long alkyl chain in the fourth position of the heterocyclic ring allows to increase the hydrophobic properties of the corresponding complex nanoparticles and as a result, it leads to an enhanced capability of precipitation in aqueous medium. Moreover, the increased insolubility of the nanoparticles in polar media permits the stabilization of such objects in colloidal suspension [87].

Several advantages appeared using such type of syntheses. (1) In contrast with the reverse micelle, the process is simple and versatile, not only because various polar and non-polar solvents can be used, but also because the whole protocol does not imply a critical step influencing the results like the destabilization of the micelle phase by an additional solvent. (2) The quantity of polymer as well as the quantity of solvent used for the synthesis is lower compared to the quantities used in the reverse micelle method. As a consequence, measurements of the properties are favorized by the high concentration of the active species in the matrix. (3) The shape and the size of the nano- and micro-objects can be different to those elaborated with the microemulsion. (4) The doping of the SCO compound with a fluorescent agent could be more controllable because of the absence of two different polarity phases like in the case of a microemulsion which could provoke the undesired migration of the luminophore species. (More details of this type of synthesis and other variations developed in our team can be found in ref. [75]).

As we have seen in the previous two strategies, changing a single parameter during the synthesis of the SCO nanoparticles can have an unpredictable impact on the size, morphology and properties of the sample. Since the synthetic conditions in this

strategy are completely different to those employed before, we continued studying the properties of rhodamine 110 and alizarin red S doping the [Fe(*hptrz*)$_3$](OTs)$_2$. Additionally, we explored two other alternative organic molecules as doping agents: calcein as a possible counter anion substitute of OTs and acridine orange as a ligand substitute to the *hptrz* ligand. The characterization of these particles will be described in the following sections.

2.3.2.3.1 Synthesis

Ligand 4-heptyl-1,2,4-triazole (*hptrz*) was obtained from N-formylhydrazine, triethyl orthoformate and n-heptylamine following the Bayer synthesis [106]. Fe(II) tosylate was synthesized by reaction of metallic iron with tosylic acid [107]. In a typical experiment two distinct solutions were prepared: (1) Iron (II) tosylate hexahydrate (15 mg, 0.03 mmol, 1 equiv), ascorbic acid (1 mg) and PEG-3350 (50- 400 mg) in 2 ml of H_2O; (2) *hptrz* (15 mg, 0.09 mmol, 1 equiv.) in 2 ml of H_2O. The two solutions were rapidly mixed. The mixture becomes turbid in a few seconds followed by a formation of a precipitate. The latter was separated by centrifugation and washed twice in H_2O; the product of the synthesis in water resulted in pink precipitates formation (Figure 2.25). For the synthesis of the doped particles the luminescent dyes were added (1%) to the ligand solution before the reaction with the iron salt. As in strategy #2, part of the luminophore added during the synthesis leaves during the washing steps and there is not an evident procedure to deduce how much of it remains in the particles. As for the location of the luminophore, it also remains unknown under this synthetic approach.

Figure 2.25: Images of the undoped [Fe(*hptrz*)$_3$](OTs)$_2$ nanoparticle powder in the LS and HS states.

2.3.2.3.2 Characterization of the un-doped [Fe(*hptrz*)$_3$](OTs)$_2$

The morphology of the precipitated sample was studied by TEM and SEM. Both techniques confirmed that the particles generated by this synthetic approach are regular rectangular shaped microcrystals (Figures 2.26 and 2.27). However, a variation of their size was observed from 250 nm to 500 nm depending on the amount of polymer added to the medium (50 mg to 400 mg, respectively) and was also confirmed by DLS

measurements. The synthesis using PEGs of different molecular weights (M = 1000 or 400 g/mol) as stabilizing agents was also tried and it led to similar crystals. We believe that the role of the PEG is mostly controlling the monodispersity of the particles, their form and aggregation rate. It is important to mention, that essays to obtain smaller size objects by this synthetic method were unsuccessful. Additionally, it is interesting to note that there is considerably less polymer in the final product; most of the times it cannot be seen in SEM images; nonetheless, the very weak aggregation of the particles suggests a very thin layer covers the particles (or at least partially) preventing their aggregation.

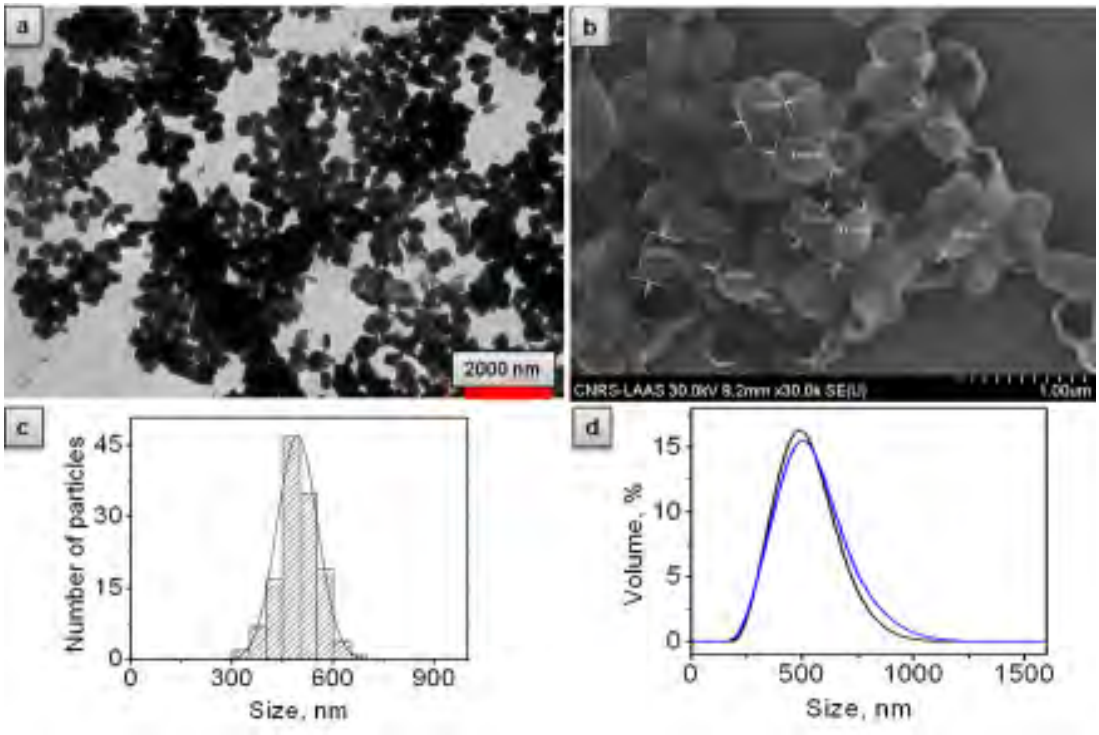

Figure 2.26: **a)** TEM and **a)** SEM images of 490 ± 70 nm nanoparticles of $[Fe(hptrz)_3](OTs)_2$ synthesized in water medium and in presence of 400 mg of PEG-3350. **c)** Corresponding histogram (distribution by size from TEM image, the largest dimension of each nanoparticle was used for the statistics) and **d)** DLS (distribution by volume)

The thermal SCO of these dehydrated (30 minutes at 363 K under N_2 flow) samples was studied with reflectivity measurements at 543 nm under the microscope with a programmed temperature cycle sweeping at 2 K/min. These observations revealed that the SCO takes place at the same region as for the bulk version of the complex with $T_{1/2} \uparrow \approx 315$ K and $T_{1/2} \downarrow \approx 309$ K. However, even under a controlled temperature, these samples are very sensitive to hydration and even small amounts of residual water in the cryostat chamber or in the powder can cause a shift on the transition temperature during the experiments. As a result, hystereses ranging from 4 to 10 K have been observed. Figure 2.28 shows the reflectivity measurements for the bulk powder of the complex and Figure 2.29 the thermal response obtained from two different syntheses of nanoparticles in presence of PEG.

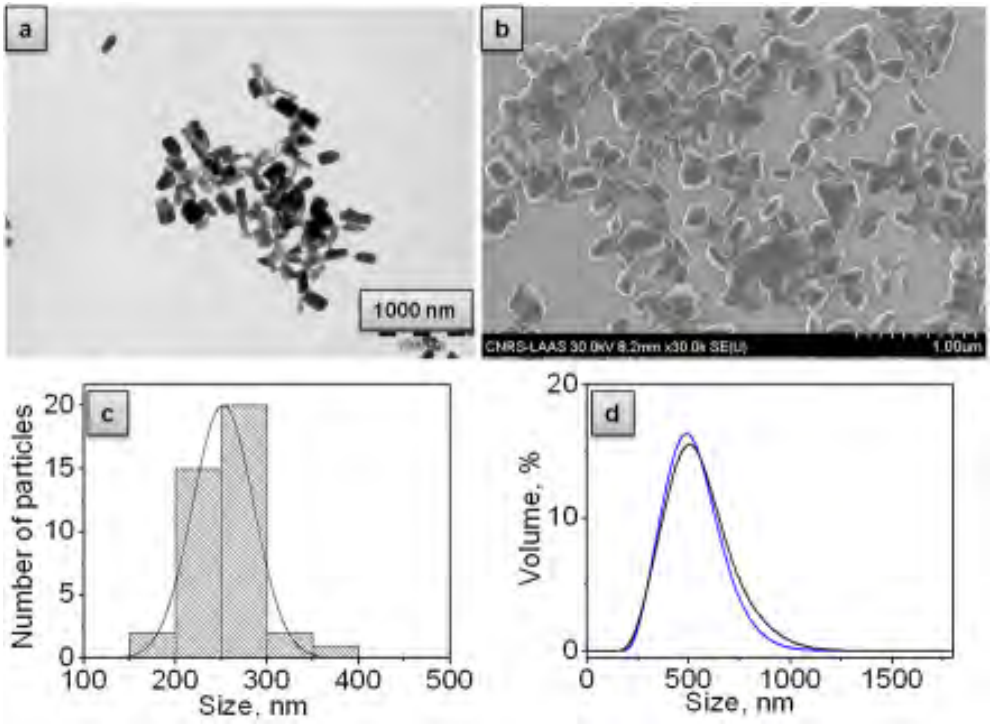

Figure 2.27: **a)** TEM and **b)** SEM images of 250 ± 40 nm nanoparticles of $[Fe(hptrz)_3](OTs)_2$ synthesized in water medium and in presence of 50 mg of PEG-3350. **c)** Corresponding histogram (distribution by size from TEM image, the largest dimension of each nanoparticles was used for the statistics) and **d)** DLS (distribution by volume)

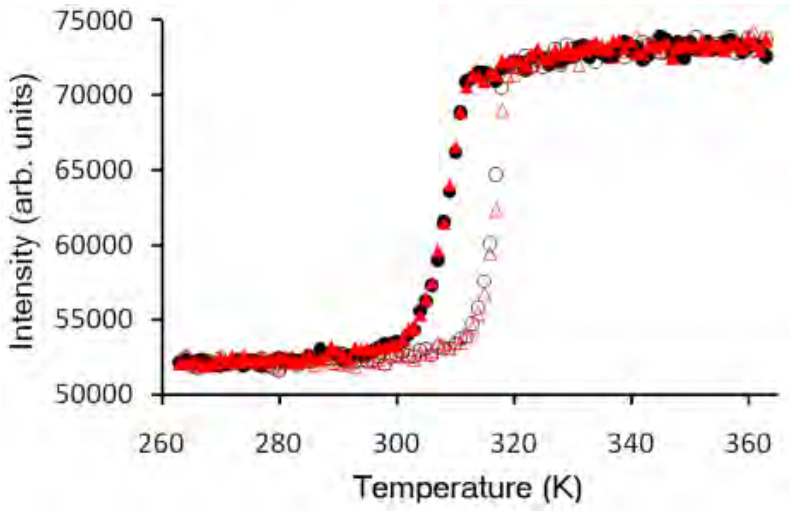

Figure 2.28: Thermal variation of the reflectance of undoped $[Fe(hptrz)_3](OTs)_2$ in bulk powder form at 543 nm for two consecutive cycles under a controlled N_2 atmosphere. (Open and closed symbols stand for heating and cooling, respectively.)

2.3.2.3.3 Characterization of luminescent doped $[Fe(hptrz)_3](OTs)_2$

In order to spectroscopically characterize the fluorescence of the different doped versions of $[Fe(hptrz)_3](OTs)_2$ particles, 1 mg of each sample was suspended in 4 ml of $CHCl_3$ and then the ensemble was put in an ultrasonic bath for a few seconds. As a result, a suspension of particles that is homogeneous and stable (at least) during a

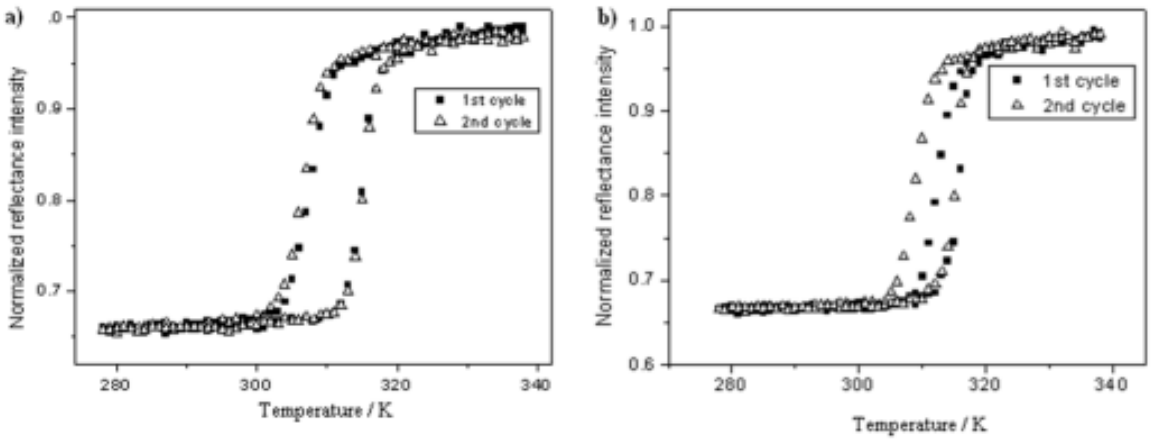

Figure 2.29: Thermal variation of the reflectivity at 543 (FWHM=22 nm) of two [Fe(*hptrz*)$_3$](OTs)$_2$ nanoparticle powders under a controlled N_2 atmosphere. Synthesis performed in presence of **a)** 400 mg and **b)** 50 mg of PEG-3350.

few minutes is obtained. (In the long term they do precipitate.) Due to the non-polar nature of the chloroform, the particles are safe from hydrolysis or oxidation. The in-

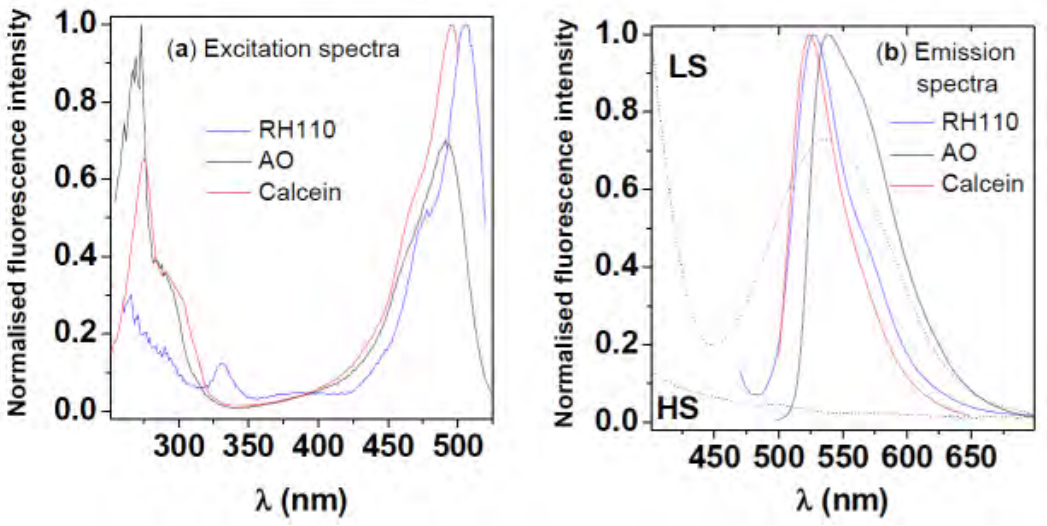

Figure 2.30: Room temperature luminescence excitation (@550 nm) and emission (@450 nm) spectra of a chloroform suspension of [Fe(*hptrz*)$_3$] (OTs)$_2$ nanoparticles synthesized in water, in presence of PEG-3350 and doped with different luminophores.

spection of the luminescence spectra in Figure 2.30 reveals that the emission bands of the rhodamine 110, alizarin red, calcein and acridine orange after the synthesis and under these experimental conditions overlap tightly with the broad absorption band of the complex in the LS state around 540 nm. The excitation spectra of the luminophores show also a partial spectral overlap at several wavelengths with the same LS absorption band. These features suggest that the spin state change of the complex from LS to HS should lead to an increase of the luminescence intensity for judiciously selected excitation (450 nm) and emission (550 nm) wavelengths.

2.3.2.3.3.1 Rhodamine 110:

The variation of the luminescence as a function of temperature for the dehydrated (30 minutes at 363K under N_2 flow) Rhodamine 110 doped nanoparticles revealed an important modulation between the two spin states (*ca.* 300%). This sample exhibited a behavior very similar to the bulk powder form with $T_{1/2} \uparrow \approx 318$ K and $T_{1/2} \downarrow \approx 311$ K (Figure 2.31). Slight variations of the transition temperature were observed; however, the response of the system is in general highly reproducible and neither a temperature dependence of the luminescence (far from the SCO) nor observable photobleaching under these experimental conditions was observed.

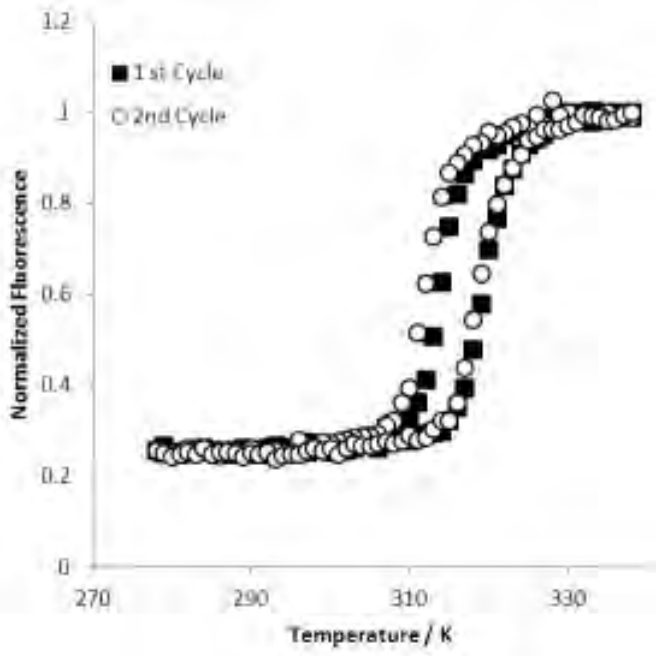

Figure 2.31: Thermal variation of the luminescence at 550 nm under a N_2 atmosphere for the Rhodamine 110 doped nanoparticle powder of $[Fe(hptrz)_3](OTs)_2$ synthesized in water in presence of PEG. Cycle temperature rate: 2K/min.

2.3.2.3.3.2 Alizarin Red:

The luminescence modulation as a function of temperature for the dehydrated (30 minutes at 363 K under N_2 flow) alizarin red doped nanoparticles is shown in Figure 2.32. A general instability of the system response is observed specially at low temperature. This behavior may be attributed to water traces remaining in the sample or photobleaching. In order to study this last scenario, after the experiment shown in Figure 2.32a, the sample was re-purged and a second experiment was launched with 60% of the excitation light intensity employed in the first experiment. Figure 2.32b displays two cycles that reveal a hysteresis similar to that of the undoped sample with $T_{1/2} \uparrow \approx 313$ K and $T_{1/2} \downarrow \approx 304$ K. Some improvement was achieved also at high temperatures (T > 330 K) since the "pure" HS state of the heating branches match their equivalent on the successive cooling branches; however, a marked decrease of the signal intensity is observed while comparing a given "pure" HS state with the previous

cooling branch. There is an unknown damaging effect that occurs at low temperatures (around 273 K) that cannot be associated exclusively to photobleaching effects. If that were the case, a general decrease of the luminescent response of the system should be observed at all temperatures during the cycles (as documented in the first experiment) and it should be particularly stronger at high temperatures where the luminophore is more susceptible of being permanently damaged. One hypothesis for explaining this behavior could be linked to the possible existence of water traces in the cryostat chamber that have higher probability of condensing in the sample rendering a detrimental environment for the complex/luminophore. Additionally, the negative slope obtained at the end of the cycles at high temperature puts in evidence a thermal dependence of the luminophore under these experimental conditions.

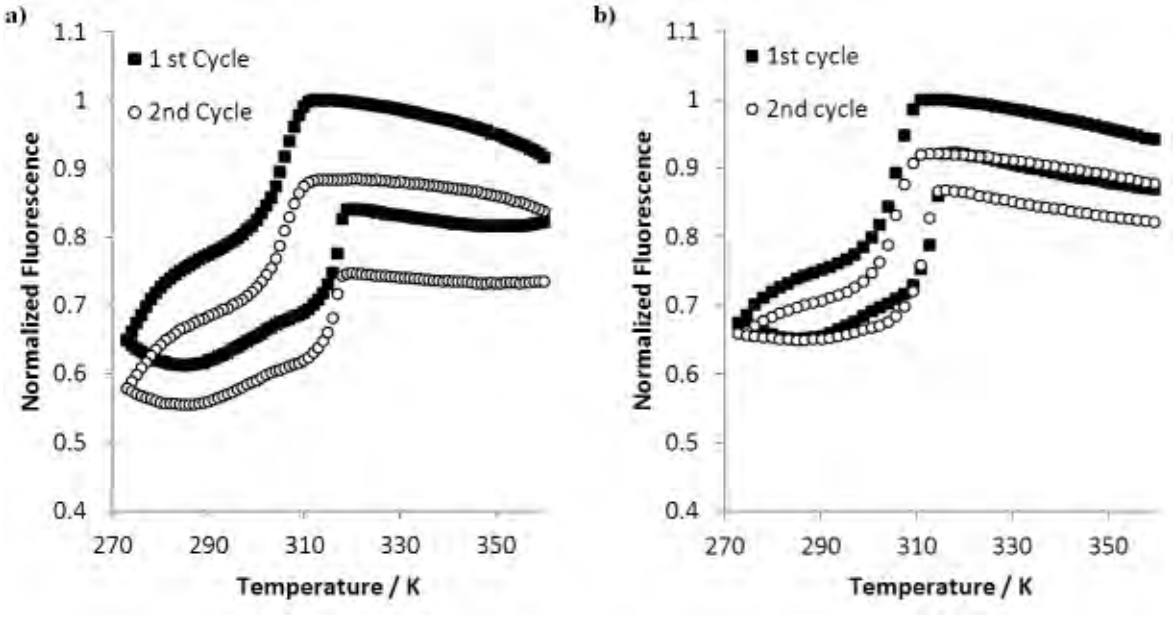

Figure 2.32: **a)** Thermal variation of the luminescence at 550 nm (under a N_2 atmosphere) for the nanoparticle powder of Alizarin Red doped $[Fe(hptrz)_3](OTs)_2$ synthesized in water in presence of PEG. **b)** Same sample, same conditions, but only 60 % of the excitation light intensity in comparison with **a)**.

2.3.2.3.3.3 Calcein:

The luminescent detection of the SCO in this type of nanoparticles did not work well under our experimental conditions, an example of one of the experiences is shown in Figure 2.33. All attempts to obtain a stable curve failed. However, it is possible to depict a modulation of the luminescence as a function of temperature that may correspond, to a certain degree, to the SCO phenomenon observed for the undoped sample in reflectivity measurements. Although the luminescent response was not as expected, it is important to note that this particular luminophore showed an important affinity for attaching to the particles. During the washing steps, the solvent was weakly colored unlike the case of the other three luminophores.

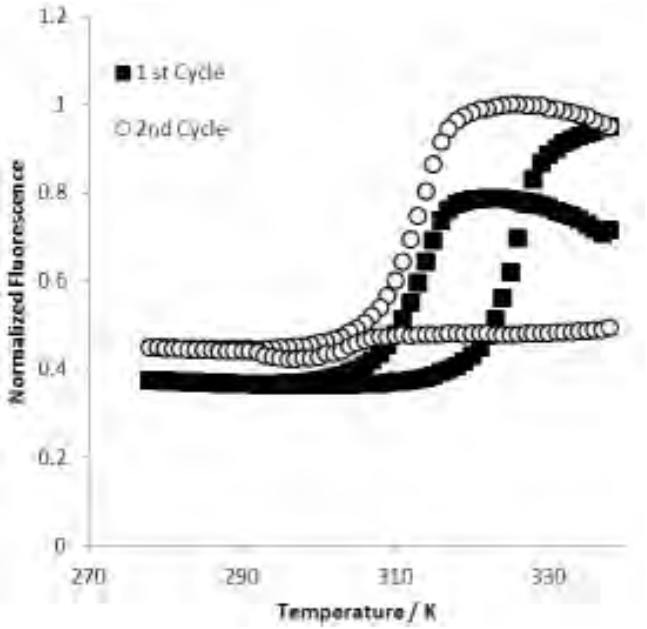

Figure 2.33: Thermal variation of the luminescence at 550 nm (under a N_2 atmosphere) for the calcein doped nanoparticle powder of $[Fe(hptrz)_3](OTs)_2$ synthesized in water in presence of PEG. Cycle temperature rate: 2K/min.

2.3.2.3.3.4 Acridine Orange:

The acridine orange dye was selected, besides its strong emission in the green spectral range, due to its N donor atom. This molecule could eventually integrate the coordination sphere of the metallic centers during the formation of the $[Fe(hptrz)_3](OTs)_2$ complex serving as a ligand substitute. The thermal variation of the luminescence of the dehydrated (30 minutes at 363 K under N_2 flow) acridine orange doped nanoparticles is shown in Figure 2.34. This sample displays an important modulation of the luminescence upon the SCO (*ca* 400% increase from LS to HS). It presents a $T_{1/2} \uparrow \approx 310$ K and $T_{1/2} \downarrow \approx 302$ K that closely matches its undoped analog. Additionally, this luminophore exhibits a rather low thermal dependence of it luminescence for the studied temperature interval. However, a similar detrimental behavior to that obtained with the alizarin red doped sample has been observed; in the pure HS state (T > 330 K), the last part of the heating branch matches the first part of its successive cooling branch but not its predecessor.

In order to explore this behavior, a series of successive cycles of different lengths was launched employing the same experimental conditions: a) 353 K - 323 K - 353 K, b) 353 K - 313K - 353 K, c) 353 K - 303 K 353 K, d) 353 K - 298 K - 353 K, e) 353 K - 293 K - 353 K and f) 353 K - 283 K - 353 K (Figure 2.35). From this experiment, it is possible to observe a highly reproducible response of the nanoparticle powder from cycles 1 to 3. Once again, a small thermal dependence of the luminescence (negative slope) was observed at high temperatures (T>323) and a negligible photobleaching effect during this time interval in spite of the constant excitation. However, in cycle 4 where the sample is cooled to 298 K, when it returns to HS state a small mismatch can be depicted; this deleterious effect is seen to increase during the remaining cycles as the

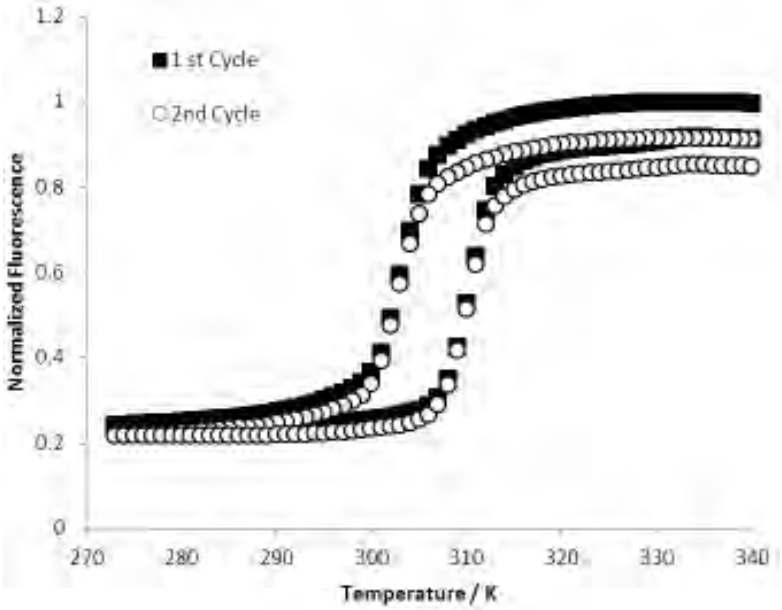

Figure 2.34: Thermal variation of the luminescence at 550 nm (under a N_2 atmosphere) for the acridine orange doped nanoparticle powder of $[Fe(hptrz)_3](OTs)_2$ synthesized in water medium in presence of PEG. Cycle temperature rate: 2K/min.

sample is cooled down to lower temperatures. Clearly the decrease of the luminescent signal upon the SCO is not a product of the photobleaching of the acridine orange. This problem is similar to that found with alizarin red doping, but less serious. Again, the possible existence of water traces may condense in the sample at low temperatures and could contribute to a nocuous environment for the complex/luminophore.

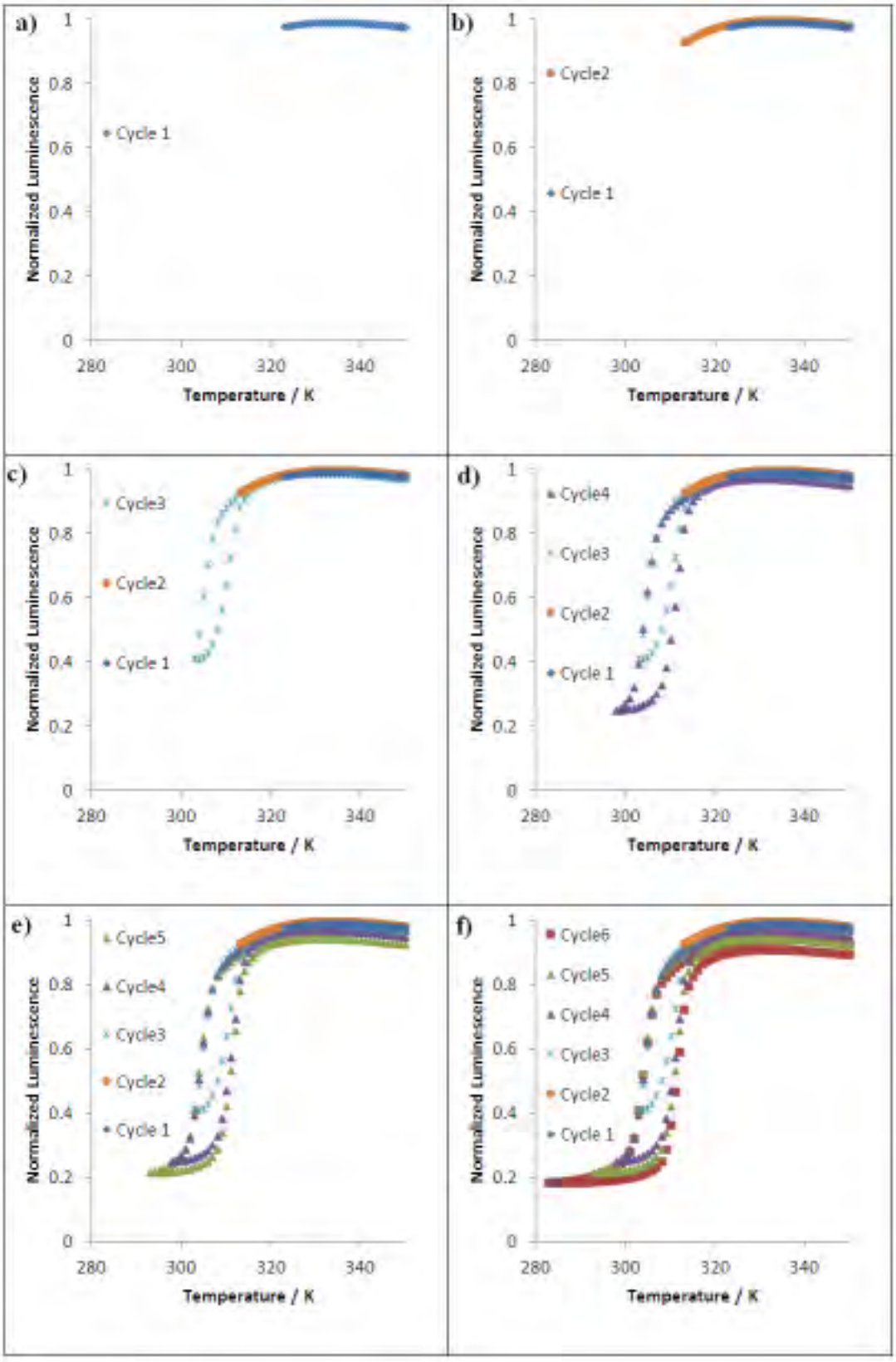

Figure 2.35: Thermal variation of the luminescence at 550 nm for the nanoparticle powder of $[Fe(hptrz)_3](OTs)_2$ synthesized doped with acridine orange under a N_2 atmosphere. Succesive cyles: **a)** 353 K - 323 K - 353 K, **b)** 353 K - 313K - 353, **c)** 353 K - 303 K 353 K, **d)** 353 K - 298 K - 353 K, **e)** 353 K - 293 K - 353 K, **f)** 353 K - 283 K - 353 K.

2.4 Conclusions

We have successfully developed luminescent Fe(II) triazole based SCO nanomaterials doped with different organic luminophores employing two synthetic approaches: the reverse micelle technique and synthesis in a homogeneous medium. Both approaches constitute simple, but powerful and complimentary techniques to obtain luminescent doped SCO nanomaterials of different composition and forms (colloidal suspensions, powders). Their morphology and size have been characterized by different methods (SEM, TEM and DLS) that revealed a variety of shapes and sizes that range from a few ($\approx$ 4 nm nanoparticles) to a few hundreds of nanometers ($\approx$ 500 nm microcrystals) depending on the synthetic procedure. The SCO properties of these nanomaterials were studied using fluorescence microscopy and spectroscopy; they have been compared to the measurements of their undoped versions *via* optical reflectivity microscopy and UV-visible absorption spectroscopy. *The luminescent doped SCO systems described in this chapter are the first of their kind reported in the literature to display an effective modulation of their luminescence upon the SCO.* Furthermore, in many cases their fluorescence measurements as a function of temperature very closely match those performed in reflectivity mode for the undoped versions, *i.e.* the luminescent agents do not affect the SCO properties. We have shown the remarkable versatility of the luminescent doping strategy: we have been able to perform the doping while changing the complex from one triazole to another (with different characteristics of their SCO) and to obtain their SCO properties at different sizes and in different forms. Hence, these promising results indicate that an organic luminophore can be effectively employed as a probe to perform a semi-invasive detection of the SCO with little impact on the original properties of the material.

Reaching an efficient FRET between the luminophore and the SCO material represents our greatest chance of performing luminescent detection of the SCO - even down to the limit of a single molecule. To accomplish this, it is crucial to have the luminophore very close to the SCO metallic centers. Even though the real location the luminophore molecules is difficult to assess after the doping process, different strategies can be employed in order to increase the probability of integrating successfully the luminescent agent into the SCO material. In this chapter we focused on employing luminophores that either play the role of a guest (rhodamine 110), a counter anion substitute (alizarine red S, calcein) or a coordinating ligand substitute (acridine orange) of different Fe(II) triazole based nanomaterials. In particular, it has been shown that the *rhodamine 110* and *acridine orange* molecules are fairly stable under our experimental conditions when employed as luminescent doping agents. Their robust behavior allowed us to monitor the thermal SCO of our materials in a reasonably reproducible manner. Depending on the synthetic conditions, these luminophores allowed us to obtain systems with a modulation of up to 400% of the luminescence upon the SCO in a LS$\rightarrow$HS transition. This concomitant modulation is apparently *not due to a radiative energy transfer* between the doping agent and the SCO material.

However, there are some additional challenges yet to overcome while employing luminescent detection of the SCO. These luminescent systems may present stability

problems due to photobleaching and other (as yet not fully understood) phenomena. A thorough control of the experimental conditions is needed to avoid a detrimental environment for the materials, particularly the luminophores, during observation. Also, the quantity and position of the luminophore molecules in the SCO material after the doping process remains unknown under the synthetic approaches employed in this work.

These different luminescent SCO solution and suspensions open also the way for the elaboration of thin films and organized nano-objects displaying both properties in synergy. This very important issue will be addressed in the next chapter.

Chapter 3

Organization of SCO nano-materials and luminescent detection of the SCO at the nanoscale

3.1 Introduction

Up to now, the SCO nano-materials have been studied by various methods such as magnetometry or optical absorption measurements. However, these methods probe a significant ensemble of objects with different size, shape, composition, etc. In order to avoid these averaging effects, it is crucial to develop precise characterization methods for single particles down to the nanoscale where conventional methods are no longer effective. The aim is to correlate accurately the SCO properties with the morphology of the objects. So far, contributions towards single SCO element measurements remain scarce [57, 79, 108]. Molnár *et al.*[108] used Raman microspectroscopy to investigate nano-patterned thin films, while Arnaud *et al.*[79] employed a differential interference microscopy set up for studying single microparticles and to correlate their thermal SCO response with their size. Alternatively to optical detection methods, Prins *et al.*[57] have tried electrical transport measurements on SCO particles placed between nano-spaced Au electrodes, but the results remain very exploratory. Despite these promising efforts for developing sensitive detection methods, one challenge yet to overcome in order to establish systematic characterization of nano-objects is the stochastic nature of the assemblage of these nano- materials into their substrates without losing their properties.

Centered in this problematic, this chapter will deal with two aspects. First, the organization/structuring of luminescent SCO nanomaterials into spin coated thin films and methods for isolating SCO nano-objects will be discussed. Second, the luminescent detection of the SCO phenomenon while probing low quantities of material down to an isolated sub-micronic object will be explored. The technical and technological aspects

implied in these two tasks will be also discussed from the sample preparation, through the data acquisition and data treatment.

3.2 Organization of SCO materials: State of the Art

3.2.1 Thin Films of SCO complexes

The pioneering approaches employed the Langmuir-Blodgett technique [109–113] or a simple mixing of the complexes with polymers or other materials, which can be spin- or dip-coated on surfaces [114–117]. In a more sophisticated approach a layer-by-layer assembly technique was used as well to deposit alternating layers of SCO cations and polyanions [118]. In any case, the inconvenience is that the resulting films were not purely composed of the spin-crossover complex, but consisted of a mixture of the complex and a polymer or a surfactant, which can alter strongly the spin crossover as well as dielectric and optical properties of the films. Also, the deposit of SCO thin films *via* thermal evaporation methods has been explored in our team [119]; however, this technique has the inconvenience that very few SCO complexes are evaporable. Other, certainly more exotic, approaches led to the synthesis of thin films in the form of liquid-crystals (Figure 3.1) [120], lipophilic, supramolecular Fe(II) complexes [101] and also as "metallo-grids" [121].

Figure 3.1: Thermochromic effect in a liquid-crystal SCO film [120].

It was recently demonstrated in our team that the 3D coordination polymers represent also an attractive platform for growth of surface thin films with spin crossover properties. In fact, the 3D network structure allows assembling, via stepwise adsorption reactions, multilayer films based entirely on intra- and interlayer coordination bonds. Thin films of the 3D SCO compounds (Fe(pyrazine)[M(CN)$_4$])(M = Ni, Pd or Pt) were grown by Cobo *et al.* [122] via a sequential assembly method using coordination reactions as shown in Figure 3.2. This assembly method, relying on the alternate adsorption of metal ions and ligands, has been proved to be very powerful and versatile to synthesize thin films of several other compounds of this family of compounds

[123, 124] and allowed the deposition of dense, ultrathin films on various substrates with precise control over molecular arrangement, chemical composition and thickness in the nanometer scale.

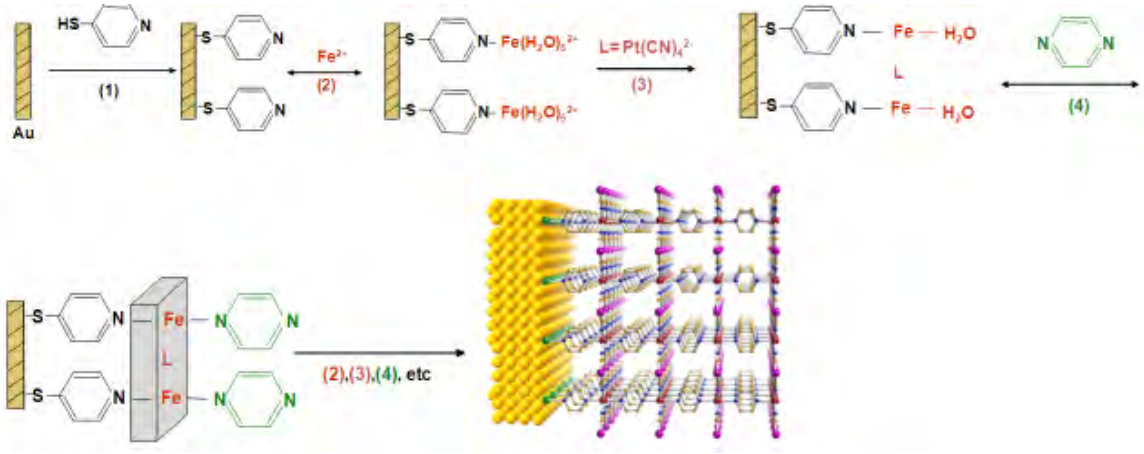

Figure 3.2: Schematic procedure of the sequential assembly of (Fe(pyrazine)[M(CN)$_4$])(M = Ni, Pd or Pt) thin films displaying room temperature spin crossover and host-guest properties [122].

3.2.2 Nano-patterning and nanoscale organization of SCO materials

In the context of an optical or electronic device, the interfacing of the molecular switching units with a micro- or nano-scaled device environment is of crucial importance. Only recently, a breakthrough in this direction has been achieved as a result of the combination of sequential assembly and electron beam lithography techniques [108, 123, 125]. As a matter of fact, the multilayer sequential assembly (MSA) process (also called directed assembly or layer-by-layer assembly in the literature [126]) has got increasingly popular not only for fabricating thin films, but many efforts have been devoted also to generate distinct patterns of the multilayer films. Various lithographic and non-lithographic methods - such as deposition on chemically patterned surfaces, inkjet printing, lift-off, etching, direct photo-patterning and micro-contact printing - have been explored with this aim [127].

Each method has, of course, different merits, but the lift-off process remains an industry standard due to its simplicity and reliability. Furthermore, when combined with electron-beam lithography, it allows obtaining patterns in a wide size range down to the sub-10 nm limit and the alignment of the patterns is also possible with respect to structures, which may already exist on the substrate. For example, as it was shown by Molnar *et al.* [108] that micro- and nanometric patterns of the (Fe(pyrazine)[M(CN)$_4$]) SCO compound can be elaborated using an electron-beam lithographic mask (PMMA) as a physical barrier. These patterns exhibit sharp borders and uniform shape for feature sizes down to 30 nm and with periods down to 200 nm (Figure 3.3). The room temperature spin crossover phenomenon was evidenced using Raman microspectroscopy in an array of dots of 200 nm size.

This powerful type of nanopatterning method is certainly very interesting for the integration of SCO materials in various devices. On the other hand, it is highly expensive and low speed due to the e-beam lithography process. Thus, one of the main challenges involves the replacement of this step to introduce active SCO material into the nanostructures using manufacturing processes which are cost-effective, but without altering their functionality.

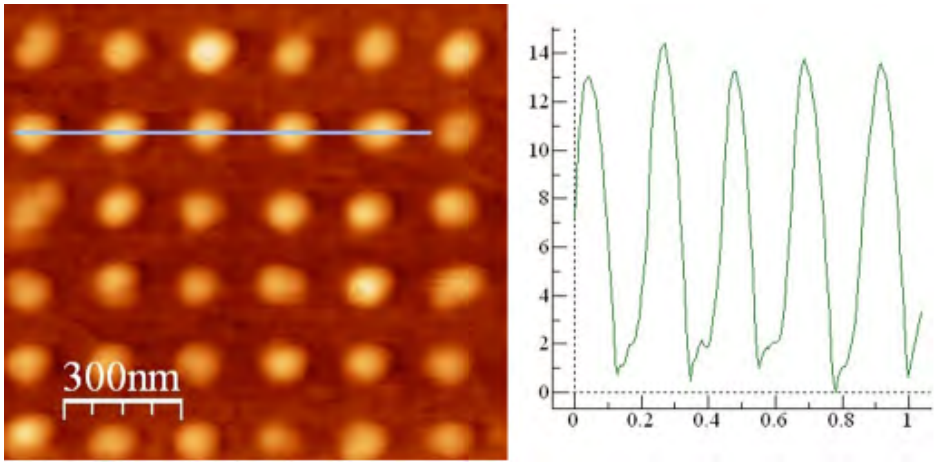

Figure 3.3: AFM topography of an array (period = 250 nm) of 80 nm diameter dots of (Fe(pyrazine)[Pt(CN)$_4$]) following 15 deposition cycles [108].

By the same token, another critical issue will be the development of assembly processes that guide the placement of SCO nanoparticles onto substrates in predetermined arrangements. Indeed, various methods using other type of nano-objects (mainly metallic and semiconductor) have been developed in the literature. Particles were deposited on substrates by capillary assembly or by the layer-by-layer assembly (LbL) approach [128]. The LbL adsorption technique can be utilized in conjunction with the concept of selective deposition on chemically patterned surfaces as well [127]. In this approach, one surface region supports the build-up of multilayer nanostructures, whereas the alternate surface region is resistant to deposition. Alternatively, other assembly methods, such as inkjet printing, micro-contact printing, and microtransfer molding will also be used. These techniques can combine deposition as well as patterning at the same time. In each case, however, the assembly technique must be adapted to the chemical and physical properties of the materials (viscosity, solubility, stability, method of synthesis, etc.), which represents an important challenge. Since it is known that the SCO properties depend critically on the local molecular environment (e.g. packing, solvent molecules, anions, etc.), the development of methods giving access to nanostructures that preserve the integrity of the material is technologically of utmost importance for the application of SCO compounds. Cavallini *et al.* [129, 130] have successfully demonstrated that microinject molding in capillaries (MIMIC) and lithographically controlled wetting (LCW) could be used to fabricate micronic and nanometric stripes of SCO materials (Figure 3.4). On the other hand, Thibault *et al.* [131] have shown that micro-transfer molding (μTM) and micro-contact printing (μCP) techniques can be used to fabricate homogeneous micro- and nano-patterns of spin crossover nanoparticles over large area (Figure 3.5). They demonstrated also

for the first time the possibility of using an aprotic solvent to pattern nanoparticles by soft-lithography from the micrometer to the nanometer scale. It was shown that the nanoparticles keep their spin crossover properties (with a transition around room T) after the soft lithography step. We believe therefore that these low-cost patterning techniques provide interesting perspectives for the integration of spin crossover materials in micro- and nanoscaled devices.

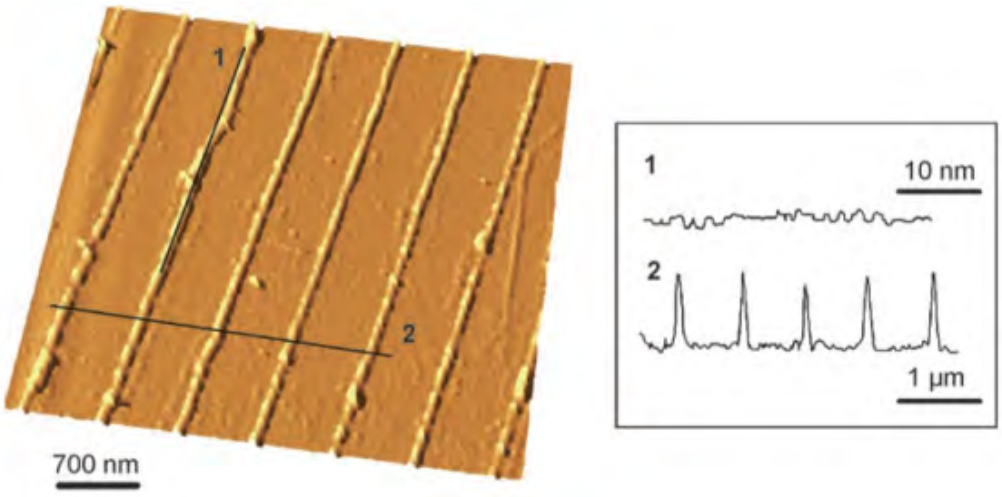

Figure 3.4: AFM topography of micro-stripes of the $(Fe(phen)_2(NCS)_2)$ complex fabricated by MIMIC on a silicon surface [129].

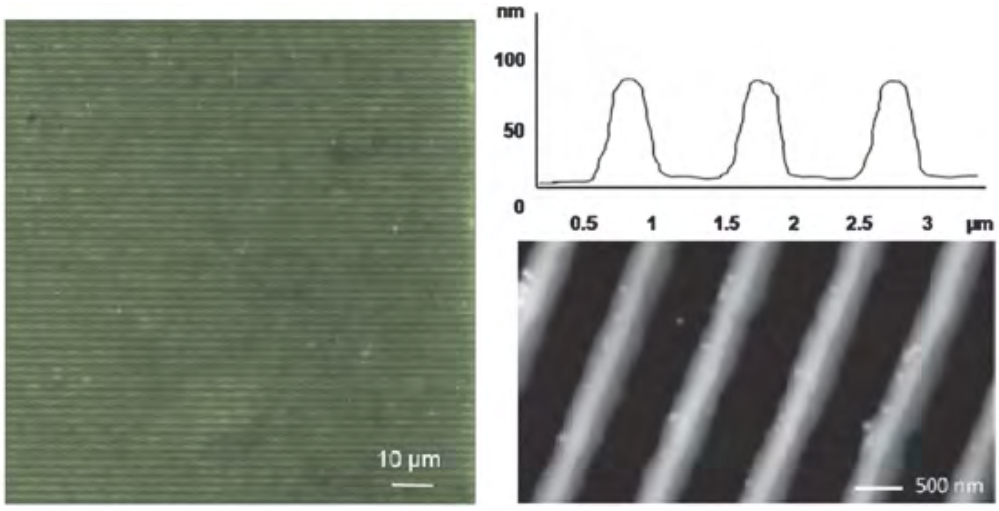

Figure 3.5: AFM topographic images of line gratings with spin crossover nanoparticles fabricated by μTM [131].

3.3 Thin films of fluorescent SCO nanomaterials

As an intermediate step for the characterization of our SCO systems at the nanoscale in luminescence mode, we spin coated a few selected luminescent SCO nanomaterials in order to create thin films over Si and quartz substrates. Producing this type of samples is easier and the technical challenges involving their characterization were less demanding than the detection of a single SCO object.

The thin films of the colloidal tergitol suspension of $[Fe(NH_2trz)_3](OTs)_2$ (strategy #2, chapter II) were studied in luminescence mode as a function of temperature between 288 and 323 K, but no modulation of the luminescence was observed. However, one particular thing observed during these experiments was that the sample tended to deteriorate after light exposition. Figure 3.6a shows an optical dark field image of a section of a thin film captured with a x50 objective. In the image one can see a homogeneous distribution of agglomerates of objects that scatter light. Howerver, after 30 minutes exposition to blue light at room temperature, what can be described as a "hole" in the film was observed in dark field mode again (Figure 3.6b). Additionally, it was observed that this type of sample turned to a yellowish color after a few days. This general detrimental behavior of the system discouraged further works with it. On the other hand, homogeneous thin films of $[Fe(\textit{hptrz})_3](OTs)_2$ nanoparticles synthesized in strategy #3 (chapter II) were not possible to make by spin coating methods; the procedure led to dispersed nanoparticles on the surface; this feature was exploited later for single object observations.

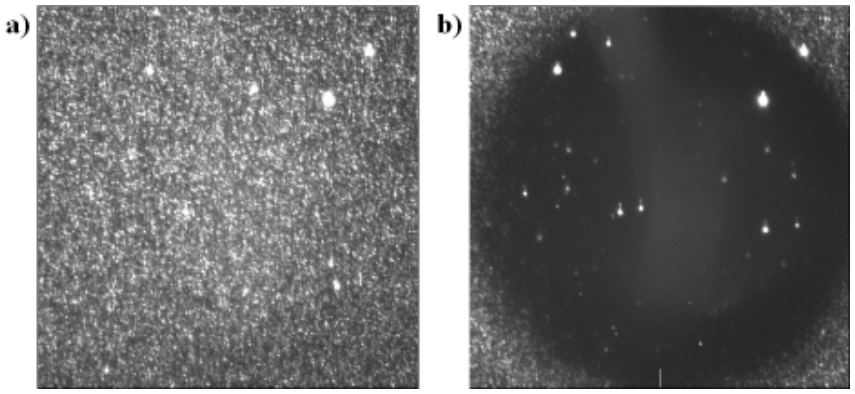

Figure 3.6: Optical dark field images of a $[Fe(NH_2trz)_3](OTs)_2$ spin coated thin film before **a)** and after **b)** a 30 minute exposition to blue light at room temperature.

3.3.1 $[Fe(NH_2trz)_3](OTs)_2$ reverse micelle system ($(H_2O$, EtOH)/ NaAOT / n-octane) doped with Rhodamine 110

We spin coated a few μl of the doped $[Fe(NH_2trz)_3](OTs)_2$ nanoparticle suspension obtained in reverse micelles from strategy #1 (Chapter II) over ≈ 1.5 cm^2 pieces of Si substrate. It was possible to obtain homogeneous films over such large surfaces. When these type of samples were prepared, a piece of Scotch tape was placed in the

upper part of the sample before the spin coating and then it was removed in order to have a height contrast between the film and the Si substrate for subsequent AFM measurements (Figure 3.7).

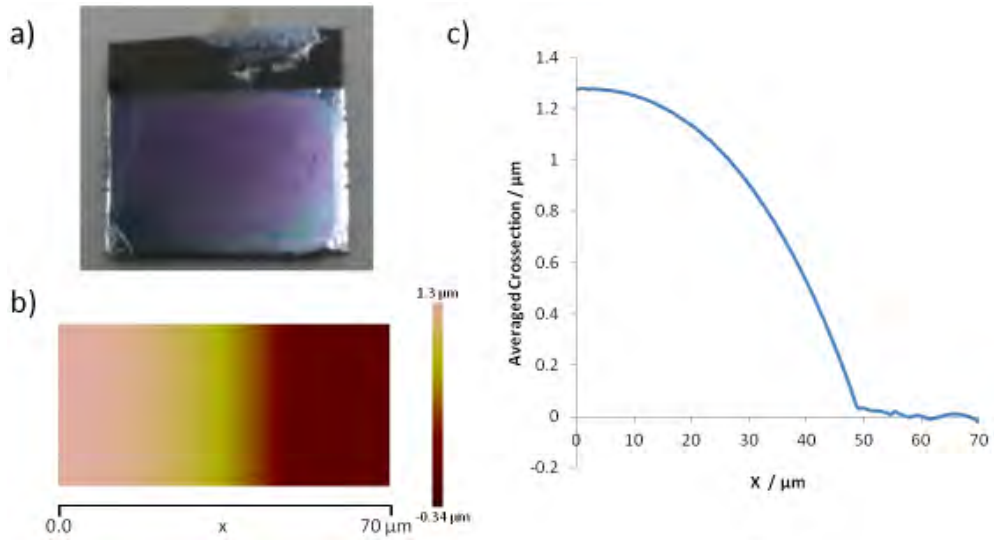

Figure 3.7: **a)** Spin coated thin films of $[Fe(NH_2trz)_3](OTs)_2$ on a ≈ 1.5 cm^2 Si substrate. Spin coater parameters: speed = 2000 rpm, acceleration = 5000 rpm^2, time 15 s. **b)** 32 x 70 μm^2 AFM image and **c)** respective averaged cross section of the film in **a**.

The luminescent response of this type of films was studied as a function of temperature under an open and a controlled N_2 atmosphere (Figure 3.8). As it can be seen in Figure 3.8a, for the sample studied under an open atmosphere there is not an evident modulation of the luminescence between 293 and 323 K. This is the temperature range where the SCO phenomenon is expected to occur for this particular system measured in solution. Nonetheless, an increase of the luminescence was observed at low temperatures (T<298 K) instead of the expected decrease. The origin of this phenomenon is not well understood. It might be associated to a temperature dependence of the rhodamine 110 luminescence. However, this behavior was never observed while performing luminescence measurements in solution. One hypothesis is that the micelles are unstable and break due to the low quantity of solvent (n-octane) in the film. This could lead deterioration of the SCO complex and at the same time a change of the environment of the luminophore. A similar experiment was also performed under a controlled N_2 atmosphere 3.8b. In this case, the increase of luminescence at low temperatures was not observed; however, a slight increase between 288 and 303 K was depicted. It is difficult to assess whether the modulation is associated to the SCO.

From these experiments it can be concluded that if the integrity of the system was conserved after the deposition process, clearly the films do not have the optical density necessary for modulating the luminescence. Since the molar ratio between surfactant and Fe is typically $\approx 9:1$, the resulting thin films are too diluted in SCO material in order to modulate the luminescence. This would confirm our first observations of the system measured in solution in terms of a radiative interaction between the luminophore and the SCO material.

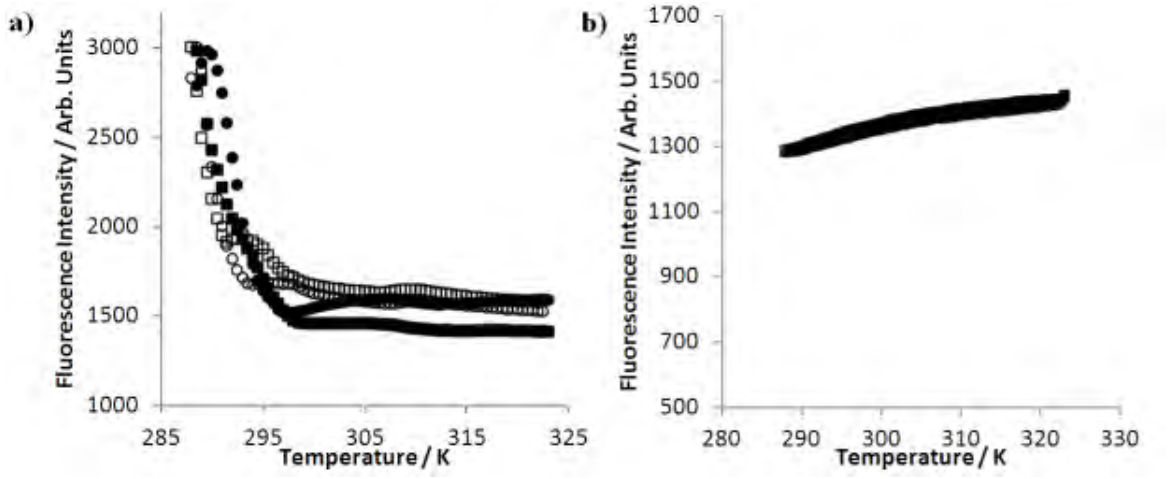

Figure 3.8: **a)** Normalized thermal variation of the luminescence intensity at 550 nm with an excitation at 450 nm of two thin films obtained with the same spin coating parameters employed in Figure 3.7. a) Measurement performed in an open atmosphere. b) Measurement performed under a controlled N_2 atmosphere after a 30 minute purge at 353 K (dT/dt = 0.5 K/min). (Squares and circles, open and closed symbols for first and second cycle, cooling and heating branches, respectively.)

3.3.2 Chloroform solution of [Fe(*hptrz*)$_3$](OTs)$_2$

The preparation of thin films by spin- or dip- coating diverse SCO complexes has been explored as well as the luminescent detection of their SCO properties. As we have seen in the previous systems, deposition of surfactant or polymer stabilized SCO nanoparticles seemed to be a promising approach for these purposes; however, it results in the preparation of films consisting of strongly diluted SCO materials, which consequently diminishes the chances of having a successful modulation of the luminescence upon the SCO. Additionally, in certain configurations we have observed the degradation of the complex under the influence of the surfactant when the mixture was heated or excessively exposed to light. To overcome these problems, we developed a synthesis that allowed us to prepare a *homogeneous* chloroform solution of Fe(OTs)$_2$ with *hptrz*. This solution is thought to contain the [Fe(*hptrz*)$_3$](OTs)$_2$ complex with a low polymerization degree, but when the solvent is evaporated longer chains might be formed. The important point to notice is that unlike other approaches, this method leads to a solid which is composed primarily of the SCO compound without the presence of surfactants or any other additives and can be easily spin coated to form homogeneous thin films. (Synthesis performed by Il'ya A. Gural'skiy.)

3.3.2.1 Synthesis

As in strategy #3 in chapter 2, the ligand 4-heptyl-1,2,4-triazole (*hptrz*) was obtained from N-formylhydrazine, triethyl orthoformate and n-heptylamine following the Bayer synthesis [106]. Fe(II) tosylate was synthesized by reaction of metallic iron with tosylic acid [107]. The mother solution of the complex was prepared by mixing two solutions; the first containing iron(II) tosylate hexahydrate (30 mg, 0.06 mmol, 1 equiv.) and p-toluenesulphonic acid monohydrate (4 mg, 0.02 mmol) in ethanol (150 μl) and the

second containing 4-heptyl-1,2,4-triazole (60 mg, 0.36 mmol, 2 equiv.) in $CHCl_3$ (4 ml). For spin coating 50 μl of the mother solution of the complex was mixed with 0.66 mM chloroform solution of acridine orange (5 μl), or 0.66 mM ethanol solution of rhodamine 110 (0.2% mol of luminophore per iron atom). We worked with these luminophores since we had found they displayed the most robust behavior with our experimental conditions.

3.3.2.2 Characterization of the $[Fe(\textit{hptrz})_3](OTs)_2$ chloroform solution

A few seconds after mixing the reagents, the color of the solution turns to violet indicating a LS complex formation, which passes to a colorless high spin (HS) form when the solution is heated from room temperature to 315 K (Figure 3.9). Light scattering (DLS) measurements as a function of time show the presence of 6.5 $\pm$ 2 nm objects in the fresh solution and their growth into micro-structures during $\approx$ 24 hours (Figure 3.10). A slow and rather minor growth of the oligomers occurs within a few hours after mixing the reagents and the mean size reaches 8.5 nm after $\approx$ 160 minutes. Then, a very sudden spontaneous formation of $\approx$400 nm crystals takes place followed by a gradual rise until $\approx$ 1400 nm. The SCO properties of such precipitates are very similar to those obtained for the bulk material ($T_{1/2} \uparrow \approx$ 315 K, $T_{1/2} \downarrow \approx$ 307 K, *i.e* 8 K hysteresis). The relative stability of this type of homogeneous solution is very fragile and it can be influenced by different factors: (1) the stability is strongly linked to the temperature at which the solution is held. If the synthesis is performed during a particular hot day (room temperature above 300 K), the growth of the micro crystals is accelerated. As a consequence, the precipitation takes a few minutes (instead of two days). The precipitation rate can also be accelerated by (2) diluting a solution with the complex already formed or (3) by preparing a solution which is too concentrated in SCO material. Additionally, (4) when adding a few μl of a luminophore solution, precipitation of the solution at room temperature after a couple of hours was also observed.

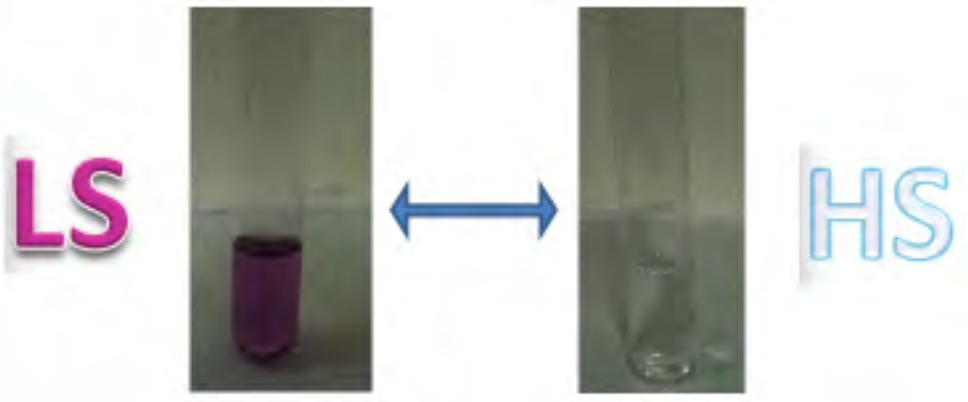

Figure 3.9: $[Fe(\textit{hptrz})_3](OTs)_2$ chloroform solution in the LS and the HS states.

The spin transition behavior of the $[Fe(\textit{hptrz})_3](OTs)_2$ chloroform solution was studied by means of UV-VIS spectroscopy. Figure 3.11a shows the visible-NIR ab-

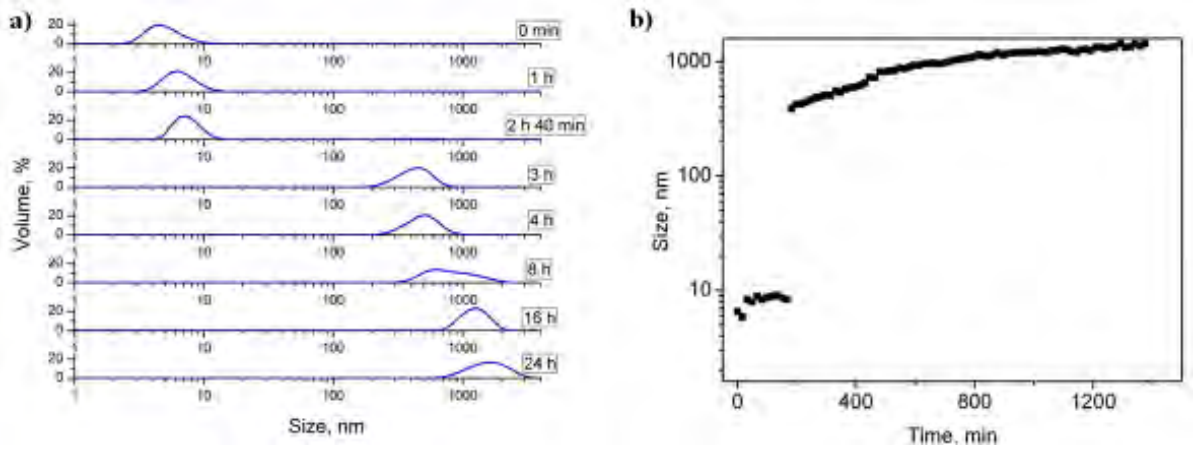

Figure 3.10: **a)** DLS measurements as a function of time for a chloroform solution of the complex [Fe(*hptrz*)$_3$](OTs)$_2$. **b)** Mean size of the particles (extracted from DLS) as a function of time.

sorption spectra of the solution at selected temperatures. The characteristic *d*-*d* absorption bands of the Fe(II)-triazole based complexes corresponding to the $^1A_1 \rightarrow {}^1T_1$ LS state transition at 540 nm and the $^5T_2 \rightarrow {}^5E$ HS state transition at 780 nm can be observed at 280 and 314 K, respectively. The SCO was monitored by following the variation of the absorbance at 540 nm. From Figure 3.11b it is seen that the SCO occurs around room temperature, it is less abrupt (spans over a range of 15 K) than that of the particles synthesized in strategy #3 and it does not present any measurable hysteresis. The transition temperature is lower than that found for its bulk counterpart due to the presence of ethanol in the solution that stabilizes the HS form in the triazole based complexes. Additionally, one shall note the cooling branch does not perfectly match the heating one revealing a small evolution of the solution when heated during the experiment (a closed cuvette was used). The extinction coefficients ϵ_{540} for the LS and HS forms here are within the typical ranges found previously for this Fe(II)-triazole based complexes and indicate a quasi-complete spin transition.

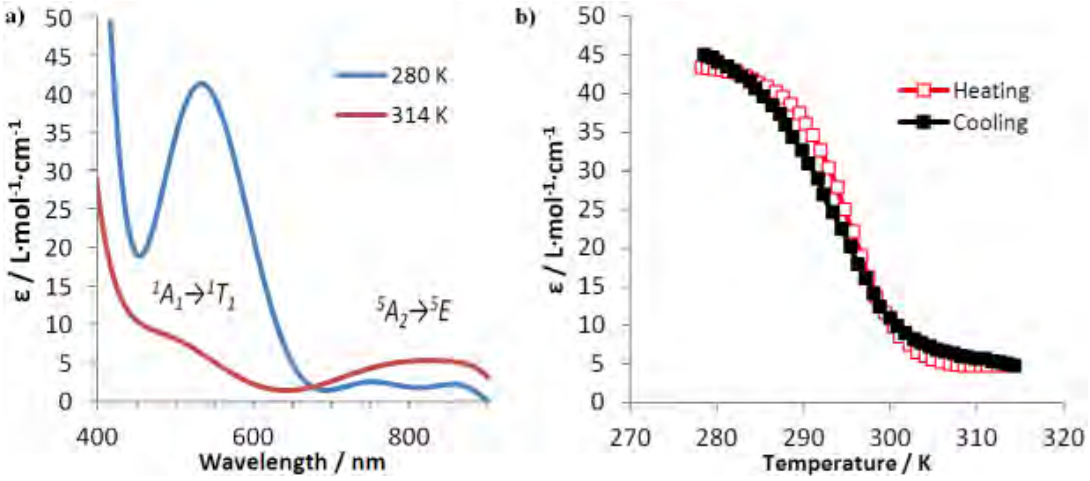

Figure 3.11: **a)** Characteristic absorption bands in the visible and NIR range for a chloroform solution of [Fe(*hptrz*)$_3$](OTs)$_2$. **b)** Thermal variation of the absorbance at 540 nm (dT/dt = 2 K/min).

Figure 3.12 displays the luminescence emission spectra with an excitation wavelength of 450 nm recorded for [Fe(*hptrz*)$_3$](OTs)$_2$ chloroform solutions doped with rhodamine 110 and acridine orange at room temperature (293 K) and at 315 K (HS state). As the $^1A_1 \rightarrow {}^1T_2$ absorption band disappears upon the SCO from the LS to the HS state, an increase of the luminescence close to 540 nm can be observed. The magnitude of the change for both samples ($I_{LS} \approx 0.5 I_{HS}$) is similar to that obtained for the reverse micelle system. However, it is worth noting two things: (1) the concentration of the SCO material in chloroform solution is twice compared to the reverse micelle system, (2) according to Figure 3.11a, the chloroform system at room temperature is approximately 50% HS state. Under these circumstances and with a pure radiative energy transfer scheme between the luminophores and the SCO nanomaterials, by taking half of $\Delta\epsilon_{540nm}$ (≈ 35 M^{-1}·cm^{-1}) on the emission side, half of $\Delta\epsilon_{450nm}$ (≈ 7 M^{-1}·cm^{-1}) on the excitation side and a molar concentration of SCO material ≈ 15 mM, the luminescence at 293 K should be around 72% ($e^{-\epsilon \cdot l \cdot c} = e^{-0.5 \cdot (35+7) \cdot 1 \cdot 0.015}$) that of the pure HS state. This might be an indication that in this type of luminescent SCO system the energy transfer is not purely radiative.

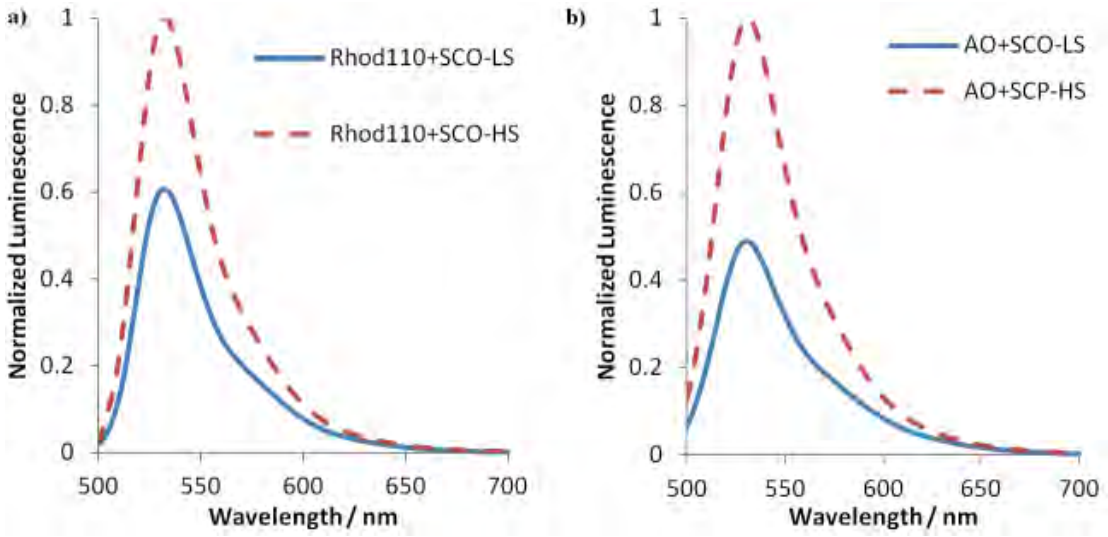

Figure 3.12: Normalized thermal variation of the luminescence emission spectra at 293 (LS) and 315 K (HS) for a chloroform solution of [Fe(*hptrz*)$_3$](OTs)$_2$ doped with **a)** rhodamine 110 and **b)** acridine orange.

3.3.2.3 Thin Films Characterization

As a first step for characterizing the luminescent response of this system at the nanoscale, a few μl of the solution was spin coated over clean pieces of a Si wafer as well as on quartz substrates as shown in Figure 3.13. Thin and homogeneous films were obtained even on large (3 x 3 cm^2) substrate surfaces. The chemical composition of undoped versions of the films was verified by means of Raman and infrared spectroscopies (Figure 3.14). Besides the additional features in the IR absorption spectroscopy at 3500 cm^{-1} and 1650 cm^{-1} associated to water traces present in the KBr substrate, the characteristic spectra obtained in both techniques for the thin films and

bulk samples are virtually indistinguishable; these observations may indicate that the integrity of the SCO material is conserved after the deposition process.

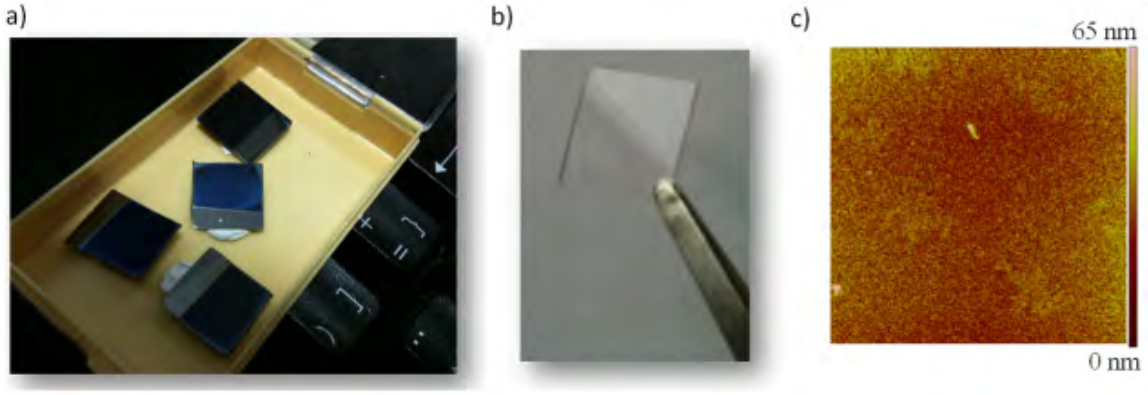

Figure 3.13: Optical (**a**, **b**) and AFM **c)** images of $[Fe(hptrz)_3](OTs)_2$ (chloroform solution) thin films spin coated on **a)** Si and **b)** quartz substrates.

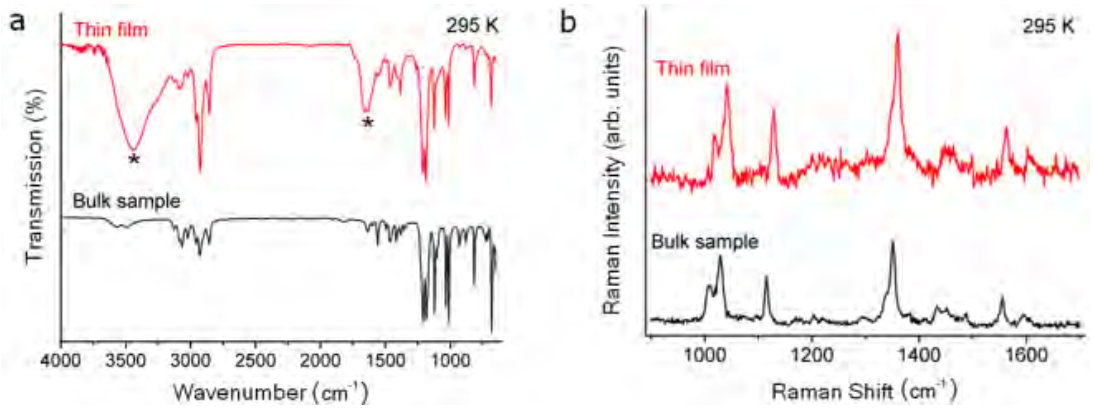

Figure 3.14: **a)** Infrared spectrum of the $[Fe(hptrz)_3](OTs)_2$ complex for a thin film (transmission mode, KBr substrate) and bulk sample (ATR mode). *Water traces found in the KBr substrate. **b)** Raman spectra (632.8 nm excitation) of the $[Fe(hptrz)_3](OTs)_2$ complex for a thin film and bulk sample.

These samples were observed with an AFM and the same average thickness was measured for different samples with the same conditions of deposition. These measurements revealed also a high quality in terms of roughness and homogeneity (Figure 3.13c). At this point we would like to emphasize the absence of additives during the deposition process; there are also no constraints concerning the nature of the substrate employed or the functionalization of its surface. Furthermore, by changing the parameters of the coater or the concentration of the reagents in the starting solution, different film thicknesses can be easily obtained over large surfaces and without any strong variation in the composition of the film. AFM images of films with thicknesses ranging from a few tens of nm to a few hundred of nm are shown in Figure 3.15.

The thermal response of $\approx$ 85 nm thick thin layers doped with rhodamine 110 and acridine orange was monitored via fluorescence microscopy at 550 nm with an excitation of 450 nm. The samples were cycled several times at a rate of 2 K/min between 253 and 353 K. As observed in Figure 3.16, between 293 and 323 K the

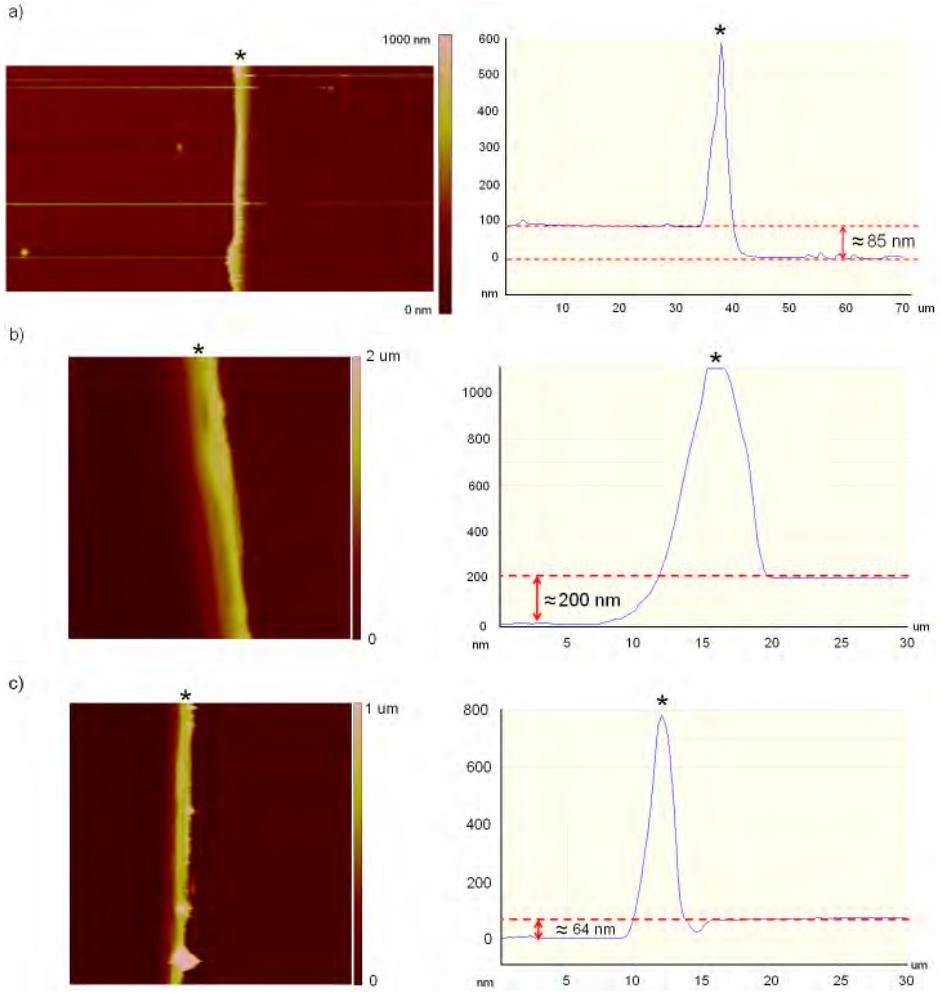

Figure 3.15: AFM images and respective averaged cross sections of spin coated thin films of $[Fe(hptrz)_3](OTs)_2$: **a)** 70 x 37 μm^2 section, spin coater parameters: speed = 5000 rpm, acceleration = 4000 rpm^2, time 30s; **b)** 30 x 30 μm^2 section, spin coater parameters: speed = 500 rpm, acceleration = 1000 rpm^2, time 30s; **c)** 30 x 30 μm^2 section, employing the initial solution diluted twice, spin coater parameters: speed = 5000 rpm, acceleration = 4000 rpm^2, time 30s. *Defect created by the scratch made on the thin films before the AFM measurements.

luminescence intensity of the films doped with either luminophore changes in an abrupt manner while heating or cooling and also a small hysteresis can be depicted within the same temperature range. These transition curves are in reasonable agreement with the reflectance measurements of the same undoped compound in bulk powder form (also with the luminescent measurements performed on doped versions) both obtained under a controlled N_2 atmosphere (see figures 2.28, 2.31, and 2.34, chapter II). Furthermore, the modulation of the luminescence in both cases is on the same order of magnitude ($I_{LS} \approx 2/3 I_{HS}$). Additionally, in the temperature intervals far from the SCO (T> 320 K and T< 270 K) the luminescence of the films is fairly flat which is an evidence of the low temperature dependence of the luminophores present in the thin films. It is worth to note also that these experiments diplayed cycles that are well reproducible and in spite of the constant excitation no significant photobleaching was observed under our experimental conditions with either dopant.

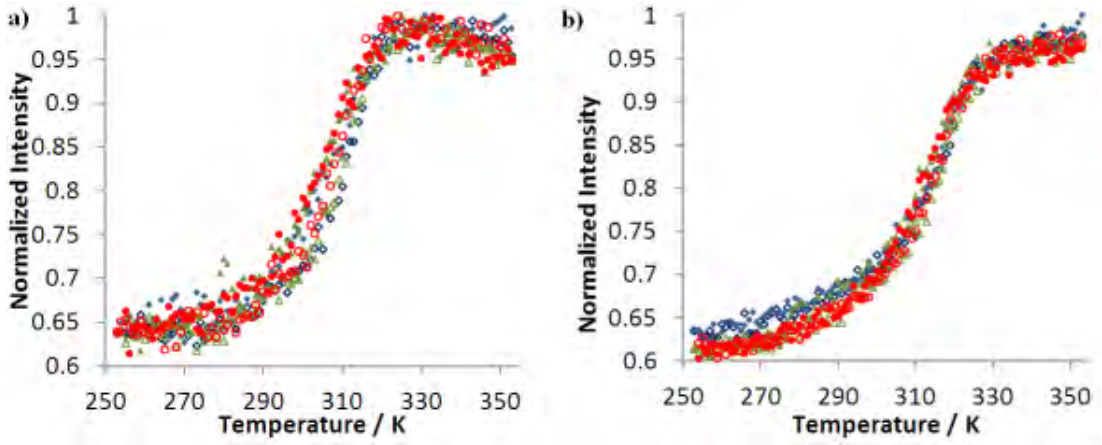

Figure 3.16: Normalized thermal variation of the luminescence intensity at 550 nm with an excitation at 450 nm in a spin coated thin film ($\approx$ 85 nm) of [Fe(*hptrz*)$_3$](OTs)$_2$ chloroform solution doped with **a)** acridine orange and **b)** rhodamine 110 during three consecutive thermal cycles (dT/dt = 2 K/min; open and closed symbols for heating and cooling modes, respectively).

Complementary experiments were performed in order to confirm the origin of the modulation in the luminescent response of these films. In a first test, undoped versions of the same thin films ($\approx$ 85 nm) deposited in quartz substrates were studied in UV-Visible absorption spectroscopy. As we have seen, the change of the spin state of a SCO molecule leads naturally to a complete change of its electronic absorption spectra, which can be used therefore conveniently to follow the spin state changes. In particular, we have been focused on metal-centered *d-d* (or ligand-field) transitions appearing in the visible spectral range. However, these transitions are relatively weak (Laporte forbidden) and their associated molar extinction coefficients ϵ span from 1 to 100 $L \cdot mol^{-1} \cdot cm^{-1}$. Taking into account the Lambert-Beer law (equation 3.1), it is clear that metal-centered absorption bands cannot be observed for very thin films with thickness (d) below *ca.* 1 μm, because their optical density (OD) will be very low, even if the concentration (c) of the metallic centers is high (*e.g.* pure, non-diluted compounds).

$$OD = 0.434 \epsilon d c \tag{3.1}$$

To illustrate this point, we studied the visible absorption spectra of an undoped film in the LS and HS states (Figure 3.17). Since there are no additives in the initial solution that may dilute the SCO material deposited in the film, we are technically measuring the absorbance of a pure 85 nm film of [Fe(*hptrz*)$_3$](OTs)$_2$. In spite of this, there is no measurable absorbance of the thin film in either spin state in the considered spectral range.

On the other hand, it is perhaps less widely recognized that charge transfer (CT) bands provide a possibility for detecting absorbance changes even in films with nanometric thickness, because ϵ can reach values as high as 10^4 - 10^5 $L \cdot mol^{-1} \cdot cm^{-1}$. For example, a chromophore with $\epsilon = 10^4$ $L \cdot mol^{-1} \cdot cm^{-1}$ provides a signal in the 10^{-3} OD range for a 1 nm thick (continuous) film, which is readily measurable by

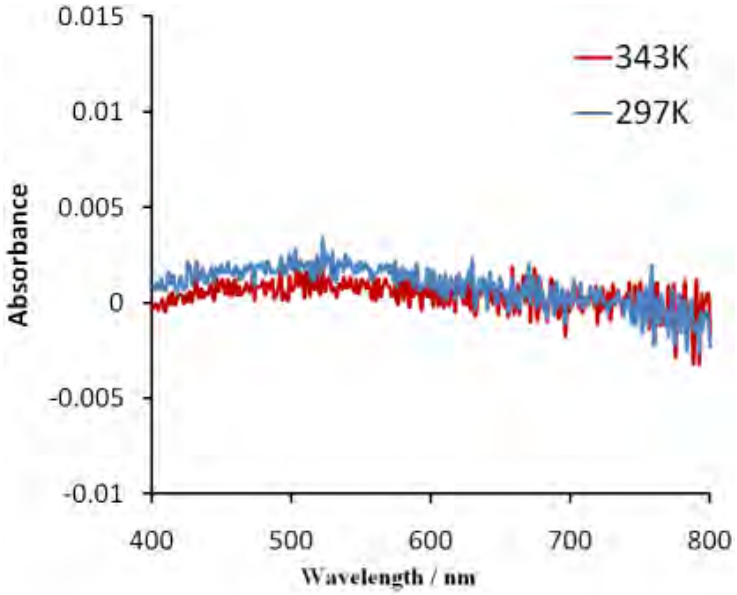

Figure 3.17: Optical density in the visible range of a ≈ 85 nm spin coated thin film on a quartz substrate of undoped [Fe(*hptrz*)$_3$](OTs)$_2$ in the high spin (343 K) and low spin (297 K) states.

conventional spectrophotometers. If CT transitions involve molecular orbitals located primarily on the metal ion, they will be also altered by the spin state of this latter. As a result, we can employ this technique on undoped versions of the thin films as an alternative detection method of the SCO besides luminescence and thus corroborate our first observations.

We have therefore recorded the variable temperature optical absorption spectra of thin films of [Fe(*hptrz*)$_3$](OTs)$_2$ in the ultraviolet (UV) wavelength range (*i.e.* where CT transitions are expected to appear) for different film thicknesses deposited over quartz substrates (Figure 3.18). We employed a Linkam PE120 (Peltier) temperature control system without windows under open atmosphere in order to make possible the measurement in the UV range. (It is not possible to work in transmission mode in the UV range with the internal three glass windows of the Linkam TS-600 cryostat.) In the HS (*i.e.* high temperature) state the films are nearly transparent through the whole UV - vis - NIR spectral domain. On the other hand, in the LS (*i.e.* low temperature) state, they display an absorption band centered at 285 nm, which can be assigned thus to a singlet CT band. As shown in Figure 3.18 a-b, for a 80 nm thick film, the temperature dependence of this absorption band reveals clearly an abrupt spin transition in the film around 338 K with a very small hysteresis loop. The variation of the absorbance at 285 nm as a function of the film thickness is shown in Figure 3.18c. A linear fit on the data yields an extinction coefficient of $1.0(2) \times 10^4$ cm^{-1}.

These experiments were compared to the luminescent response of an analogue doped version of the thin film under the same experimental conditions with fluorescence microscopy (*i.e.* same temperature controller, same temperature ramp and the sample in an open atmosphere. See Figure 3.19). Two major observations can be noted: first, the transition temperature of the thin films in both UV transmission and fluorescence mode is shifted towards higher temperatures (≈ 335 K) compared to the

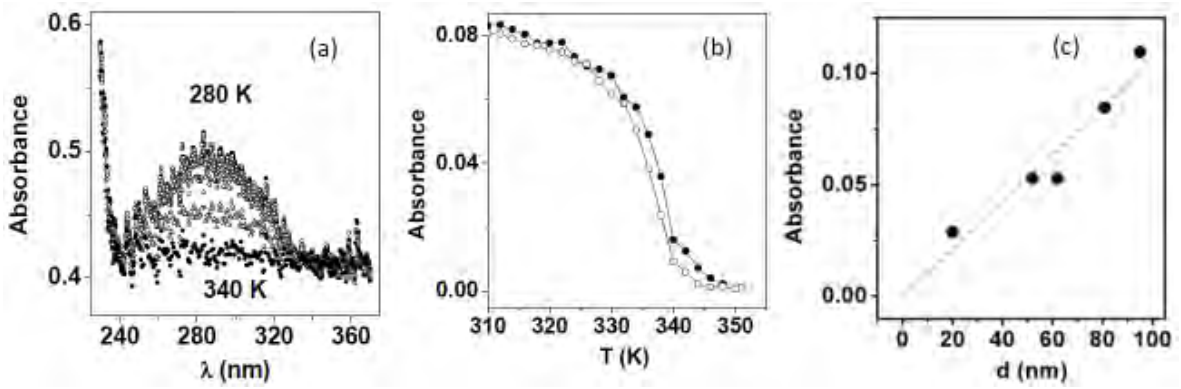

Figure 3.18: **a)** Selected temperature-dependent absorption spectra of a 80 nm thin film of the compound [Fe(*hptrz*)$_3$](OTs)$_2$ in the UV spectral region. **b)** Temperature dependence of the absorbance of the same film at 285 nm (dT/dt = 2 K/min, in air). Open and closed symbols indicate the cooling and heating modes, respectively. **c)** Variation of the absorbance (285 nm, room T) as a function of the film thickness. (The values of d were determined by atomic force microscopy.)

first measurements in fluorescence performed on the dehydrated fluorescent nanoparticle powder and luminescent thin films under a controlled N_2 atmosphere (Figure 3.16). This can be explained by the semi-hydrated state of the films in open atmosphere that shifts the transition to higher temperatures. Furthermore, this behavior seems reproducible after consecutive cycles, which can be understood as the sample hydrates and dehydrates always in the same manner unlike the powder form of the complex (which displays a non reproducible cycle when measured in open atmosphere). Second, the transition curve monitored by the MLCT band of the undoped film (Figure 3.18b) matches closely that of the luminescent one (Figure 3.19a). Clearly this modulation of the luminescence displayed by the thin film is opposite to the ordinary thermal extinction of the luminescence and should be associated with the spin crossover.

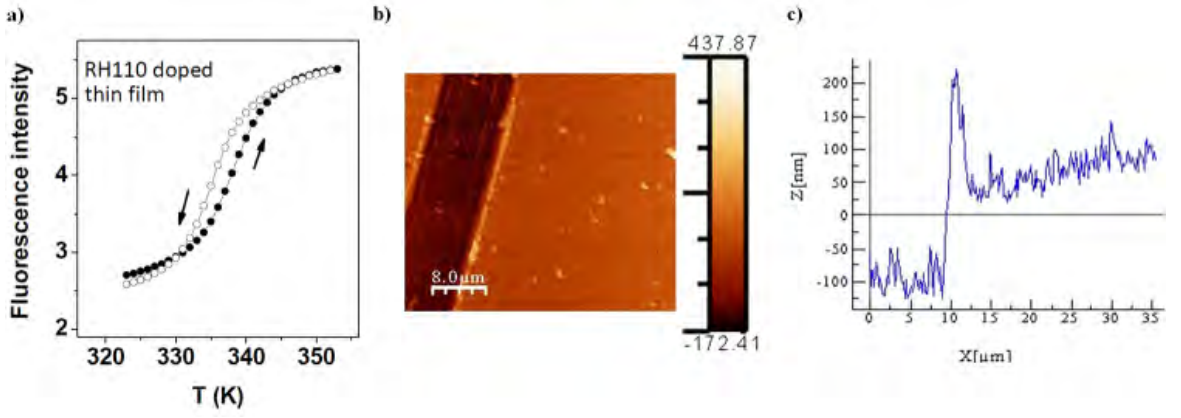

Figure 3.19: **a)** Temperature dependence of the fluorescence intensity (excitation at 450 nm, emission at 550 nm) of a 150 nm thin film of the complex [Fe(*hptrz*)$_3$](OTs)$_2$ doped with rhodamine 110. The experiment was performed in air with a temperature ramp of 2 K/min. **b)** 35 x 30 AFM image of the film in **a)**. **c)** Averaged crossection of the image.

Even if we have no precise structural information concerning the localization of the luminophore molecules in the SCO material, the mechanism responsible for quenching

the luminescence can be attributed essentially to a non-radiative transfer between the acridine orange or rhodamine 110 and the Fe(II) ions present in the complex. This hypothesis corroborates the increase of $\approx 50\%$ of the signal during the transition. Indeed, given the thickness of our film ($\approx$ 150 or 85 nm) and the variation of the molar absorption coefficient (ϵ) of this complex during the SCO at the selected excitation and emission wavelengths of the luminophore ($\Delta\epsilon \approx 7$ L$\cdot mol^{-1} \cdot cm^{-1}$ @450 nm, $\Delta\epsilon \approx 35$ L $\cdot mol^{-1} \cdot cm^{-1}$ @550 nm), the modulation of luminescence cannot be explained by means of radiative energy transfer.

To further investigate this aspect, an additional experiment in which the luminophore and the complex were physically separated was designed. In this way, if the interaction between the luminophore and the complex is basically radiative, the modulation of the luminescence should be still detectable. To this end, we spin-coated a thin film of the undoped [Fe(*hptrz*)$_3$](OTs)$_2$ complex over a glass slide and an acridine orange doped poly(methyl-methacrylate) (PMMA) film on a Si wafer. The deposition conditions and the concentrations of the complex and luminophore were the same as those employed before. Here, the glass substrate was used as a physical barrier between the two films by putting it on top of the PMMA sample (Figure 3.20a). After cycling the ensemble under similar conditions as in the previous experiments, no modulation of the luminescence by the SCO was observed (Figure 3.20b).

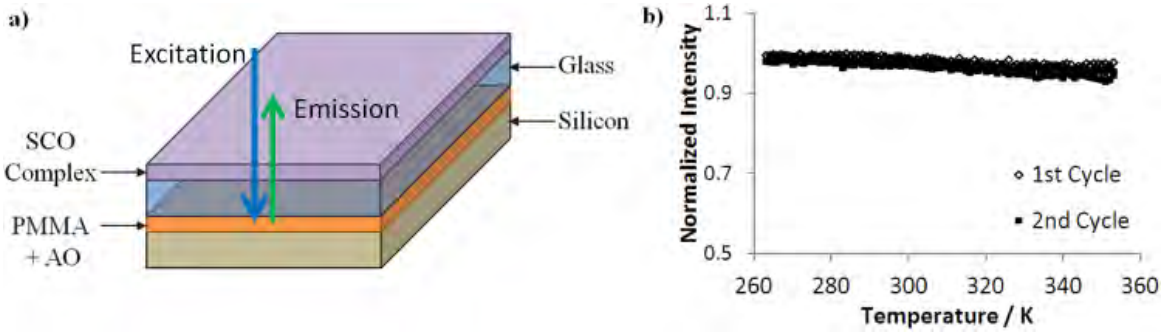

Figure 3.20: **a)** Scheme of a thin film of undoped of [Fe(*hptrz*)$_3$](OTs)$_2$ over a glass slide on top of a thin film of poly(methyl-methacrylate) (PMMA) doped with acridine orange (AO). **b)** Luminescent response of the ensemble during two cycles under a controlled N_2 atmosphere and monitored in 550 nm with an excitation at 450 nm. (Open and closed symbols for first and second cycle, respectively.)

3.3.2.4 Luminescence Lifetime Studies

A collaboration with the Molecular Systems and Interfaces group of Dr Wesley R. Browne and one of his PhD students Lili Hou, from the University of Groningen in the Netherlands has been undertaken in order to investigate the luminescence lifetime of our system.

In order to better understand the quenching mechanism that occurs upon the SCO in the doped version of the [Fe(*hptrz*)$_3$](OTs)$_2$ synthesized in chloroform, we performed a preliminary study of the luminescence lifetime of the system in solution. Assuming a Föster type energy transfer interaction (Section 1.2.3.2) between the luminophore and the SCO material, the latter in its LS form constitutes an additional relaxation

pathway for the excited state of the luminophore. As a result, the luminescence lifetime of the pure luminophore should be more important than that obtained when it is in proximity to the SCO material in the LS state (See equation 1.16, chapter I). On the other hand, if the transfer is radiative, no change of the lifetime is expected.

Up to now, it is not clear to us the actual location of the luminophore after adding it to the homogeneous solution of $[Fe(hptrz)_3](OTs)_2$. Depending on the luminophore employed, it could be coordinated into the polymer chains, inside or on the surface of the forming SCO particles, or just suspended in the solvent of the solution. For this reason while working in solution, additional quenching phenomena should be taken into account due to a variety of diverse molecular interactions besides the energy transfer such as dynamic and static quenching. The dynamic or collisional quenching originates from the deactivation of excited luminophores due to collisions with quenchers suspended in the solution. On the other hand, the static quenching results from the formation of a (quasi) non-fluorescent complex between the luminophore and the quencher; when this type of complex absorbs light, it returns to the ground state without emission of a photon. The collisional quenching of luminescence is described by the Stern-Volmer equation as [6]:

$$\frac{F_0}{F} = 1 + k_q \tau [Q] = \frac{\tau_0}{\tau} \tag{3.2}$$

Here, F_0, F and τ_0, τ are the luminescence intensities and luminescence lifetimes in absence and presence of the quencher, respectively. k_q is the bimolecular quenching constant and [Q] is the concentration of the quencher. The plot of F_0/F as a function of [Q] are denominated the Stern-Volmer Plot (Figure 3.21).

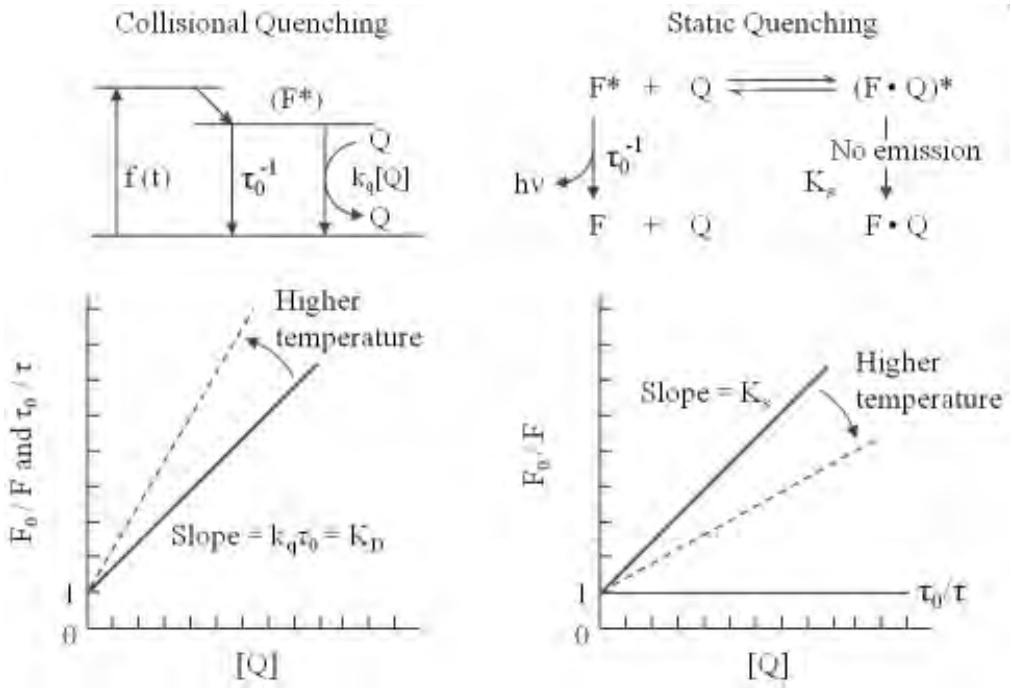

Figure 3.21: Comparison of dynamic and static quenching Stern-Volmer plots [6].

On the other hand, the pure static quenching of the luminescence can be described as a function of [Q] and the association constant of the non-luminescent complex formation K_S as [6]:

$$\frac{F_0}{F} = 1 + K_s[Q]. \tag{3.3}$$

It is worth noting that the ratio F_0/F has a linear dependence on [Q] under a purely static or a purely dynamic quenching regime unlike the ratio τ_0/τ. In static quenching, the luminophores that are complexed with the quenchers do not emit light; thus, the measured lifetime is strictly due to the unperturbed free luminophores in the solution whose $\tau = \tau_0$ regardless the value of [Q] and as a consequence the ratio τ/τ_0 is equal to 1. For this reason, the measurement of luminescent lifetimes constitutes the most definitive method to recognize the two quenching regimes. An additional method to differentiate the two phenomena is their temperature dependence. For the dynamic quenching, higher temperatures lead to faster diffusion of the quenchers in the solution and thus, more collisional quenching. Conversely in the static quenching, higher temperatures can dissociate the luminophores bound to quenchers and as a result, less quenching will be observed (Figure 3.21).

To perform the luminescence lifetime measurements we have used a *Time-Correlated Single-Photon Counting* (TCSPC) set up from PicoQuant with a 40 MHz pulsed laser diode at 460 ± 10 nm as excitation source and filtered the emitted photons of our sample with a band pass filter at 550 nm (FWHM 25 nm). As a first step, we measured the room temperature luminescence lifetimes of rhodamine 110 and acridine orange (solution $CHCl_3$ - ethanol, 19:1, 1 μM in both cases); the results of the TCSPC experiments displayed in Figure 3.22 reveal lifetimes (room temperature) of 5.5 ns and 3.8 ns for the rhodamine110 and acridine orange, respectively.

In a second step, we focalized on the role of acridine orange in the $[Fe(hptrz)_3](OTs)_2$ chloroform system. As seen in chapter II, this luminophore was chosen because this organic molecule could eventually integrate the coordination sphere of the metallic centers of the polymeric chains of the Triazole based - SCO complexes. Thus, lifetime measurements of the doped system can give us valuable information about the localization of the luminophore relative to the Fe centers of the SCO complex (at least in solution).

To explore this aspect, a Stern-Volmer plot was built from measurements performed at room temperature on solutions with a fixed concentration of 1μM of acridine orange and varying the concentration of the SCO complex ([Q]) from 0 to 7.5 mM. The calculated lifetimes and total counts of emitted photons at 550 nm from the TCSPC experiments (same experimental conditions for all of them, two hours observation) are summarized in Table 3.1.

Since the emission of the different solutions is also affected by the optical absorption properties of the SCO material itself (at room temperature the solution is in the LS state), we have corrected the measured luminescence intensities. We divided each of them by the corresponding transmission coefficient (T_x) for each concentration to compensate the quenching effects due to radiative energy transfer in the solution.

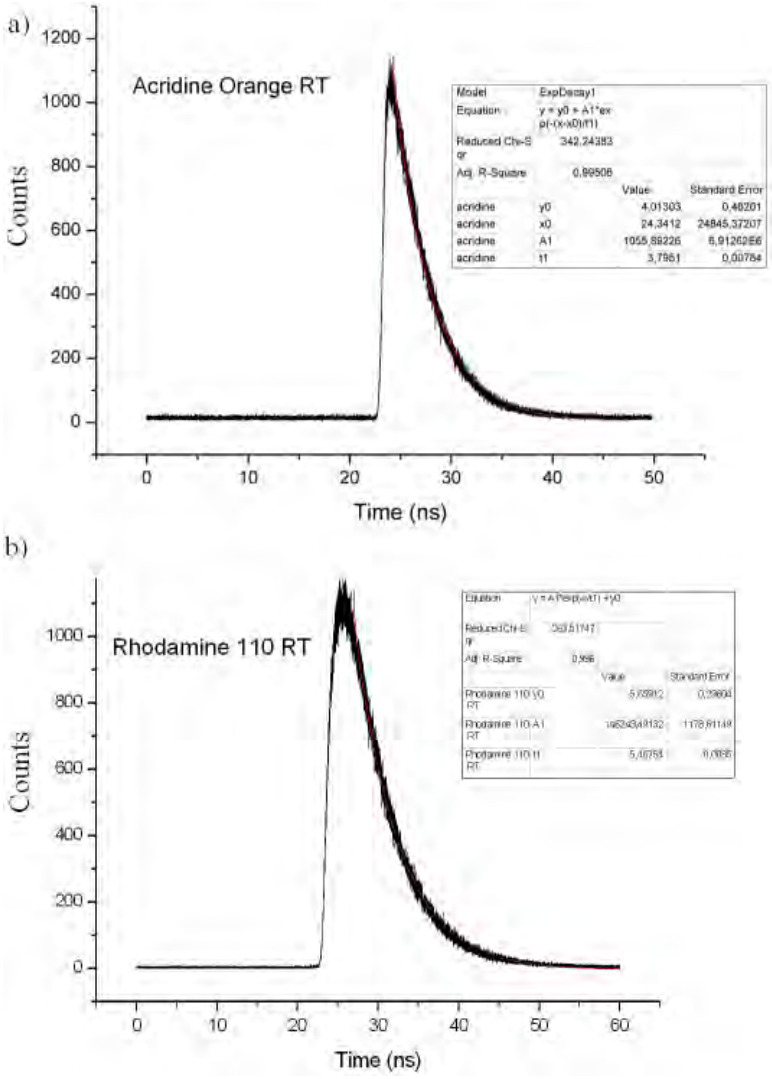

Figure 3.22: TCSCP luminescence emission data for room temperature solutions of **a)** acridine orange and **b)** rhodamine 110.

[Q] / mM	τ/ ns	Fluo @550 nm / Total Counts	T_x	Fluo T_x Corrected	τ_0/τ	F_0/F	F_0/F Corrected
0	3.79	1123747	1.00	1123747.00	1.00	1.00	1.00
0.375	4.25	901190	0.98	915496.11	0.89	1.25	1.23
1.50	3.91	789679	0.94	841029.33	0.97	1.42	1.34
3.00	4.01	632166	0.88	717054.62	0.95	1.78	1.57
4.50	3.90	516178	0.83	623564.16	0.97	2.18	1.80
6.00	3.92	409031	0.78	526257.66	0.97	2.75	2.14
7.50	3.53	316776	0.73	434065.26	1.07	3.55	2.59

Table 3.1: Data obtained from TCSPC experiments from the solutions prepared for the Stern-Volmer plot of acridine orange as a function of the $[Fe(hptrz)_3](OTs)_2$ concentration.

Assuming that each of the solutions is completely in the LS state, these coefficients were calculated with the Lambert-Beer law taking into account the lateral size of the

cuvette employed (1 cm), the molar absorption (ϵ) at 450 nm $\approx$ 7 $M^{-1}{\cdot}cm^{-1}$ and at 540 nm $\approx$ 35 $M^{-1}{\cdot}cm^{-1}$ as $T_x = e^{-(\epsilon_{540}+\epsilon_{450})*1*[Q]}$.

In spite of the correction of the luminescence data, a dramatic decrease of the luminescence is still observed as the quantity of SCO material increases in the solution and it should be associated to additional quenching mechanisms. Figure 3.23 displays the Stern-Volmer plot and the ratio τ_0/τ as a function of [Q] in our experiments. The Stern-Volmer plot shows a slight upward curvature that is completely different from the behavior displayed by the ratio of the luminescence lifetimes. The curvature is a characteristic feature of a system where the luminophore is quenched by complexation and collisions at the same time. Furthermore, the small slope obtained from the τ_0/τ plot can be interpreted as a very poor collisional quenching component in the system. These experiments seem to indicate that the acridine orange is binding to a second entity, perhaps the SCO nanomaterials, and as a result a highly efficient non-radiative transfer is suppressing almost completely the luminescence of those molecules. This hypothesis could be supported by the fact that very little change of the luminescence lifetime of the solution is observed as a function of the SCO material concentration and yet, a concomitant luminescence quenching is occurring besides the partial optical absorption of the acridine orange emission by the LS Fe(II) centers.

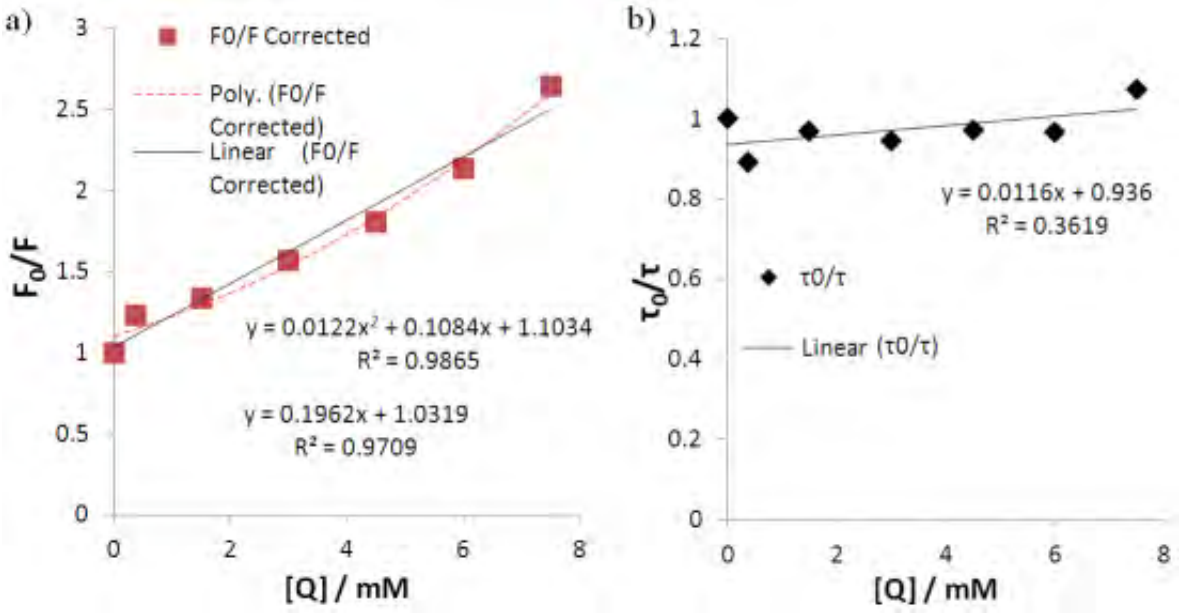

Figure 3.23: **a)** Stern-Volmer and **b)** τ_0/τ room temperature plots for acridine orange (1 μM, ethanol - chloroform (1:19) solution)as a function of the $[Fe(hptrz)_3](OTs)_2$ concentration.

We performed some additional experiments to observe the lifetime temperature dependence of our luminescent SCO system. Unfortunately, we did not have a temperature controller to couple with the TCSPC set up. For this reason, we designed an experiment to observe roughly how the chloroform solution behaved in both spin states. Here, we took two solutions with a luminophore concentration (acridine orange or rhodamine 110) of 1 μM and SCO material of 15 mM. For each solution we performed an observation at room temperature; then, we heated with a hair dryer

the cuvette until the solution turned completely to HS state (transparent) and subsequently we launched the TCSPC experiment. Since we did not have a temperature controller, the observations had to be done fast; otherwise the HS (hot) state solution could turn to the LS state during the measurement. To do this, the power of the excitation source was increased in order to have enough counts from a 30 second TCSPC experiment to observe an exponential decay (in contrast to the two hour experiments performed before). However, we would like to emphasize that this experimental condition leads to a bias towards shorter times since more than one photon per laser shot will be detected (instead of the usual rate of 1 photon per 100 laser shots [6]). In consequence, the results obtained from these experiments are merely qualitative. These observations were compared to experiments performed under the same experimental conditions with pure solutions of the luminophores.

Figure 3.24 shows the TCSPC data for these four solutions at room and high temperatures. From these experiments it is observed: (1) the room temperature luminescence lifetimes of the pure luminophore solutions (τ_{RT-Lum}) are lower than those measured in our first experiments; as mentioned before, this effect was expected due to the excessive excitation and emission rates of the setup in order to perform an unbiased TCSPC experiment. (2) These solutions displayed a shorter luminescence lifetime at high temperatures ($\tau_{HT-Lum} < \tau_{RT-Lum}$) when compared to room temperature. This effect can be associated with the thermal agitation in the solution that leads to higher collisional quenching and other non radiative relaxation mechanisms of the luminophores in solution. (3) On the contrary, in the case of the solutions of SCO material with luminophore (acridine orange or rhodamine 110), an increase of the luminescence lifetime was depicted while passing from RT to high temperature ($\tau_{HT-Mix} > \tau_{RT-Mix}$). If the quenching of luminescence were mainly collisional, the lifetime of the mixture at high temperatures should decrease instead of increasing. Conversely, if we consider static quenching in the system, higher temperatures can dissociate weakly bonded luminophore molecules to the SCO nanomaterial in solution which would lead to an increase of the general luminescence (less static quenching), but it would not explain the increase of the lifetime. In consequence, these observations seem to confirm our initial hypothesis: there is a non radiative energy transfer in our doped luminescent SCO system that disappears as it reaches the HS state; this reasoning can explain the increase of the luminescence lifetime measured for the SCO doped solutions at high temperature.

In spite of these promising results for unveiling the quenching mechanisms in our luminescent SCO materials, further experiments need to be done. Thorough studies of the luminescence lifetime and Stern-Volmer plots of our systems in solution as a function of temperature and with other luminophores that display less chance to bind to SCO materials would provide crucial information to confirm our hypotheses. Another interesting alternative to explore with the TCSPC set up is the study of this particular SCO system in the form of doped thin films as a function of temperature. Under this scenario, the possibility of dynamic quenching will be completely removed simplifying, at least to some extent, the complexity of the interpretation of the data. It is worth to note also that TCSPC measurements on these samples in the LS state are rather challenging due to the simultaneous excitation of the luminophore and the

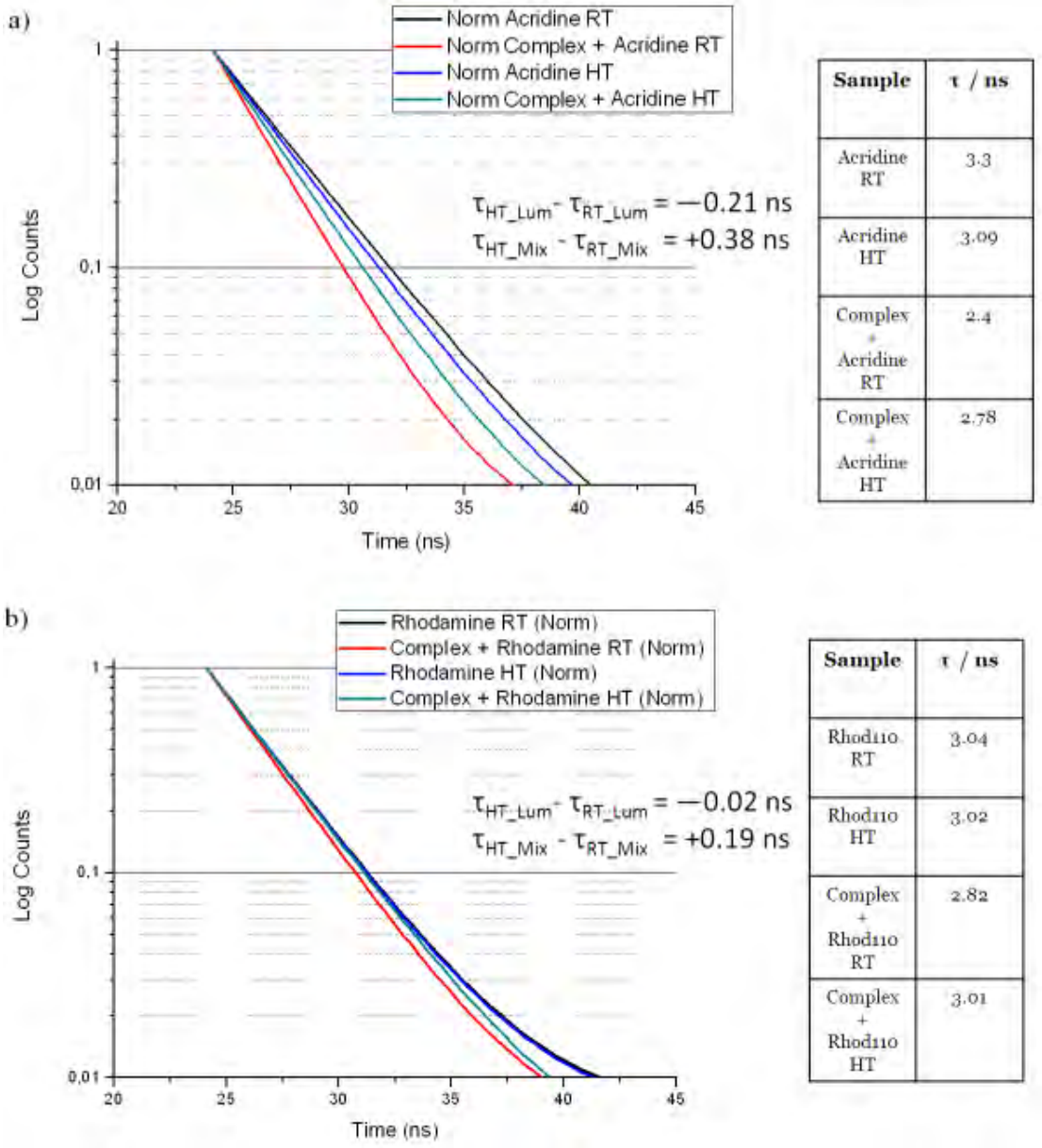

Sample	τ / ns
Acridine RT	3.3
Acridine HT	3.09
Complex + Acridine RT	2.4
Complex + Acridine HT	2.78

Sample	τ / ns
Rhod110 RT	3.04
Rhod110 HT	3.02
Complex + Rhod110 RT	2.82
Complex + Rhod110 HT	3.01

Figure 3.24: Normalized TCSPC data obtained from pure luminophore solutions and luminophore doped $[Fe(hptrz)_3](OTs)_2$ chloroform system at room and high temperatures. The luminophore employed in **a)** is acridine orange and in **b)** rhodamine 110.

SCO complex (which also absorbs light in the visible) - leading to a photoperturbation of the LS⇌HS equilibrium. This may bring additional complexity to the comparison of the measurements in the LS and the HS states.

3.3.2.5 Measurement of photobleaching rates to determine non-radiative energy transfer efficiency

Usually, the photobleaching of the luminophore during an experiment constitutes a limitation to perform accurate intensity based measurements in fluorescence. However,

this phenomenon can be useful for estimating the efficiency of the energy transfer between a sensitizer (S) - acceptor (A) pair [11]. Even though the photobleaching process can be easily 10 orders of magnitude slower than the fluorescence emission processes (the time scale of the phenomenon spans from seconds to minutes depending on the power of the excitation), it is possible to observe its effects during the measurements because it is *irreversible*. For example, Figure 3.25 illustrates the photobleaching damage that can be done to our films films after a long period exposition with a 50x or a 10x objective; due to the higher power density sent to the sample while using a high magnification objective, the damage to the film is more dramatic than when a low magnification one is employed.

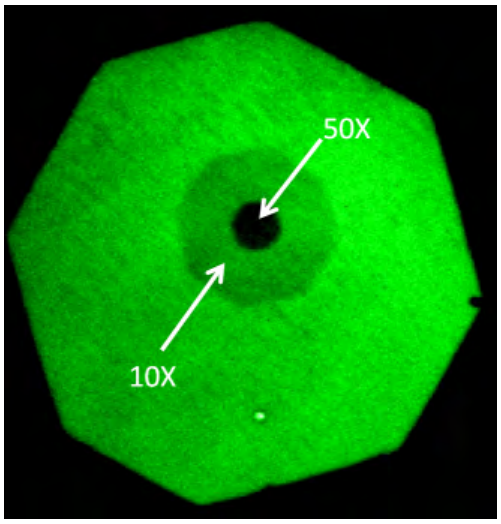

Figure 3.25: Fluorescence image displaying the photobleaching damage produced to a fluorescent thin film of $[Fe(hptrz)_3](OTs)_2$ doped with rhodamine 110 after a long exposition period.

As mentioned in section 1.2.2.2, a luminophore in an excited state has a certain probability per unit of time k_{pb} to be destroyed by photobleaching. The majority of fluorophores photodestruct typically after $10^4 - 10^7$ excitation events depending on its molecular structure and the environment; this means that the probability of destruction is very low compared to fluorescence, energy transfer or other relaxation mechanism. Nonetheless, while observing the luminescent response of an ensemble of luminophore molecules over an appropriate time window, the number of molecules able to fluoresce will decrease exponentially as a function of time. The probability per unit of time for a sensitizer (S) of undergoing photobleaching k_{pb} will always be the same in presence or absence of an acceptor (A). However, a non-radiative energy transfer between the pair will definitely affect the effective photobleaching of S since both are competing deactivation processes. The efficiency of FRET (Q_{FRET}) can be calculated employing the difference of the photobleaching rates measured for the sensitizer in presence or in absence of the acceptor as shown in equation 3.4 [11]:

$$Q_{FRET} = \frac{[\tau_{pb,S}]^{-1} - [\tau_{pb,SA}]^{-1}}{[\tau_{pb,SA}]^{-1}}, \tag{3.4}$$

where $\tau_{pb,S}$ is the photobleaching time constant of the S in absence of A and $\tau_{pb,SA}$ in presence of A.

In order to explore this idea, we carried out an experiment to measure the photobleaching rates of the luminophore (sensitizer, S) in both spin states for two films of [Fe(*hptrz*)$_3$](OTs)$_2$ doped with rhodamine 110 that were deposited on a glass/Au substrate at the same time and starting from the same mother solution. Two microscopy experiments were performed in luminescence mode, with constant excitation (maximum power of our blue LED), a X50 magnification objective, under open atmosphere and one acquisition every ten minutes. The first experiment was performed on the thin film at 328 K (LS state) during 7000 minutes ($\approx$ 5 days) and the second was done on the other film at 348 K (HS state) during 3600 minutes ($\approx$ 2.5 days).

Figure 3.26 shows the decay of the luminescence as a function of time with a continuous excitation for both experiments. Each graph displays a double exponential decay that may indicate the existence of two different luminophore species in the thin films. In the LS state, the photobleaching behavior is composed by exponentials with time constants $\tau_{LS1} \approx 2770$ minutes and $\tau_{LS2} \approx 450$ minutes; conversely, in the HS state the time constants are $\tau_{HS1} \approx 660$ minutes and $\tau_{HS2} \approx 80$ minutes. If it is assumed that the time constants τ_{LS1} and τ_{HS1} as well as τ_{LS2} and τ_{HS2} are different due to the SCO, according to equation 3.4 the energy transfer efficiency in our system in the LS state seems to be of the order of 0.76 to 0.82. This seems a little elevated when compared to the luminescent modulation in the films ($\approx$ 50%). Even though these experiments could be a proof of the non-radiative energy transfer in our luminescent SCO material, it should not be forgotten that the photobleaching rates and other de-excitation phenomena may be affected drastically by temperature in similar sense as temperature rises (*i.e.*, higher photobleaching at higher temperatures). In any case, from these experiments it is certain that there is a concomitant difference of the photobleaching rates between the LS and the HS states. Further experiments need to be done in order to decorrelate the effects of temperature from those of the SCO in the measurements of the FRET efficiency.

3.3.2.6 Estimation of R_0 and r_{SA} in luminescent doped SCO thin films

So far, we have gathered enough information to have a more quantitative point of view for a possible non radiative energy transfer in our luminescent triazole based SCO nanomaterials. At this point, we are able to estimate the characteristic R_0 for a sensitizer - acceptor pair (S-A) with the optical properties of Fe(*hptrz*)$_3$](OTs)$_2$ and one of our selected luminophores (acridine orange or rhodamine 110) by means of equation 3.5 (See section 1.2.3.2):

$$(R_0)^6 = \frac{9000(ln10)k^2Q_s}{N_A 128\pi^5 n^4}\left[J(\lambda)\right] \ . \tag{3.5}$$

Figure 3.27 shows the LS state absorption band for the Fe(*hptrz*)$_3$](OTs)$_2$ complex centered at 543 nm superposed to the emission spectra of acridine arange and rhodamine 110. From this figure, the overlap integral for each of the luminophores gives $J_{AO}(\lambda) = 2.8311 \cdot 10^{-16}\ L \cdot mol^{-1} \cdot$ cm^3 and $J_{Rh110}(\lambda) = 2.3914 \cdot 10^{-16}\ L \cdot mol^{-1} \cdot$ cm^3 (integral calculated from 480 nm to 700 nm). Then, assuming an average refractive

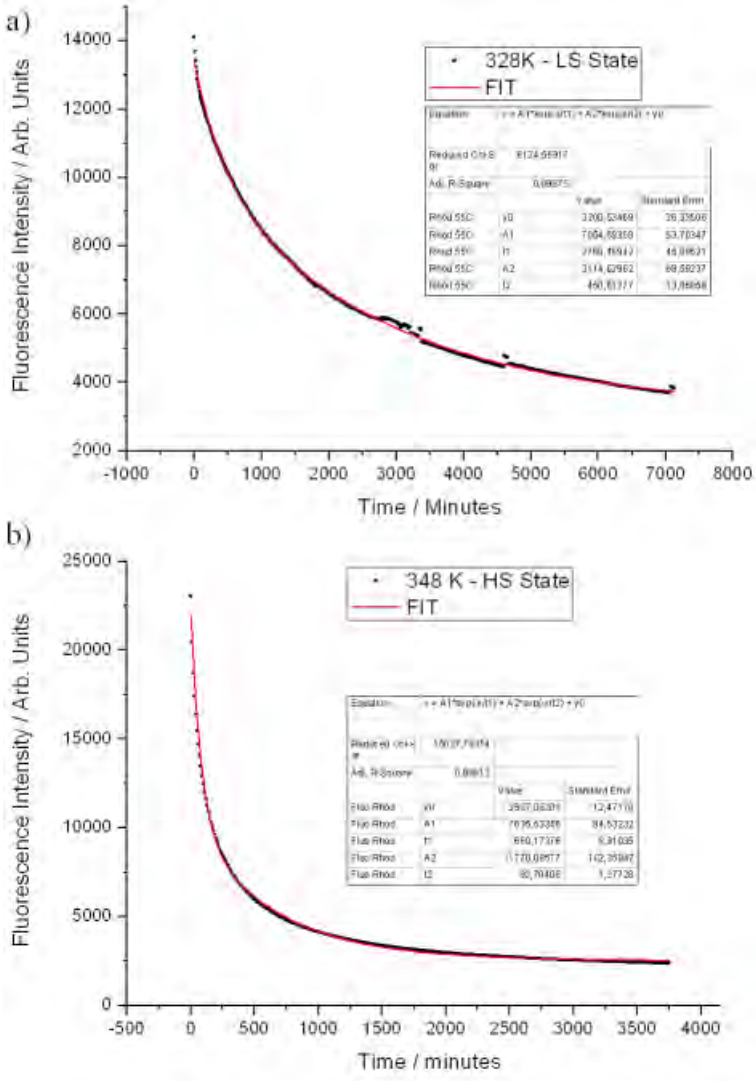

Figure 3.26: Temporal variation of the luminescence (photobleaching) with a constant excitation for a film of Fe($hptrz$)$_3$](OTs)$_2$ doped with rhodamine 110 at **a)** 328 K and **b)** 348 K.

index of the material in that spectral window as 1.5 [38], $k = 2/3$ since *a priori* there is no privileged orientation of the interacting dipoles and the quantum yield for the luminophores as $Q_{Rh110} = 0.9$ [132] and $Q_{AO} = 0.25$ [133], we obtain R_0=1.59 nm in the case of rhodamine 110 and R_0=1.32 nm for acridine orange. It is worth to note that the quantum yield adopted for these calculations was measured in solution and not in solid state. This parameter is very sensitive to the experimental conditions and it can either increase or decrease depending on the environment of the luminophore. However, since R_0 has a sixth root dependence on Q_s ($R_0 = \alpha \cdot Q_s^{-6}$) small errors in Q_s do not have a huge impact on the calculation of R_0. For example if the quantum yield is increased by a factor of two, the R_0 will be within $\pm 12\%$. From this point of view, and given the fact that the overlap integrals for both luminophores provide very similar values, we can estimate a R_0 that spans between 1 and 2 nm for either luminophore.

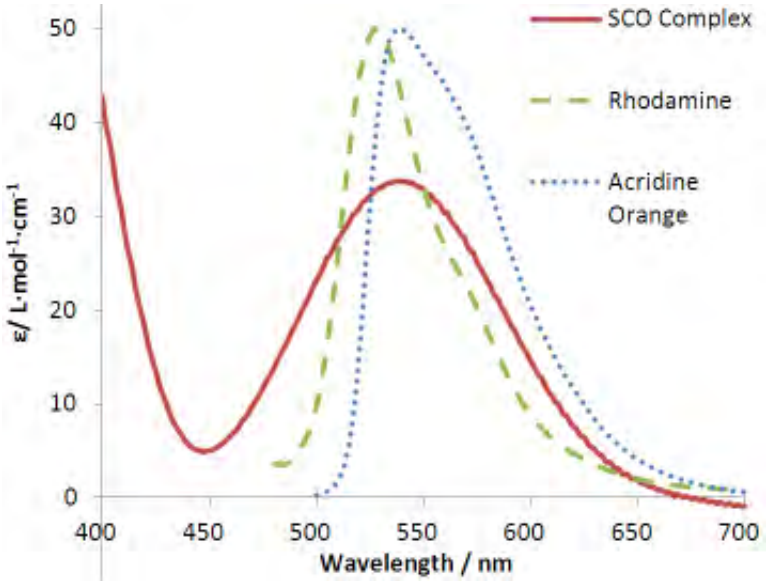

Figure 3.27: Spectral overlap of the LS state absorption band of the Fe($hptrz$)$_3$](OTs)$_2$ complex centered at 543 nm superposed to the emission spectra of acridine orange and rhodamine 110.

The efficiency of FRET can be measured comparing the fluorescence intensities of the sensitizer in absence (F_S) and in presence (F_{SA}) of the acceptor (assuming absence of a radiative energy transfer) or it can also be expressed in terms of exit rates from the excited state of S as:

$$Q_{FRET} = 1 - \frac{F_{SA}}{F_S} = \frac{k_T}{(1/\tau_S) + k_T}, \tag{3.6}$$

where k_T is the transfer rate between the pair S-A. For example, for the thin films from Figure 3.16, Q_{FRET} is approximately 0.4; if we assume that the calculated values of R_0 are of the correct order of magnitude, we can calculate k_T from equation 3.6 and then calculate an approximate r_{SA} as:

$$r_{SA} = \frac{R_0}{(k_T \cdot 1/\tau_S)^{1/6}}. \tag{3.7}$$

From equation 3.7, the separation between the rhodamine 110 and the Fe atoms would be $r_{SA} \approx 1.7$ nm and for acridine orange $r_{SA} \approx 1.5$ nm.

3.4 Fluorescent Detection of SCO in Single Nano-Objects

One of the main issues to perform the detection of the SCO properties in a single object and to correlate them with their morphology lays on the effective isolation of the objects in order to make the measurement. This is particularly essential when a conventional optical microscope is used for the detection of the property (luminescence detection) and another completely different technique to study the morphology of

the object (AFM, SEM). Since in the first characterization stage we do not have enough resolution to distinguish whether the measurement is taken place for a single nano-object or a small agglomerate of objects, we need to be sure that the "targets" are appropriately dispersed on the surface of observation. At this point it becomes evident the need of some sort of reference or roadmap in the sample to locate us independently of the microscopy technique and thus, establish a link between an object of the sample and its properties. Another key issue is the separation of the objects at a distance, which is higher than the spatial resolution of the optical microscope ($R = 1.2\lambda/NA$). To solve these issues, we have identified two options: either organize the SCO nanomaterials into arrays or depose the objects into a substrate with marks or features that can be recognized in all characterization stages.

Most of the synthetic methods for obtaining SCO nano-materials produce important amounts of objects and it is not always evident to find a procedure for depositing them in a controlled manner. This part of the thesis work explores four strategies centered on the isolation of SCO nano-objects: capillary-convective directed assembly of arrays of single-nano-objects, random assembly on a nanopatterned Si master and two different types of *in situ* synthesis for arrays of SCO nano-objects. The results of these strategies were all studied with luminescence microscopy and with SEM and AFM observations when possible.

3.4.1 Technical considerations for performing the luminescence detection of the SCO at the small scales

3.4.1.1 Image Acquisition

In the case of luminescence microscopy, it is worth noting that the choice and configuration of the detector is crucial to measure properly the signal coming from the sample. For a CCD detector, the key factor is its architecture. Our iKon-M camera (Andro Technology) comes with a full frame CCD, back-illuminated and deep cooled to -70 °C (without employing a heat exchange liquid flow) or to -100 °C if the Peltier is assited by a water cooling system. In a full frame CCD, the whole surface of the sensor is exposed to the incoming photons of the sample. Thus the accumulated charge generated by these photons on each pixel is vertically shifted row by row until the readout register and then, each of its values is shifted horizontally (serial output) to read each individual pixel (See Figure 3.28). The quantum efficiency (QE) of a CCD depends strongly on the ability of the photons to reach the depletion region of the detector. It is in this region where the photons are converted into electronic charges and are subsequently accumulated on each pixel. Contrary to a conventional CCD where the incoming photons have to go through the gate electrode structure of each sensor (pixel), in the back-illuminated CCD light falls onto the back of the CCD in a region where the bulk of the silicon has been thinned by etching until it is essentially transparent (from 10 to 15 μm) (Figure 3.28 b and c). Hence, the probability of a given photon being absorbed by the gate structure is considerably reduced independently of their wavelength (which governs the penetration distance of the photon into the

sensor); for the iKon-M, the QE in the visible is nearly 100% at 540 nm (See Figure 3.29).

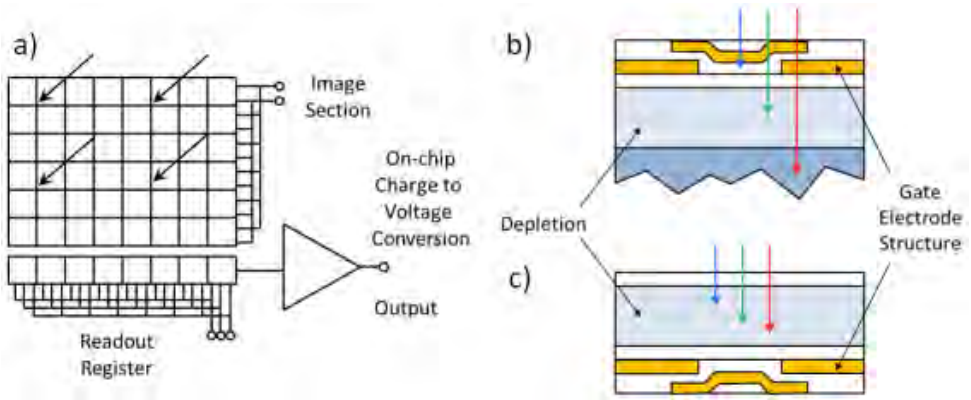

Figure 3.28: **a)** Scheme of the architecture for a full frame CCD. **b)**, **c)** Front and back illuminated CCD pixel cross section, respectively. Adapted from [134].

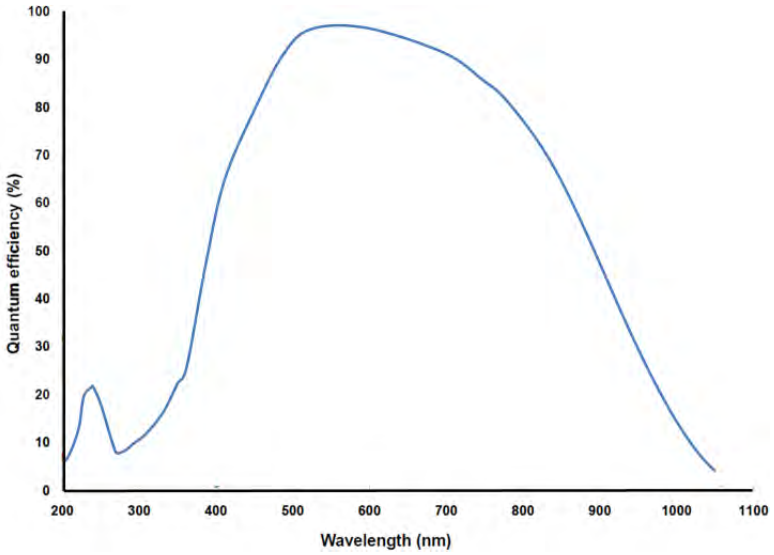

Figure 3.29: Quantum efficiency (QE) curve for the CCD of the Ikon-M camera [134].

When it comes to measuring signals with very low intensities, it is important to consider avoiding all types of noise in the measurement. One parameter is the temperature of the CCD. The lower the temperature of the detector, the lower the dark noise (also called dark current) will be. This is a thermally induced noise that arises from the camera in the absence of light (See Figure 3.30). It is usually a good practice before launching an experiment to take a "dark" image without sending any light to the CCD. Hence, the baseline given by the detector at each pixel can be removed from latter acquisitions and only charges generated by photons will be taken into account in the observations.

Another way to avoid noise in the measurement is by employing the lowest readout rate of the camera. This has the advantage that the bandwidth required for reading

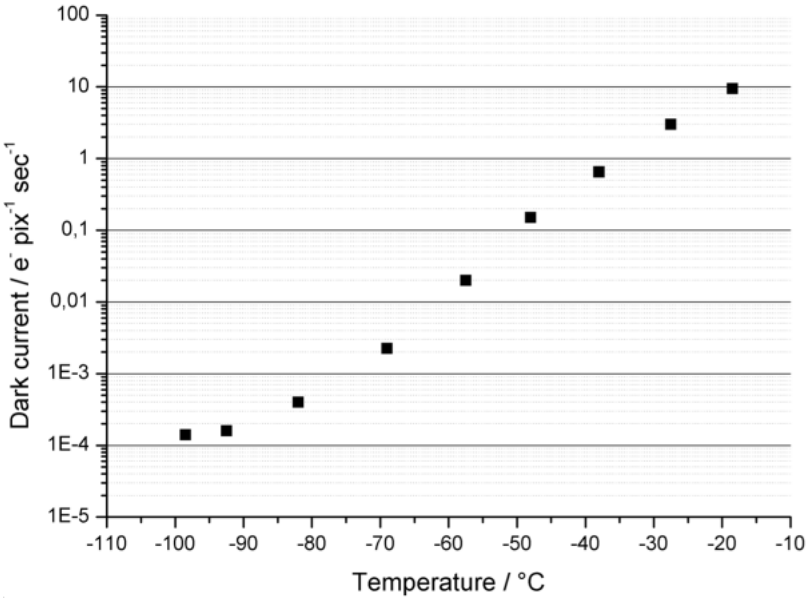

Figure 3.30: Dark current of the CCD embedded in the iKon-M camera as a function of temperature [134].

the CCD is less thus the noise generated while reading the CCD is minimal. However, it has the inconvenience of rendering the acquisition process very slow and not adapted for observing the dynamics of relatively fast events. For the iKon-M, there are three possible reading rates: 2.5 MHz, 1 MHz and 50 kHz (the full frame reading time ranges from 0.5 to 21 s). Nonetheless, an effective way to decrease the total acquisition time of the CCD is employing the binning and/or sub-imaging options. Binning is the process where a group of pixels act as one so their charge is added; thus the number of readings necessary to go over the whole CCD is less, the equivalent pixel well capacity also increases and the readout noise (per pixel) decreases, but at the expense of reducing the spatial resolution of the image. With the sub-imaging option instead, only a part of the CCD is read; in contrast to the binning option, the resolution is unaltered, but the size of the field of view is decreased.

An additional parameter to keep in mind is the adjustment of the analog to digital converter (ADC) sensitivity (or pre-amplification gain). Most of the times, the CCDs have a dynamic range that exceed the representation capacity of the ADC. For example, in the iKon-M the typical shift register pixel well is 200k electrons; however the 16 bit ADC (with 3 pre-gain options: x1, x2, x4) at the output of the shift register of the CCD is only able to make reference to 65536 (2^{16})levels. Here, the dilemma becomes clear: if we set the sensitivity to the maximum (x4, *i.e.* 1 electron/ ADC count), we will have the highest sensitivity for the digital conversion of the data, but at the same time, the ADC will saturate approximately at 65.5k electrons. Conversely, if the minimum sensitivity is selected (x1, *i.e.* 4 electrons/ADC count), we will not be able to detect small variations (at least not the smallest possible for the detector), but in return, the ADC will be able to address the full well capacity of the shift register. There will always be a trade between the sensitivity and the ability of representing small and big signals at the same time (dynamic range) in the same measurement.

While of course the choice for the pre-amp parameter depends strongly on the type of measurement to be performed, we have found out that for the low signal levels from our luminescence experiments, the most suited choice is to work with the highest sensitivity mode (pre-amp = x4).

3.4.1.2 Image Analysis

As mentioned in chapter II, the data treatment performed on the images captured by the CCD is centered on choosing a region of interest (ROI), calculating its mean value and then plotting this information as a function of an experimental parameter (time, temperature, *etc*). However, this type of analysis may become a difficult task while making observations as a function of temperature. Due to thermal dilation of the heating stage and/or the substrate or mechanical constraints of the cryostat support, it is possible to depict a drift of the sample not only in X and Y directions, but also a variation of the focal plane (Z direction) during the experiment. This drift will be more problematic as we increase the level of magnification employed in the microscopy measurements. Hence, a particular object studied in the first image of a given experiment will not necessarily be on the same place in the next acquisition; as a consequence, the ROI needs to be displaced for each acquisition of the experiment in order to analyze the same object in its new location.

This aspect of the microscopy measurements became a real issue in the case of the single object observations along this thesis work. At the beginning, the ROI was placed manually on each of the images of the thermal cycles. This procedure had the inconvenience of (1) it was excessively time consuming and (2) it was subjective to errors introduced by the user. A typical experiment as a function of temperature observing a substrate with dispersed SCO objects can have several hundreds of images. Furthermore, usually the quantity of ROIs per experiment was more than one, which rendered the analysis even more difficult.

After defining a set of ROIs for the first image of an experiment and assuming that each point of the sample has the same drift in the X and Y direction on each successive acquisition, then by adding the necessary offset to the coordinates of the set of ROIs to compensate the drift should be enough to track many objects simultaneously. For this reason, we studied the text file generated by the ANDOR Solis software and we wrote an EXCEL file that receives as inputs a ROI configuration file and a set of X - Y offsets for generating a new compensated ROI configuration file. In this manner, a file with several ROIs could be generated by judging the displacement of one point in an image relative to the first acquisition of the experiment. This approach lowered to some extent the complexity of the image analysis since all defined ROIs were modified at the same time instead of one at a time. However, it was found that the sample slightly rotated during the observations and simple X-Y offsets for the ROIs put them close to their respective targets, but it was not accurate enough. Additionally, all the calculations for the offsets remained manual and thus, a time consuming task.

In order to give a more rigorous solution to this problem, we developed an image registration routine under MATLAB® environment employing the Image Processing

Toolbox software. Image registration is the process of aligning two or more images of the same scene. Our routine compensates automatically any drift of the sample obtained during the experiments. It receives a stack of images (in TIFF format) and asks from the user two inputs: (1) a section of interest or *feature* in the first image of the stack that will be tracked during the alignment process and (2) at least three reference points (it could be more) present in all the images of the stack (since the sample drifts, there are some regions of the image that may appear/disappear from the field of view) that would be used later for fine tuning of the alignment. Once these parameters are defined by the user, the routine executes the function of, what it is called in signal processing, normalized 2D cross-correlation between the feature and the rest of the images of the stack following equation 3.8 [135, 136]:

$$CCR(u,v) = \frac{\sum_{x,y}[f(x,y) - \bar{f}_{u,v}][t(x-u,y-v) - t]}{\left\{\sum_{x,y}[f(x,y) - \bar{f}_{u,v}]^2 \sum_{x,y}[t(x-u,y-v) - \bar{t}]^2\right\}^{0.5}}, \tag{3.8}$$

where $CCR(u,v)$ is the crosscorrelation, $f(x,y)$ is the image to be analyzed, t is the feature, $\bar{t}$ is the mean value of the selected feature and $\bar{f}_{u,v}$ is the mean value of $f(x,y)$ in the region under the feature.

The cross-correlation is a measure of similarity of two waveforms as a function of a parameter-lag (time, space, frequency, etc.) applied to one of them. In our case, this procedure can be understood as a spatial sweep of the feature over a given image seeking the place of maximum similitude. Thus, a preliminary set of offset values for X and Y can be inferred from each cross-correlation. However, this operation does not take into account the slight rotations that the sample has during the experiment (it involves only translation); as a result, we have the stack of images closely aligned but they do not match exactly. To solve this, the routine uses a punctual cross-correlation in the vicinity of the coordinates of the reference points in each pre-aligned image searching the real positions of the reference points. With this information, the routine can establish a spatial transformation for each image of the stack in order to match them with the first image of the experiment. In this manner, in the aligned stack of images it will be possible to monitor multiple targets (even very small with 5x5 pixel ROIs) easily and employing just one set of ROIs for the whole experiment.

An example of this procedure is shown in Figure 3.31. Panel a) displays an optical bright field image of a SCO nano-object array. The blue square would constitute the feature to be tracked in the stack (the array of objects) and the blue circles signal three possible reference points. Panel b displays a second image of the sample after a drift. Then, by calculating the normalized 2D cross-correlation, a maximum can be found (darkest point in panel c). With this information, a spatial transformation can be established and applied to the image in b) to compensate the drift as it can be observed in d). More detailed information about the code developed for this routine can be found in Appendix B.

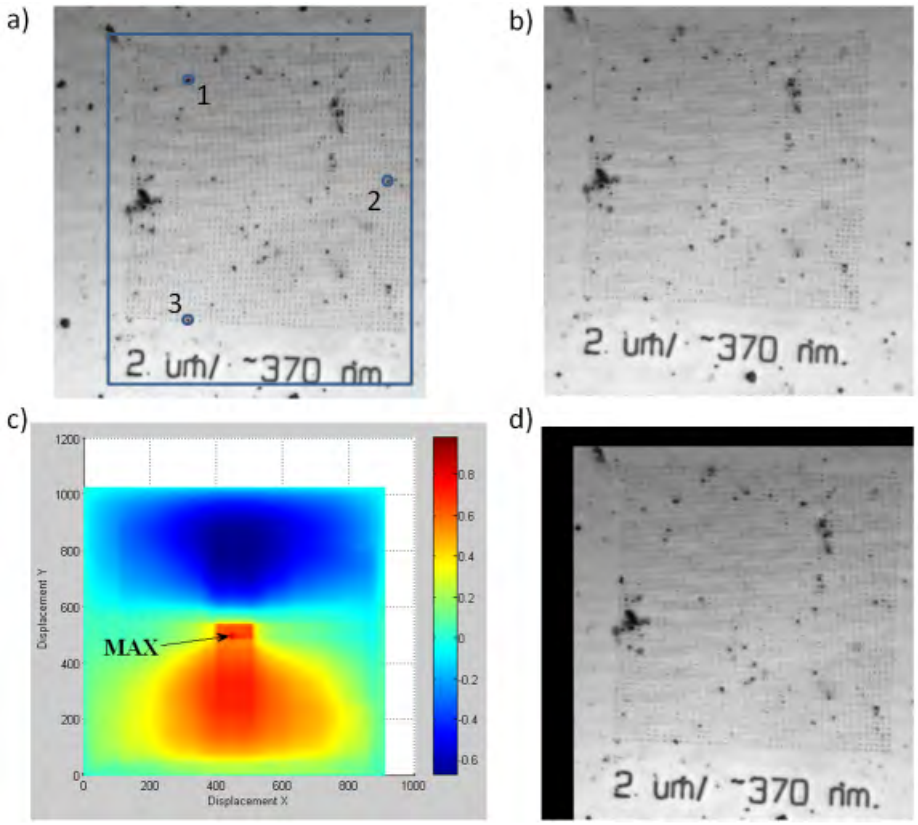

Figure 3.31: Image registration process. **a)** Reference image. The blue square and circles represent the feature (t)to be tracked down and the reference points for fine tuning. **b)** Image to align with **a)**. **c)** Cross-correlation between the feature selected in **a)** and **b)**. **d)** Image from **b)** aligned with **a)** after a spatial transformation inferred from the two cross-correlation processes.

3.4.2 Capillary-Convective Directed assembly

A collaboration with the Nanobiosystems group , with Prof. Christophe Vieu and one of his PhD students Aline Cerf at CNRS-LAAS in Toulouse, has been undertaken in order to explore this idea.

When a liquid drop is deposited over a surface, the points of contact between the three phases solid-liquid-gas (s-l-g) is called the *three phase contact line* or *triple line*. Along this line, each interface attempts to minimize its energy and as a result,to minimize the surface. The combination of the interfacial tensions (γ_{sg}, γ_{sl}, γ_{lg}) determine the contact angle θ_e that is defined by the interface liquid-gas and the interface solid-liquid in contact with a solid substrate. The scheme 3.32 represents the three phase contact line of a drop over a substrate. γ_{sg}, γ_{sl}, γ_{lg} are the capillary forces per length unit that are exerted on the triple line.

Real surfaces are composed by physical (roughness) or chemical irregularities. If a drop on top of a substrate is dragged at a certain speed, the contact line will reach one of these defects, it will be anchored and deformed (see Figure 3.33). This phenomenon will elongate the drop and create a thin film on the surface near where the triple line is formed. At the same time, the fast evaporation of the solvent in that zone (at the

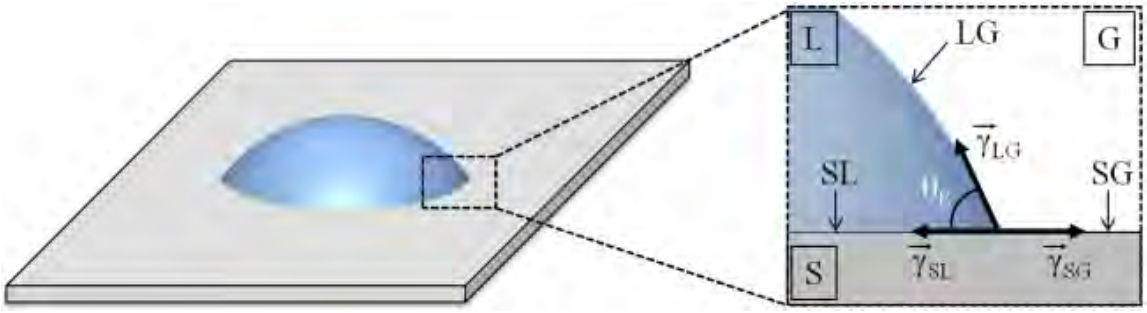

Figure 3.32: Scheme of a liquid drop deposited over a solid plane. In the three phase (solid-liquid-gas) contact line, the interface solid-liquid (sl) and liquid-gas (lg) define the contact angle θ_e that corresponds to the angle between the tangent of the drop at the contact point and the surface.

liquid/air interface) constitutes a liquid loss of the drop, that an internal flow (J_w) will try to compensate. If the drop is further displaced, the drop will be released from the defect dissipating some energy.

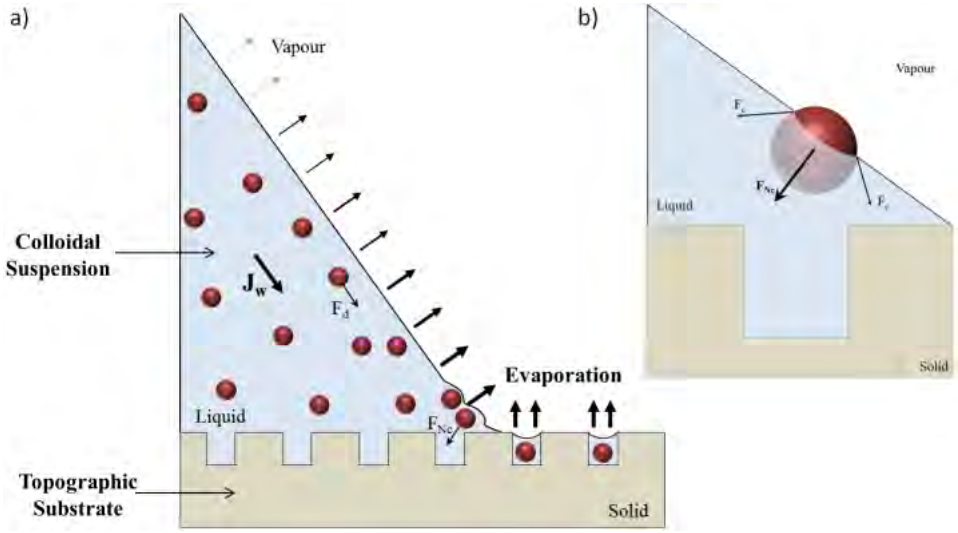

Figure 3.33: Cappillary-convective directed assembly principle on topographic patterns. As a droplet is displaced on a patterned surface, the triple line will be anchored to the surface defects. A flow J_w will transport the objects suspended in the liquid towards the triple line to be trapped by capillary forces.

Under these circumstances, if the drop which is being displaced is made out of a colloidal suspension, the objects suspended in the liquid will be transported by J_w to the evaporation zone near the triple line. As a result, a controlled deposition of the suspended objects can be obtained as the drop evaporates while it is being displaced. The concept of directed assembly is based on the intentional creation of "organized defects" or patterns on a surface generated by lithographic methods (e-beam / photo lithography) to guide and place objects of a solution. In the scope of this work, we have focused on topographic defects. The border effects caused by abrupt changes in the topography of a hydrophobic surface in a solid will be the responsible of anchoring the triple line to the patterns. The principal forces that play a role in the capillary-convective directed assembly are the hydrodynamic force (F_d that directs the suspended objects towards the triple line and the capillary force (F_c) that fixes the

objects on the patterns. The origin of F_d is attributed to the convective phenomena induced by the increase of the evaporation rate near the contact line.

The net capillary force F_{nc} in the interface particle/solvent/air for a partially immersed particle is normal to the plane defined by the contact line particle/solvent/air (see inset Figure 3.33). In the particular case of the displacement of a triple line over a polydimethylsiloxane (PDMS) substrate with cavities, the different mechanisms that lead to a directed assembly of objects suspended in the solution into the patterns of the surface are [137]:

- *Approach of the meniscus to a pattern* (Figure 3.34a): If the surface is completely flat, the evaporation rate is not excessive, the contact angle θ_e is high enough, the meniscus will not be deformed and its relative movement to the substrate will induce a recirculation flow J_r that will move the particles from the contact line region to the bulk liquid region. As a result, the capillary net forces F_{nc} will not be effective on and no deposition will take place.

- *Anchoring and deformation of the meniscus* (Figure 3.34b): The triple line is anchored locally by the pattern and then elongated progressively due to the displacement of the drop. The contact angle decreases and then the liquid forms a thin film near the defect. Close to the contact line in movement with respect to the substrate, the evaporation of the solvent generates a flow of solvent J_w that goes towards the front of the meniscus to replace the loss of solvent. As a result, the suspended objects migrate from the interior of the drop towards the front of the meniscus where they are trapped in the interior of the cavities due to capillary forces F_{nc}.

- *Rupture and relaxation of the meniscus* (Figure 3.34c): The displacement of the drop takes the triple line to its elasticity limit and as a result, the meniscus is released from the surface defect. This phenomenon can be more or less fast and brutal depending on the experimental conditions. Once the triple line has dissipated all the accumulated energy, it relaxes and returns to its original form and contact angle. Again, the movement of the drop relative to the substrate generates a recirculation flow J_r that sweeps the suspended objects far from the contact line. The particles that got blocked in the cavities are still subjected to capillary forces that will force them to approach to each other as the solvent of the cavity evaporates.

3.4.2.1 Description of the Technique

The setup of the system of directed assembly of objects by capillary and convective forces is displayed in Figure 3.35. The patterned substrate where we want to depose the objects is placed on a Peltier plate that will allow us to control the temperature of the substrate (278 K - 328 K). At the same time, this Peltier stage is placed on a motorized platform that can move along the X axis. The speed at which this platform

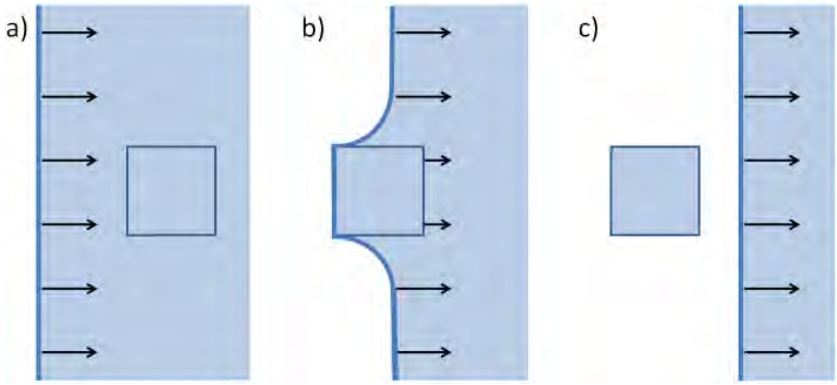

Figure 3.34: Anchoring mechanism of the triple line on a topographic pattern. **a)** The contact line scans the surface. **b)** the contact line is anchored by the pattern. **c)** The contact line is released by the structure.

moves (100 nm/s to 1 mm/s) and the position in X (precision of 10 nm) can be controlled with a stepper motor*via* a computer interface. Then, a drop of 30 μl of the colloidal suspension is placed on top of the host substrate. After this, a fixed glass slide (independent from the mobile platform) is placed horizontally over the drop and maintained at a fixed height ($\approx$ 1 mm) to confine the drop between the two surfaces (slide - substrate). Under this configuration, the triple line formed at the surface of the substrate is essentially a straight line (except on the corners of the glass slide) and it is possible to move it along the surface in a controlled manner as the platform is displaced. There is also an optical microscope mounted on top of the setup in order to monitor the meniscus and the assembly process [137].

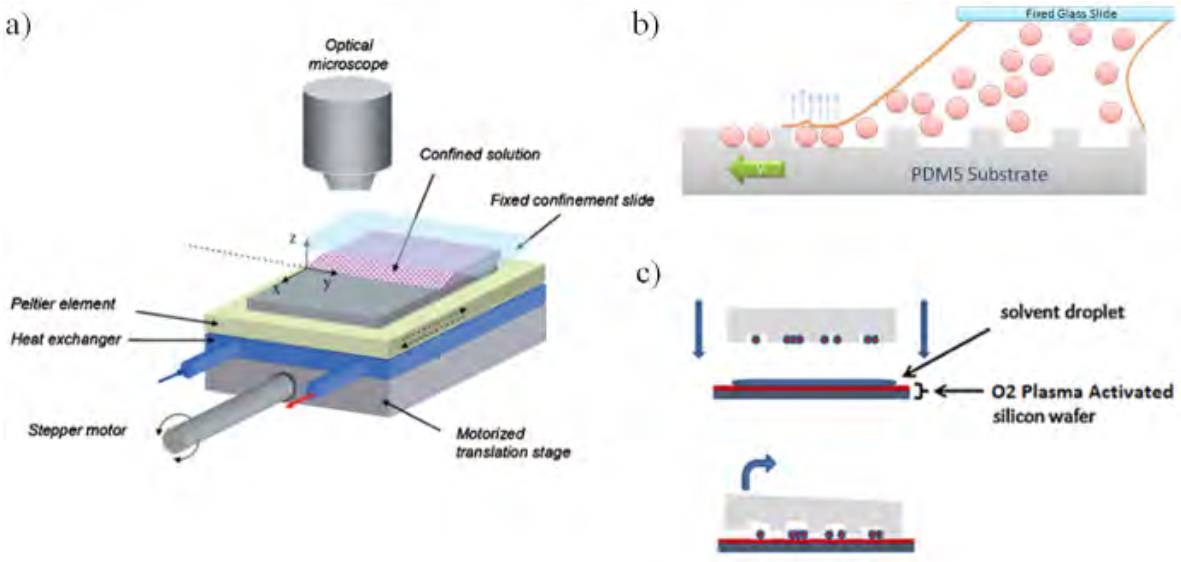

Figure 3.35: **a)** Scheme of the setup for the directed assembly of objects by capillary and convective forces. **b)** Colloidal drop confined between a fixed glass slide and a nanopaterned PDMS stamp. **c)** Transfer of the organized objects by microcontact printing with solvent mediation [138].

For this work, the substrates that we employed for assemblying the nano-objects from suspension are polydimethylsiloxane (PDMS) stamps with nano/micro-patterned

cavities (Figure 3.35). Once the objects have been assembled we employed the method developed by Cerf *et al.* denominated micro-contact printing with solvent mediation [138] in order to transfer the particules from the stamps to a Si substrate. The method consists on putting a small ethanol or deionized water drop on top of a Si or glass surface, then placing the stamp with the assembly of particles on top and putting the ensemble into an oven at 373 K during 20 minutes until the solvent is completely evaporated (Figure 3.35c). After this, the PDMS stamp is peeled off and the objects remain on the substrate ready for observation.

3.4.2.2 Fabrication of the Si master and PDMS stamps

The master employed for generating the PDMS stamps was produced by means of an electrom beam lithography process combined with deep reactive ion etching (RIE). Arrays of squares or circles with different widths (500, 370, 350, 300 and 250 nm) and different pitches (1.5, 2, 3 and 5 μm) were patterned on a standard Si wafer. The different steps of this fabrication process are (see Figure 3.36):

- *Step 0:* before starting a lithography process, it is imperative to clean properly the Si wafer by inmersion in RT2 (sulfochromic acid) for 5 minutes, rinsing with deionized (DI) water and then dehydration in a hot plate at 170 °C for another 5 minutes.
- *Step 1* : the Si wafer is covered with $\approx$ 150 nm of an electron-sensible resist called Poly(methyl methacrylate) (PMMA) by spin coating (3000 rpm, 5000rpm^2, 30 s).
- *Step 2* : the si wafer is introduced into an "electronic masker" RAITH150. Here, the wafer is selectively exposed to a focalized electron beam. The beam is displaced and activated only at certain places following a file that contains the design to pattern into the wafer.
- *Step 3* : once the exposition to the electron beam is finished, the wafer is placed into a beaker containing a developer that in the case of the PMMA is a solution of Methyl isobutyl ketone (MIBK) and isopropanol (IPA) 1:3 in volume. Since the PMMA is a positive resist, the regions of the layer that have been exposed to the e-beam become soluble to the developer. A few seconds after the wafer is immersed in the solution, the patterns appear on the PMMA layer exposing the selected regions of the Si substrate.
- *Step 4* : a 50 nm layer of Ti is deposited on the wafer by evaporation.
- *Step 5* : a lift-off process is performed by immersing the wafer into acetone in order to remove the PMMA from the wafer; only the Ti that is in contact with the Si wafer remains on the surface.
- *Step 6*: The patterns are transferred onto the substrate via reactive ion etching (RIE) with a nominal etch depth set to 150 nm. The Ti deposited on the Si

surface act as a metallic mask that protects locally the surface from the etching. The RIE technique was employed due to its very anisotropic etch profiles that allow us to form nano and micrometric Si "columns" with fairly right angles on their borders (See Figure 3.37).

- *Step 7*: The wafer is immersed on a buffered hydrofluoric acid (HF) to remove the Ti mask.

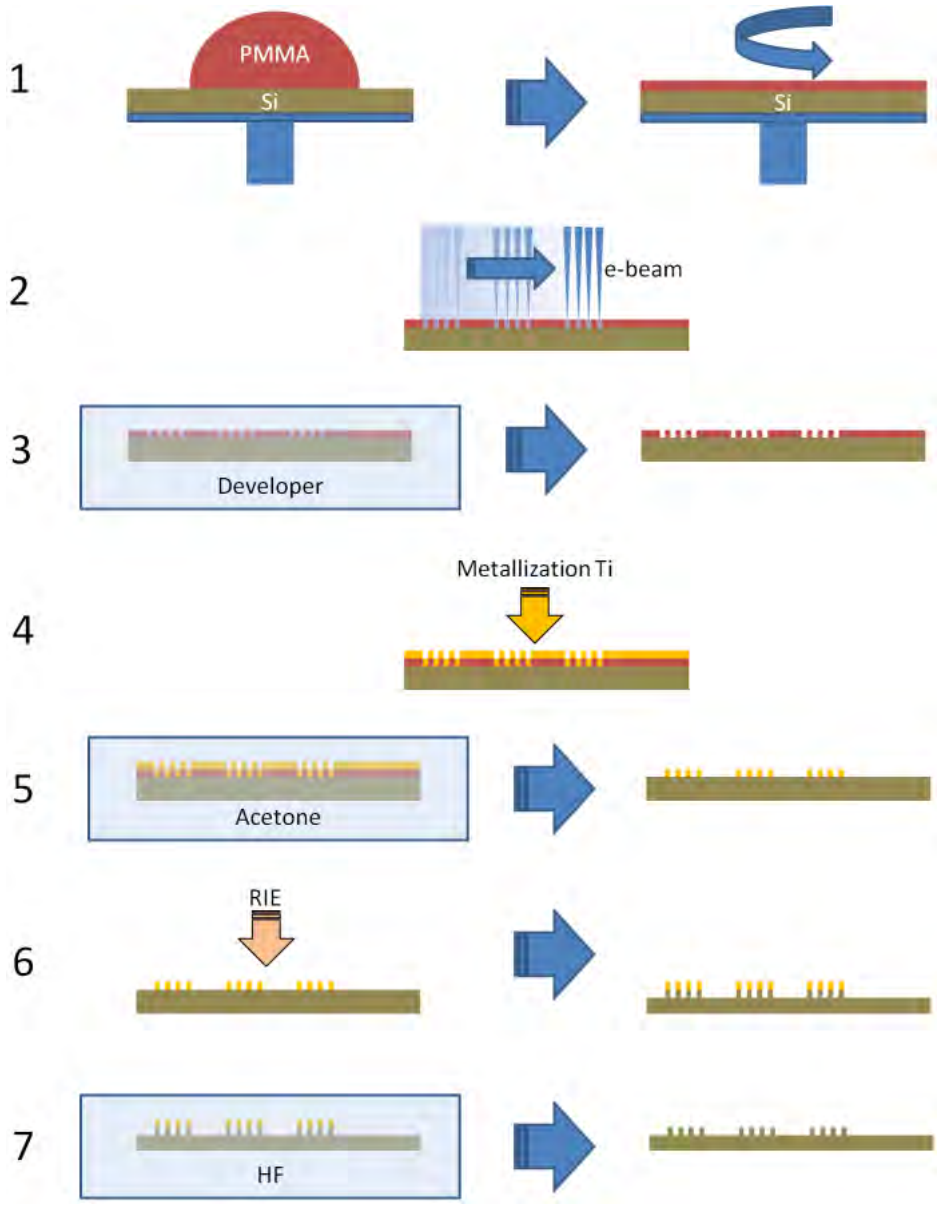

Figure 3.36: E-beam lithography and reactive ion etching processes employed for the Si master of nanopatterned PDMS stamps

A Si master cannot be employed directly after its fabrication for the reticulation of PDMS stamps. First, it is necessary to depose an anti-adhesive layer for assuring that the PDMS, once reticulated, can be released (several times) from the Si surface without

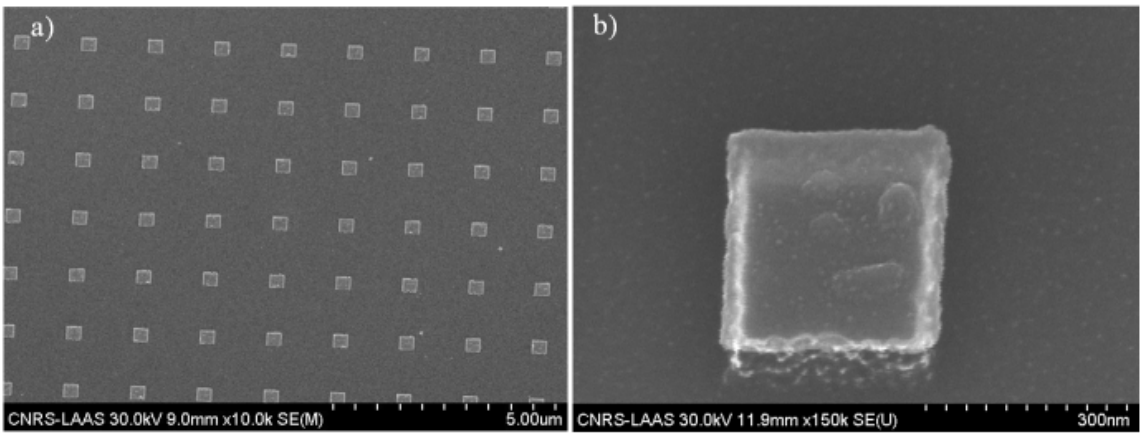

Figure 3.37: **a)** SEM image of an array of 300 nm lateral size and 1.5 μm pitch. **b)** SEM image with a tilt of 30 ° of one of the dots from **a**.

doing any damage to the master. To this purpose, we have employed a silanization treatment with the molecule octadecyltrichlorosilane (OTS). The OTS molecules are able to bind in a covalent manner to the Si-OH groups present on the surface of a Si wafer (see Figure 3.38). Due to the carbonated chain, not saturated and inert of the OTS molecules, it is not possible to have a chemical bond between the surface of a Si master treated with OTS and PDMS. Thus, after the wafer has been immersed in the buffered HF solution (step 7 of the fabrication of the Si master), the substrate is put into an oxygen plasma chamber (5 minutes, 400 W, 1L/min) in order to create a homogeneous layer of Si-OH groups on its surface. Then, the wafer is immersed during 3 minutes in a solution of OTS in trichloroethylene (1% volume). After this, the substrate is removed and rinsed several times with trichloroethylene in order to remove all the molecules that did not bond covalently and then dryed with a N_2 flow.

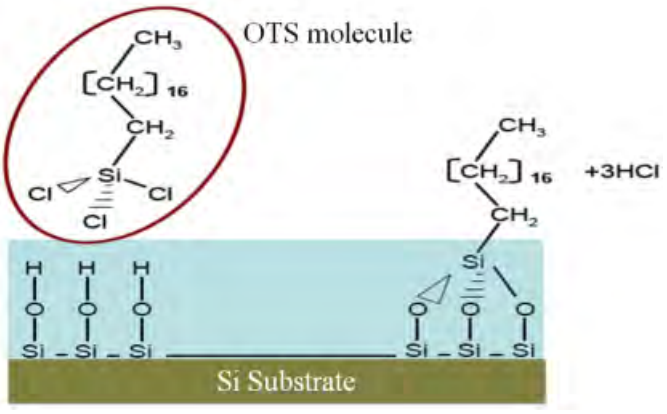

Figure 3.38: Silanization of a Si substrate with an OTS molecule.

In the Nanobiosystems group, the polymer of predilection for the fabrication of the stamps is the PDMS Sylgard® 184 of Dow Corning (Figure 3.39a). It is an elastomer inert, hydrophobic, and biocompatible. In the same manner as most of the Polydimethylsiloxanes, the Sylgard® 184 is prepared by mixing (in a 10:1 weight

ratio) a base containing the PDMS oligomers and a reticulation agent (composed by platinum catalyst). Once the mixture is prepared, it is degassed for a few minutes until all air bubbles are eliminated; then, the PDMS is spread over the Si master and the ensemble is left to cure in an oven at 333 K, typically for 12 hours. Finally, stamps of $\approx 1x1$ cm^2 are cut and peeled from the Si master (Figure 3.39b).

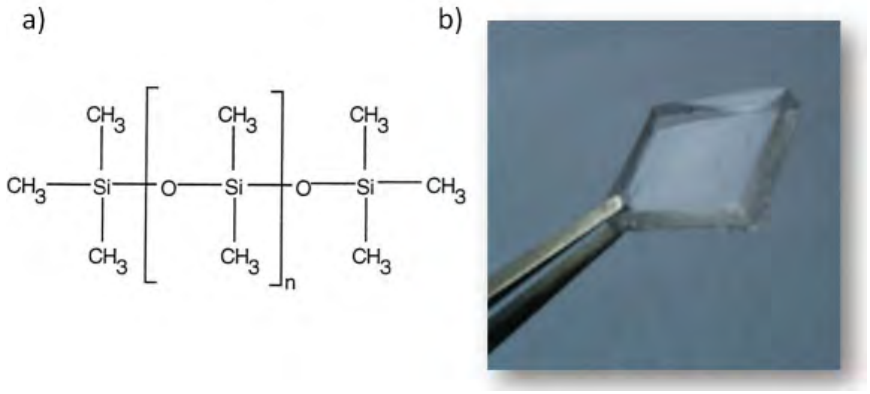

Figure 3.39: **a)** Scheme of the PDMS oligomer. **b)** PDMS stamp obtained from a Si master.

3.4.2.3 Results

It should be kept in mind that capillary-convective directed assembly experiments were conceived originally to organize nano-objects that were suspended in polar solvents and its parameters had been optimized to work in water. However, the triazole-based nanoparticles are not very stable in polar solvents (and particularly in water). For this reason, we were forced to make different attempts of directed assembly from nanoparticle powder suspensions in non-polar solvents such as cyclohexane, octane and toluene. However, by changing the solvent where the SCO particles were suspended, we faced a different issue involving the compatibility of the PDMS with non-polar solvents. It is well known from literature that this type of polymer swells (sometimes dramatically) when it is put into contact to a non polar solvent [131, 139]. Figure 3.40a illustrates how a PDMS stamp deforms a few seconds after a drop of toluene is deposited on its surface. Typically, a directed assembly experiment can take several minutes (speed of the stage 1 μm/min) which makes impossible to perform it following the original protocol. Thus, we partially counteracted these effects employing thick ($\approx$ 4 mm), highly polymerized PDMS stamps. (The PDMS was left to reticulate in the oven during 48 hours, this increased its rigidity.) Figure 3.40a shows one of these thick stamps under the same experimental conditions as its thinner counterpart. Additionally, to decrease the deformation during the experiments, the back side of the stamps was fixed with a thin double side Scotch tape to a Si substrate (Figure 3.40b).

Another parameter of the directed assembly protocol that we altered was the step for the transfer from the stamp to the Si substrate by solvent mediation. As reported by Cerf *et al.* [138], they improved the efficiency of the transfer by previously functionalizing with (3-Aminopropyl)triethoxisilane (APTES) the surface to which the

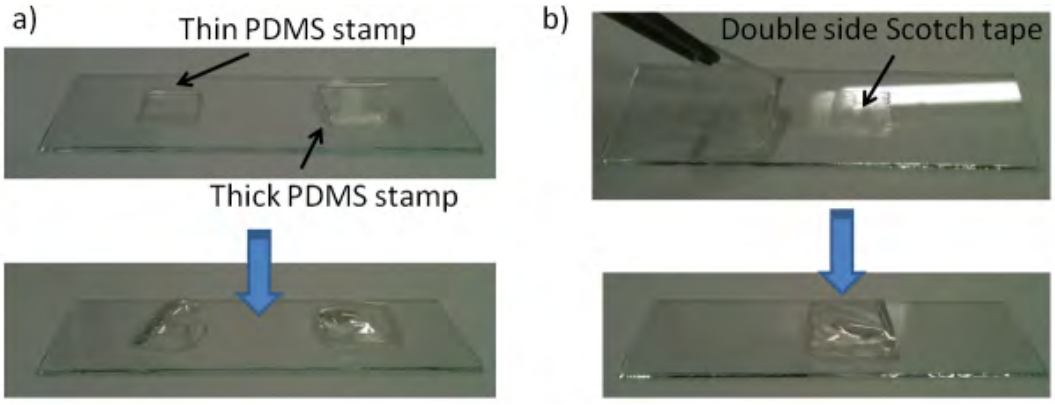

Figure 3.40: **a)** PDMS swelling effect in a thin (left) and a thick (right) PDMS stamp before and after a drop of Toluene is deposited on their surface. **b)** Thick and highly polymerized PDMS stamp with its backside fixed with a double side Scotch tape to the substrate for reducing its overall deformation after exposure to toluene.

array was transferred. This molecule was employed because it charges positively the Si or glass surface where it is attached and the objects that they ussually worked with were negatively charged. In our case, we remarked that the material on the surface of the PDMS stamp was not successfully transferred to Si surfaces with this type of functionalization. The nanoparticle powder when suspended in a solvent displayed a preference for negatively charged surfaces. Figure 3.41 shows two optical dark field images captured from a Si surface without a treatment **(a)** and negatively charged with a O_2 plasma treatment **(b)** after a drop of ethanol solution (1 mg/ml) of $[Fe(NH_2trz)_3](OTs)_2$ nanoparticles was deposited on it. In the first case (untreated surface) it is possible to observe that the particles tended to accumulate in the outer part of the drop as it dried and in the end, a fringe with a high density of particles was formed with almost no nanoparticles left in the middle. However, when the surface was activated with O_2 plasma, a rather homogeneous deposition of particles was observed along the whole surface that the drop covered.

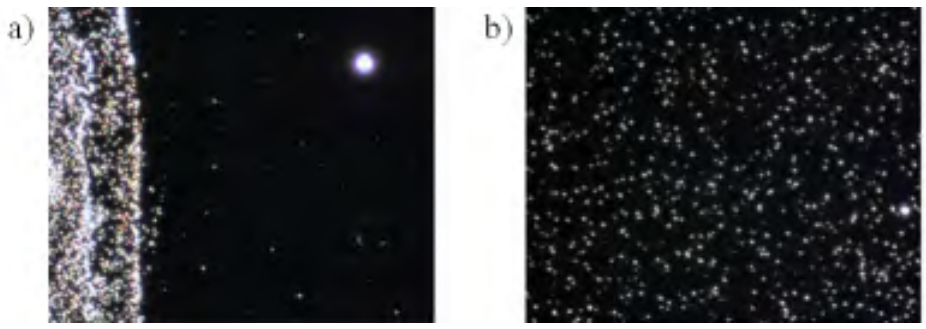

Figure 3.41: Dark field images of a Si surface without a treatment **a)** and negatively charged with a O_2 plasma treatment **b)** after a drop of ethanol solution (1 mg/ml) of SCO nanoparticles was deposited on it.

The first set of attempts of performing a capillary-convective directed assembly were done with $[Fe(NH_2trz)_3](OTs)_2$ nanoparticles doped with alizarin red (strategy #2, chapter II) and suspended in octane or cyclohexane. The concentration of the solution was fixed to $\approx$ 0.0625 mg/ml where the suspensions seemed to be stable

within the timeframe of one experiment ($\approx$ 20 minutes), the speed of the step motor was set to 1 μm/min and the temperature of the substrate to 298 K. Figure 3.42 displays a typical result of one of these experiments obtained with a PDMS pattern of 370 nm lateral size cavities separated 1.5 μm. After the transfer process from the PDMS stamp to a Si substrate, the patterns seemed to be successfully assembled and transferred when observed in optical dark field and bright field (Figure 3.42a and b, respectively.). However, when the samples were observed in luminescence mode, absolutely nothing was detected. In order to obtain more information about what was deposited, the sample was examined in AFM and SEM microscopies (Figure 3.43). The AFM observations revealed that the dots depicted in optical microscopy had an average height of 25 nm; which is much smaller than the size of these particles (50 - 300 nm). Additionally, SEM images did not display any particle on the surface. The low electron signal detected from the dots indicates the absence of heavy atoms (such as Fe); this suggests that no SCO material had been deposited on the arrays.

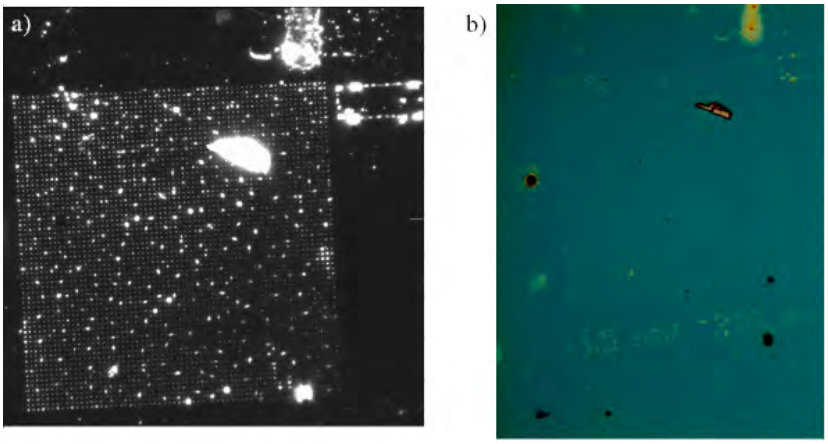

Figure 3.42: Optical dark field **a)** and bright field **b)** images from a Si substrate of one of the arrays transfered by solvent mediation from a PDMS stamp of 370 nm lateral size cavities separated 1.5 μm after a capillary-convective directed assembly performed with an octane solution of $[Fe(NH_2trz)_3](OTs)_2$ nanoparticles.

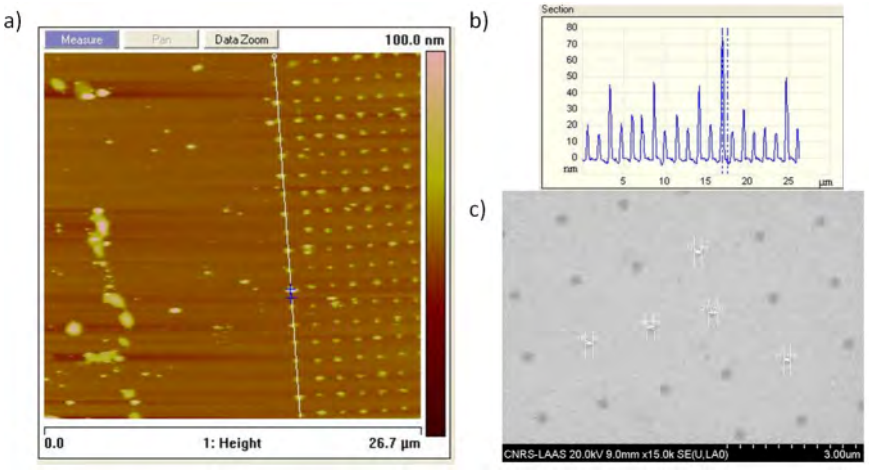

Figure 3.43: **a)** AFM image (27 μm^2) of one of the borders of the array observed in Figure 3.42. **b)** Height profile along the line in **a**. **c)** SEM image from a region of the same array studied in **a**.

A second approach was performed employing toluene as a solvent for the nanoparticle suspension of the same $[Fe(NH_2trz)_3](OTs)_2$ nanoparticle powder. Comparatively to cyclohexane and octane, toluene produces less swelling effect on the PDMS. (Swelling ratio cyclohexane $\approx$ 1.33, toluene $\approx$ 1.31 [139].) The other experimental parameters were not modified for this set of experiments (speed of the step motor, temperature of the substrate, nanoparticle concentration). These samples were studied in luminescence mode (excitation @450 nm, emission @550 nm), purged for 30 minutes at 353 K and cycled between 223 K and 343 K in a controlled N_2 atmosphere.

In contrast to our previous samples, we were able to detect luminescence form the arrays deposited under this experimental configuration. However, it was not possible to observe a modulation of the luminescence that could be associated to the SCO within the temperature range studied. Figures 3.44 and 3.45 show the luminescence image from two different samples and the respective thermal variation of the luminescence of one of the ROIs schematized on their luminescence image. In general, either a flat or decreasing profile (thermal quenching) of the luminescence was obtained for the dots obtained in this type of samples as the temperature of the sample increased. It seems that the SCO material deposited is affected during the deposition process. Given the fact that $[Fe(NH_2trz)_3](OTs)_2$ nanoparticles are not so stable in ethanol, one hypothesis is that the SCO material is decomposed (oxidized) during the ethanol mediated transfer process when the stamp and the substrate are put in the oven in presence of the solvent. It is worth to note that this type of experiments led to an organization of SCO objects in the area of the patterns in the PDMS stamp; however, SCO material was also deposited in other parts of the surface of the stamp. Thus, the transfer of the patterns was not clean, but instead it was accompanied by random material localized everywhere around the patterns (See Figure 3.46)

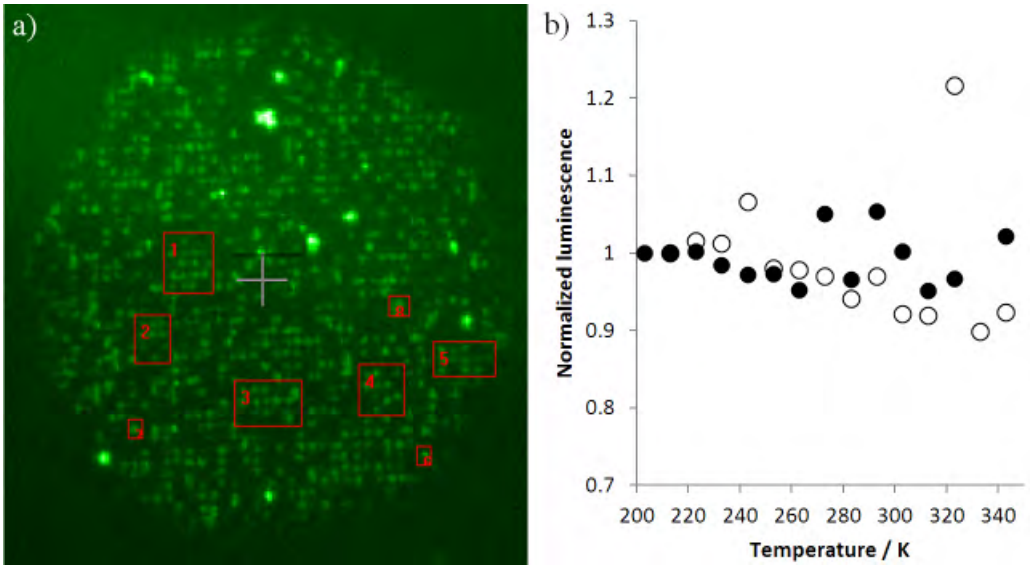

Figure 3.44: **a)** Fluorescence microscopy image of a particle array transferred from a stamp with a pattern of 500 nm lateral size and 1.5 μm pitch after a capillary-convective directed assembly from an alizarin red doped $[Fe(NH_2trz)_3](OTs)_2$ nanoparticle suspension in toluene. **b)** Typical normalized thermal variation of the luminescence emitted by the dots in **a**. (Open and closed symbols for heating and cooling modes, respectively.)

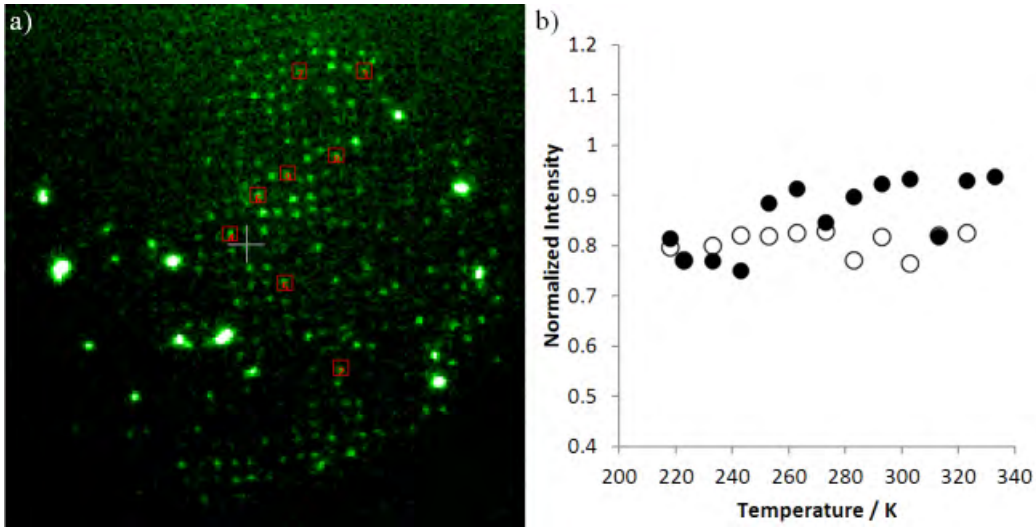

Figure 3.45: **a)** Fluorescence microscopy image of a particle array transferred from a stamp with a pattern of 300 nm lateral size and 1.5 μm pitch after a capillary-convective directed assembly from an alizarin red doped $[Fe(NH_2trz)_3](OTs)_2$ nanoparticle suspension in toluene. **b)** Typical normalized thermal variation of the luminescence emitted by the dots in **a**. (Open and closed symbols for heating and cooling modes, respectively.)

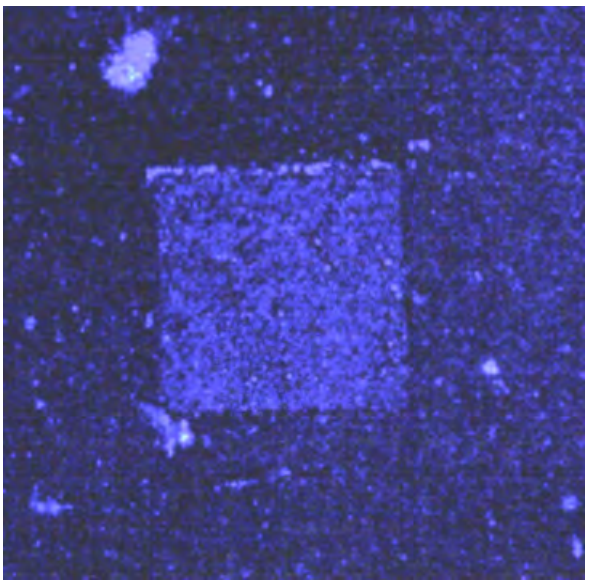

Figure 3.46: Optical dark field image of one of the arrays from a Si substrate transfered by solvent mediation from a PDMS stamp after a directed assembly from a SCO nanoparticle suspension in toluene.

A third set of experiments was carried out with the particles of $[Fe(hptrz)_3](OTs)_2$ synthesized in water in prescence of PEG (strategy #3, chapter II). These particles present an enhanced insolubility in polar media due to the long alkyl chain of the *hptrz* ligand and as a result, they have lower chance to decompose when suspended in a polar solvent such as ethanol. For this reason, we employed an ethanol solution of this nanoparticle powder doped with acridine orange (0.25 mg/ml) with a few crystals of ascorbic acid to further avoid the risks of oxidation during the assembly process. Due to the higher average size of these particles ($\approx$ 300 nm), a different stamp with

cavities of 4 μm in lateral size and 20 μm pitch was employed. Figure 3.47a displays an image in fluorescence mode taken at the edge of an array successfully transferred to a Si substrate. In this case the transfer was cleaner compared to our previous experiments; no additional material was deposited in the vicinity of the pattern or in between the dots despite their important separation. The thermal variation of the luminescence for this sample during a cycle between 278 and 338 K is shown in Figure 3.47b. Here, a variation of the luminescence can be depicted between 298 and 313 K during the heating and cooling modes that resembles to a SCO curve and is in agreement with the transition temperature measured for the nanoparticle powder in reflectivity. However, the modulation during the cycle is very weak, it is affected by photobleaching and it displays a general decrease of the luminescence intensity as the temperature increases. In spite of the improvement reached under this particular configuration, the organization of SCO nanoparticles by this method remained very difficult and the yield of exploitable samples was very low. For further progress it would be necessary to synthesize nanoparticles which are stable in water and ethanol for longer periods.

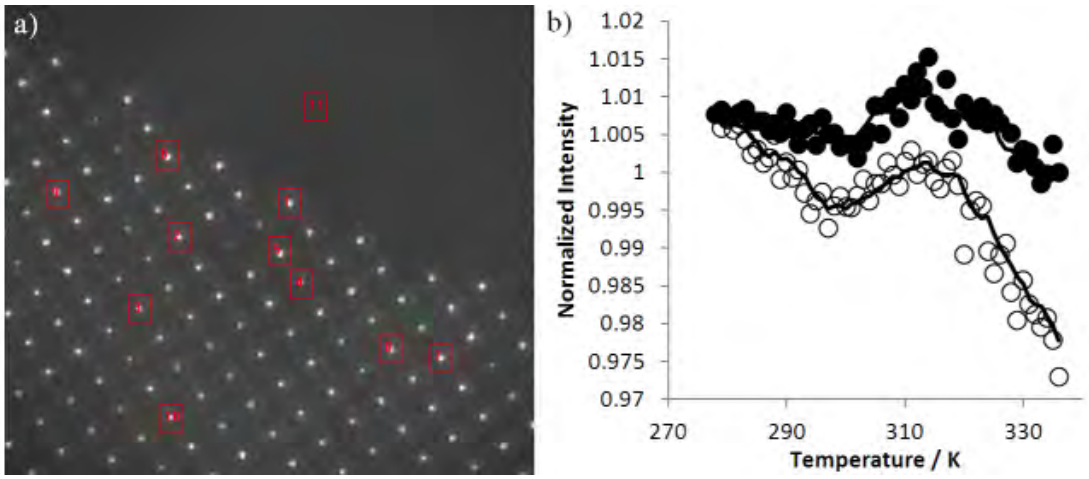

Figure 3.47: **a)**Fluorescence microscopy image of a particle array transferred from a stamp with a pattern of 4 μm lateral size and 20 μm pitch after a capillary-convective directed assembly from an acridine orange doped $[Fe(hptrz)_3](OTs)_2$ nanoparticle suspension in ethanol. **b)** Normalized thermal variation of the luminescence emitted by the dot in ROI4 from **a**. (Open and closed symbols for heating and cooling modes, respectively.)

3.4.3 Random Assembly on a nanopatterned Si master

A different approach that we have employed in order to reduce to some extent the complexity of our problem by avoiding the organization of our nanomaterials has been the random assembly on a substrate with some embedded marks that are visible in all characterization stages. In this manner, even though the materials are not really organized, we can use the relative position of randomly positioned objects with respect to these reference marks to locate them independently of the characterization technique. To do this, we employed clean nanopatterned Si masters developed for generating stamps for the capillary-convective directed assembly (Section 3.4.2). The

patterns in these substrates provide easily recognizable marks in optical microscopy and the arrays constituted a grid built with nanometric precision where it is possible to navigate even at high magnifications in SEM. Furthermore, these marks do not interfere with our measurements in fluorescence unlike marks on the substrate done with inks, which are usually luminescent.

In this approach, we employed the doped nanoparticles synthesized in water in presence of PEG from strategy #3 (Chapter II) since they seemed to be the generally more stable particles when suspended in a solvent and less prone to agglomeration. The procedure for deposing the particles is schematized in Figure 3.48. We put a drop of an ethanol suspension of the particles (0.125 mg/ml, a few minutes in ultrasonic bath) on top of the patterns zone. After a couple of minutes, the drop is driven away with an argon flow to avoid excessive precipitation of the particles on the surface and an excessive expousure to ethanol. The grid besides working as a reference, it can also play the role of a "trap" for objects suspended in the drop. After this procedure, we can obtain a few SCO objects deposited on the different grids of the Si master.

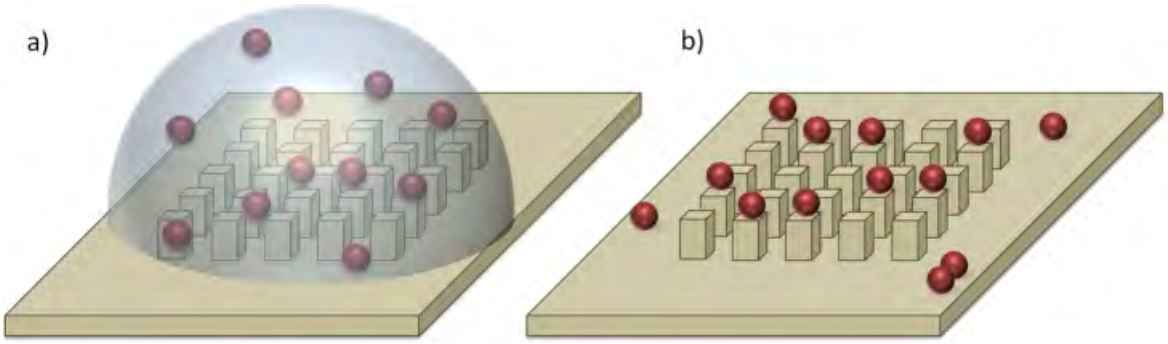

Figure 3.48: Random assembly on a nanopatterned Si master. **a)** ethanol suspension of SCO nanoparticles deposited on the nanopatterned region of the Si master. **b)** Once the solvent is removed by an argon flow, a few SCO particles remain on the patterns.

The characterization of these samples is performed first in luminescence mode under a N_2 atmosphere with a 50X magnification objective. Then, an optical dark field (and sometimes bright field) image is taken in the same place of observation in order to establish a link between the two of them. Since the Si patterns are not necessarily observable in luminescence mode, the dark field or bright field images will give complimentary information in order to localize a particular target in the substrate during other characterization steps. It is worth to note that a particular array of the Si master is wider than the field of view of the detector while working with a X50 objective magnification. For this reason we focused our attention on the corners of the array; this way, we can define the origin of our observations on the first dot of the corner in the array.

Figure 3.49 shows an optical dark field (a) and luminescence (b) image of acridine orange doped particles deposited on Si substrate with a nanopatterned array (150 nm height, 300 nm lateral size and 1.5 μm pitch). As we can see in a), some bright luminescent spots, associated to SCO nanomaterial can be found within the field of view. At the same time, it is also possible to observe the array patterned on the

substrate. These weak signals can be associated to acridine orange molecules that have detached from the particles and deposited on the surface; however, this weak luminescence ends up disappearing (possibly due to photobleaching) as a thermal cycle is performed on the sample.

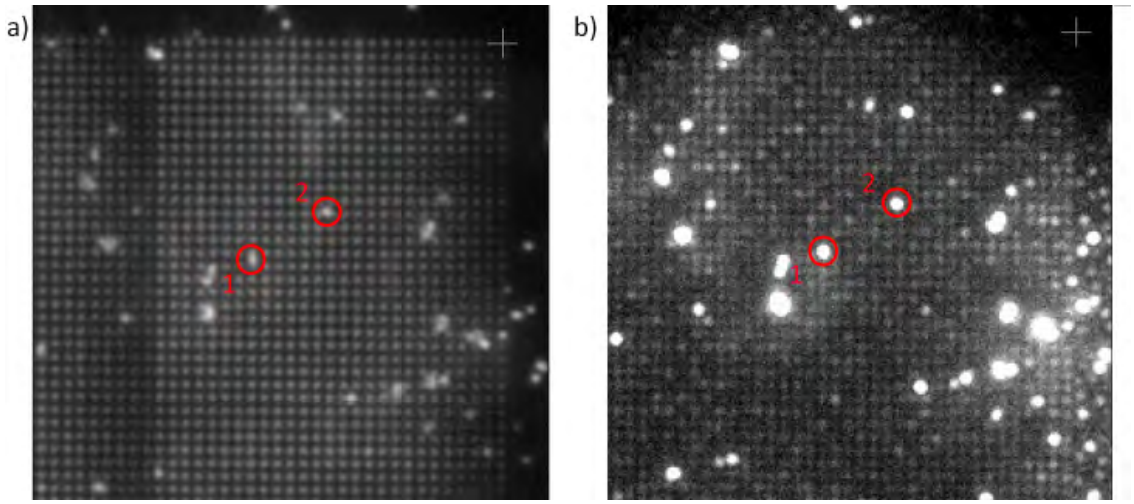

Figure 3.49: **a)** Optical dark field microscopy image of a Si array of 300 nm lateral side columns and a pitch of 1.5 μm after a random deposition of SCO nanoparticles doped with acridine orange. **b)** Fluorescence microscopy image of **a**. Red circles represent two ROIs to be characterized.

The thermal variation of the luminescence as a function of temperature for ROI1 and ROI2 is shown in Figure 3.50. In both cases the plot reveals a small hysteresis defined by a rather abrupt modulation of the luminescence in the cooling and heating branches ($T_{1/2} \downarrow \approx 309$ K and $T_{1/2} \uparrow \approx 312$ K for both ROIs) that closely matches our previous observations of the same type of powder in luminescence and reflectivity modes. As previously observed for this type of particles, the first part of the cooling branch does not match the last part of the successive heating branch. Additionally, due to the low level of the luminescence, higher excitation light intensities were employed for this type of experiments as well as higher numerical aperture objectives (X50, NA = 0.5); as a result, higher photobleaching rates were observed on this samples. Additionally, it should not be forgotten that the particles were suspended in ethanol, although for a short time, and it is not clear if the particles were deposited on the surface unharmed. As for the morphological characterization, we employed SEM to study the same dots that we characterized in luminescence (Figure 3.51). From these observations we can conclude that this method leads to a fairly clean deposition of SCO nano-objects (surface of the substrate is not poluted). We found that ROI1 corresponded to a small agglomerate of SCO nano-objects and ROI2 to a single one.

With this type of experiments, we were able for the first time to perform a detection of the SCO of a small number of nanoparticles *via* fluorescence detection and morphologically characterize the same objects with SEM observations. However, this technique presents the drawback of a very low yield of isolated particles. Further work involving a meticulous study of different parameters such as the concentration of SCO material in the solution, different type of solvents or a selective functionalization of the substrate may increase the effectiveness of this method.

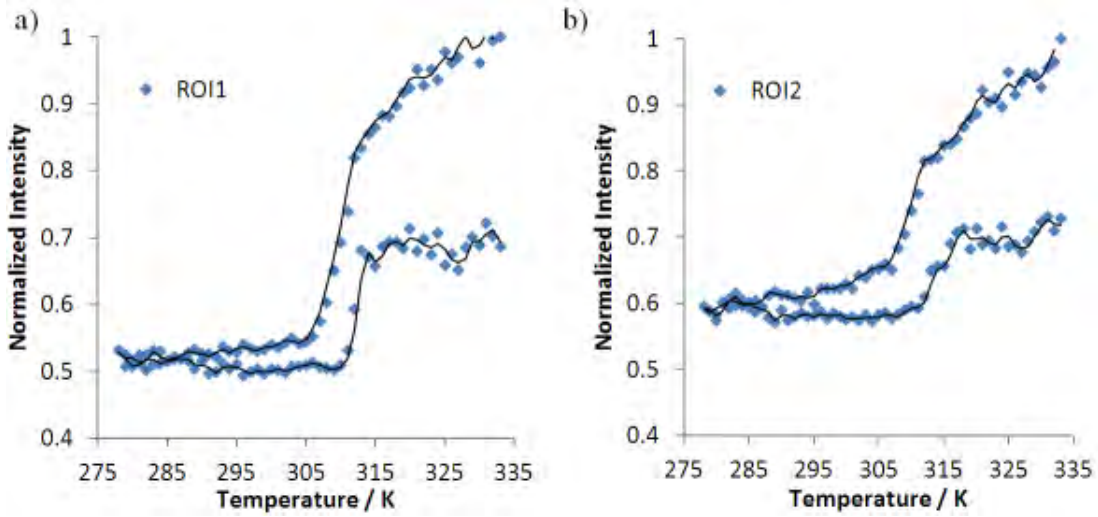

Figure 3.50: Normalized thermal variation of the luminescence in **a)** ROI1 and **b)** ROI2.

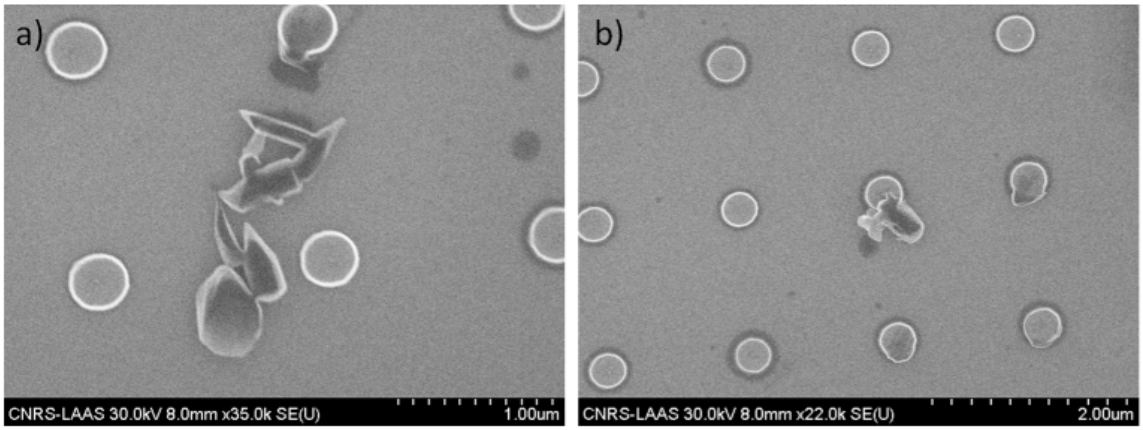

Figure 3.51: SEM images for **a)** ROI1 and **b)** ROI2.

3.4.4 Synthesis of SCO objects in PDMS stamps

Given the difficulties that we had in in order to organize SCO nano-objects with capillary assembly (possible instability of the particles when suspended in polar solvents or the possible detachment of the luminophore from the particle), we decided to employ a different approach to the problem. In general, a common feature of the syntheses of SCO nano-objects is the use of an element that constrains or limits the growth of the complex during its formation (reverse micelle, stabilizing polymer, a porous matrix, *etc*). Here, we employed the nano-patterns of our PDMS stamps as micro/ nano - reactors for the organized formation of nano-objects of the SCO complex $Fe(hptrz)_3](OTs)_2$. To do this, two solutions were prepared: (1) 7.5 mg $Fe(OTs)_2 \cdot 6H_2O$, 1 crystal of ascorbic acid, 5 ml H_2O (solution #1) and (2) 15 mg of *hptrz*, 14 mg of p-toluenesulphonic acid, 0.1 ml of ethanol and 0.04ml of 0.1% rhodamine 110 aqueous solution (solution #2).

The scheme of the procedure is shown if Figure 3.52. At the beginning, a nanopat-

terned PDMS stamp is taken and placed with the patterns on the upper side (a). Then, a drop of solution #1 is deposited on the stamp (b) and the excess is removed by capillarity while putting next to the drop a piece of paper (far from the patterns). In this manner, the cavities of the stamp are filled with the Fe precursor (c). After this, a drop of solution #2 is deposited over the patterns (d) and the excess is removed rapidly as in the first step. At this point, the SCO complex should be formed inside the cavities of the stamp (e). At the end, the patterns are transferred following the same procedure as in the microcapilary directed assembly approach. A drop of ethanol is deposited on a Si substrate and the stamp is placed on top of it and then the ensemble is put into an oven at 348 K for a few minutes and then the stamp was peeled off.

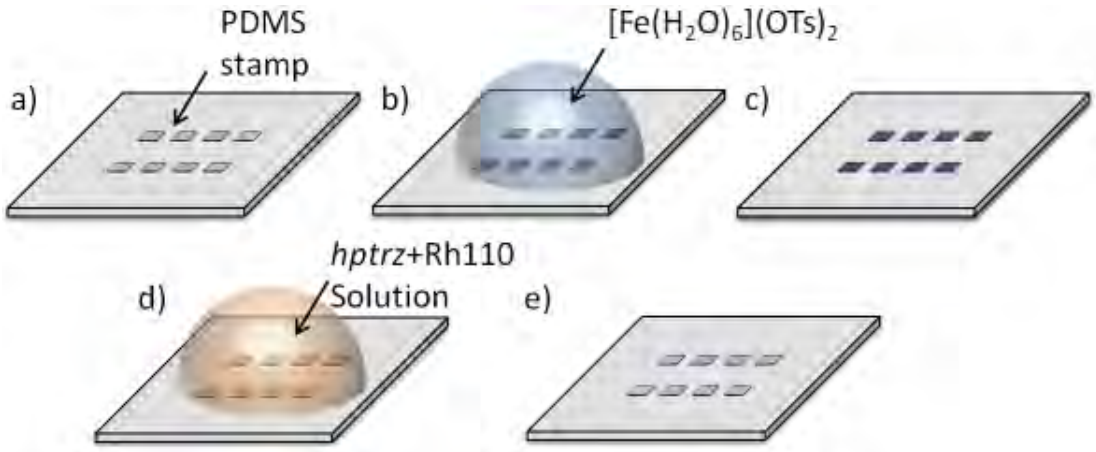

Figure 3.52: Synthesis of SCO objects in PDMS stamps. **a)** Nanopatterned PDMS stamp with cavities. **b)** A drop of $[Fe(H_2O)_6](OTs)_2$ solution is deposited on the nanopatterned region of the stamp. **c)** The excess of solvent is removed leaving a few traces of the solution in the cavities of the stamp. **d)** A drop of the ligand *hptrz* and rhodamine 110 solution is put on the surface of the stamp and triggers the formation of the complex in the patterns. **d)** The excess of the solution is removed and an array of doped SCO nano-objects is ready for a solvent mediated transfer to a Si substrate.

An SCO array of objects with 500 nm in lateral size and 1.5 μm pitch synthesized by this method was studied in luminescence mode as a function of temperature during two cycles. The fluorescent microscopy images allowed us to monitor the luminescent response of several objects of the array (Figure 3.53a). By plotting the mean value of a ROI that encircled one of this dots (8X8 pixel region) as a function of temperature, a variation of the luminescence and also a small hysteresis was typically observed in the same temperature range where the SCO takes place, very close to our observations performed in the thin films for $[Fe(\textit{hptrz})_3](OTs)_2$. A similar behavior was obtained for all the objects of the studied array (for example, Figure 3.53b). Here for the first time, we were able to monitor the SCO several isolated micro objects employing luminescent detection. However, this synthetic approach was very difficult to reproduce. Additionally, it was not possible to clean properly the surface around the patterns of the stamp and this lead to a deposition of important amounts of macroscopic material everywhere in the sample. This situation did not allow us to perform other types of morphological characterization such as SEM or AFM due to the difficulty for finding the patterns.

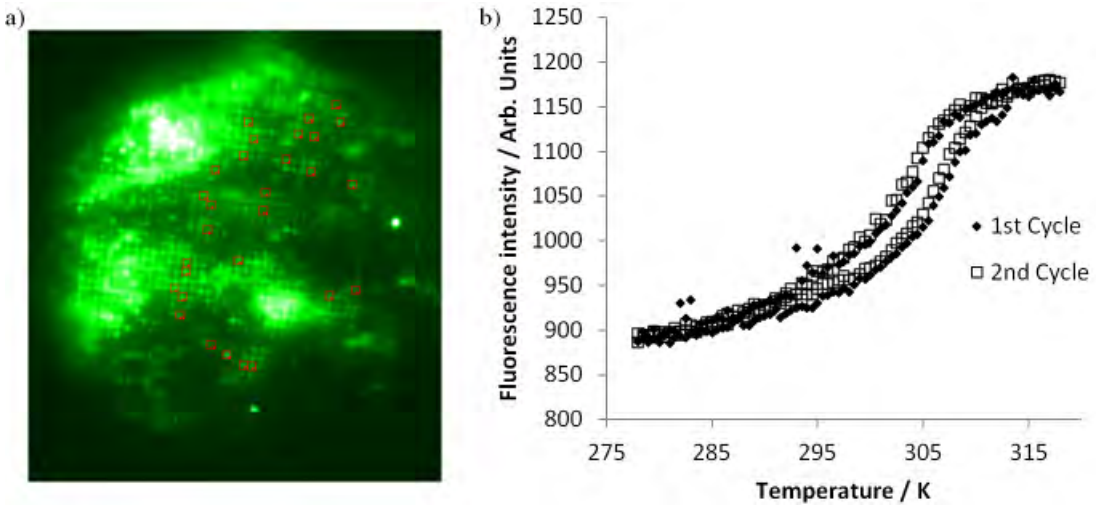

Figure 3.53: **a)** Fluorescence image of an array of SCO dots of 500 nm lateral size and 1.5 μm pitch synthesized in a PDMS stamp and transferred to a Si substrate. **b)** Typical thermal variation of the luminescence emitted by one of the dots in **a**.

3.4.5 Soft Lithographic Nanopatterning of SCO materials with PDMS stamps

In order to go one step further in the observation of the $[Fe(hptrz)_3](OTs)_2$ chloroform system developed in section 3.3.2 at even smaller dimensions, we have developed a soft lithography approach, derivate of the solvent-assisted micromolding technique (SAMIM) [140]), using the nanopatterned PDMS stamps developed in the previous sections to create arrays of nanodots. Micro- and nanometric patterns have been previously reported employing similar approaches for depositing different forms of SCO materials [129–131]. A key aspect here to obtain nanometric patterns of the pure complex is the successful solubilization of the complex in an appropriate solvent.

For the patterning, 3.5 μl of fresh solution of the complex oligomers in chloroform (synthesized in the same manner than section 3.3.2 mixed with acridine orange (0.8 mol% acridine orange per iron atom) was spread onto a piece of Si wafer. Then, a nano-patterned PDMS stamp was put rapidly on top of the drop and the ensemble was placed into an oven at 353 K for a few minutes. Due to the homogeneous nature of the solution, the moderately high surface tension and high vapor pressure of the chloroform, the solution can easily penetrate into the openings and also evaporate rapidly enough to sweep the excess complex out to the surroundings of the stamp. As a result, nano-droplets of the solution become trapped in the cavities of the PDMS stamp and once the solvent is evaporated, they form nanodots that precipitate in an organized manner onto the Si substrate (Figure 3.54). After use, the stamp can be cleaned with ethanol in an ultrasonic bath and be employed for additional patterning processes.

It is important to note that we have been able to build up submicronic patterns in a reproducible way (See Figure 3.55) in spite of the important swelling effect that chloroform has when it is in contact with PDMS (swelling ratio = 1.39) [139]. We

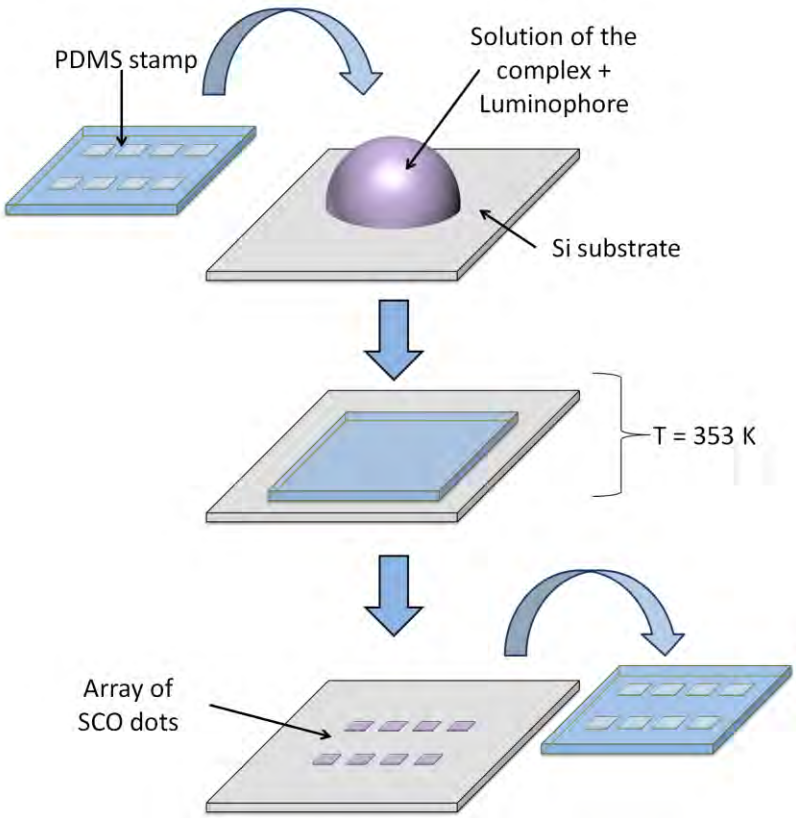

Figure 3.54: Scheme of the fabrication process for the arrays of SCO nanodots with PDMS stamps.

employed thick (around 4 mm thickness) and highly polymerized (rigid) stamps in order to circumvent this problem; due to the small amount of time during which the solvent is in contact with the PDMS before the evaporation, there is no significant or permanent damage of the stamp for several uses. In fact, we believe that this small deformation enhances the adherence of the stamp to the substrate and by the same token the formation of the droplets in the cavities of the stamp.

The size and the shape of the cavities in the PDMS stamps are the two factors that essentially define the geometry of the nanodots. As an example, Figure 3.56a displays a dark field image of a fluorescent nano-dot array obtained with patterns of cavities with 370 nm lateral size, 3 μm pitch and a nominal depth of 150 nm. The AFM profiles of a few dots from the lower right corner of this network reveal that the height of the dots is fairly uniform with an average value of *ca.* 150 nm which is in agreement with the initial height value of the cavities in the stamp (Figure 3.56c). Alternatively, SEM images (Figure 3.56b) give a better idea of the shape of the same nano-dots; here, it can be seen that the average lateral size of the structures ($\approx$200 nm) is less than the nominal size of their respective mold ($\approx$ 370 nm). A priori, this could be attributed to a few causes: first, it could be simply that the size of the patterns in the stamp after demolding is smaller; second, the swelling of the PDMS in contact with chloroform reduces the effective volume for trapping the solution and finally, the quantity of complex in solution flowing into the cavities of the stamp is not enough

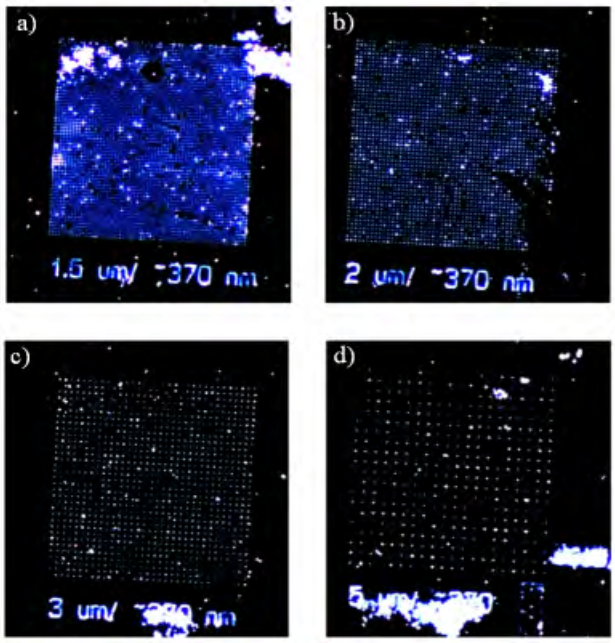

Figure 3.55: Dark field optical microscopy images of nano-dot arrays (370 nm lateral size patterns) of $[Fe(hptrz)_3](OTs)_2$ with different pitches: **a)** 1.5, **b)** 2, **c)** 3 and **a)** 5 μm.

to completely fill them. In fact, we have seen a size reduction effect while varying the lateral size of the motif from 370 nm to 250 nm at a constant complex concentration in the solution; the resulting dimensions of the structure are usually beneath the nominal value of the pattern. (Actually, this observation could be a powerful tool to reach smaller structures beyond the capabilities of the fabrication technique of the Si master.)

The luminescence of the arrays was followed with the same experimental setup employed for the thin film samples except that a higher numerical aperture objective was used in order to improve the signal-to-noise ratio. Figure 3.56b displays a luminescence image of the lower right corner of the array studied in Figure 3.56a. Due to the thermal dilation of the sample holder, correction of the focus had to be applied every few images. Nonetheless, for making a reliable analysis of the luminescence coming from the sample and due to the large quantity of images that each experiment produces, we employed the alignment routine developed in MATLAB® environment for post- treating the stack of images and compensating automatically any drift of the sample during the experiments.

The most important result is that *the fluorescent microscopy images allowed us to follow the variation of the luminescence coming from the individual dots when the temperature was changed*. As shown in Figure 3.56b, the CCD image can be divided in small regions of interest (ROI) each corresponding to a unique dot. Then, by plotting the mean value of the signal against temperature for a given ROI (Figure 3.57), a variation of the luminescence and even a hysteresis can be typically depicted in the same temperature range where the SCO phenomenon is expected to take place. We have been able to detect this type of response also for dots with $\approx$ 150 nm in

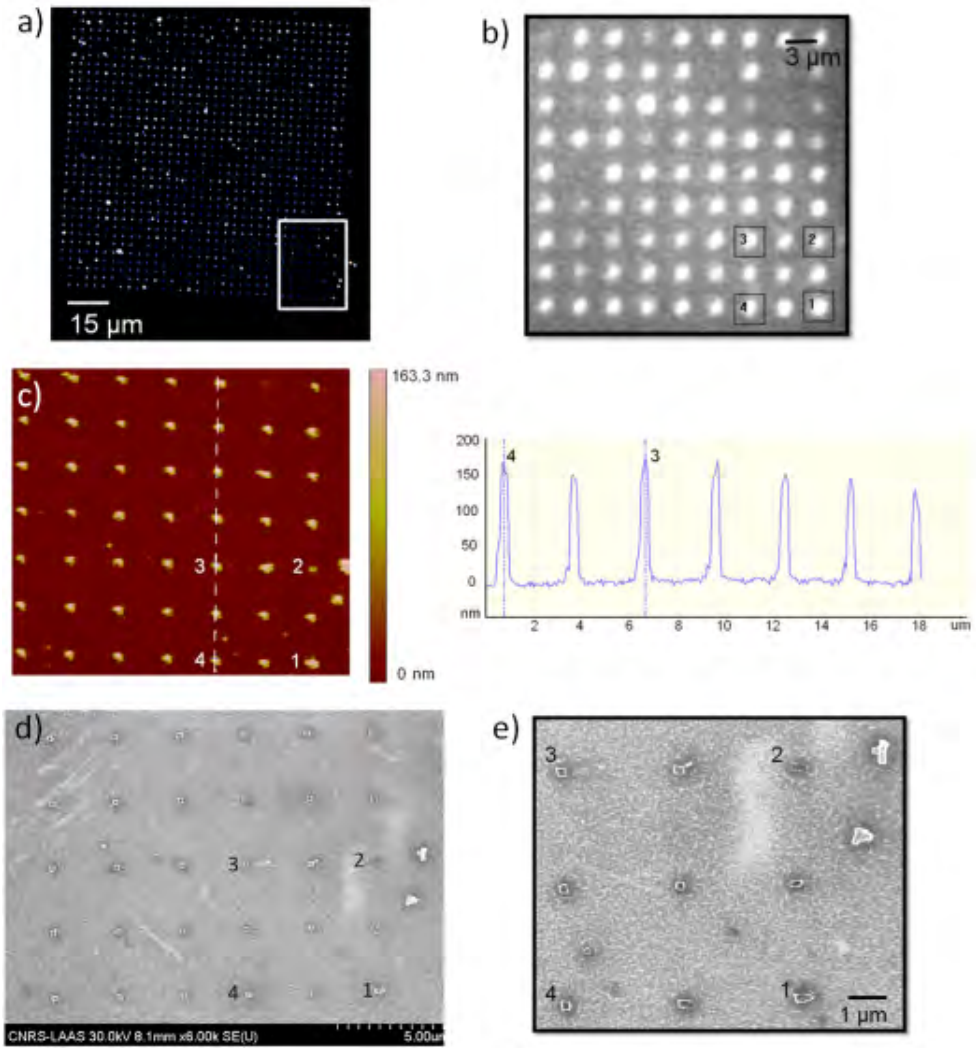

Figure 3.56: **a)** Dark field image of a nano-dot array obtained with motifs of 370 nm lateral size, 3 μm pitch and a nominal depth of 150 nm. **b**) Fluorescence image of the dots in the area highlighted in **a**. **c**) AFM image (21 x 21 μm^2) and a height profile of the luminescent nano-dot array from **b** along the dashed line in the area highlighted in the AFM image. **d,e)** SEM images of the same area of the luminescent array studied in **a,b,c**. Structures with 200 nm of lateral size are typically observed.

lateral size formed from 250 nm PDMS networks (See Figures 3.58 and 3.59). The numbers present in each figure that displays an array of nano-objects refer always to a specific dot of the ensemble, regardless the type of imaging technique employed. In consequence, it is possible to associate to each structure its own geometry and specific SCO behavior.

Here for the first time, we report a platform and methodology to systematically produce with a controlled size, to organize essentially over any substrate, to characterize morphologically and to monitor in a massively parallel way the SCO phenomenon for a large number of isolated single SCO nano-objects via fluorescence microscopy.

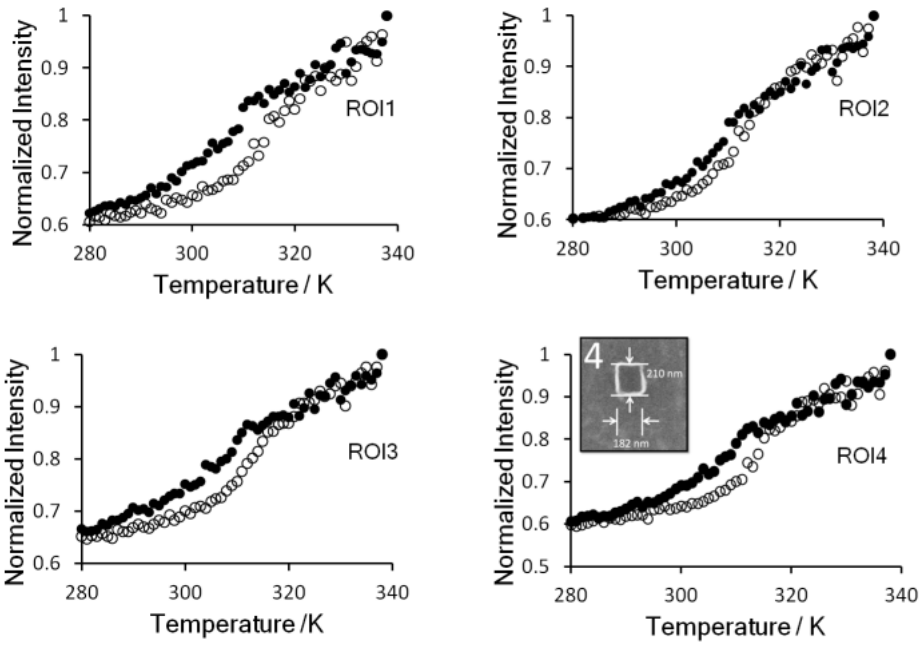

Figure 3.57: Normalized thermal variation of the luminescence at 550 nm of different nano-dots (open and close symbols for heating and cooling modes, respectively) from the area studied in Figure 3.56.

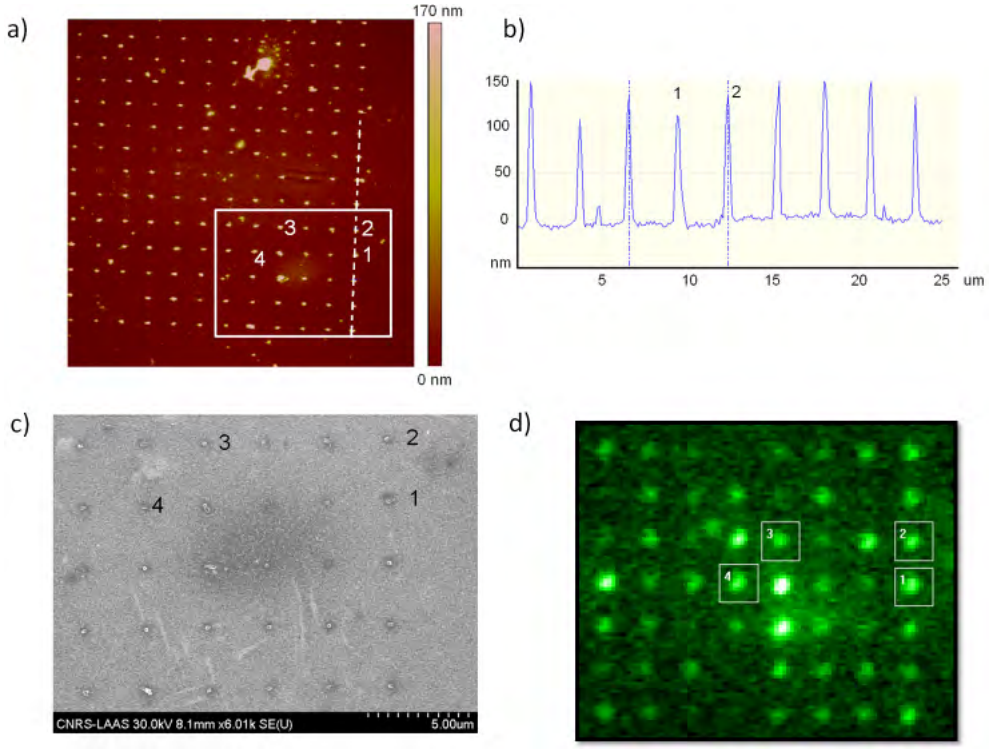

Figure 3.58: **a)** AFM image (40 x 40 μm^2) of a luminescent array of nano-dots obtained with a motif of 250 nm lateral size, 3 μm pitch and a nominal depth of 150 nm. **b)** Height profile along the dashed line in **a**. **c,d)** SEM and fluorescence image of the array in the area highlighted in **a**, respectively.

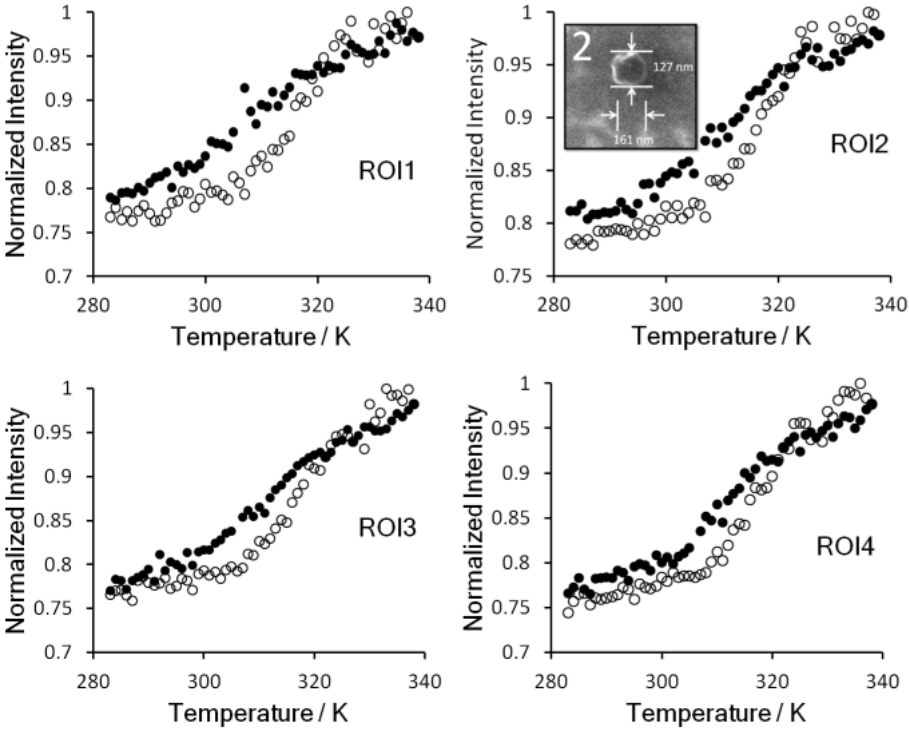

Figure 3.59: Normalized thermal variation of the luminescence at 550 nm of different nano-dots (open and close symbols for heating and cooling modes, respectively) from the area highlighted in Figure 3.58.

To better illustrate the potential of our approach in monitoring SCO at a small scale, undoped versions of these samples were also prepared in order to study them with other optical techniques. We tried - under the same experimental conditions - to perform reflectance measurements (543 nm) for different patterns in bright field and dark field microscopy modes. From these experiments it was impossible to observe any variation that could be attributed to the SCO phenomenon (Figure 3.60).

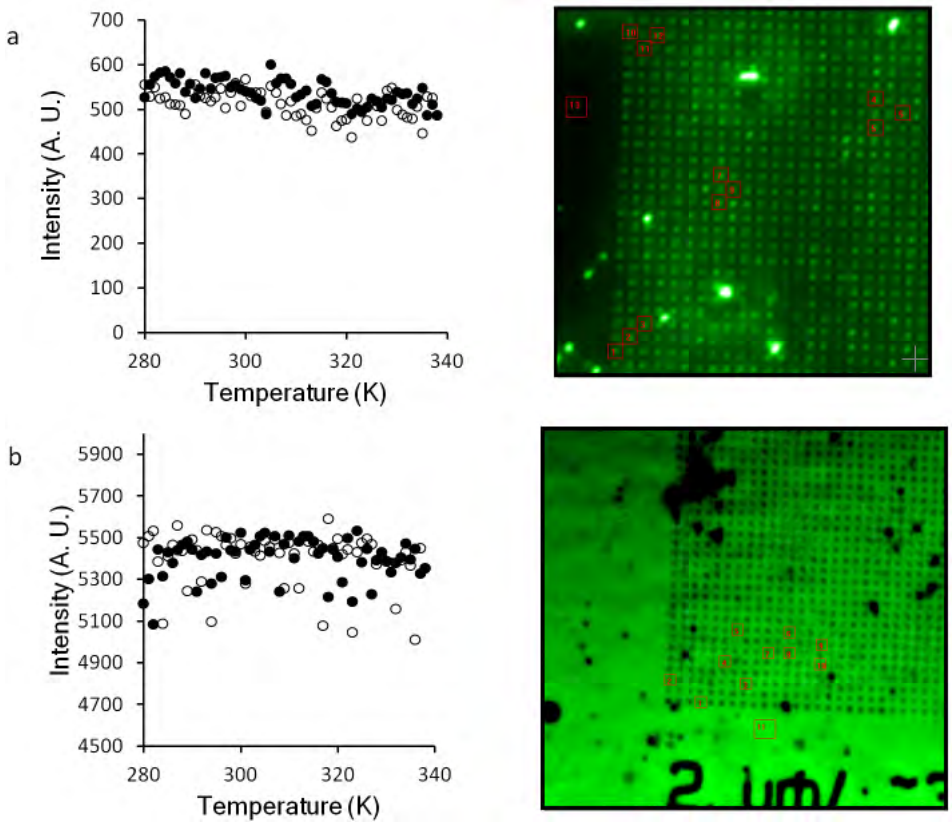

Figure 3.60: Thermal variation of the reflected light intensity measured at 543 nm (FWHM = 23 nm) in **a)** dark field mode for a nano-dot from an undoped array obtained with a motif of 300 nm lateral size and 2 μm pitch and **b)** bright field mode for a nano-dot from an undoped array obtained with a motif of 370 nm lateral size and 2 μm pitch. Open and closed symbols stand for heating and cooling modes, respectively.

Beside temperature changes several other external stimuli (application of an external pressure, light irradiation or exposure to gas/vapor molecules) can also trigger the SCO phenomenon. These possibilites in combination with our luminescent SCO dot arrays can thus be used to develop SCO nanomaterial based optical devices. The SCO phenomenon can be used to detect changes in the physicochemical environment of the compound. For example certain SCO compounds can be used in chemical sensors [51, 52]. To implement this idea in practical devices it may be useful to process the SCO compound as thin films or nano-patterns just as those we are capable to make with our chloroform system. For instance, when the $[Fe(hptrz)_3](OTs)_2$ complex is put in contact with ethanol, its HS state form is stabilized. Figure 3.61 demonstrates this effect: panel **a** shows some $[Fe(hptrz)_3](OTs)_2$ nanoparticle powder in the LS state (violet) at room temperature on a Si substrate. Then, panel **b** displays how the pow-

der pases to its HS state form (white) after a few picoliters of ethanol are deposited in the middle of the powder. As the ethanol evaporates, the system returns gradually to the LS state (panel **e**).

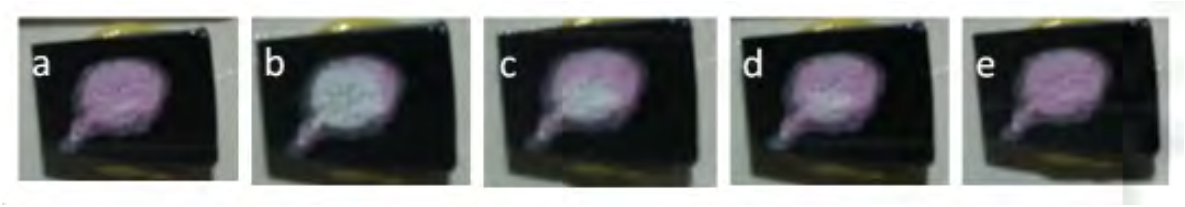

Figure 3.61: **a)** Nanoparticle powder of $[Fe(hptrz)_3](OTs)_2$ in the LS state at room temperature. **b-e)** Change from the HS state (white) to the LS state (violet) as an ethanol drop deposited in the middle of the sample evaporates.

The same property can be monitored with our luminescent SCO nanomaterials. Figure 3.62a shows a nano-object array of $[Fe(hptrz)_3](OTs)_2$ doped with acridine orange. The adsorption of ethanol vapor by the compound at room temperature results in the change of its spin state from LS to HS and should lead thus to an increase of the luminescence intensity of the nano-dots. This is shown in Figure 3.62b where the luminescence intensity of two selected dots is followed as a function of time. During the experiment the sample chamber is successively purged by dry nitrogen gas or by ethanol vapor leading to a significant decrease and increase of the luminescence signal, respectively. This type of experiment provides perspectives thus for real-time gas/vapour monitoring and even for very efficient multiplexing of signals if the nanodot compositions are different. An additional application idea based on luminescent SCO nanomaterials is in the microthermometry field. This idea will be explored in more detail in chapter IV.

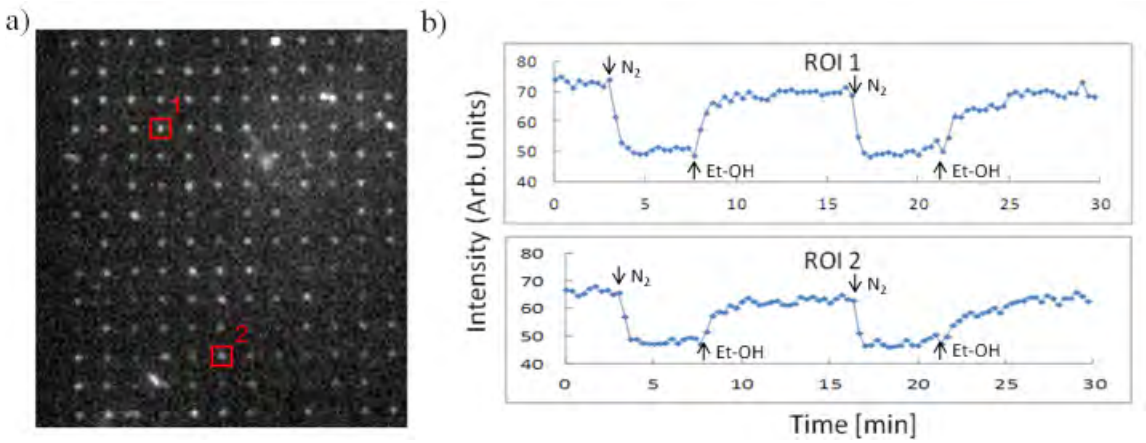

Figure 3.62: **a)** Fluorescent microscopy image (excitation 450 nm, emission 550 nm) of an array of nano-dots (5 μm pitch) of the compound $[Fe(hptrz)_3](OTs)_2$ doped by acridine orange (b) Variation of the luminescent intensity of the nano-dot n°1 (top panel) and n°2 (bottom panel) upon the alternate injection of ethanol vapor and dry nitrogen gas over the luminescent array at room temperature.

3.5 Conclusions

The main objective of the work described in this chapter was to show the potential of the luminescent detection of the SCO phenomenon as a powerful characterization technique down to a single nano-object. To demonstrate this, we dealt on one hand, with the complexity that the detection of the SCO at the small scales involves and on the other, with the isolation of a SCO object in order to perform the measurement in optimal conditions. We explored the organization of SCO nano-materials in two different levels of complexity for the detection: as an intermediate step, *spin coated thin films* of SCO nanomaterials and then, the *isolation of SCO nano-objects* by different methods.

In a first time, we have elaborated good quality thin films of three luminescent doped SCO systems; however, only one of these allowed us to perform a successful luminescent detection of the SCO. The thin films obtained from some of these systems were either too diluted in SCO material (due to the presence of additives) or they were unstable. In order to depose a thin film of non-diluted SCO nanomaterial, we have therefore developed a homogenous chloroform solution of the $[Fe(hptrz)_3](OTs)_2$ SCO complex with a low polymerization degree that can be easily doped with an organic luminophore (such as acridine orange or rhodamine 110). This system has allowed us to spin coat high quality thin films over large surfaces (several cm^2), whose thickness can be tuned from a few tens of nanometers to a few hundred nm. In spite of the negligible absorbance of this type of films in the visible range, *we have been able to follow, for the first time with luminescent detection, the spin crossover phenomenon in thin films even of thicknesses of a few tens of nm.* These results have been corroborated monitoring the charge transfer band of the SCO complex with UV absorption spectroscopy as a function of temperature for undoped versions of the films. We shall note that the advantage of transmittance measurements is that they provide a quantitative determination of the spin fractions, the absorbance being closely proportional to the concentration of the SCO complex present in the sample. Nonetheless, this type of measurements is limited to the study of films with high surface density of SCO complexes displaying HS and/or LS absorption bands of large oscillator strength. Moreover, such intense bands appear usually in the UV spectral range, which may represent a limitation for the implementation of the measurements in conventional microscopy setups or on photonic devices.

The energy transfer in this particular system has been studied in solution (doped with acridine orange) by luminescence lifetime measurements. These studies revealed a low component of collisional quenching and an important contribution of static quenching of the luminescence in this type of solutions. Judging from the little change of the luminescence lifetime measured on the different solutions and the concomitant quenching effects observed, it seems that some of the acridine orange molecules are binding to a second entity (probably the SCO nanomaterial) and as a result a highly efficient non-radiative energy transfer occurs and suppresses almost completely their emission. Preliminary lifetime measurements were performed at room temperature (LS state) and high temperature (HS state) for SCO doped solutions with acridine

orange and rhodamine 110. These experiments indicate that for these luminescent SCO systems in solution there is a non radiative energy transfer between the luminophore molecules and the LS Fe(II) centers of the complex that disappears as it reaches the HS state. Complimentary measurements of the photobleaching rates were performed and it was found that these samples photobleached considerably faster in the HS state (high temperature) than in the LS state (low temperature) indicating a more efficient non-radiative energy transfer in the LS state. However, careful interpretations of these results must be done since the effects of the temperature are not clearly decorrelated from those of the SCO and further experiments can be done to better understand the quenching mechanism(s) of this luminescent SCO material.

The R_0 for a sensitizer - acceptor pair (S-A) with the optical properties of one of our selected luminophores (acridine orange or rhodamine 110) and [Fe(*hptrz*)$_3$](OTs)$_2$ has been also estimated. It was found that a typical organic dye luminophore with a broad spectral overlap with the characteristic *d-d* absorption band of the complex centred at 543 nm presents a R_0 value that spans between 1 and 2 nm. These calculations indicate that while using this type of luminophores it is not necessary to bring them too close to the iron centers; in fact, according to these values if they are at a distance shorter than 0.5 nm ($0.5R_0$), more than 98.5% of the luminescence will be quenched in the LS state. Moreover, with a sensitive enough setup, *these luminophores could be employed to probe the SCO of an iron centre as far as 4 nm* ($2R_0$) obtaining a modulation of the luminescence upon the SCO equivalent to 1.5%.

In the second step, we dealt with the luminescent detection of the SCO properties in a single nano-object and the development of a methodology to correlate these with the morphology of the object under observation. To accomplish this, we identified two key points: (1) we need to be sure that the SCO objects are appropriately dispersed and isolated with a separation higher than the spatial resolution of the optical microscope. (2) Since more than one microscopy set up is employed to perform this type of studies (optical microscope of the detection of the SCO property, SEM and AFM for the morphology), it is imperative to have some sort of road map in the sample to be able to find the object independently of the characterization technique. To solve these issues, we focalized on either organizing the SCO nanomaterials or deposing them into substrates with features that could be recognized in all microscopy techniques.

Our first attempt involved a capillary-convective directed assembly of fluorescent SCO nanoparticles in suspension using nanopatterned PDMS stamps. This method was however, very difficult to implement due to solvent compatibility issues either with the SCO particles or with the PDMS stamps. Triazole-based SCO nanoparticles are not so stable in polar solvents contrary to non polar ones; however, PDMS presents swelling effects when it is put into contact with non-polar solvents. Further work to synthesize additive free nanoparticles of a few tens of nanometers in size, which are stable in water and ethanol for larger periods will be necessary in order to take advantage of this method.

Nonetheless, this directed assembly technique provided the building blocks for the other strategies implemented for the isolation of SCO nano-objects. For example, nanopatterned substrates analog to that employed for generating the PDMS stamps

were successfully used as substrates with embedded grids that worked as references for the different microscopy techniques after a random deposition of SCO nanoparticles on their surface. Here, for the first time, we were able to detect the SCO properties of a single object *via* fluorescence detection and morphologically characterize the same objects with SEM observations. Furthermore, the SCO properties detected in these isolated objects displayed a behaviour that closely matches that found for the powder samples. Even though this technique presented a rather low yield of isolated objects, there is still room for improving it; different solvents for suspending the SCO particles, optimization of the concentration of the suspension, different topologies of the Si substrate combined with selective a functionalization of its surface are the main ideas.

In an attempt of obtaining a high number of organized isolated SCO objects and avoid possible instability of the particles when suspended in solvents, we developed a method for employing the cavities of the PDMS stamps as a constraining element to limit the growth of the SCO material. We were able to transfer some of these arrays to a Si substrate by solvent mediation and detect, for the first time in a parallel manner, the SCO properties of several isolated objects. However, this procedure leads to polluted substrates that rendered the morphological characterization a very difficult task.

In order to continue the idea of the *in-situ* synthesis of organized SCO luminescent doped nano-objects, we have also demonstrated the possibility to pattern regular arrays of nano-objects of $[Fe(hptrz)_3](OTs)_2$ using the chloroform system employed previously for the fabrication of thin films. Here, we developed a soft lithography approach, derivate of the solvent-assisted micromolding technique (SAMIM). By pressing a drop of the chloroform system with a thick, highly polymerized nanopatterned PDMS stamp to a substrate, micro/nano droplets are trapped in the cavities of the stamp. Then, after the evaporation of the solvent, nano-objects precipitate in an organized manner on the surface. *We have been able to monitor the SCO behavior in a large number of widely spaced individual nano-objects simultaneously for sizes down to 150 nm.* Even at this small scale, basically similar transition curves have been obtained implying no significant size effect on the SCO in our nano-structures. One should note that in this approach there are no surfactants or other stabilizing agents around the nano-objects, hence possible *matrix effects are totally discarded.* This nanopatterning technique allowed us to completely fulfill our main objective. This method provides a *direct way to determine single-particle spin transition curves and the corresponding particle morphologies or even spectral or structural information.* Clearly, the limits of the technology employed for fabricating the silicon master or that of the PDMS molding are not yet reached and the luminescence detection limits can be also easily pushed further. Hence we expect that using this approach one can gain systematic statistical data about the size reduction effects in SCO materials of general relevance to size effects in molecular solids.

Due to the large variety of stimuli that can be employed to trigger the SCO phenomenon, the luminescent doped SCO chloroform solution in the form of thin films or arrays of nano-objects present a very interesting platform for developing low dimensional SCO nanomaterial based optical devices. As a proof of concept, we have

shown how a luminescent array of SCO dots can be employed as a chemical sensor by monitoring the luminescence increase of the dots as they transit from the LS to the HS state after being exposed to ethanol vapors. These SCO nano-dot arrays open up interesting perspectives for real time gas/vapor detection. On the other hand, the thermal SCO of this system in the form of thin films can be exploited for high spatial resolution thermometry for performing surface temperature measurements *via* luminescent detection. The exciting perspectives of this idea will be explored in more detail in chapter IV.

Chapter 4

Microthermometry

4.1 Introduction

The work described in this chapter is part of a common project between our team, Christian Bergaud and Nadia Belaid, researcher and PhD student, from the Nanobiosystems group (NBS) in the Laboratory of Analysis and Architecture of Systems (LAAS). Their work is centered on the realization of a tool for the study of temperature dependent phenomena in chemical and biological processes with high spatial and temporal resolution. An increased understanding of temperature dependent fundamental properties is likely to have great impact for the development of medical diagnosis and treatment techniques. For these reasons, nanowires are targeted as submicrometer scale elements for temperature control. Due to their small thermal mass, micro and nanowires based devices are particularly interesting in terms of response times and also in terms of confinement of their induced temperature changes when heated by Joule effect. The temperature characterization of these heating elements is a critical step and it is being performed by fluorescent thermometry, which has the capability to work as a full-field technique and thus to map temperatures over large areas with high recording speed. It is precisely under these circumstances where the present work is conceived. *Our main objective was to explore the potential of the luminescent SCO nanomaterials to perform surface temperature mapping with high spatial resolution via luminescence detection.* To accomplish this, we employed our *hybrid SCO systems as luminescent temperature probes on gold nanowire circuits heated by Joule Effect.*

4.2 Microthermometry, Why?

The development of temperature sensors continues to attract much attention in various areas of science and technology, such as hyperthermal and photothermal tumor therapy, aerospace engineering, microelectronic circuit testing, lab-on-a-chip research, *etc.* In particular, with the advent of nano(bio)technologies, measuring temperature on the

micro- and nanometric scales is becoming an increasingly important issue [141]. Thus, not only the need for development of new thermal nano-characterization techniques along with the use of novel nanomaterials has been amplified, but also the demands for measuring and controlling temperature with nanoscale spatial resolution and high temporal-resolution have become a major concern for further developments.

Within this general picture, two major issues can be put forward. First, recent developments in the microelectronic industry towards organic semiconductors have introduced yet higher requirements for good thermal design, owing to the low mobility of carriers in these materials. Thus, good thermal management is a key issue to assure the optimal performance and lifetime of a circuit, which needs thermal mapping in order to have more effective circuit architectures from a heat dissipation point of view [142, 143]. Second, the tendency to miniaturization is also observed in biomedical sciences. Miniaturized systems offer improvements such as reduced consumption of chemicals and higher throughput. In terms of thermal control, the miniaturization also provides advantages, *e.g.* the reduction of the response times during temperature cycling processes. Fundamental studies on protein folding and denaturation have been carried out (with high spatial and temporal resolution), which has relevance to a number of diseases, such as BSE, CJD, Alzheimer's and Parkinson's disease [144, 145]. Thermal imaging capability appears also crucial in connection with a variety of cancer therapies, which use heat to damage or kill cancer cells (hyperthermia and photothermal therapy) [146].

As a result, it is vital to rely on precise thermometry down to the nanoscale regime where conventional methods are no more relevant. However, the development of a micro / nanoscale thermometer is not only a matter of size, but also requires materials with novel physical properties along with dedicated nanocharacterization techniques.

Centered in this problematic, the following paragraphs will describe the most commonly used thermometry methods and analyze their potential application in the thermal characterization of micro and nano structures. Then, the viability of luminescence as a thermal characterization technique for small structures is discussed. Finally, the promising use of nanowires as efective heat sources for the development of new technologies is mentioned.

4.2.1 Thermometry Methods

It is worth taking an overview of the most commonly used thermometry techniques to get a better understanding of the limitations involved with measurements of micro and nanosystems. One important question to keep in mind about thermometry methods at this scale is: Does the method involve physical contact? Figure 4.1 summarizes these techniques.

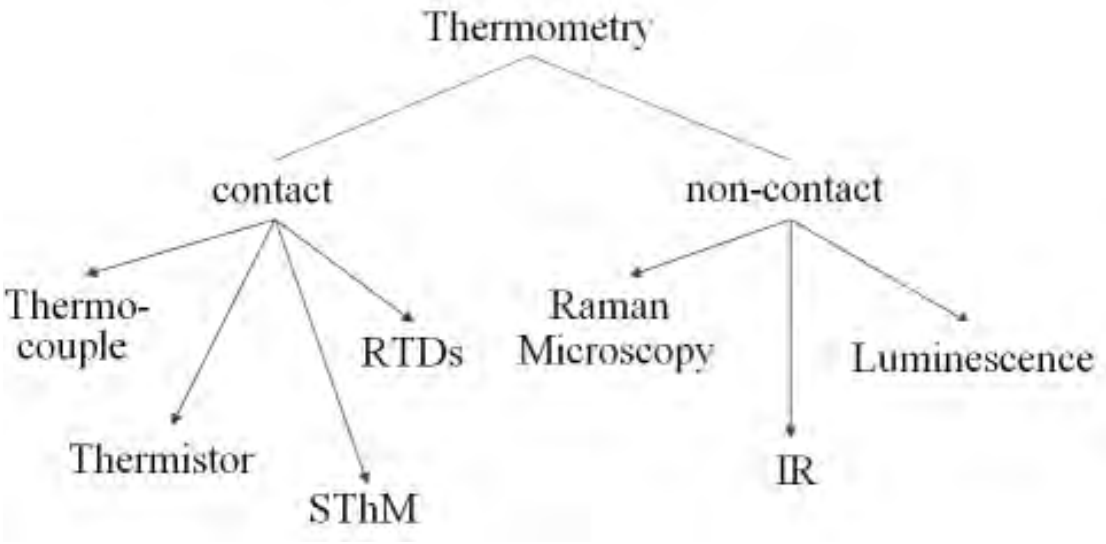

Figure 4.1: Diagram of the most common thermometry methods separated in contact and non-contact categories.

4.2.1.1 Contact Methods

Some of the methods that use a physical contact approach are: thermistors, resistance temperature detectors (RTD) and thermocouples. The first two elements take advantage of the fact that the resistance of almost any conductor or semiconductor material changes with several factors and one of those is the temperature. Thermistors are made out of ceramic or polymer materials; in contrast, RTDs are based on pure metals such as platinum [147, 148]. On the other hand, thermocouples rely on the Seebeck effect, also known as the thermoelectric effect. When one of two junctions of two different metals (the measuring junction) has a temperature difference with another junction (the reference junction), a proportional voltage is generated between the two of them.

Frequently, the easiest way to make a temperature measurement is using a contact method. Nonetheless, if the object to be measured is of reduced size, contact methods are not the best option. The measuring probe can easily modify the temperature of the sample as soon as it touches its surface. This way, the probe constitutes a heat leakage for the system to be analyzed and as a consequence it leads to errors in the measurements [94]. Furthermore, if the mass of the probe is higher than the mass of the sample, two things happen: the errors are more significant to the readings and it takes longer to get a stable measurement [149].

Because of the reasons mentioned above, the need of the miniaturization of the measuring probe is a key factor to achieve higher spatial and temporal resolution. With this in mind, some efforts have been made through the development of scanning thermal microscopy (SThM) [150, 151]. This method is a variation of the scanning probe microscopy that can make thermal characterizations of nanostructured materials with high spatial resolution. This technique employs a probe tip to scan the surface of a sample and sense the local thermal characteristics. As a result, a map of

temperature and other thermal information can be plotted after scanning the whole sample. Some mechanisms behind the sensing schemes of SThM involve the same principles of thermistors, RTDs and thermocouples [152–155]. The main differences are the size of the probe and its precise positioning capabilities. There is also an additional variation for SThM that uses a fluorescent - temperature dependent - tip [156–158]. However, despite the exceptional spatial resolution that SThM may offer, it presents some drawbacks independently of the sensing mechanism used. First, the tips entail highly complex fabrication procedures. Second, the thermal information is acquired in a serial way, one point at the time (point probe method); thus, this method has slow image rendering which gives poor temporal performance for the transient thermal characterization of a sample. Third, it is not fully understood the heat transference between the probe and the micro - nano structure. The probe may still be a considerable heat leakage for the analyzed system and the establishment of the appropriate correction factors is a complex task [149].

4.2.1.2 Non-Contact Methods

Non-contact method is an effective way to avoid the typical problems found with contact methods. Non-contact techniques analyze the light emitted from or reflected on an object. The greatest advantage of this approach is that the temperature that is being measured is not (or less) influenced by the measurement process. Among the most commonly used techniques are: IR thermography, thermoreflectance, Raman spectroscopy and fluorescent thermometry.

All matter emits electromagnetic radiation usually called thermal radiation. This radiation is the result of the movement of charged particles in matter. The characteristic spectrum of this radiation is around the infrared and it is strongly dependent on the absolute temperature of the object that is being analyzed. IR thermography analyses the radiation emitted by a body and returns information about its temperature. This method is simple and there are many well developed solutions available in the market; it has been integrated to microscopy setups since the 1960s [159, 160]. In addition, IR thermography constitutes a quick full field technique since data from every point of the sample can be obtained with only one measurement. Furthermore, the method is efficient in characterizing fast temperature changes [149].

However, IR thermography has also its own weaknesses and one of them is the spatial resolution. Since the temperature information is carried by low energy radiation, the photons have large wavelengths; hence, the method is constricted by the diffraction limit down to a few micrometers ($\approx 5\mu$m) [161–163]. Another drawback of the technique is that in order to have an accurate measurement, it is necessary to know first the emissivity of the sample. The process is more complex if there are different materials because there is more than one emissivity coefficients involved. Finally, IR thermography is not an adequate method for experimentation under liquid conditions because infrared radiation tends to be largely absorbed by water and glass.

Another full field method is the thermoreflectance based technique. This procedure analyses the thermally induced changes of the reflectivity on a surface. Usually, these

changes are associated with thermal expansion in most of the materials; particularly, the reflectance in semiconductors is also affected by the modification of the band gap with temperature variations [164]. Hence, light reflected from any material has information about its temperature encoded in its amplitude, phase and polarization. If the temperature of a material changes ΔT, this variation induces a change of its reflectivity on its surface that can be expressed as:

$$\frac{\Delta R}{R} = \frac{1}{R}\frac{dR}{dT} \cdot \Delta T = k\Delta T, \tag{4.1}$$

where R is the mean reflectance of the sample and k is its thermoreflectance coefficient. The setup needed for the thermoreflectance method is relatively cheap and simple [164]. However, precise knowledge of the reflectance coefficients of the surfaces is necessary to make accurate inferences of the light collected. This task is particularly challenging because the coefficients are strongly dependent on too many factors. In addition, for micro and nano scale, the calibration process is difficult because of the high magnification conditions [165].

Scanning thermal Raman microscopy can be also employed to perform temperature measurements. The Raman (vibration) modes are affected by temperature changes due to thermally induced structural changes (thermal expansion) of the material under examination as well as due to the population of higher energy vibrational levels. An analysis of Raman spectra in terms of absolute or relative intensity, Stokes/antiStokes ratio, position and width variations of the vibration modes can be eventually translated into temperature. Raman "offers spatial resolution" around the micrometer and a broad temperature measurement range with a sensitivity no better than 10 K [166]. This technique is also capable to perform measurements a few microns underneath the surface if a confocal microscope is used. However, one of the main problems with Raman is its invasive nature due to laser heating. Also, the measurements obtained are, inevitably, the mean over the depth of penetration of the laser. Due to its serial data acquisition nature, μRaman thermometry has a slow image rendering. Additionally, the calibration process can be very complex and it is dependent on each sample. Finally, this technique is relevant only to materials that display a large and very sensitive Raman response to temperature changes [166].

The last non-contact method considered in this section is the luminescence thermometry. Here, the light emitted by a temperature dependent fluorescent probe is used in order to extract thermal information from the sample. Common luminescent thermal probes include organic dyes, ruthenium complexes, polymers, semiconductor quantum dots and lanthanide (Ln^{3+}) -based materials [167]. In contrast to other non-contact methods, luminescence thermometry is considered as semi invasive; even though a thin film of a fluorescent probe is placed on top of the region to be analyzed, the information is transported only by the light emitted from the probe and not from the film itself. It should be emphasized that, if the size of the structure to be measured is comparable with the thickness of the luminophore film employed, the measurement would fall down under a sort of contact method measurement. Under these circumstances, the thermal behavior of the system could be modified by the presence of the sensing film and special considerations have to be taken in order to

avoid misinterpretations from the acquired data [168].

The luminescence thermometry spatial resolution, as in the case of Raman spectroscopy, is limited by the diffraction of the light. Nonetheless, with short wavelengths and appropriate optics, sub-micrometer resolution has been reported [168, 169]. The temporal resolution of this technique is limited by the device used to capture the light; in full field studies, CCD cameras can typically take images every 1 ms. Compared to the thermoreflectance method, this approach is simpler and is not affected by the emissivity of the materials present in the sample [149].

4.2.1.3 Luminescence Thermometry: Principal Techniques

As mentioned in Chapter I, the shape and the intensity of the emission spectrum of a particular luminophore can be modified due to temperature changes. It is precisely these variations that luminescence based thermometry exploits with different methods to infer the local temperature around a luminophore. Among the most popular techniques we can mention [149, 166, 167]:

- **Intensity based Luminescence Thermometry**: The light intensity from a portion of the emission spectrum is analyzed as a function of temperature. Even though this approach leads to setups which are easy to implement, it can be vulnerable to several factors. A change in the intensity of the excitation source, a slight loss of focus in the microscope, variation in the concentration of the luminophore or photobleaching effects can be misinterpreted as a change of temperature.

- **Luminescence Intensity Ratio Thermometry**: Some luminophores display an emission spectrum composed by well defined emission lines (for example, some lanthanides ions). If the energy levels that originate two of these lines are energetically close, it is possible that the population of both levels is thermally linked. Thus, the ratio of the emitted intensities from these two thermally coupled levels will be only dependent on temperature and immune to variations of the local concentration of the luminophore, its photobleaching or drift of the sample.

- **Spectral Shift Luminescence Thermometry**: In some rare cases, it is easy to measure the movement of the emission lines displayed by some luminophores to estimate the temperature in the sample; thus, the temperature measurement will not be affected by fluctuations of the luminescence intensity. However, in order to have accurate temperature measurements, it is necessary to employ a luminophore with a remarkable spectral shift as a function of temperature.

- **Two Color Thermometry**: In this approach, the intensity ratio of the emission from two different luminophores is employed to estimate the temperature. Typically, one of the probes is heavily temperature dependent and the other is poorly dependent (considered as a reference probe). This is useful in order to get

rid of the influence of the drifts of the system. However, this method is sensitive to the individual behavior of the probes (for example different photobleaching rates), spectral overlap between emission of both luminophores and inhomogeneous concentration of both luminescent agents over the analyzed sample.

- **Luminescence Lifetime Thermometry**: The decay probabilities form the emitting electronic levels depend on several factors that are directly or indirectly related to temperature (for example, phonon assisted energy transfer processes or multiphonon decays [166]). Lifetime-based methods are essentially immune to reflection, intensity fluctuation of the excitation light, inhomogeneous distribution of the luminophore, *etc.* This type of measurements can be performed in time domain, frequency domain, with one or two luminophores (one temperature sensitive, the other for the reference) [170].

- **Polarization Luminescence Themometry**: Employing a linearly polarized excitation light source, this technique analyses the polarization anisotropy of the luminescence (*i.e.* the ratio between the light emitted at two orthogonal polarization states: one parallel and the other perpendicular to the polarization of the excitation beam) as a function of temperature.

4.2.1.4 Why SCO materials and luminescence?

Besides the doubtlessly interesting fundamental aspects, potential applications such as sensors draw increasing attention on the SCO phenomenon. The main advantages of using such molecular materials are: (1) the transitions can be obtained even at the nanometer scales, (2) they involve a change of the electronic states, resulting in very fast and sharp transitions at the molecular level, (3) there is a wide flexibility for designing SCO-based materials, (4) the bistability associated to the SCO comes with a spectacular change of various physical properties (magnetic susceptibility, compressibility, color, electric permittivity) which may be employed to probe the spin state of the system, (4) various physical perturbations can be employed to switch these materials between the bistable states and among these, we have the temperature.

In luminescence based thermometry it is usual to detect the changes of temperature by following the thermal quenching of the luminescence of a given probe. In other words, the system is composed of a single element that performs two tasks at the same time: temperature sensing and signal transduction. Nevertheless, it is also possible to take a two element approach where the two functions are assigned to two different entities; thus, an additional flexibility is obtained in order to better tune the probe to different environments by varying the properties of each component independently [171]. From this point of view, in the course of this thesis we have designed two element systems for thermometry constituted of spin-crossover nanoparticles, whose bistability and associated changes of optical properties modulate the intensity of the response of a luminophore. These systems could thus be adapted in a straightforward manner to various problems where the use of fluorescent thermometry would be beneficial. We should stress that the main advantage here over traditional fluorescence thermometry

comes from the fact that the temperature range and sensitivity of the detection can be adjusted independently of the fluorescent probe via well-established methods, such as metal-dilution, anion exchange, ligand engineering or particle size tuning [5].

4.3 Nanowires for Heating Purposes

A nanowire could be heated using an electrical current flow. Due to its low dimensions and low heat capacitance, the temporal responses for temperature variations produced by the current flow in a nanowire are expected to be fast. Furthermore, under the appropriate conditions of the surroundings, it has been demonstrated that the temperature shifts can be highly localized [168]. As a result, nanowires as heat sources is a promising mean for the development and optimization of high speed temperature control on-chip systems. Nanowires based heating devices could be used in a number of applications. This approach could be taken to develop thermal control strategies for lab on-a-chip systems to perform complex and effective biological samples analysis. Also, this concept could be applied to induce highly localized surface modifications on biosensors to create binding sites. Another interesting application is the characterization of molecular kinetics; by producing a fast temperature variation (T-jumping), the beginning of folding or unfolding molecular events could be triggered in a controlled way for further observation. The major advantage of using this nanowire assisted scheme is its simplicity; current methods for T-jumping employ laser based setups that tend to be complex and expensive. Furthermore, nanowire devices could be integrated to existing on-chip technologies. Even though the temporal responses of nanowires (micro seconds regime) are not as fast as the laser setups (nano seconds regime), it is enough for characterizing most of molecular events in biology [149].

4.3.1 Fabrication Process of Gold Nanowires

The production of the chips that contain the nanowires is divided in two processes, one electron beam lithography (EBL) stage where the nanowires are fabricated on a Si substrate and then, an additional photolithography process in order to build the electrodes necessary for connecting the nanowires to an external circuit. These two are necessary due to the differences in their lateral size (nanometric for the width of the nanowires and micrometric for the electrodes).

The basic substrates used for Au nanowire fabrication were $< 100 >$, 4-inch, 525 μm thick n-type silicon wafers. The silicon wafers were primarily cleaned in a 1:3 mix of H_2O_2 and concentrated H_2SO_4 (known as Piranha solution). In order to remove the oxide formed in the previous step and remove all impurities deposited on their surface, the wafers are then immersed in a buffered HF solution. After this, a wet thermal oxidation step is performed for creating a 200 nm thick SiO_2 layer over the substrate and providing an electrically isolated substrate for the nanowires.

4.3.1.1 Electron Beam Lithography (EBL) Process

Here, a similar process described in section 3.4.2.2 (Chapter III) was also employed for generating our metallic nanowires. A positive EBL PMMA resist layer is spin coated on the surface of an oxidized Si wafer and then it is exposed in the EBL chamber of a RAITH-150 e-beam writer. Here, a focused electron beam is used to "pattern" 80 μm long - 500 nm or 1 μm width nanowires on the PMMA film. Each section of the film that has been exposed to the beam becomes soluble in a solution (1:3) of MIBK (Methyl isobutyl ketone) and IPA (isopropanol). As a result, after immersing the wafer in this developer solution, the different nanowire patterns will appear in the form of cavities of the PMMA layer. After this, a Ti/Au deposition process with a respective thickness of 10 nm and 40 nm (the Ti layer works as an anchoring layer between Au and SiO_2) is performed. Then, by means of a lift off process in 3-chlorethylene solvent, the rest of the resist is removed from the surface leaving only the metal that was in touch with the substrate *i.e.*, the metallic nanowires.

4.3.1.2 Photolithography Process

A similar procedure to that described in the EBL process is performed. In this case, a photo-sensitive positive resist (AZ 5214) is spin coated and selectively exposed to UV radiation in order to pattern the electrodes corresponding to each nanowire. Once again, after the exposure process, the sections of the film that were exposed become soluble and they are revealed in a 1:1 mix of AZ developer solution and DI (de-ionized) water. After this, a second metallization (Ti/Au of 10 nm and 800 nm, respectively) is performed. Finally, a lift off in acetone medium is done in order to remove the remaining resist leaving only the electrodes and nanowires on the surface. The chips are then passivated with a 100 nm layer of SiO_2 deposited by Plasma Enhanced Chemical Vapor Deposition (PECVD); the outer edges of the electrodes are left free in order to have micro- soldering of the wires to an external PCB (Printed Circuit Board). Figure 4.2 shows a photo of the final chip and SEM images of the nanowire devices.

4.3.2 Electrical Characterization of Au nanowires

The electrical characterization of the Au nanowires was performed by means of two types of electrical experiments. First, the variation of the resistance of the nanowires was observed as a function of temperature employing a Temptronic Thermostream machine; this type of systems are widely used to test different types of electronic devices such as multi chips modules (MCM), PCBs and other types of assemblies at different temperatures. This device sends a temperature controlled airflow to the surface of the target device (*i.e.* nanowire chip with the PCB) and changes directly the temperature of the components at the surface (*i.e.* the nanowires). Thus, the resistance of each nanowire in the chip is monitored with an ohmmeter as a function of temperature from 298 K up to 353 K. Second, the variation of the resistance of the nanowires was measured as a function of an applied electrical current. Assuming

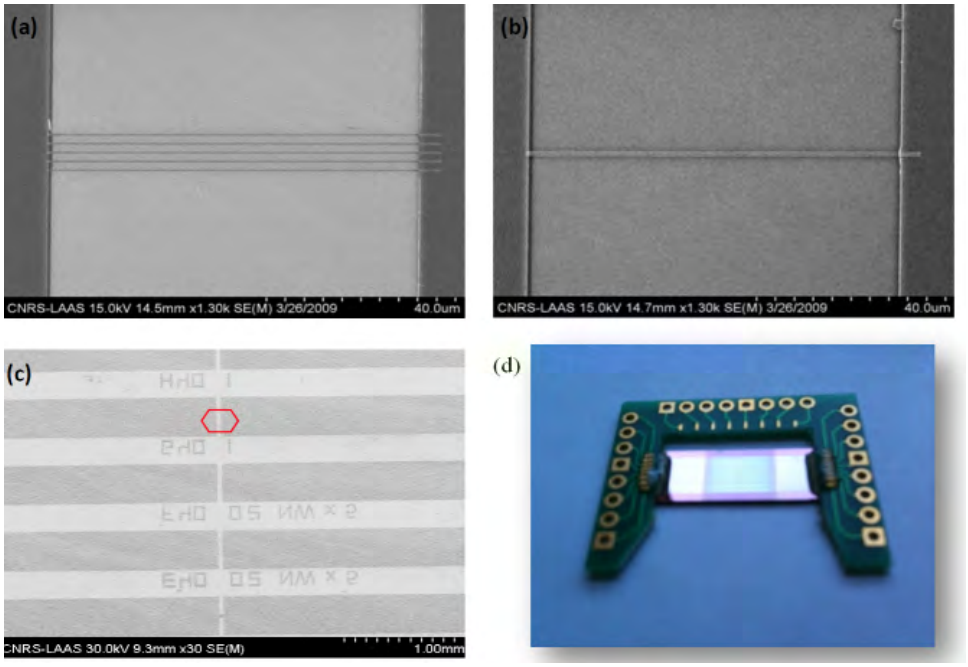

Figure 4.2: Scanning Electron Microscopy images of: **a)** five 80 μm x 500 nm x 50 nm Au nanowires, **b)** 80 μm x 1 μm x 50 nm nanowire, **c)** general view of the nanowires connected to their electrodes. **d)** Photo of the final chip connected to an external PCB.

that all variations of the measured resistance in each experience (or at least most of them) come from the change of temperature of the nanowire, it is possible to relate the variation of the resistance (ΔR), current, and temperature (ΔT) for each type of wire. It is worth noting that the ΔT inferred from these experiences can be understood as an average value of the ΔT induced in the whole nanowire. The ΔT dependences as a function of the applied current for two types of nanowires are displayed in figure 4.3; these plots will be used as a guide for designing our experiments in fluorescence.

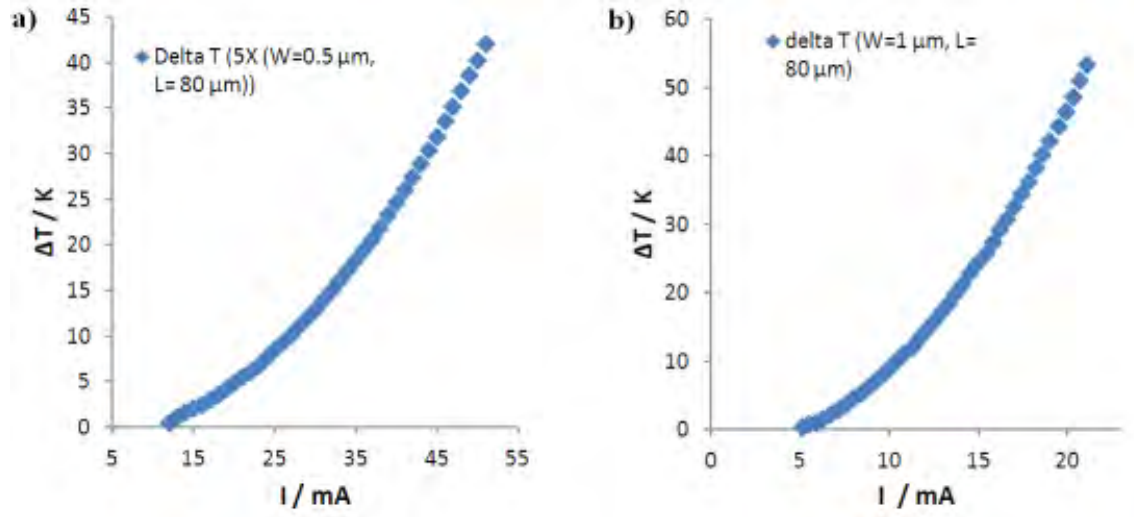

Figure 4.3: Variation of temperature induced as a function of applied electrical current for gold nanowires: **a)** set of 5 nanowires of 80 μm long, 500 nm width and **b)** 80 μm long, 1 μm width wire.

4.4 Thermal Characterization of Nanowires with Luminescence Microscopy

The main idea of the experiments described in this chapter consists of employing one of our luminescent SCO systems as a temperature sensor on the surface of a nanowire circuit. Once the layer of our material is deposited on the chip, fluorescence images are taken from the circuit with different bias (Figure 4.4). The reduced cross section of the wire allows for a local confinement of the heating along its axis when passing an electrical current through the device (Joule effect) [71, 168]. As the temperature increases, the spin state of the system will change locally from LS to HS and consequently, the luminescence intensity from the heated area will increase. With a precise knowledge of the relationship between the luminescence intensity and the temperature, a given change in intensity can be converted to temperature.

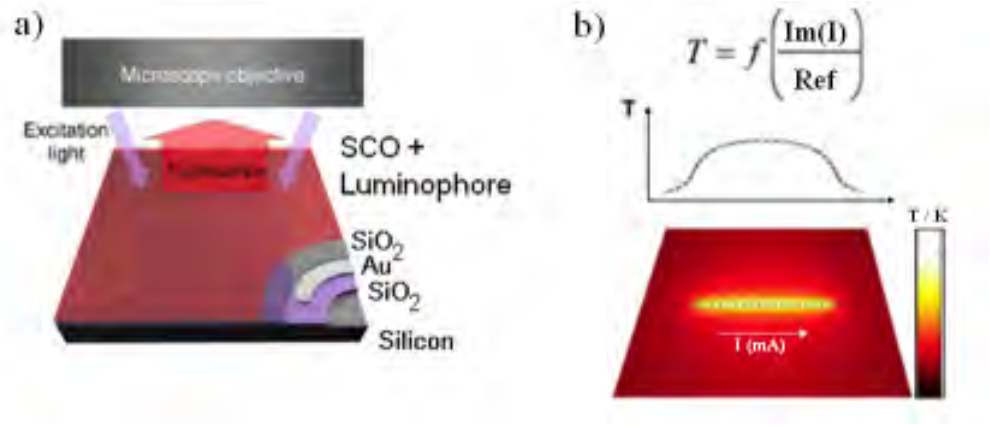

Figure 4.4: **a)** Schematic image of the Au nanowire device in the microscopy setup. **b)** The thermal cartography of the chip can be calculated as a function the luminescence image captured at a given bias and a reference that comprises the subtraction of an image of the circuit unbiased at low temperature (LS state) from another taken at high temperature (HS state).

It is important to note that these experiments must be done as a function of applied current instead of applied voltage between the electrodes in order to make comparisons between measurements of different nanowires with the same geometry. The lithographic procedures, the micro soldering process to the PCB as well as the connection cables to the measuring instrument may introduce more or less resistive paths to the studied equivalent series circuit. As a result, if two experiments for two similar nanowires are done as a function of voltage between their corresponding electrodes, there is no guarantee that at a given voltage, both wires will be under the same current; thus, the induced temperature change will not be necessarily the same. However, with measurements as a function of the applied current, the wires will always be under a known stimulus regardless the random resistive elements that may be included to the circuit while making the observations. In order to perform the thermal characterization of the wires in luminescence, we employed as an input a source-meter Kethley 6430 in current source mode combined with a Linkam LTS120 Peltier based system in open atmosphere with embedded electrical connections in the chamber of the cryostat. This configuration allowed us to have at the same time a

temperature control of the chip's substrate as well as an adequate platform to easily bias the nanowires (Figure 4.5).

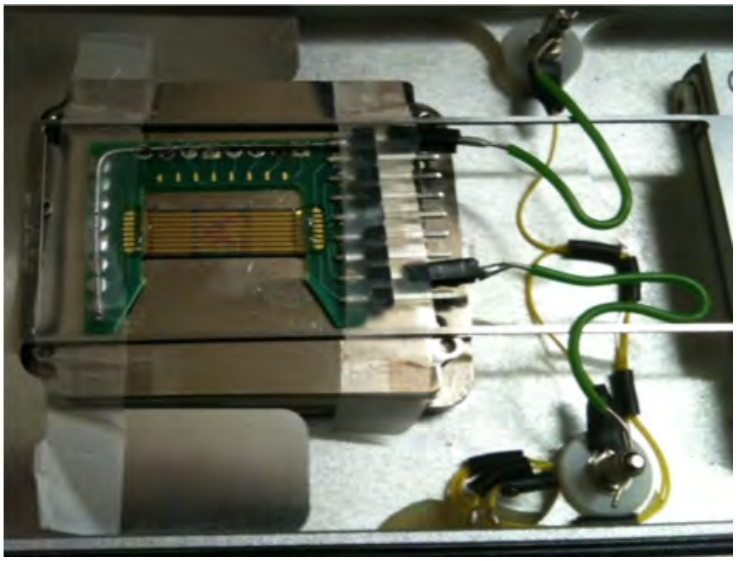

Figure 4.5: Picture of a nanowire chip with electrical connections in the chamber of a Linkam LTS120. The additional tape pieces at each side of the circuit work as dampers that have two purposes: (1) to partially block the movements of the sample induced by the tensions of the connecting cables and (2) to improve the thermal contact between the substrate of the chip and the platform of the system.

4.4.1 Microthermometry with $[Fe(NH_2trz)_3](OTs)_2$ doped with rhodamine 110

The $[Fe(NH_2trz)_3](OTs)_2$ reverse micelle system doped with rhodamine 110, was the first system that we employed to investigate the potential of the luminescent SCO nanomaterials to detect temperature variations with high spatial resolution. As a proof of concept, we deposited an important amount ($\approx$ 0.5 mm thickness) of Rhodamine 110-doped nanoparticle suspension on top of nickel nanowires (5 wires, 500 nm wide, 40 μm long, separated by 4 μm) in which temperature changes were induced by resistive heating with a DC current. (Back in the day when these measurements were done, the group of C. Bergaud worked with nickel nanowires instead of gold. The metal was changed because it was observed that in the long term, the Ni wires oxidized and it constituted an impediment when working with biological samples.) The fluorescence microscopy images were recorded at room temperature, through a x50 magnification objective and the excitation and the collected light beams were filtered by band-pass filters (FWHM: 23 nm) centred at 500 nm and 543 nm, respectively.

Figure 4.6 displays the images obtained in the off-state (I = 0) and in the on-state (I = 6 mA) of the nanowire heaters. One can observe a significant increase of the luminescence when current flows through the wires. This current value was chosen for maximum intensity, *i.e.* for complete LS$\rightarrow$HS transition; this current induced switching was observed several times in a reproducible manner. The difference image (Figure 4.6c) reveals clearly that the temperature change is confined to the close vicinity of

the nanowires, as would be expected. This observation highlights *the potential of our luminescent SCO nanomaterials for high-spatial resolution thermometry, which is a priori only restricted by the diffraction limit.* However, as demonstrated in chapter III, due to the radiative quenching regime between the SCO complex and the rhodamine 110, an important thickness of luminescent SCO nanomaterial is necessary to successfully detect the SCO. Thus, this system is not well suited for performing temperature measurements without having a strong impact on the temperature distribution of the surface under observation.

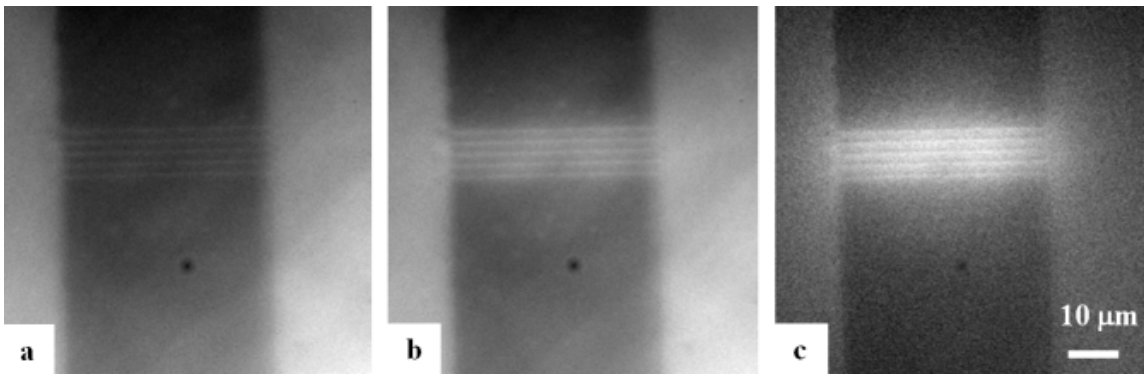

Figure 4.6: Fluorescence microscopy images of Ni nano-wires covered by rhodamine-110 doped $[Fe(NH_2trz)_3](OTs)_2$ nanoparticles. **a)** no external bias (I=0 mA), **b)** wires under external bias (I=6 mA), **c = b - a**.

4.4.2 Microthermometry with Luminescent $[Fe(\textit{hptrz})_3](OTs)_2$ Thin Films

The development of the thin films from the $[Fe(\textit{hptrz})_3](OTs)_2$ doped chloroform solution opened up exciting perspectives for the luminescent SCO-based microthermometry. To this purpose, we spin coated the SCO chloroform system on the surface of a nanowire chip. In chapter III it was shown that the transition temperature of these films under an uncontrolled atmosphere shifts to 338 K; for this reason, the experiments we performed in this section were not carried out at room temperature but instead, the substrate was heated up in order to bring the film near the beginning of the SCO ($\approx$ 328 K under these experimental conditions, see section 3.3.2.3). Under these circumstances, a small current could induce a delta of temperature that would be detected by the CCD through the SCO modulation of luminescence. However, one shall note that working at relatively high temperatures in an open atmosphere might constitute a drawback since the probability of damaging (oxidation) the luminophore increases.

In order to explore the capabilities of this system in microthermometry, we designed a more elaborated experiment where the camera, the excitation and the current sources were synchronized in order to perform cycles as a function of the current applied to the nanowire circuit. For this batch of experiments we employed a Clara (Andor Technology) front illuminated, interlined CCD sensor, a blue LED (centered @450 nm)

for the excitation and the Keithley 6430 as a current source. These three components have TTL inputs and/or outputs that allowed us to interconnect them as shown if figure 4.7a. In spite of the electronic shutter of our Clara camera, the head of this detector has a TTL output to drive an external shutter with an active high or low voltage. We have employed this signal to trigger the Keithley current source with a falling edge (as required by the device); hence, we have set the current source of the Keithley to perform stair case current cycles with a waveform similar to that illustrated in Figure 4.7b. This way, every time the device receives a falling edge, the output current will change cyclically between a minimum and a maximum current value with a step, previously defined by the user. The fire signal of the camera is another TTL output that is active only when the CCD is accumulating charge; thus, we used it to activate the LED and to expose the samples exclusively during the accumulation time of the CCD. This signal and the voltage difference between the electrodes of the nanowire devices were monitored with an oscilloscope.

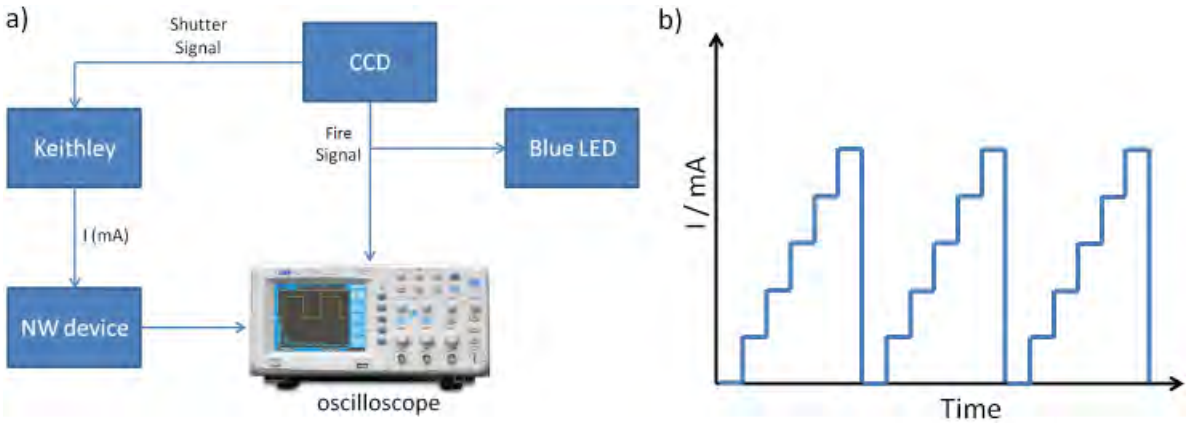

Figure 4.7: **a)** Diagram of the different connections for the setup employed for the thermal characterization of the NW devices as a function of applied current. **b)** Example of a current staircase waveform employed in our experiments. Once a maximum value is reached, the current source returns to 0 mA.

Figure 4.8 displays a time diagram that relates the different events that occur in the setup during a current cycle. The falling edge in the shutter signal marks the beginning of an acquisition and triggers a variation in the current output. The delay time D_{os} is a delay that can be programmed by the user in order to give enough time to a mechanical shutter to be fully opened before starting an accumulation with the CCD. In our case, however, this time could be programmed to zero or employed as a delay after a delta of current to assure that the system is in a steady state. Following this delay, the CCD begins to accumulate charge; as a result, the fire signal becomes active and the LED is turned on. When the accumulation time is expired, the fire signal goes back to zero and the LED goes to a standby state. A second delay D_{cs} corresponding to the closing time of a shutter can also be programmed; to our purposes it was left to zero. Once this set of events has occurred, a new falling edge of the trigger signal will be generated, the current will change and the cycle repeats again.

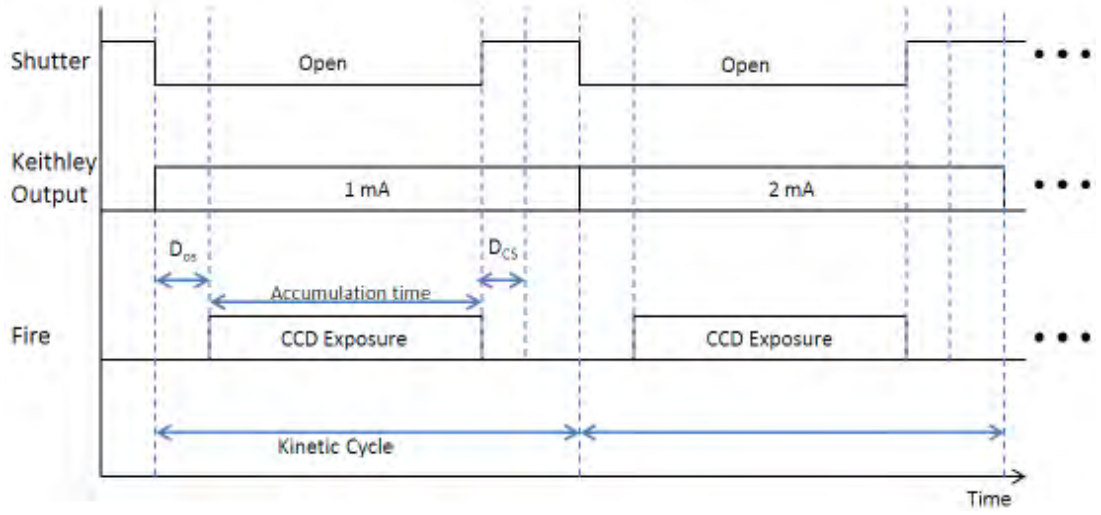

Figure 4.8: Time diagram displaying the different control signals employed to synchronize the CCD camera, light and current sources during a cycle as a function of current applied to a nanowire.

4.4.2.1 Protocol and Data Treatment

So far we have focused on the detection of the SCO through a modulation in luminescence. However, this is the first time we try to infer from a change in luminescence the local temperature of the sample. To accomplish this, we have employed the following experimental protocol: first, we fixed the temperature of the nanowire device at 328 K. Second, we launched an experiment performing some current cycles; we set the D_{OS} delay to 500 ms, more than enough to assure that the transient response of the system is over. (From electrical measurements, it has been observed that the transient for this device is in the microsecond range.) Third,with the circuit unbiased (I=0 mA), reference images at low (LT) and high (HT) temperature are taken at 328 K (LS state) and 348 K (HS state), respectively. These two images are included in the stack of images from the electrical cycle and then, they are all aligned employing the image registration routine developed in MATLAB®. The LT and HT reference images are very important because once aligned, their difference provides the luminescence variation upon the SCO for each pixel of the images under study. In this manner, we avoid calibration problems due to irregularities on the film; for example, due to the fabrication process of the nanowire device, the spin coated thin film can be thicker near the edges of the nanowires close to the electrodes due to the height difference ($\approx$ 750 nm) between the two of them (see Figure 4.9).

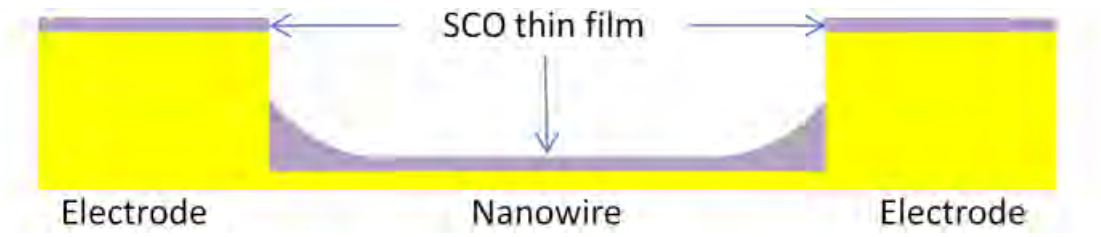

Figure 4.9: Scheme of the cross section of a nanowire circuit with the SCO thin film deposited on its surface.

With the knowledge of the maximum change of the luminescence at each pixel, we should be able to estimate the fraction of the maximum modulation on each sector of an image at a specific current as:

$$\text{Modulation} = \frac{\text{Im(I) - LT}}{\text{HT - LT}}, \tag{4.2}$$

where Im(I) is an image of the circuit with a given current I, LT and HT are the reference images of the circuit at low (LS state) and high (HS state) temperature.

The synchronization of our experimental setup allowed us to launch long experiments with little intervention form the user and as a result, to generate easily several images per experiment. To have a rigorous analysis of the luminescence variation along the nanowires on each image of the stacks, we developed a set of macros and functions in Image J (Appendix C). This free software allows us to exploit its graphic interface and program its embedded image treatment functions in order to create more complex routines. The set of macros comprises:

- *Create, save, charge ROIs*: Through the ROI manager utilities of ImageJ, these three macros allow the user to create, save or charge a specific set of ROIs employed for an experiment.

- *Stack Treatment*: This macro receives as parameters the position number of the LT and HT references from a stack of images. Then, the macro calculates for each image the expression 4.2 and it returns a new stack with the results. In order to reduce the quantity of noise involved in this treatment, this macro receives also an additional value (r) that corresponds to the radius of a median filter that is applied to all images before doing any calculations. This filter is employed to smooth an image, very similar to a mean filter, but conserving the edges of the image (very important to not modify the information in the vicinity of the nanowires). The median filter examines each pixel of an image together with its nearby neighbors (in a region of r x r pixels, with the pixel under study in the center) to decide whether or not it is representative of its surroundings; then, the pixel is replaced by the median value of the region under consideration. This filter gives more robust smoothing of the image since the median value is weakly affected by abnormal pixel readings (as those produced by cosmic rays) [134, 135]. Figure 4.10 shows an example of the results from two image treatments: one employing the raw images and another with a median filter before performing any calculations. Here, it is possible to see how the filter eliminates an important amount of noise and even though it seems to slightly blur the image, the borders of the nanowire are totally respected.

- *Nanowire profiles*: This macro receives a ROI predefined by the user in the form of a line drawn on one of the images already treated. Then, it records the values of the pixels on each image along this line and returns a table with the information ready to be pasted and plotted with any software (Matlab, Excel, *etc*).

- *ROI Cycle*: This macro was developed for building plots of the mean value of the pixels inside a ROI as a function of the current applied to the nanowire device during consecutive cycles. This macro receives the number of pictures per cycle, the initial value in mA, the step size employed in the cycle, the quantity of cycles contained in the stack of images and a ROI. Then,it returns a table with the information organized as a function of applied current and cycle number (see figure 4.11).

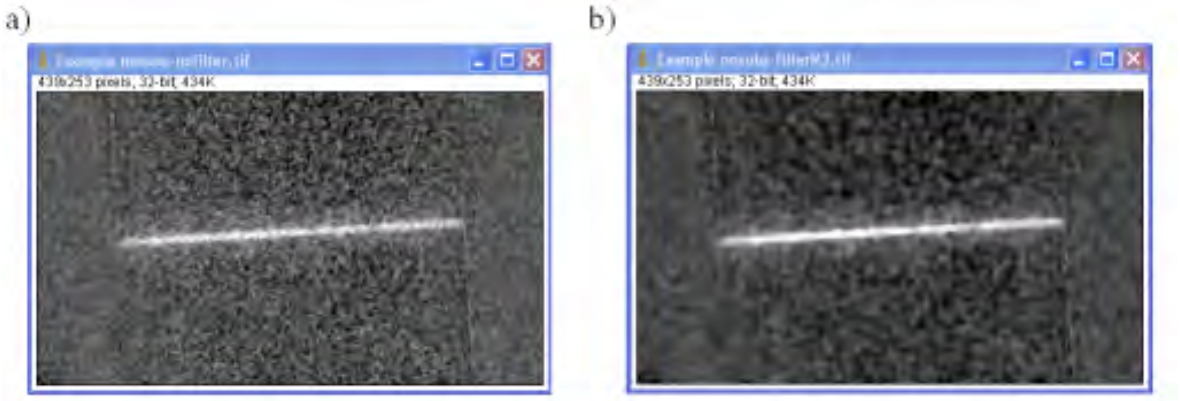

Figure 4.10: Resulting image from a treatment employing raw images **a)** and images previously filtered with a median filter of r=3 **b)**.

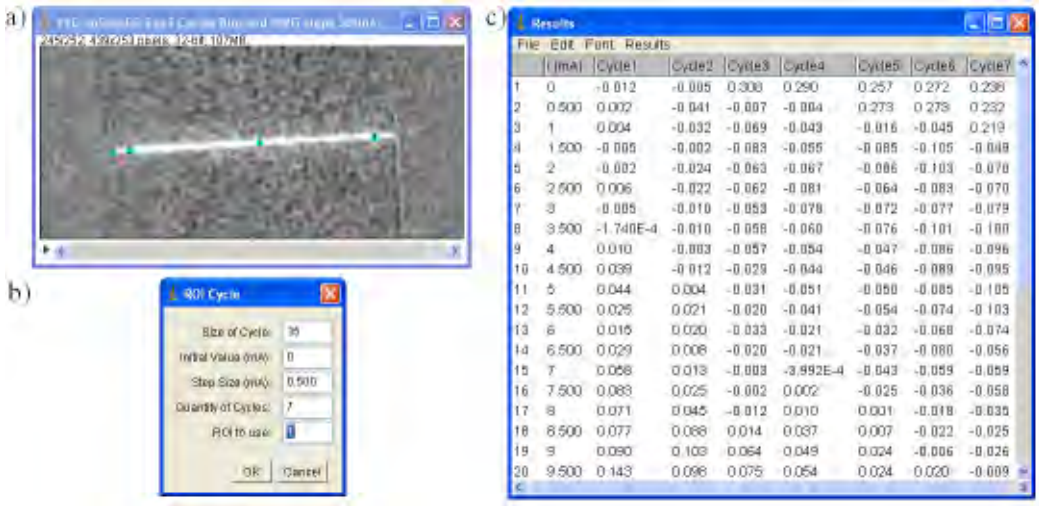

Figure 4.11: **a)** Treated stack of images with 4 ROIs defined along the nanowire axis. **b)** Dialog window of the ROI Cycle macro. **c)** Results returned by the macro after scanning a stack of 245 images. The information is organized by cycles as a function of the current applied to the nanowire.

4.4.2.2 Results and discussion

Thin films of $[Fe(hptrz)_3](OTs)_2$ doped with Rhodamine 110 were deposited over different nanowire devices. When an electrical current was passed through one of the nanowires, the spin state of the thin film locally transited from LS to HS and as a

consequence the luminescence intensity increased. Figure 4.12 shows one of our experiments performed on a 150 nm film, with a 1 μm wide nanowire, during the first of two consecutive electrical cycles between 0 and 15 mA (staircase waveform). In Figure 4.12a, the left panel displays the treated fluorescent image around the wire when no current is applied. The middle and right panels show the same measurement, but for increasing currents of 9 mA and 15 mA. The strong confinement of the temperature increase in the vicinity of the wire is clearly perceptible. As observed in Figure 4.12b, the measured temperature distribution profile along the wire (X direction) is reasonably flat, with a steep increase of the temperature at the ends of the wire and a relatively constant value between. Also, Figure 4.12c shows the profiles across the wire (Y direction) that permits to better illustrate the high confinement of the heating on the nanowire at different bias. The shape of these profiles is in good agreement to those previously reported on literature under similar experimental conditions by Löw *et al.* [149, 168].

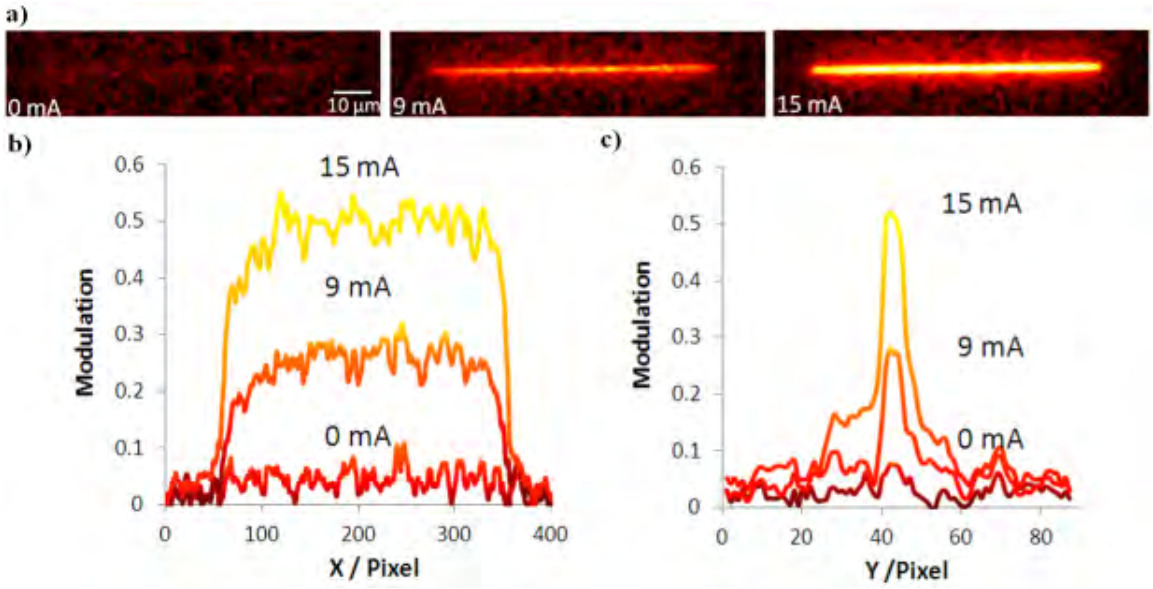

Figure 4.12: **a)** Treated fluorescence microscopy (excitation 450 nm, emission 550 nm, X50 objective) images of a gold nanowire (80 μm length, 1 μm width, 50 nm thickness) covered by a thin film of the spin crossover compound $[Fe(hptrz)_3](OTs)_2$ doped with rhodamine 110. During the fluorescence measurements the nanowires were heated by Joule effect: the current intensity is indicated for each image. Cross-section of the fluorescence images **b)** along (X direction) and **c)** across (Y direction) the nanowire.

Figure 4.13a displays the mean variation of the luminescence modulation during the two electrical cycles for a ROI that covers a small section of the nanowire (see inset panel **a**). As observed in the electrical characterization of this type of wires (Figure 4.3), in the 0 - 5 mA interval there is not a significant delta of temperature induced on the nanowire. However, as the current reaches higher values, in both cycles it was observed that the modulation of the luminescence increased significantly until it reached a maximum value for a bias current of $\approx$ 13 mA; according to the electrical characterization, this current value corresponds to an induced $\Delta T \approx$ 19 K. Figure 4.13b illustrates a thermal characterization in luminescence mode of the same thin film carried out before performing the electrical cycle measurements. In order

to compare quantitatively these two experiments, the data obtained from the thermal cycles was normalized employing equation 4.2 with luminescence values obtained at 328 and 348 K as the LT and HT references, respectively. Here, it is possible to realize that under these experimental conditions, a $\Delta T \approx 19$ K is sufficient to induce a complete LS $\rightarrow$ HS transition of the film. Nonetheless, one shall note that the increase of the luminescence along the nanowire when heated by Joule effect is less than that obtained in the same region when compared to the HT image; in fact, the luminescence in the electrical cycles reached at the "saturation point" (in the HS state, I > 13 mA) is approximately 45% of the reference image HT. Clearly, this effect cannot be explained by photobleaching effects since the reference images are always taken at the end of the electrical cycles.

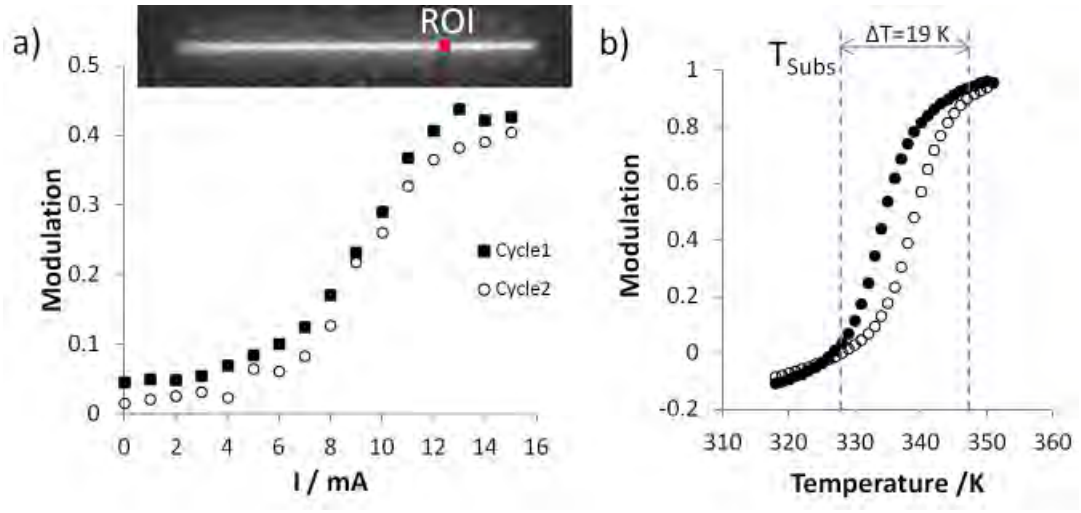

Figure 4.13: **a)** Mean variation of the luminescence modulation during two consecutive electrical cycles from 0 to 15 mA (stair case wave form) with the temperature of the substrate set to 328 K. Inset: Treated fluorescent image of the nanowire with the analyzed ROI. **b)** Thermal characterization in fluorescence mode of the thin film employed in **a**. The data has been normalized applying equation 4.2. (Open and closed symbols for heating and cooling modes, respectively.)

In a subsequent experiment, we realized that our observations could be explained, to some extent, due to water absorption/desorption processes. In order to explore the reproducibility of the luminescent response of the film with the nanowire heating in our experimental conditions, we launched an experiment of 8 cycles between 0 and 15 mA. At the end of these cycles and within the same series (the camera did not stop making acquisitions), we took a few more images to the nanowire circuit unbiased for the LT reference and then we heated the substrate to obtain a few images for the HT reference. However, this time we cool down to 328 K again and subsequently, during only one more acquisition we put 15 mA directly into the nanowire. Figure 4.14 displays the average modulation of the luminescence of the pixels inside the same ROI analyzed before. (The images taken during the heating and cooling process for the HT image have been removed for simplicity). Here, it is possible to depict for all the cycles a modulation of the same order of magnitude of that from in our previous experiment (≈ 0.4) as well as a general decrease of the luminescent signal as the cycles advanced. The latter observation could be associated on one hand, to photobleaching effects, but on the other, to a water absorption process of the thin film as a function

of time. This gain of water would favor the LS state form of the film and lead to a progressive decrease of the overall luminescence. Thus, after the nanowire device is heated for the HT reference image, the film loses some water that is not immediately recovered when the substrate is cooled down to 328 K. Consequently, a partial recovery of the modulation efficiency of the luminescence is observed when the 15 mA are sent to the nanowire.

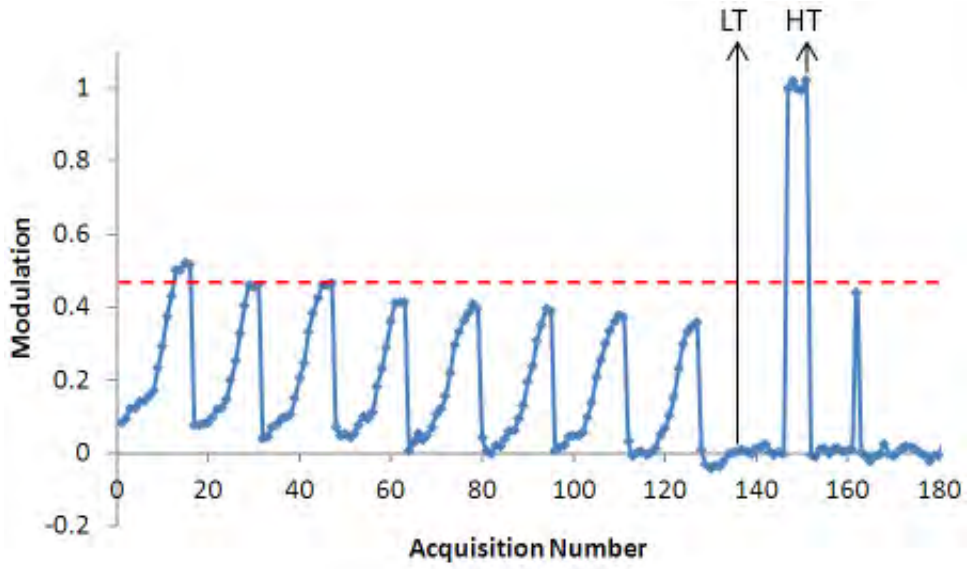

Figure 4.14: Average modulation of the luminescence of the pixels inside a ROI placed on the same nanowire studied in figures 4.12 and 4.13.

Another possible explanation for the lack of luminescence at the "saturation point" reached with the nanowire heating, could be that we are able to induce a thermal SCO transition only to one portion of the film. Several attempts were done to reach higher values of luminescence by sending more current to the wire (up to 20 mA, $\Delta T \approx 45$ K). However, these experiments ended up on permanent damage of the films without any perceptible increment of the luminescence or the rupture of the nanowire.

4.5 Conclusions

We have explored for the *first time* the use of novel *two-element systems composed of spin crossover nanoparticles and organic luminophores for thermometry and high spatial resolution imaging purposes*. In contrast to other luminescent approaches, our system displays an increase of its luminescent response as the temperature augments. Additionally, the versatility obtained with these SCO nanoparticle based probes provides the possibility not only of obtaining the inverse behaviour by working with an overlap on the absorption band in the near-infrared, but also a two-colour measurement strategy can be conceived by employing two wavelengths at the same time (visible and NIR). This last approach is very effective for avoiding problems of signal drift.

The great benefit from our system relies on the fact that *the temperature range where the spin transition of the particles takes place can be tuned by well known chemical synthesis methods and without necessarily modifying the luminescent agent*. This can be translated into a *flexible design* when it comes to the *sensitivity* and *working range* of the probe at a *fixed wavelength*. Furthermore, particles with a gradual transition could be employed for real-time thermometry while others exhibiting a thermal hysteresis loop (memory effect) can be used to detect ex-situ the overshoot of a certain threshold temperature whenever real-time measurements cannot be accomplished.

In particular, we have demonstrated that *thin films* of $[Fe(hptrz)_3](OTs)_2$ doped with rhodamine 110 *can be successfully employed as luminescent surface temperature sensors with high spatial resolution*. To this purpose, we have spin coated a thin film of our hybrid nanomaterial on gold nanowire circuits. Then, highly localized temperature variations on the circuit were produced by Joule effect when a current was passed through the nanowires. The heat produced by the nanowires locally induced LS→HS transitions on SCO film that were later detected in luminescence microscopy. To make these experiments, a setup where the detector, the excitation light and the current source of the circuit were synchronized in order to perform several electrical cycles. Additionally, to have a reliable analysis of the information, an image processing protocol was established and programmed into a toolbox of macros and functions developed in ImageJ software.

Our experiments revealed some issues concerning the calibration of the probe in order to successfully infer a temperature value from a measurement in luminescence. These challenges seem to be related on one hand to photobleaching effects (in the long term, due to the high temperature of the film and the presence of oxygen) and on the other to water absorption/desorption processes of the samples during our measurements. Further experiments with the nanowire circuits in a controlled N_2 atmosphere could provide valuable information for better understanding our observations. For this reason, our team has bought a new cryostat with this feature and also with embedded electrical connections. Unfortunately, the delivery time of the instrument is out of the course of this thesis work.

In spite of these challenges, exciting perspectives can be imagined for studying these luminescent SCO films together with the nanowire platform. For example, the films can be employed for characterizing the *dynamic thermal response* or the nanowires with

the fluorescence microscopy setup equipped with our intensified charge coupled device (ICCD camera). This way, we could perform *pump-probe experiments* of luminescence *imaging* and *spectroscopy* with *high temporal resolution*. Complementary, it is possible to exploit the *near field scanning optical microscope* (NSOM), recently bought by our team, to characterize the temperature distribution on the nanowire circuit with an *optical lateral resolution underneath 100 nm* (depending on the aperture diameter of the optical fiber). These two experiments may provide valuable insights of the thermal behavior of the nanowire devices with unprecedented temporal and spatial resolutions.

General Conclusions and Perspectives

The fundamental study of *size reduction effects in SCO* as the number of interacting metallic centers diminishes constitutes one of the most active research areas in the SCO community. Hence, the main motivation for this work has been attempting to understand the differences of the spin crossover phenomenon when going from bulk macroscopic materials to *isolated nano-objects*, where the increase of the surface / volume ratio is expected to alter the overall physico-chemical properties of the material.

The central aim of this thesis was to develop a method for performing the *detection* of the SCO properties in a *single nano-object*. Current characterization techniques are restricted to the observation of a significant number or ensemble of objects; these methods are not sensitive enough to detect the SCO in a single object of a few tens of nanometers in size. As a result, these measurements involve *strong averaging effects* produced by the observation of several objects with different degrees of size dispersion and composition. To solve this problem, we proposed luminescence as an alternative and sensitive characterization method; we aimed to introduce a luminescent agent into SCO nanomaterials in order to probe their SCO properties via luminescent detection. During the course of this work, we have developed this concept in two main stages. First, we developed hybrid materials with SCO and luminescent functionalities and second, we explored *the luminescent detection of SCO in a single nano-object*.

For the development of luminescent SCO nanomaterials, we have chosen a luminescent doping approach. We employed different organic luminescent dyes that displayed a strong emission at green wavelengths; *i.e.*, that overlapped the characteristic LS absorption band of the Triazole-based ferrous SCO complexes centered at 540 nm. We have shown the immense versatility of this approach by developing different luminescent doped SCO triazole nanomaterials, with different SCO properties, in both colloidal suspensions and powder samples of different shapes and sizes. Furthermore, we are able to do this without the necessity to change the luminescent agent. *These systems are the first of their kind reported in the literature to display an effective modulation of their luminescence upon the SCO.* In most cases the transition curves obtained from these systems in luminescence mode are very similar to those obtained from reflectivity or transmission measurements as a function of temperature. Thus, we have demonstrated that *it is possible to integrate an organic luminophore dye with SCO nanomaterials and use it as a probe for performing detection of SCO with negligible*

impact on their original properties.

In order to exploit the luminescent detection down to the limit of a single SCO molecule, we have focused our efforts on reaching an efficient FRET between the luminophore and the SCO metallic centers. To accomplish this, in addition to a significant overlap between the two entities, it is necessary to place them in close proximity. It has been shown that there are different strategies to increase the probability of incorporating the luminescent agent into the SCO material - close to the metallic centers. We have developed some of these strategies through the use of different luminophores that could eventually play the role of a guest (rhodamine 110), a counter anion substitute (alizarin red S, calcein) or a coordinating ligand substitute (acridine orange). From these attempts, we have identified the *rhodamine 110* and *acridine orange* molecules as fairly stable molecules under our experimental conditions. Depending on the synthetic method, these molecules have allowed us to develop luminescent SCO systems with modulation of the luminescence in a LS→HS transition of up to 400%. These modulations cannot be easily explained solely due to a radiative energy transfer between the luminophore and the SCO material and indicates the success of our strategy.

We have estimated the characteristic R_0 for a sensitizer - acceptor pair (S-A) with the optical properties of one of our selected luminophores (acridine orange or rhodamine 110) and [Fe(*hptrz*)$_3$](OTs)$_2$. It has been demonstrated that its value is in the range of 1 to 2 nm. Consequently, while using this type of luminophore it is not necessary to bring them too close to the iron centers of the SCO material in order to reach high energy transfer rates. With a setup sensitive enough, these luminophores could be employed to probe the SCO of an iron center as far away as 4 nm ($2R_0$) obtaining a modulation of the luminescence upon the SCO equivalent to 1.5 %.

These luminescent SCO systems enabled us to explore the luminescent detection of SCO down to a single nano-object. However, to succeed in this task we needed not only a suitably sensitive characterization technique, but also an isolated object to perform the measurement in the most optimal conditions. For this reason, we worked on the organization of SCO nanomaterials in two different levels of complexity for the detection: *spin coated thin films* of SCO nanomaterials and *isolated SCO nano-objects* by different methods.

We have been able to elaborate high quality thin films of luminescent doped SCO systems over large surfaces of different substrates. Our first attempts revealed issues with the amount of SCO material deposited in the films (too dilute) and its stability after the deposition process. Therefore, in order to depose a thin film of non-diluted SCO nanomaterial, we have developed a homogeneous chloroform solution of the [Fe(*hptrz*)$_3$](OTs)$_2$ complex with a low degree of polymerization that can be easily doped with our organic luminophores. From this system we have also succeeded to deposit high quality thin films, with a tunable thickness (from a few tens to a few hundred nanometers), composed of non-diluted SCO material that was stable after the deposition process. Here, *for the first time via luminescent detection and in spite of its negligible absorbance in the visible range, we have been able to follow the SCO phenomenon in thin films down to the thicknesses of just a few tens of nanometers.*

The energy transfer mechanism in the [Fe(*hptrz*)$_3$](OTs)$_2$ homogeneous chloroform solution doped with acridine orange was studied by luminescence lifetime measurements combined with a Stern-Volmer plot analysis. *These studies revealed a large degree of static quenching in solution, suggesting a highly efficient non-radiative enery transfer between the acridine orange molecules and a second entity* (probably the SCO nanomaterial in the solution). Preliminary lifetime studies of this type of solutions as a function of temperature have been also carried out; they indicate the same quenching mechanism, which becomes less efficient as the system goes from LS to HS state. In this section of the thesis we have shown how time resolved measurements in solution can constitute a powerful tool to understand the quenching mechanisms occurring in our luminescent SCO systems.

The detection of SCO in a single nano-object is not sufficient, it is also necessary to be able to correlate the SCO properties to the morphology of the object under observation. To achieve this, we have shown that it is necessary: (1) to appropriately disperse the SCO nano-objects with a separation higher than the spatial resolution of the optical microscope and (2) have a way to find the object independently of the characterization technique employed (optical microscope, AFM, SEM). Thus, we have explored different methods to organize SCO nano-objects or to depose them onto substrates with embedded features that could be recognized using all microscopy techniques.

Our first attempts for organizing SCO nanoparticles suspended in diverse solvents were carried out with a capillary-convective directed assembly technique. However, this technique presented the difficulty that the solvents where our SCO nanoparticles could be safely suspended (without oxidation) seriously lowered the yield of the assembly process. However, all of these experiments helped us to develop a whole set of novel approaches to obtain isolated SCO objects, leading to an *in situ* synthesis of organized SCO luminescent doped nano-objects of [Fe(*hptrz*)$_3$](OTs)$_2$. We have demonstrated the possibility of patterning regular arrays of SCO nano-objects with a nanopatterned PDMS stamp using the SCO chloroform system and a soft lithography approach, derived from the solvent-assisted micromolding technique (SAMIM). *For the first time, we have been able to simultaneously detect the SCO in many isolated nano-objects for sizes down to 150 nm.* Given the fact that the chloroform system *has a complete absence of additives*, we can totally *discard any possible matrix effect* in the properties of the SCO objects under observation. This type of sample provides *for the first time the opportunity to determine the spin transition curves of single objects and their corresponding morphologies for multiple isolated particles in a parallel manner*, employing a combination of complimentary microscopy techniques.

One shall not forget that the luminescent detection of the SCO properties for several isolated objects as a function of temperature generates a high number of images. After each experiment these need to be treated and they are not necessarily aligned; this complicates the analysis of the observations and may render it inaccurate and/or excessively time consuming when it is done manually. To solve this, an image registration routine under MATLAB environment based on cross-correlation has been developed to post treat and automatically compensate the drift generated on each

image due to the temperature ramp applied to the sample. Such computer aided strategies appear thus indispensible to facilitate and make more reliable analysis of the acquired data.

In an approach more oriented towards application, we have shown how the luminescent SCO dot arrays could eventually be integrated into photonic devices to work as real time monitoring gas/vapor sensors. Also, *the potential of the luminescent SCO thin films to detect temperature variations with high spatial resolution* while imaging gold micro/nano wires heated by Joule effect has been demonstrated. The possibility for tuning the SCO properties (transition temperature, abruptness) independently of the luminescent probe provides a unique flexibility to these two-element systems, providing a versatile platform for thermometry and thermal imaging that can be employed in diverse scenarios.

All the developments achieved during the course of this thesis raise exciting perspectives that may lead to fruitful research not only from a fundamental point of view, but also towards the development of devices based on SCO nanomaterials. Among these we can mention:

- An option to improve the modulation of the luminescence upon the SCO is the doping of SCO materials with *a luminescent metal ion that can replace some SCO active metal centers*. Completely new strategies may be also envisaged; for example, developing *SCO materials in which the metal ions display both functionalities*. Manganese may be a good candidate due to its potential to present luminescent properties and also to form SCO complexes.

- The development of polymer free SCO nanoparticles of a few tens of nanometers in size that are stable in water or ethanol for long periods of time could be employed to exploit the capillary-convective directed assembly technique.

- The luminescence lifetime experiments on the doped versions of the $[Fe(hptrz)_3](OTs)_2$ chloroform solution may allow us to elucidate the manner in which the luminophore is attached to the complex (permanently or weakly bonded). To this purpose, thorough observations should be performed as a function of temperature and diverse luminophores to build different Stern-Volmer plots. Complimentary experiments can be performed on luminescent thin films of this complex by observing the variation of its luminescence lifetime as a function of temperature. These observations could eventually be corroborated with photobleaching rate measurements.

- The limits of the technology employed for generating the Si master of the PDMS stamps or the molding capacity of PDMS has not been reached yet. The SAMIM derivative technique developed in this thesis combined with luminescent detection could be employed to *acquire relevant statistical data about the size reduction effects in SCO materials*. Such systematic studies represent a huge fundamental interest.

- Further work involving the calibration of the luminescence of the SCO thin films as a function of temperature is necessary to fully exploit these type of systems

in thermometry imaging applications. However, these films can already be employed for *characterizing the dynamics of the heating response* in gold micro/nano wires employing a cryostat with a N_2 controlled atmosphere in combination with a time resolved setup equipped with a gated CCD camera. This way, we could perform pump-probe experiments and profit the short response time of our system (≈ 5 ns) *to image with high temporal resolution the power dissipation in the wires* (μs range).

- The use of a *near field scanning optical microscope* (NSOM) may allow us to perform *luminescence measurements with a spatial resolution underneath 100 nm*, opening exciting perspectives for the study with luminescence detection our luminescent SCO nanodots and the power disipation in the nanowire platform with unprecedented spatial resolution.

Appendix A

Nanomatériaux Luminescents à Transition de spin : Propriétés physiques et Applications

Contents

A.1 Phénomènes de luminescence et de transition de spin

Ce chapitre commence par une introduction générale sur les matériaux luminescents avec un accent particulier sur le transfert de l'énergie de luminescence puis présente le phénomène de transition de spin.

A.1.1 Matériaux luminescents

Ces matériaux absorbent le rayonnement électromagnétique (la lumière) puis ré-émettent une partie de celui-ci à une longueur d'onde différente. En général, la luminescence conduit à la conversion de types spécifiques de l'énergie en rayonnement au-delà du rayonnement thermique. La photoluminescence est un cas particulier de la luminescence qui peut être divisé en deux étapes principales (excitation et relaxation) qui sont généralement représentées dans un diagramme de Jablonski comme le montre la figure A.1.

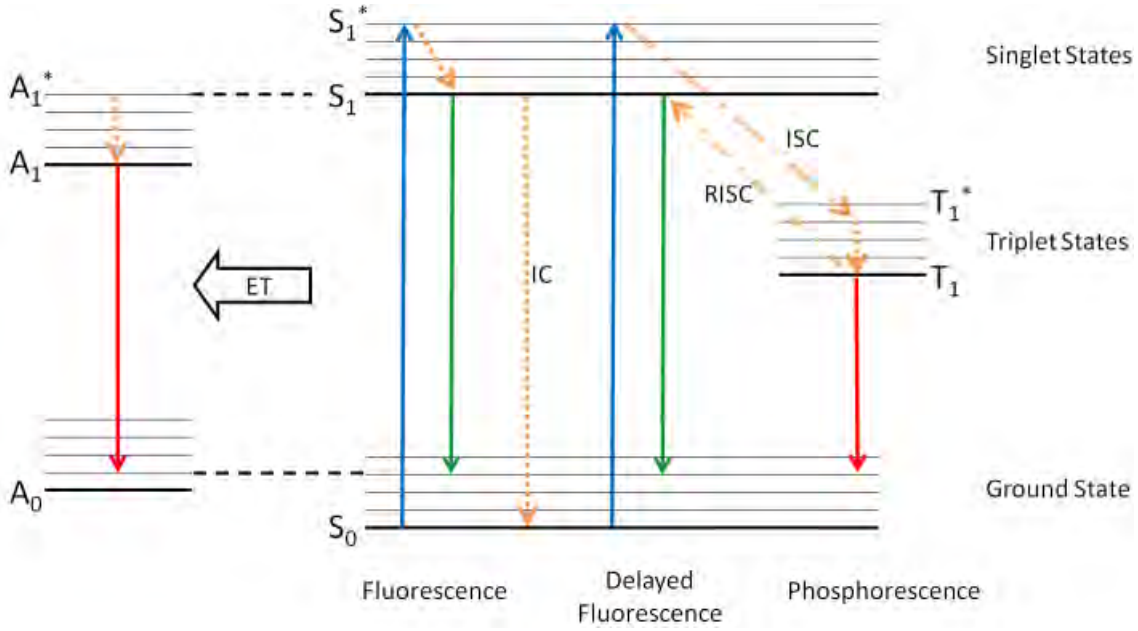

Figure A.1: Diagramme de Jablonski montrant l'excitation, la conversion interne (IC), la fluorescence, le croisement intersystème (ISC), le croisement inverse intersystème (RISC), la phosphorescence, la fluorescence décalée et le processus de transfert dénergie (ET).

A.1.1.1 Photo-excitation de matériaux luminescents

Le diagramme des courbes d'énergie potentielle d'un centre d'absorption en fonction d'une coordonnée interne de la molécule est utilisé (Figure A.2) afin de connaitre et d'expliquer les différentes caractéristiques de structure de bandes ou de raies dans les phénomènes d'absorption et d'émission de divers matériaux et montre aussi leur

dépendance à la température et la pression. Il permet donc de décrire les origines des transitions optiques ainsi que leur largeur.

Une autre caractéristique à considérer est l'intensité de ces transitions qui peut être modifiée par beaucoup de facteurs : les règles de Laporte (transition de même symétrie interdite), les règles de sélection de spin (changement de multiplicité de spin interdit), les couplages spin-orbite, électron-vibration, des termes inégaux du champ cristallin, *etc.* Ainsi, le spectre d'absorption d'un centre luminescent diffère souvent s'il s'agit d'un ion libre / molécule ou coordiné à différents types de ligands. Le coefficient d'extinction molaire (ϵ) et la force d'oscillateur (f) sont souvent utilisés pour comparer les intensités des bandes d'absorption d'un matériau donné. En outre, d'autres facteurs peuvent modifier l'absorption d'un matériau et sont regroupés dans la loi de Beer Lambert (A = ϵlc).

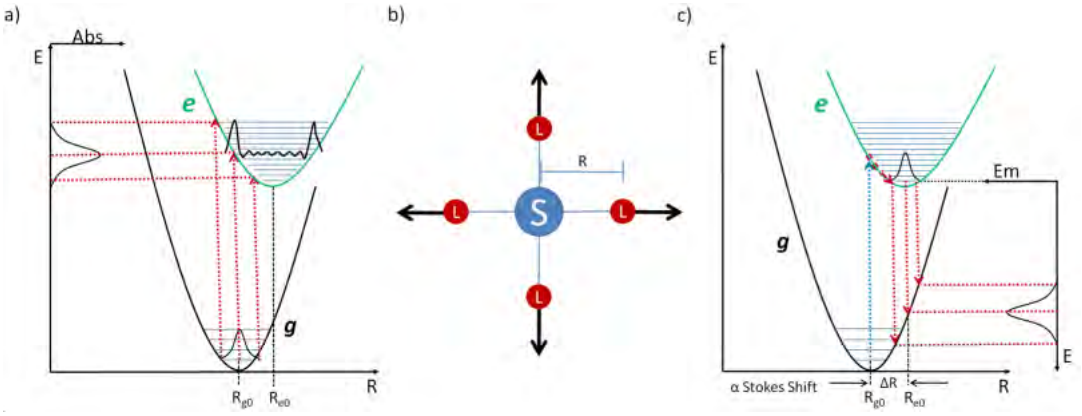

Figure A.2: **a)** Diagramme de l'énergie potentielle en fonction de la distance metal - ligand R pour l'état fondamental et un état excité pour le système représenté en b) dans un processus d'absorption optique. **b)** Centre d'absorption avec quatre ligands oscillant dans le mode d'élongation symétrique. **c)** Processus de relaxation par émission d'un photon.

A.1.1.2 Retour à l'état fondamental

Après l'excitation, le système peut réaliser d'abord une IC en passant dans le plus bas niveau d'énergie du puits de potentiel de l'état excité ($\boldsymbol{e_0}$). Par la suite, le système passe de l'état excité ($\boldsymbol{e_0}$) à l'état fondamental ($\boldsymbol{g_n}$) par une transition radiative (émission d'un photon, luminescente (L)) ou par transition non radiative (non luminescente NL). Enfin, le système peut encore réaliser une deuxième IC en passant dans le plus bas niveau d'énergie du puits de potentiel de l'état fondamental ($\boldsymbol{g_0}$). Le déplacement de Stokes (ΔE entre les photons excités et les photons émis) donne des informations directes sur ΔR des états excité et fondamental. Un grand déplacement de Stokes entraîne un plus grand ΔR et donc une plus large bande d'émission du système. Ainsi, l'émission d'un centre luminescent sera sensible à la rigidité de son environnement et aux interactions avec les espèces environnantes. En outre, il est également possible de confirmer que les longueurs d'onde des émissions sont pratiquement indépendantes de l'énergie d'excitation, à condition qu'elle soit suffisamment élevée pour peupler l'état excité [2].

A.1.1.2.1 Retour radiatif

Les paramètres clés pour étudier la luminescence sont la durée de vie de luminescence et le rendement quantique. Le temps T auquel le système quitte l'état excité $\boldsymbol{e}$ est une variable aléatoire continue avec une densité de probabilité $p_{_T}(t)$. La durée de vie ($\tau_{_e}$) est définie comme la espérance mathématique de T et se calcule grâce à la formule :

$$< T > \ = \int_0^\infty t \cdot p_{_T}(t) = \frac{1}{k_{_L} + k_{_{NL}}} = \tau_{_e} \ , \tag{A.1}$$

où k_L et k_{NL} sont les taux d'émission spontanée et non radiative du centre actif, respectivement.

Le rendement quantique (Q) est le rapport entre le taux d'émission spontanée du centre actif et son taux de sortie totale de l'état excité. Ce définie comme:

$$Q = \frac{k_{_L}}{k_{_L} + k_{_{NL}}} \ ; \tag{A.2}$$

ce rendement permet de mesurer combien de fois le système se désexcite par voie radiative par rapport à ses processus de relaxation totale.

De plus, les électrons dans l'état excité sont susceptibles de subir une conversion de spin et de passer à un niveau inférieur excité avec une multiplicité différente de celle de l'état fondamental, même si le remplissage d'un niveau excité avec une multiplicité différente à celle de l'état fondamental est peu probable (règle de sélection de spin). Ce processus est connu sous le nom de croisement intersystème (ISC) et permet d'avoir deux émissions radiatives différentes :

- Fluorescence: luminescence obtenue avec $\Delta S = 0$. Cette transition est permise, ce qui engendre un processus rapide et une durée de vie courte $\approx 10^{-7} - 10^{-5}$ s.
- Phosphorescence: luminescence obtenue avec $\Delta S \neq 0$. Cette transition est interdite, ce qui engendre un processus plus lent et une durée de vie plus longue $\approx 10^{-3} - 1$ s voire plus.

A.1.1.2.2 Retour non radiatif

L'énergie qui a été absorbée et n'a pas été émise sous la forme d'un rayonnement doit être dissipée sous forme de chaleur à l'environnement par l'intermédiaire d'un IC. Si deux puits de potentiel présentant une différence ΔR et si l'énergie de l'état excité est suffisamment haute, le système peut se relaxer en passant à travers un point de croisement des deux puits de potentiel et ainsi revenir à l'état fondamental avec des émissions non radiatives. Ces transitions sont des processus primaires concurrents de la luminescence. Ainsi, toutes les bandes sur le spectre d'absorption n'engendreront pas forcément des transitions luminescentes. C'est pourquoi il est plus intéressant d'étudier le spectre d'excitation pour des matériaux luminescents : il permet de connaître à la fois les longueurs d'onde d'absorption et celles d'émissions luminescentes.

Un phénomène supplémentaire à considérer dans le contexte de la relaxation vers l'état fondamental par voies non-radiatives est la photodestruction du système pendant

l'état excité ou *photoblanchiment* , modifiant, de façon irréversible, la structure du luminophore qui n'absorbe ou n'émet pas la lumière. Ces processus possèdent une échelle de temps de quelques secondes ou minutes (selon la puissance de l'excitation), temps dix fois plus grand que celui de la fluorescence. Par conséquent, une interprétation prudente du spectre d'émission en fonction du temps est nécessaire, en particulier dans le cas d'expériences avec des longues durées d'exposition et / ou excitation de forte puissance.

A.1.1.3 Transfert d'énergie

L'énergie d'excitation se dissipe dans le système soit grâce à la même entité qui l'a absorbée (avec de transitions radiatives ou non radiatives), soit par sa transmission d'un endroit à un autre dans un milieu donné (transfert d'énergie). Cette transmission constitue le mécanisme par lequel un matériau luminescent à transition de spin fonctionnera et utilise deux entités: un agent de sensibilisation (S) responsable de l'absorption de l'énergie d'excitation et un accepteur (A), qui reçoit l'énergie du sensibilisateur excité.

A.1.1.3.1 Transfert d'énergie radiatif

Le transfert d'énergie radiatif, également connu sous le nom de processus d'émission-réabsorption est le cas trivial où le sensibilisateur (S) absorbe de l'énergie, émet un photon, puis l'accepteur (A) réabsorbe le photon émis. Si l'accepteur excité est un luminophore, il va émettre un deuxième photon et nous aurons une luminescence en cascade [3]. Toutefois, si l'accepteur dissipe l'énergie, un effet d'extinction ou *quenching* (suppression de luminescence) sera observé.

A.1.1.3.2 Transfert d'énergie non radiatif

On considère une paire sensibilisateur-accepteur (SA) fixé dans un matériau, séparés par une distance, r_{SA}. Si r_{SA} est suffisamment petite pour qu'il y ait une interaction non nulle entre eux (comme un chevauchement de fonctions d'onde ou une interaction électrique ou magnétique multipolaire) ou qu'il y ait un chevauchement spectral entre les deux (condition de résonance), il existe une probabilité par unité de temps que l'énergie soit transférée de S à A par un procédé non-radiatif, c'est à dire sans émission-réabsorption d'un photon. Contrairement à un transfert d'énergie radiative, dans un FRET (transfert d'énergie par résonance Förster), S et A sont en interaction, se comportant comme un seul système (Figure A.3). Ainsi, le taux de transfert k_T pour une paire donnée SA séparée par une distance r_{SA} est défini par l'équation [163]:

$$k_T = \left(\frac{1}{\tau_S}\right)\left(\frac{R_0}{r_{SA}}\right)^6 , \tag{A.3}$$

où R_0 est la distance de Förster de la paire SA définie comme :

$$(R_0)^6 = \frac{9000(ln10)k^2Q_s}{N_A 128\pi^5 n^4}\left[\frac{\int_0^\infty \epsilon_A(\lambda)F_S(\lambda)\lambda^4 d\lambda}{\int_0^\infty F_S(\lambda)d\lambda}\right] . \tag{A.4}$$

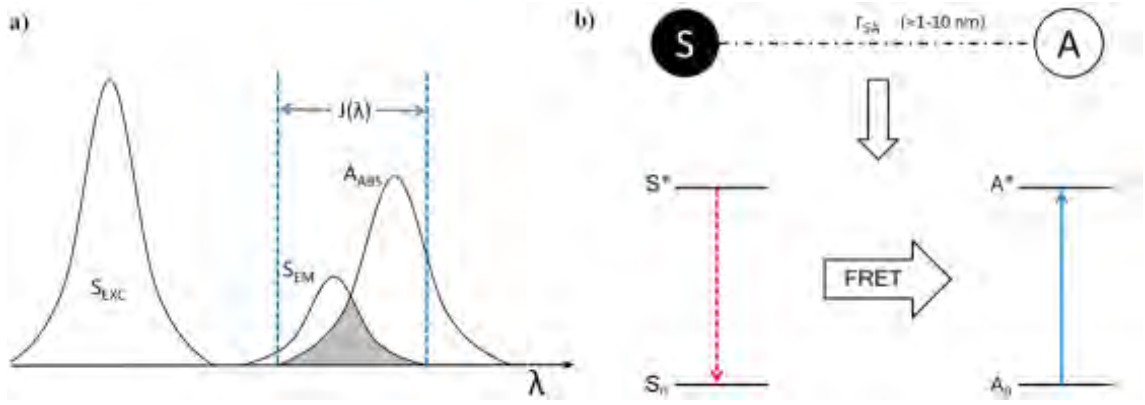

Figure A.3: **a)** Chevauchement spectral (condition de résonance) entre S et A. **b)** Schéma d'un transfert d'énergie résonant entre deux centres.

Chaque fois que A est assez proche de S, la durée de vie de l'état excité de S et sa réponse radiative sont réduites en raison de la voie de relaxation supplémentaire créée par le FRET. Ainsi, le FRET est un phénomène très sensible à la distance r_{SA} et est souvent utilisé pour mesurer les distances entre A et S dans une molécule. Il peut constituer un outil puissant permettant de déduire l'information spatiale en dessous de la limite de diffraction en utilisant la lumière visible. En outre, si S et A sont tous les deux luminescents, la luminescence de A peut être utilisée comme marqueur pour indiquer les points spécifiques où les deux espèces luminescentes, qui ont été répartis de façon indépendante dans un milieu, entrent en contact. Une autre application intéressante du FRET est l'analyse de l'environnement local de la paire SA. Le transfert d'énergie non radiatif est sensible aux fluctuations des propriétés optiques de la paire; tout changement de leur environnement local pourrait conduire à un changement de l'orientation des dipôles, d'émission et d'absorption ou des rendements quantiques impliqués dans le processus et par conséquent une variation drastique de k_T.

A.1.2 Introduction sur la transition de spin (TS)

Certains complexes de métaux de transition ($3d^4$ - $3d^7$) peuvent commuter d'un état bas spin (BS) à un état haut spin (HS) sous l'application d'un stimulus externe, c'est la transition de spin (TS). La commutation entre les deux états de spin est accompagnée d'un changement significatif de la forme et du volume moléculaires en raison du changement de la sphère de coordination du métal, ce qui entraîne des variations des propriétés magnétiques, optiques, mécaniques, électriques, *etc.* du matériau. Nous allons nous concentrer principalement sur les concepts importants permettant de comprendre et relier des interactions possibles entre les propriétés de luminescence et celles de transition de spin des composés. De plus, nous nous intéressons aux composés de Fe(II) car ils présentent des propriétés très prometteuses pour des applications potentielles.

A.1.2.1 Description de la transition de spin avec l'approche de la théorie du champ de ligands

Le phénomène de TS peut être expliqué par la théorie du champ de ligands (LFT). D'autre part, cette théorie est également un outil important pour comprendre les propriétés optiques des composés à TS (plus de détails peuvent être trouvés dans l'article de Hauser [23]).

Lorsque l'ion Fe(II) est complexé à six ligands, il adopte une configuration octaédrique qui entraîne la levée de dégénérescence des 5 orbitales d en niveaux de symétrie t_{2g} triplement dégénérés et en niveaux de symétrie e_g doublement dégénérés de plus haute énergie (Figure A.4a). La différence d'énergie qui sépare les deux niveaux t_{2g} et e_g est corrélée au champ cristallin par l'expression $\Delta E = 10$ Dq, où Dq est défini comme le paramètre de force du champ. Ainsi les six électrons du fer(II) peuvent alors se répartir de deux façons différentes selon les valeurs relatives du champ de ligand et de l'énergie d'appariement, des électrons, Π. Si 10Dq > Π c'est l'état bas-spin (BS, $^1A_1$), diamagnétique et si 10Dq < Π, c'est l'état haut spin (HS, $^5T_2$), paramagnétique. Le diagramme de Tanabe-Sugano de la Figure A.4b montre, pour un ion de configuration d6 dans un environnement octaédrique, qu'un état $^5T_2$ correspond à l'état HS, stabilisé par les champs faibles alors que l'état $^1A_1$ correspond à l'état BS, stabilisé par les champ forts. Ainsi, pour des complexes ayant une éclatement du champ cristallin 10Dq proche de Π, le système peut passer d'un état à l'autre sous l'effet d'une perturbation extérieure comme la température, une pression, une irradiation lumineuse ou l'application d'un champ magnétique ou électrique.

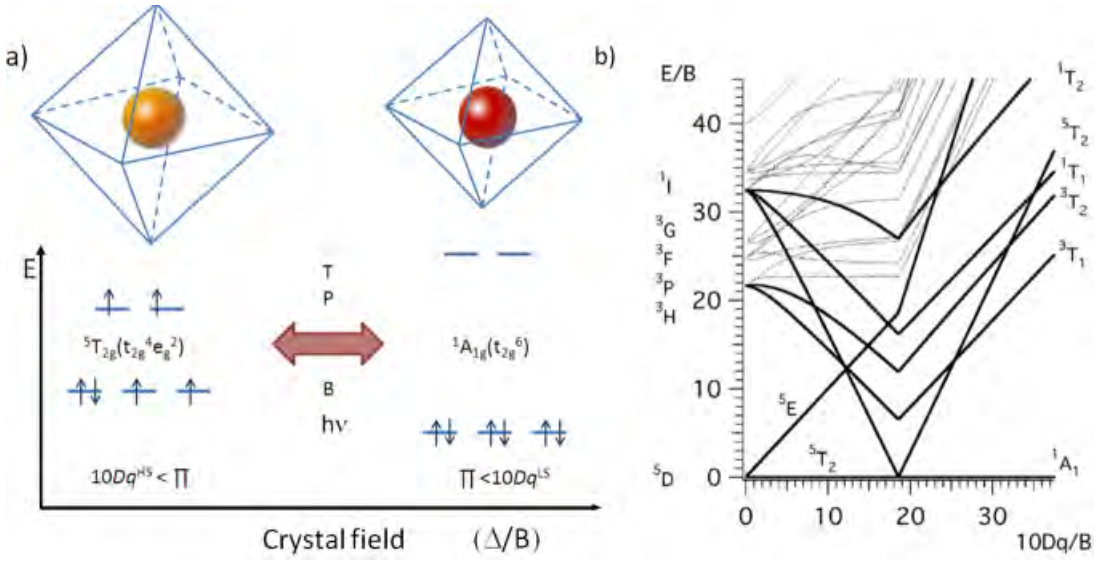

Figure A.4: **a)** Configurations électroniques haut Spin (champ crystallin faible) et bas spin (champ crystallin fort) pour un ion $3d^6$ (Fe(II), Co(III)) dans un champ électrostatique octaédrique. **b)** Diagramme de Tanabe-Sugano pour un ion $3d^6$ dans la même situation.

A.1.2.2 Transitions électroniques et propriétés optiques des complexes à transition de spin

Ainsi, le phénomène de transition de spin se produit pour une gamme étroite de forces de champ des ligands. Par conséquent, les spectres d'absorption dans le visible de différents complexes possédant le même métal central et les mêmes atomes donneurs (p. ex Fe(II)N_6) devraient être similaires. Dans la réalité, la couleur des composés peut beaucoup varier en raison de l'apparition de différentes transitions de transfert de charge metal - ligand (MLCT) dans le domaine du visible. Par exemple, les spectres d'absorption optique de monocristaux du complexe $[Fe(bbtr)_3](ClO_4)_2$ (bbtr = 1,4-di (1,2,3-triazole-1-yl)) ont été étudiés dans les domaines visible et proche infrarouge (Figure A.5) [37]. L'état HS présente seulement une bande d'absorption de faible intensité vers 830 nm correspondant à la transition $^5T_2 \rightarrow {}^5E$, donnant un composé presque incolore, alors que l'état BS présente deux bandes très intenses, la première à $\approx$ 590 nm correspondant à la transition $^1A_1 \rightarrow {}^1T_1$ et la deuxième qui commence à $\approx$ 430 nm correspondant à un transfert de charge metal-ligand, donnant au composé une couleur pourpre. De plus, les matériaux à TS présentent également d'importants

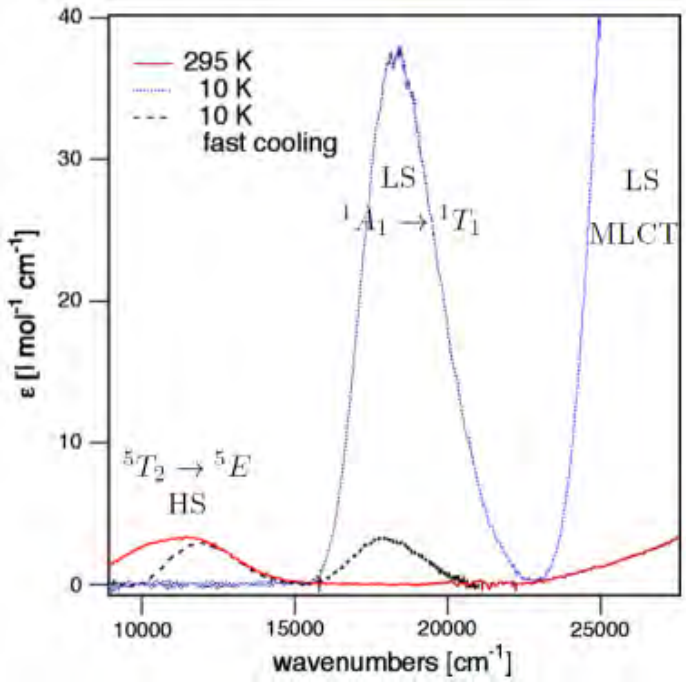

Figure A.5: Spectre d'absorption d'un monocristal de composé $[Fe(bbtr)_3](ClO_4)_2$ à 295 K (rouge) et 10 K (bleu) [37]

changements de l'indice de réfraction, principalement en raison du changement de densité lors de la transition provenant de l'augmentation du volume de la maille.

A.1.2.3 Détection de la transition de spin

Différentes techniques courantes peuvent être utilisées pour détecter la transition de spin : les mesures de susceptibilité magnétique, la spectroscopie Mössbauer, la diffrac-

tion des rayons X, les mesures de capacité calorifique, les spectroscopies IR et Raman, les mesures de spectres électroniques, *etc.* Des techniques émergentes sont aussi développées : la mesure du changement d'indice de réfraction, des mesures électriques comme la conductivité, *etc.*

Parallèlement aux méthodes existantes pour la détection de la transition de spin à l'échelle macro, micro et nanométrique, l'objectif de cette thèse est d'utiliser la détection de la fluorescence comme un puissant nouvel outil pour caractériser les matériaux à transition de spin, à une échelle allant jusqu'à la molécule unique.

A.2 Matériaux combinant les propriétés de transition de spin et de luminescence

Dans les complexes de Fe(II) triazole, il est difficile de savoir où se situe l'agent dopant. Cependant, la structure en chaînes de ces composés permet d'avoir une faible distance entre les cations de fer et les agents dopant, ce qui peut permettre un transfert d'énergie et d'avoir une bonne efficacité de FRET. Différents scénarii sont envisagés en fonction du rôle du luminophore dans le matériau: molécule invitée, contre-anion, ligand de coordination ou centre métallique de coordination (Figure A.6). Dans tous les cas, le niveau de dopage est faible (moins de 1% en moles de luminophore par mole d'atome de fer).

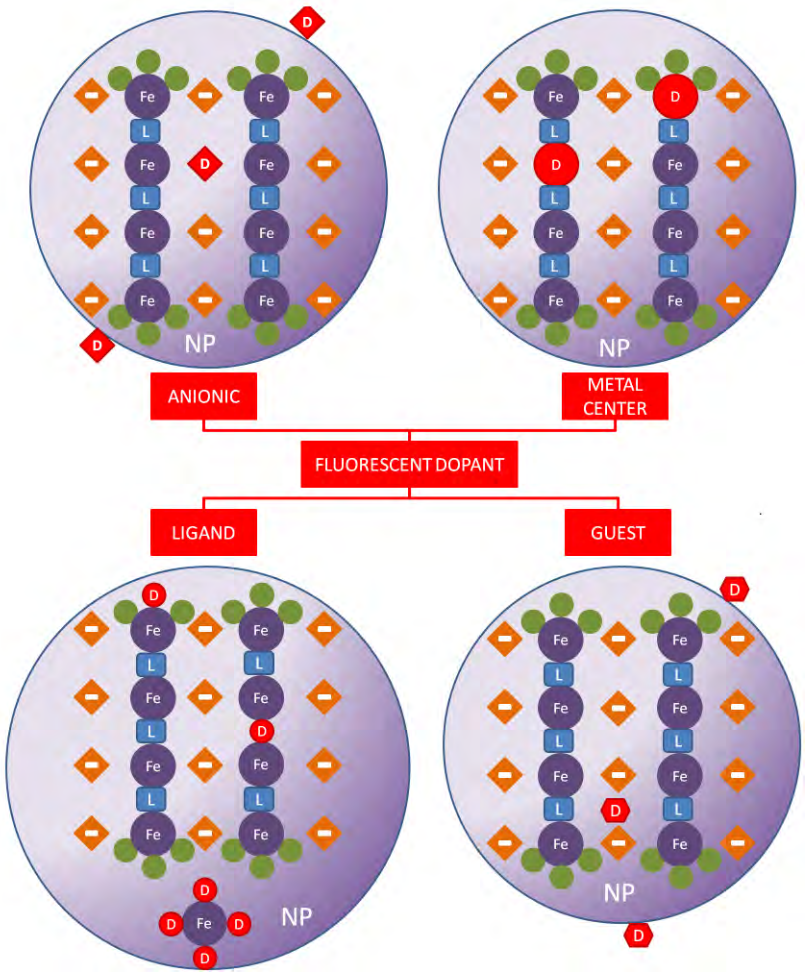

Figure A.6: Schéma des scenarios possibles pour l'emplacement d'un agent luminescent dans des nanoparticules de structure Fe(II) triazole.

En conséquence, nous avons regroupé nos tentatives dans trois différentes stratégies qui seront discutées dans les sections suivantes.

A.2.1 Stratégie # 1 : Molécule organique luminophore invitée grâce aux micelles inverses

A.2.1.1 Synthèse des nanoparticules de $[Fe(NH_2trz)_3](A)_2$ (A = tosylate (OTs) ou NO_3^-)

Les micelles inverses sont une dispersion de gouttelettes liquides polaires stabilisée par un tensio-actif qui contient à la fois une queue hydrophobe et une tête hydrophile dans une phase huileuse.

Ces nanoparticules ont été synthétisées en utilisant la technique des micelles inverses, avec l'AOT comme agent tensio-actif ionique et la rhodamine 110 (Rh110) comme agent de dopage (Synthèse réalisée par Lionel Salmon). Rh110 a été utilisée parce que (1) elle possède une très faible extinction thermique de la luminescence autour de la température ambiante (environ 0,13%. K-1) [91], (2) son spectre d'émission ainsi que la queue de faible énergie de son spectre d'excitation chevauchent la bande d'absorption de $^1A_1 \rightarrow {}^1T_1$ des complexes de Fe(II)-triazole (3) elle présente une faible photo-extinction et (4) ses propriétés à l'intérieur des micelles inverses ont déjà été explorées [92]. Toutefois, l'AOT employée lors de la synthèse a présenté un inconvénient double : sa séparation d'avec le matériau à TS a été très difficile et il y avait un éventuel échange anionique dans les particules.

A.2.1.2 Caractérisation des nanoparticules non dopées de $[Fe(NH_2trz)_3](OTs)_2$

La suspension de nanoparticules non dopées est violette à basse température et incolore à haute température avec une transition à température ambiante. La distribution de taille des nanoparticules montre un diamètre moyen de 10 (6) nm. Les spectres d'absorption de la suspension (Figure A.7a) montrent deux bandes d'absorption dans le visible (centrée à ≈540 nm) et dans le proche infrarouge (≈660 nm) assignées aux transitions $^1A_1 \rightarrow {}^1T_1$ et $^5T_2 \rightarrow {}^5E$ respectivement. La variation thermique de l'absorbance maximale à 540 nm révèle une transition de spin plutôt abrupte avec une hystérésis thermique de largeur 9 K large (Figure A.7b). Les températures de transition lors du chauffage et du refroidissement sont 306 et 297 K, respectivement.

A.2.1.3 Caractérisation des nanoparticules de $[Fe(NH_2trz)_3](OTs)_2$ dopées avec Rh110

La suspension de nanoparticules a été caractérisée par spectrofluorimètre. Les maxima de l'excitation (475 nm) et de l'émission (541 nm) des bandes de la rhodamine 110 (Rh110) dans la suspension de nanoparticules dopées (3%) diffèrent légèrement des données de la littérature mais restent proches (Figure A.8a). La variation thermique de l'intensité de fluorescence à 540 nm est représentée dans la Figure A.8b et permet de suivre la transition de spin. Dans l'état BS, une partie de l'émission de Rh110 est absorbée par le Fe(triazole) alors qu'à l'état HS, le Fe(triazole) n'absorbe

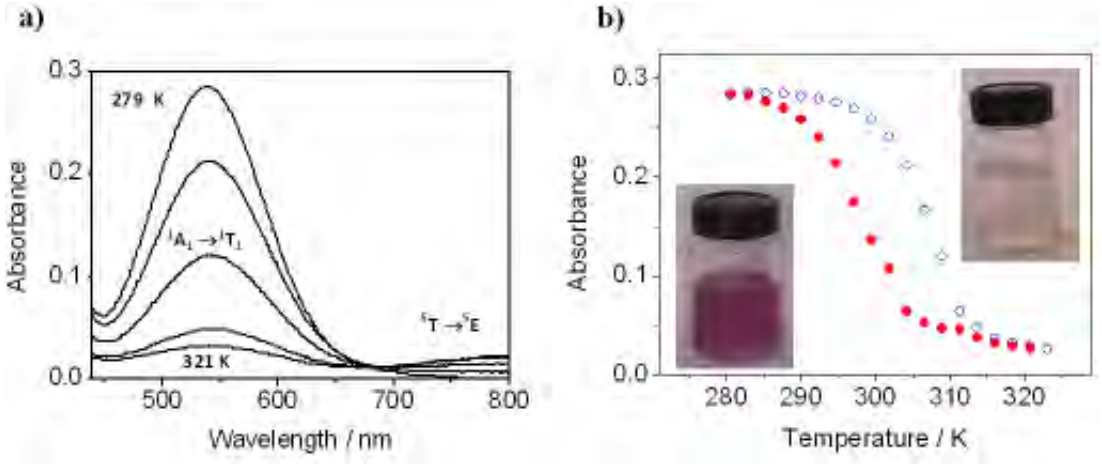

Figure A.7: Thermochromisme de nanoparticules à TS en suspension. **a)** Spectre d'absorption de nanoparticules du composé $[Fe(NH_2trz)_3](OTs)_2$ en suspension de l'octane pour différentes températures sélectionnées pendant le refroidissement. **b)** Variation thermique d'absorbance de la suspension à 540 nm pendant le chauffage (symboles ouvertes) et le refroidissement (symboles fermées). Les photos insérées montrent l'échantillon à 295 K (violet) et 320 K (transparent).

plus et l'intensité d'émission est maximale. Le changement de fluorescence peut être aussi vu à l'oeil nu. Les températures de transition obtenues à partir de cette mesure sont 306 et 301 K lors du chauffage et du refroidissement, respectivement. Les détails du mécanisme du transfert d'énergie entre les deux n'ont pas été étudiés mais nous pensons que les luminophores sont accumulés dans les micelles inverses (sous forme de molécules libres ou attachées à l'interface) et un FRET est observé. Des changements de concentration en Rh110 ou en nanoparticules ont été réalisés et donnent des résultats similaires voire moins bons (ainsi, le meilleur dopage est de 3%).

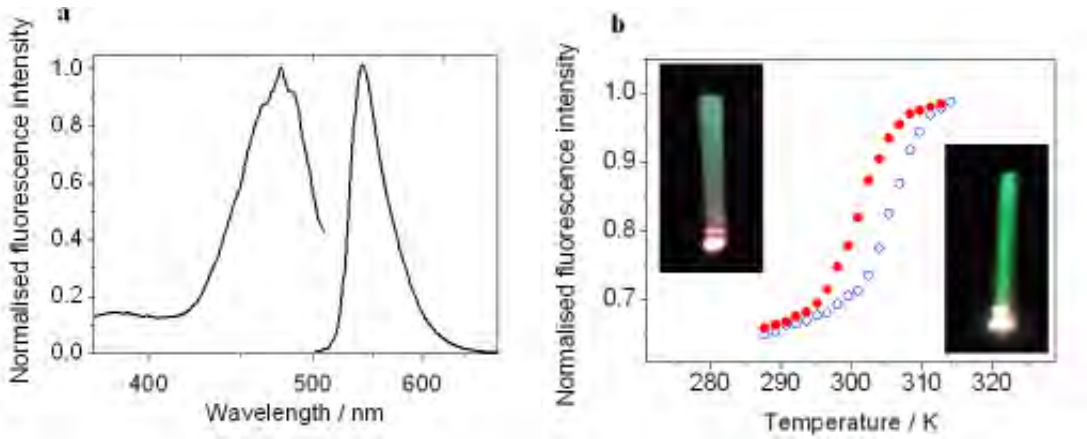

Figure A.8: Fluorescence des nanoparticules du composé [Fe(NH2trz)3](OTs)2 en suspension. **a)** Spectres d'excitation (émission à 540 nm) et d'émission (excitation à 475 nm) pour des nanoparticules de $[Fe(NH_2trz)_3](OTs)_2$ en suspension dopées avec de la rhodamine 110 (3%) à température ambiante. **b)** Variation thermique de l'intensité d'émission à 540 nm pour le chauffage (symboles ouvertes) et le refroidissement (symboles fermées). Les photos insérées montrent un échantillon (0.001% dopé) avec une source de lumière blanche comme excitation à 295 K et 320 K.

A.2.2 Stratégie # 2 : Substitution d'un contre-anion

A.2.2.1 Synthèse des nanoparticules de $[Fe(NH_2trz)_3](OTs)_2$

Ces nanoparticules ont été synthétisées grâce à la technique de micelles inverses. Du tergitol a été utilisé comme agent tensio-actif neutre afin d'éviter un éventuel échange anionique (Synthèse réalisée par Alexei Tokarev). Ce type de synthèse nous a permis d'avoir pour la première fois une suspension colloïdale et la précipitation d'une poudre de nanoparticules dopées à TS avec des quantités beaucoup plus faibles de surfactant permettant la possibilité de dispersion dans d'autres solvants. L'alizarine rouge a été employé comme agent de dopage comme substituant du contre-anion dans le complexe à TS dans le but de mieux intégrer le luminophore dans le matériau (plus près des centres Fe).

A.2.2.2 Caractérisation des nanoparticules non dopées de $[Fe(NH_2trz)_3](OTs)_2$

Les nanoparticules en suspension non dopées sont uniformes, sphériques, non agrégées et ont une granulométrie moyenne de 3,6 (0,8) nm. Le spectre d'absorption en fonction de la température a été étudié pour une suspension colloïdale contenant 2% en poids de complexes de Fe. Le comportement est similaire à celui obtenu dans la suspension du composé réalisé dans la stratégie 1. Cependant, quelques différences sont visibles (intensité des bandes) et peuvent être dues soit au tensio-actif différent, soit à la taille des particules ou autres. La poudre, quand à elle, présente des particules plus grandes (50 - 300 nm). Des études de réflectivité (comme dans la stratégie 1) sur cette poudre ont été réalisées à 543 nm en fonction de la température à l'aide du microscope afin d'étudier la transition de spin. L'échantillon déshydraté est placé dans un système clos thermostaté sous atmosphère d'azote. Les températures de transition sont de 288 K et 270 K lors du chauffage et du refroidissement, respectivement (hystérésis de 18 K). Ainsi, la croissance des nanoparticules générées lors de la précipitation des micelles inverses conduit à un changement morphologique des particules qui est associé à l'observation d'une hystérésis non présente dans la suspension colloïdale de la stratégie 1.

A.2.2.3 Caractérisation des nanoparticules de $[Fe(NH_2trz)_3]$ $(OTs)_2$ dopées avec l'alizarine rouge

La luminescence de la suspension colloïdale dopée à 0,5% molaire d'alizarine rouge a été étudiée en fonction de la température (Figure A.9). L'intensité maximale de l'excitation a été observée à environ 450 nm et celle de l'émission à 640 nm. Les échantillons ont été étudiés à 540 nm, car même si ce n'est pas le maximum d'émission, c'est autour de cette longueur d'onde qu'est attendu la plus forte modulation de la luminescence. La variation thermique de la luminescence à 540 nm montre une TS similaire à celle obtenue dans la suspension non dopée et l'intensité de la luminescence

triple entre l'état BS et l'état HS. Ceci constitue donc une amélioration par rapport à la stratégie 1.

Les échantillons de poudre dopée obtenus à partir de microémulsions analogues ont été étudiés en microscopie de fluorescence. La réponse luminescente thermique de la poudre déshydratée peut être observé à 550 nm avec une excitation de 450 nm (Figure A.10).

La luminescence du matériau augmente avec la température montrant la TS. Les températures de la TS sont de 300 K et 278 K lors du chauffage et du refroidissement respectivement, ce qui montre une hystérésis centrée autour de la même température que celle de la poudre non dopée mesurée par réflectivité. Cependant, on doit noter que la comparaison des données de réflectivité avec les mesures de fluorescence n'est pas simple car aucun de ces signaux n'est strictement proportionnel à la fraction HS.

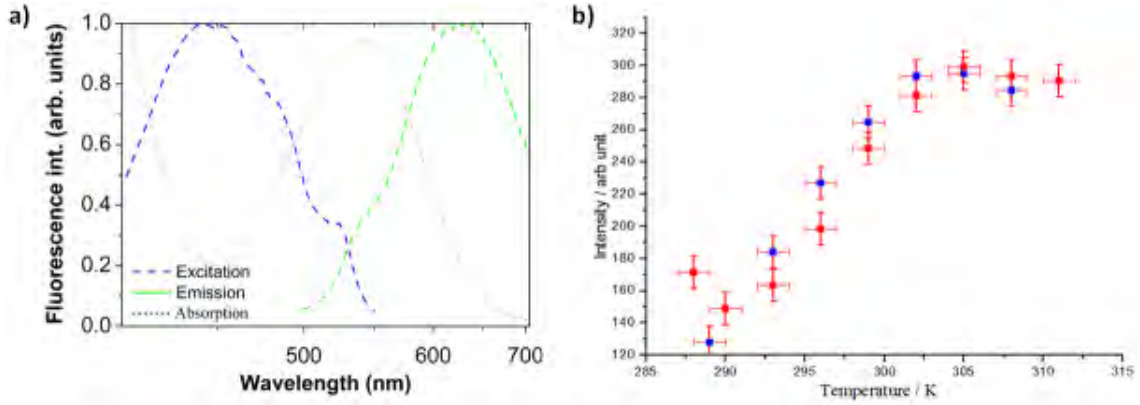

Figure A.9: **a)** Spectres d'excitation (émission à 540 nm) et d'émission (excitation à 475 nm) de nanoparticules du composé $[Fe(NH_2trz)_3]$ $(OTs)_2$ en suspension dopées avec de l'alizarin rouge superposés avec la bande d'absoprtion d-d centrée à 543 nm de l'état bas spin d'une solution analogue non-dopée. **b)** Variation thermique de l'intensité d'émission à 540 nm (excitation à 475 nm) de nanoparticules du composé $[Fe(NH_2trz)_3]$ $(OTs)_2$ dopées avec l'alizarin rouge (0.5%) en suspension.

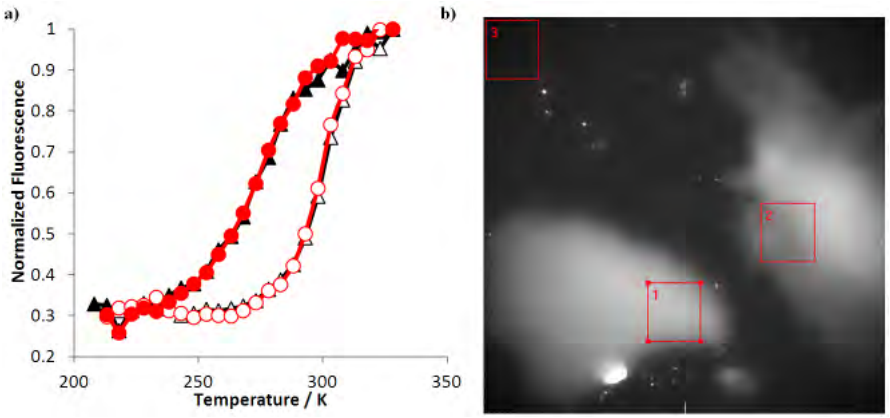

Figure A.10: **a)** Variation thermique de l'intensité d'émission à 550 nm (excitation à 450 nm) de la poudre de nanoparticule du composé $[Fe(NH_2trz)_3]$ $(OTs)_2$ dopé avec de l'alizarin rouge dans une atmosphère d'azote. (Symboles ouverts et fermés representant respectivement le chauffage et le refroidissement.) **b)** Image en luminescence de la poudre.

A.2.3 Stratégie # 3 : Synthèse dans un milieu homogène

A.2.3.1 Synthèse des nanoparticules du composé [Fe(*hptrz*)$_3$](OTs)$_2$ (*hptrz* = 4-heptyl-1,2,4-triazole)

Une autre méthode pour limiter la croissance de nanoparticules en solution implique l'utilisation d'un polymère stabilisant. Nous avons choisi le polyéthylène glycol comme agent stabilisant (PEG-3350) et un milieu aqueux pour synthétiser les micro-et nano-objets à TS sur la base du complexe [Fe(*hptrz*)$_3$](OTs)$_2$. Ce complexe est caractérisé par une transition de spin brusque avec une boucle d'hystérésis à proximité de la température ambiante (T_{up} = 318 K et T_{dwn} = 308 K pour la poudre déshydratée), température plus élevée que celle observée pour le composé [Fe(*hptrz*)$_3$](OTs)$_2$. Le ligand *hptrz*, grâce à sa longue chaîne alkyle en 4eme position de l'hétérocycle, permet d'augmenter les propriétés hydrophobes des nanoparticules correspondantes et par conséquent, il conduit à une capacité accrue de précipitations en milieu aqueux. En outre, l'insolubilité accrue des nanoparticules dans les milieux polaires permet la stabilisation de ces objets en suspension colloïdale [87]

Ces nanoparticules sont en croissance dans un milieu homogène utilisant un polymère stabilisant (PEG-3350). La Rhodamine 110, l'alizarine rouge et deux nouveaux agents de dopage, la calcéine (contre-anion substituant l'OTs) et l'acridine orange (ligand substituant l'hptrz), ont été utilisés comme luminophores (synthèse réalisée par Il'ya Gural'skiy). L'utilisation de cette approche synthétique a permis de réduire au minimum la quantité d'additifs (polymère-tensioactif) lors de la synthèse conduisant à des matériaux plus purs après les étapes de lavage.

Plusieurs avantages sont apparus en utilisant ce type de synthèses. (1) En contraste avec la micelle inverse, le processus est simple et versatile, non seulement parce que divers solvants polaires et non polaires peuvent être utilisés, mais aussi parce que l'ensemble du protocole n'implique pas une étape critique qui influe sur les résultats comme la déstabilisation de la phase micellaire par un solvant supplémentaire. (2) La quantité de polymère ainsi que la quantité de solvant utilisé pour la synthèse est inférieure par rapport à la quantité utilisée dans le procédé micelles inverses. En conséquence, la mesure des propriétés sont favorisés par la forte concentration de l'espèce active dans la matrice. (3) La forme et la taille des nano-et micro-objets peuvent être différentes de celles élaborées avec les microémulsions. (4) Le dopage du composé TS avec un agent fluorescent est plus simple a mètre en ouvre en raison de l'absence de deux phases de polarité différentes comme dans le cas d'une microémulsion qui pourrait provoquer la migration de l'espèce luminophore [75].

A.2.3.2 Caractérisation des nanoparticules de [Fe(*hptrz*)$_3$](OTs)$_2$ non dopées

Les particules générées par cette synthèse ont une morphologie régulière rectangulaire en forme de microcristaux. La variation de la concentration ou du poids moléculaire du PEG a entrainé la formation de particules de même forme mais avec des tailles allant de

250 à 500 nm. Le PEG permet dans la plupart des cas de contrôler la monodispersité des particules, leur forme et le taux d'agrégation. Les essais pour obtenir des objets de plus petite taille par cette méthode de synthèse ont été infructueux. De plus, ce type de synthèse permet une présence beaucoup plus faible de polymères dans les nanoparticules et l'agrégation très faible des particules suggère qu'une très fine couche recouvre les particules (ou au moins partiellement) et prévient leur agrégation.

Des mesures de réflectivité à 543 nm sous microscope (cycle de température programmée balayant à 2 K / min) des échantillons déshydratés sous atmosphère d'azote montrent une TS avec des températures T_{up} = 315 K et T_{dwn} = 309 K, températures similaires à celles du complexe en poudre. Cependant, même sous atmosphère contrôlée, ces échantillons sont hygroscopiques et même de petites quantités d'eau résiduelle dans la chambre du cryostat ou dans la poudre peut provoquer un décalage de la température de transition au cours des expériences, provoquant une variation de l'hystérésis de 4 à 10 K.

A.2.3.3 Caractérisation des nanoparticules de [Fe(*hptrz*)$_3$](OTs)$_2$ dopées avec différents agents luminescents

Afin de caractériser par spectroscopie la fluorescence des différentes nanoparticules dopées, une suspension de 1 mg de chaque échantillon dans 4 ml de $CHCl_3$ a été réalisée, suspension stable et homogène durant le temps de l'expérience. De plus, cela permet d'éviter l'hydrolyse ou l'oxydation des particules. Les spectres de luminescence (Figure A.11) des quatre agents dopants inserés dans les nanoparticules montrent que leurs bandes d'émission chevauchent la large bande d'absorption du complexe à l'état BS. Les spectres d'excitation des luminophores montrent également un chevauchement partiel spectral à plusieurs longueurs d'onde avec la bande d'absorption BS. Ces caractéristiques suggèrent que la TS devrait conduire à une augmentation de l'intensité de luminescence pour les longueurs d'onde judicieusement choisies d'excitation (450 nm) et d'émission (550 nm).

La variation de la luminescence en fonction de la température des nanoparticules déshydratées dopées avec la Rh110 a révélé une modulation importante entre les deux états de spin (environ 300%). Cet échantillon présentent un comportement très similaire à celui de la poudre avec T_{up} = 318 K et T_{dwn} 311 K (Figure A.12a). De légères variations des températures de transition ont été observées mais la réponse du système est en général hautement reproductible.

La variation de la luminescence en fonction de la température des nanoparticules déshydratées dopées avec l'alizarine rouge montre une TS similaire à celle de l'échantillon non dopé avec une hystérésis (T_{up} = 313 K et T_{dwn} = 304 K) (Figure A.12b). Cependant, à hautes températures, il y a une diminution d'intensité ne provenant pas de la TS. Une hypothèse pour expliquer ce comportement serait l'existence éventuelle de traces d'eau dans la chambre du cryostat qui peuvent contribuer a l'oxydation soit du composé ou de l'agent luminescent. En outre, la pente négative obtenue à la fin des cycles à température élevée met en évidence une dépendance thermique du luminophore dans ces conditions expérimentales.

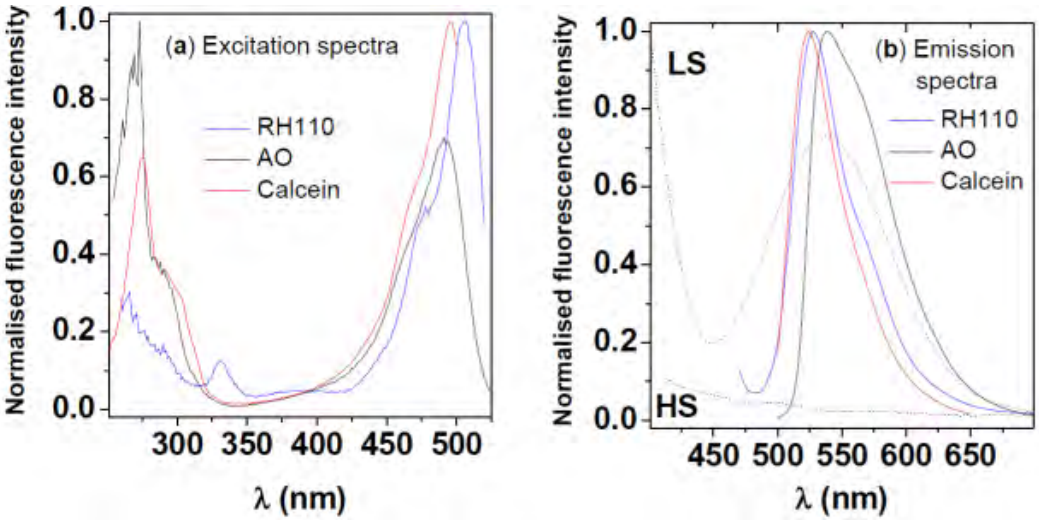

Figure A.11: Spectres d'excitation (émission à 550 nm) et d'émission (excitation à 450 nm) mesurés à température ambiante pour des nanoparticules du composé [Fe(*hptrz*)$_3$](OTs)$_2$ en suspension dans du chloroforme préalablement synthétisées dans l'eau, en présence du PEG-3350 et dopées avec différents luminophores.

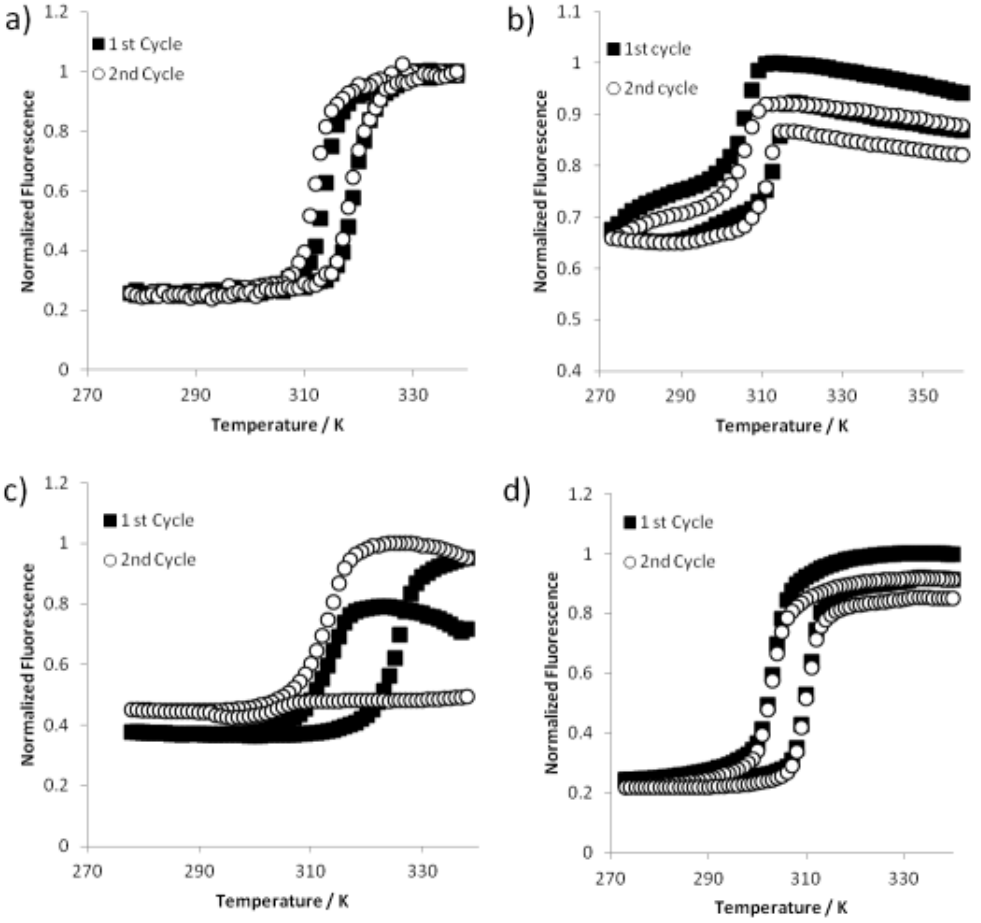

Figure A.12: Variation thermique de l'intensité d'émission à 550 nm (excitation à 450 nm) de la poudre de nanoparticules du composé [Fe(*hptrz*)$_3$](OTs)$_2$ dopée avec **a)** rhodamine 110, **b)** alizarin rouge, **c)** calcein and **d)** acridine orange. (Vitesse de balayage de température : 2 K/min)

Dans le cas de la calcein, la détection de luminescence de la TS dans ce type de nanoparticules n'est pas possible dans nos conditions expérimentales (Figure A.12c). Toutes les tentatives pour obtenir une courbe stable ont échouées. Il est important de noter cependant que ce luminophore particulier a montré une affinité importante pour la fixation des particules. Au cours des étapes de lavage, le solvant a été faiblement coloré, contrairement au cas des trois autres luminophores.

Enfin, la variation thermique de la luminescence des nanoparticules déshydratées dopées avec l'acridine orange montre une modulation importante de la luminescence de la TS (augmentation de 400% de BS à HS) (Figure A.12d). Les températures de transition sont T_{up} = 310 K et T_{dwn} = 302 K et sont similaires à celle du produit non dopé. En outre, ce luminophore présente une dépendance thermique assez faible pour l'intervalle de température étudié. Toutefois, une diminution d'intensité similaire à l'azarine rouge a été observée. Afin d'explorer ce comportement, une série de cycles successifs de longueurs différentes a été lancé en employant les mêmes conditions expérimentales. Ceci a permis de montrer que la diminution du signal luminescent sur la TS n'est pas dû au photoblanchiment de l'acridine orange. Encore une fois, l'existence éventuelle de traces d'eau qui peut se condenser dans l'échantillon à des températures basses pourraient contribuer à un environnement nocif pour le complexe / luminophore.

A.3 Organisation d'un nanomatériau à transition de spin et détection en luminescence d'une transition de spin à l'échelle nanométrique

L'objectif principal de ce travail décrit dans ce chapitre est de montrer le potentiel de la détection de la transition de spin (TS) par luminescence pour un nano-objet unique. Grâce à cette technique et malgré la difficulté que cela implique, nous avons pu sonder un objet à TS isolé dans des conditions optimales. Nous avons essayé d'organiser des nanomatériaux à TS de deux manières : d'abord sous forme de films minces, puis en isolant des nano-objets à TS par différentes méthodes.

A.3.1 Couches minces de nanomatériaux luminescents à transition de spin

Nous avons élaboré des films minces de bonne qualité à base de trois materiaux à TS luminescents dopés, mais seul l'un d'entre eux nous a permis de mesurer une TS par luminescence. Les films minces obtenus à partir de certains de ces systèmes ont soit été trop dilué dans le matériau à TS (en raison de la présence d'additifs), soit trop instables. Afin de déposer un film mince de nanomatériaux à TS non-dilué, nous avons élaboré une solution de chloroforme homogène de complexe $[Fe(hptrz)_3](OTs)_2$ à TS avec un faible degré de polymérisation qui peut facilement être dopé avec un luminophore organique (telles que l'acridine orange ou la rhodamine 110). Ce système nous a permis de déposer par "spin coating" des films minces de haute qualité sur de grandes surfaces (plusieurs cm^2, voir Figure A.13), dont l'épaisseur peut être ajustée de quelques dizaines de nanomètres à quelques centaines de nm.

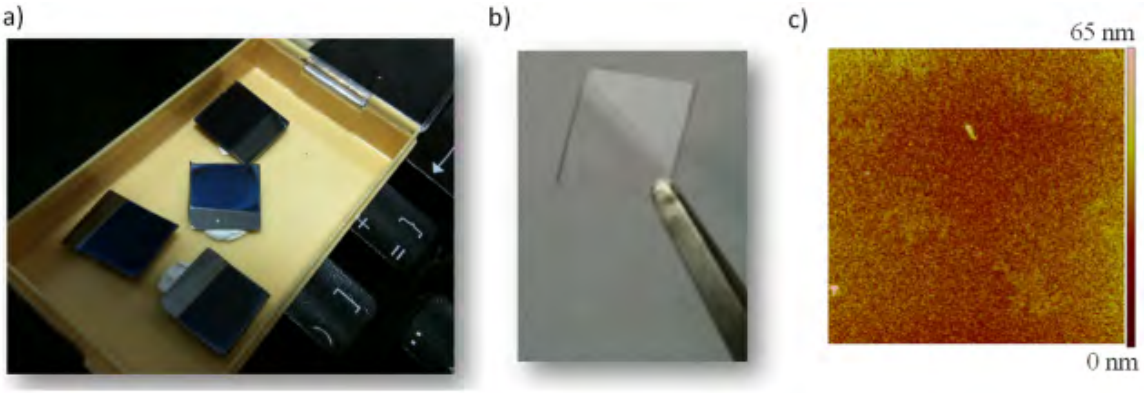

Figure A.13: Image du dépôt du composé [Fe(hptrz)3](OTs)2 (solution de chloroforme). Couche "*spin coaté*" sur **a)** Si et **b)** quartz. **c)** Image AFM.

En dépit de l'absorbance négligeable de ce type de films dans le domaine du visible, nous avons pu suivre, pour la première fois avec une détection par luminescence, le phénomène de transition de spin (Figure A.14). Ces résultats ont été confirmés en sondant la bande de transfert de charge du complexe à TS avec la spectroscopie

d'absorption UV en fonction de la température pour les versions non dopées des films minces (Figure A.15). L'absorbance étant étroitement proportionnelle à la concentration de complexe à TS dans l'échantillon, les mesures de transmittance ont permis de déterminer de manière quantitative la fraction de spin. Néanmoins, ce type de mesures se limite à l'étude des films avec une densité de complexe à TS élevée, présentant des bandes d'absorption HS et/ou BS avec une force d'oscillateur importante. De plus, ces bandes intenses apparaissent habituellement dans la gamme spectrale UV, ce qui peut représenter une contrainte pour la mise en oeuvre des mesures dans des configurations classiques de microscopie ou sur des dispositifs photoniques.

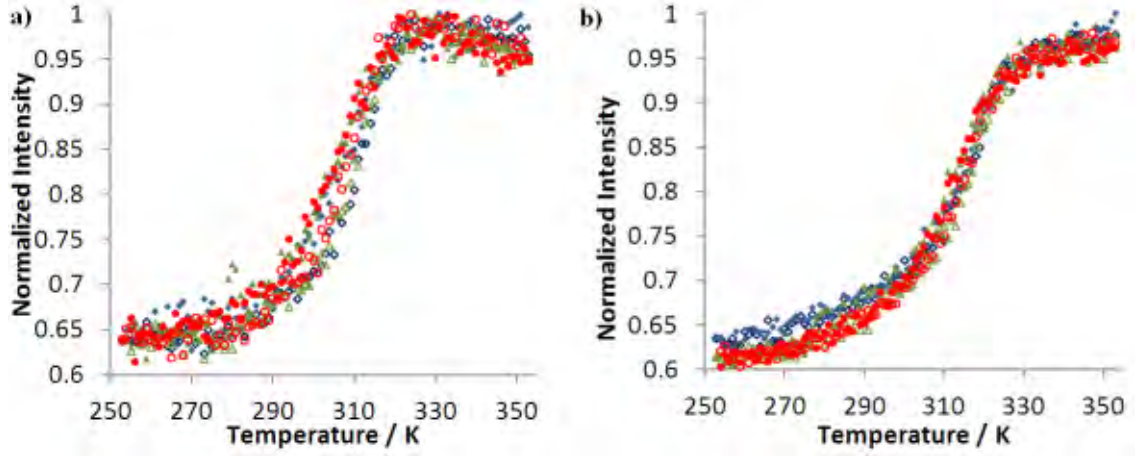

Figure A.14: Variation thermique normalisée de l'intensité de luminescence à 550 nm avec une excitation à 450 nm pour une couche mince ($\approx$ 85 nm) du composé [Fe(*hptrz*)$_3$](OTs)$_2$ dopée avec **a)** de acridine d'orange et **b)** de la rhodamine 110 pendant trois cycles thermiques consécutifs (dT/dt = 2 K/min, en atmosphère azote : symboles ouverts et fermés respectivement pour le chauffage et le refroidissement).

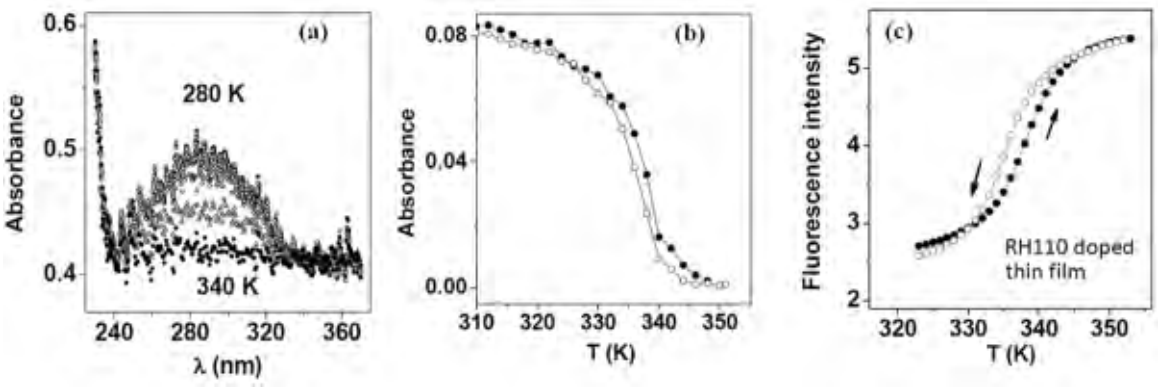

Figure A.15: **a)** Spectre d'absorption d'une couche mince de 80 nm à différentes températures pour le composé [Fe(*hptrz*)$_3$](OTs)$_2$ en région spectrale UV. **b)** Dépendance en température de l'absorbance d'une couche mince de composition similaire de 285 nm (dT/dt = 2 K/min, dans l'air). **c)** Dépendance en température de l'intensité de fluorescence (excitation à 450 nm, émission à 550 nm) d'une couche mince de complexe [Fe(*hptrz*)$_3$](OTs)$_2$ de 150 nm dopée avec de la rhodamine 110 (dT/dt = 2 K/min, dans l'air). Symboles ouverts et fermés indiquant respectivement le refroidissement et le chauffage.

Des mesures de transfert d'énergie par temps de vie de luminescence avec un dispositif de comptage de photon unique corrélé en temps (TCSPC) ont été réalisées sur une solution de chloroforme du composé [Fe(*hptrz*)$_3$](OTs)$_2$ en solution (dopé avec de

l'acridine d'orange). Ces études ont révélé une composition faible de *extinction dynamique* et une importante contribution de *extinction statique* de luminescence dans ce type de solutions (Figure A.16). À en juger par le petit changement du temps de vie de luminescence mesuré sur différentes solutions et les effets d'extinction concomitants observés, il semblerait que quelques molécules d'acridine d'orange soient fixées à une seconde entité (probablement le nanomatériau à TS), il en résulte un transfert d'énergie efficace non-radiatif qui se produit et supprime quasiment toute leur émission. Au préalable les mesures du temps de vie ont été réalisées à température ambiante (état BS) et à haute température (état HS) pour des solutions à TS dopées avec de l'acridine d'orange et de la rhodamine 110. Ces expériences ont montré que, pour ces systèmes à TS luminescent en solution, un transfert d'énergie non-radiatif entre les molécules luminophores et les centres Fe(II) BS du complexe se produit, ceci disparaît avec l'augmentation de l'état HS. Des mesures complémentaires du taux de photoblanchiment ont été réalisées et il en découle que ces échantillons photoblanchissent considérablement plus vite dans l'état HS (haute température) que dans l'état BS (basse température), ce qui indique un transfert d'énergie non-radiatif plus effectif dans l'état BS. Cependant, ces résultats doivent être interprétés prudemment car les effets de la température de ce phénomène ne sont pas clairement dissociés des effets de la température sur la TS. De futures expériences peuvent être faites afin de mieux comprendre le(s) mécanisme(s) de l'extinction dans les matériaux luminescents à TS.

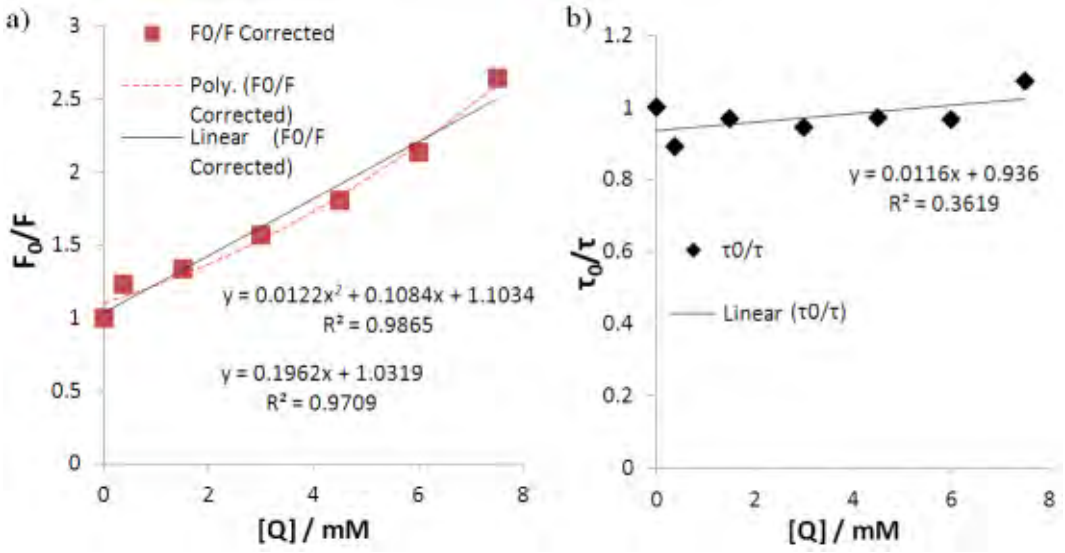

Figure A.16: Courbes a température ambiante **a)** Stern-Volmer et **b)** τ_0/τ pour de l'acridine d'orange (1 μM, solution ethanol - chloroform (1:19)) en function de la concentration de [Fe(*hptrz*)$_3$](OTs)$_2$

Le R_0 pour une paire sensibilisateur - accepteur (S-A) avec des propriétés optiques de l'un des luminophores sélectionnés (acridine d'orange ou rhodamine 110) et de [Fe(*hptrz*)$_3$](OTs)$_2$ a aussi été estimé. Il a été constaté qu'un colorant organique luminophore typique avec un large chevauchement spectral et un complexe avec une bande d'absorption d-d caractéristique centrée à 543 nm présente une valeur R_0 s'étendant entre 1 et 2 nm. Ces calculs montrent que quand on utilise ce genre de luminophores il est nécessaire de les fixer proche du centre fer, en fait, ces valeurs

indiquent que si la distance est plus courte que 0,5 nm (0,5 R_0), alors plus de 98,5% de la luminescence sera "*éteinte*" dans l'état BS. De plus, avec un dispositif assez sensible, *ces luminophores pourraient être utilisés pour sonder l'état de spin d'un centre fer jusqu'à 4 nm* (2 R_0) obtenant ainsi une modulation de la luminescence par rapport à la TS équivalente à 1,5%.

A.3.2 Détection par fluorescence d'une TS sur un nano-objet unique

Nous avons étudié les propriétés de la TS par détection en luminescence dans un nano-objet unique et développé une méthodologie pour les corréler avec la morphologie de l'objet observé. Afin de réaliser cela, nous avons identifié deux points clés : (1) nous avons besoin d'être sûr que les objets à TS sont dispersés et isolés de manière appropriée avec une séparation plus grande que la résolution spatiale du microscope optique. (2) Comme plusieurs de microscopes sont utilisés pour réaliser ce type d'études (microscope optique pour la détection des propriétés de la TS, MEB et AFM pour la morphologie), il est impératif d'avoir des repères sur l'échantillon afin d'être en mesure de trouver l'objet rapidement, indépendamment de la technique de caractérisation. Pour résoudre ces problèmes, nous nous sommes concentrés sur l'organisation des nanomatériaux à TS, et le dépôt des nanomatériaux sur un substrat avec des caractéristiques pouvant être reconnues par toutes les techniques de microscopies.

Le premier essai consista à utiliser la technique d'assemblage dirigé par capillarité-convective des nanoparticules fluorescente à TS en suspension et en utilisant des timbres PDMS nanostructurés. Cette méthode fut cependant très difficile à mettre en oeuvre de par les problèmes de compatibilité, soit entre le solvant et les particules à TS, soit entre le solvant et les timbres de PDMS. Les nanoparticules à TS à base de Triazole ne sont pas très stables dans des solvants polaires à l'inverse des solvants non-polaires. Cependant, la mise en contact du PDMS avec un solvant non-polaire provoque un effet de gonflement du PDMS. Des travaux complémentaires pour synthétiser des nanoparticules sans additifs de quelques dizaines de nanomètres, qui soient stables sur longues périodes dans l'eau et l'éthanol, seront nécessaires afin de tirer avantage de cette méthode.

Toutefois, cette technique d'assemblage dirigé a fourni les briques élémentaires pour d'autres stratégies de mis en oeuvre de nano-objets à TS isolés. Par exemple, des substrats de silicium nanostructurés analogues à celui utilisé pour créer les timbres de PDMS ont été utilisés avec succès. Ces substrats possèdent des grilles intégrées, qui après un dépôt aléatoire des nanoparticules à TS à la surface, fonctionnent comme références pour les différentes techniques de microscopie. Et pour la première fois, nous avons pu détecter les propriétés de TS d'un objet unique via une détection par fluorescence, et caractériser la morphologie du même objet par microscopie MEB (Figure A.17). De plus, les propriétés de TS détectées pour ces objets uniques se rapprochent des propriétés des échantillons sous forme de poudre. Même si cette technique a présenté un rendement assez faible d'objets isolés, les possibilités d'amélioration sont

encore vastes : utilisation des différents solvants pour les particules TS en suspension, optimisation de la concentration de la suspension, différentes topologies de substrats de Si combinés avec une fonctionnalisation sélective de ces surfaces, *etc.*

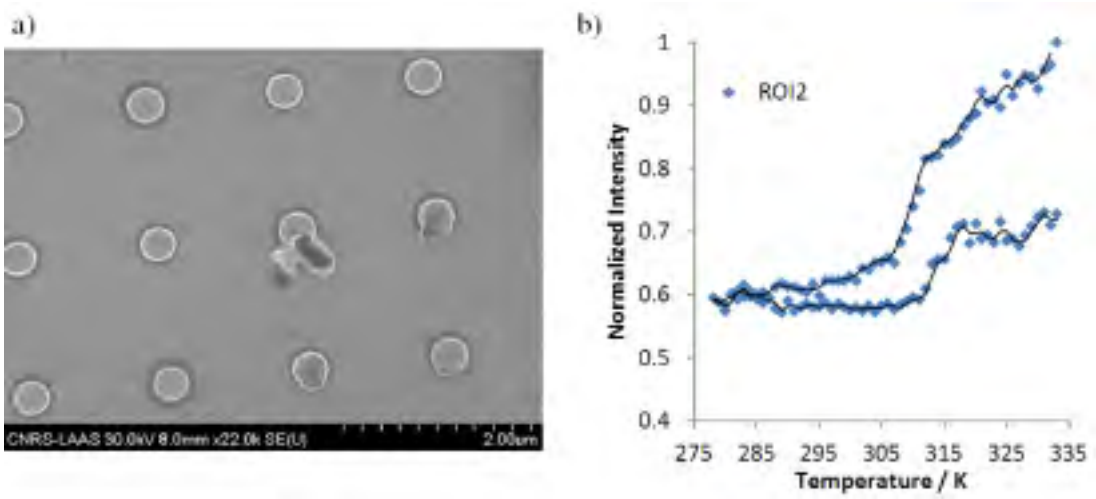

Figure A.17: **a)** Image MEB d'une nanoparticule TS isolée dopée avec de l'acridine orange sur un substrat de Si structuré avec un réseau de 300 nm de côté et un pas de 1,5 μm après une déposition aléatoire. **b)** Variation thermique normalisée de la luminescence de l'objet observé en **a)**.

Quelque soit la méthode utilisée pour la synthèse de nano-objets a TS, le caractère commun à ces processus est d'utiliser un élément qui contraint et limite la croissance du matériau pendant la formation du complexe (micelle inverse, polymère de stabilisation, une matrice poreuse, *etc*). Ainsi, nous avons utilisé les nano-cavités de notre timbres de PDMS comme micro/nano-réacteurs pour une création organisée de nano-objets du complexe $[Fe(hptrz)_3](OTs)_2$ à TS. Nous avons réussi à transférer une partie de ces réseaux sur un substrat de Si par une technique de tamponnage assistée par un solvant et de détecter, pour la première fois et de façon simultanée, les propriétés de plusieurs objets à TS isolés (Figure A.18). Cependant, cette procédure conduit à une pollution des substrats qui rend la caractérisation morphologique très difficile.

Afin de poursuivre l'idée d'une synthèse de nano-objets luminescents à TS organisés in-situ, nous avons également démontré la possibilité de structurer des réseaux de nano-objets du composé $[Fe(hptrz)_3](OTs)_2$, en utilisant le système chloroforme utilisé précédemment pour la fabrication de films minces. Ici, nous avons développé une approche de lithographie douce, dérivée de la technique de micromoulage assistée par un solvant (SAMIM). Un timbre en PDMS hautement polymérisé et nanostructuré (avec des cavités) est appliqué sur un goutte du système chloroforme ; nous piégeons ainsi des micro/nano gouttelettes dans les cavités du timbre. Après l'évaporation du solvant, les nano-objets sont précipités de manière organisée à la surface. *Nous avons été en mesure de sonder le comportement de la TS dans un grand nombre de nano-objets individuels largement espacés de manière simultanée pour des tailles descendant jusqu'à 150 nm* (Figure A.19). Même à ces petites échelles, des courbes standards de transition ont été obtenues, des effets de tailles n'ont donc pas été obtenus dans nos nano-structures à TS. Il faut noter que dans cette approche, il n'y a pas de tensio-actifs ou d'autres agents de stabilisation autour des nano-objets, *les effets de matrice*

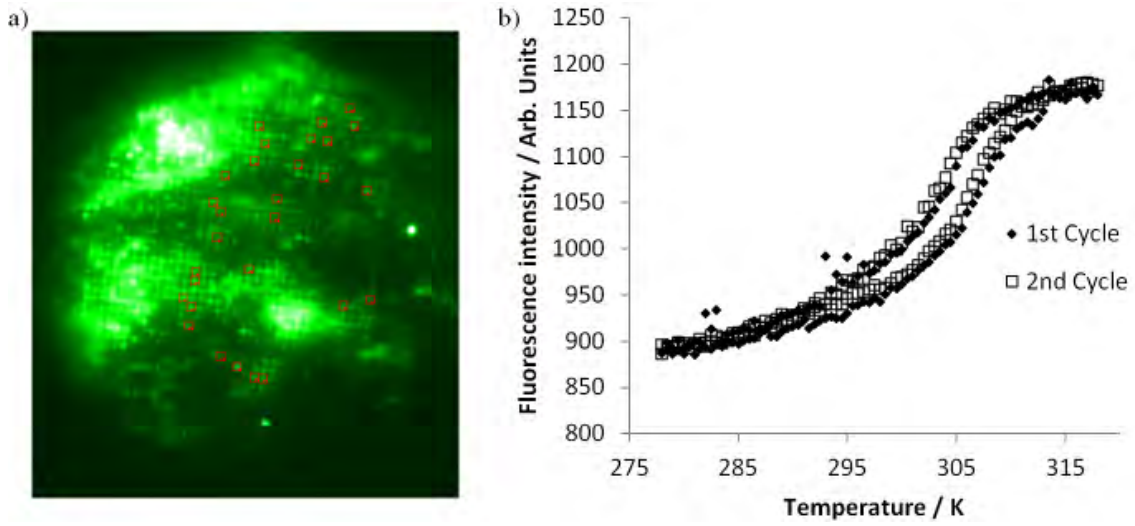

Figure A.18: **a)** Image en fluorescence d'un réseau de plots TS de 500 nm de latéral et un pas de 1,5 μm synthétisés dans un timbre PDMS et transféré sur un substrat de Si. **b)** Variation thermique typique de la luminescence émise par un plot de **a)**.

sont donc totalement écarter. Cette technique de nanostructuration nous a permis de remplir notre objectif principal. Cette méthode fournit *une manière directe pour détecter les courbes de transition de spin de particules uniques, et de caractériser leurs morphologies ou leurs informations spectrales ou structurales.* Il est clair que les limites des technologies employées pour la fabrication du moule de silicium ou de PDMS ne sont pas encore atteintes ; les limites de détection de luminescence peuvent être elles aussi facilement poussées plus loin. C'est pourquoi nous nous attendons à ce que cette approche nous permetre d'obtenir des données statistiques systématiques sur les effets de réduction de taille des matériaux TS, et même plus généralement pour les effets de taille dans les solides moléculaires.

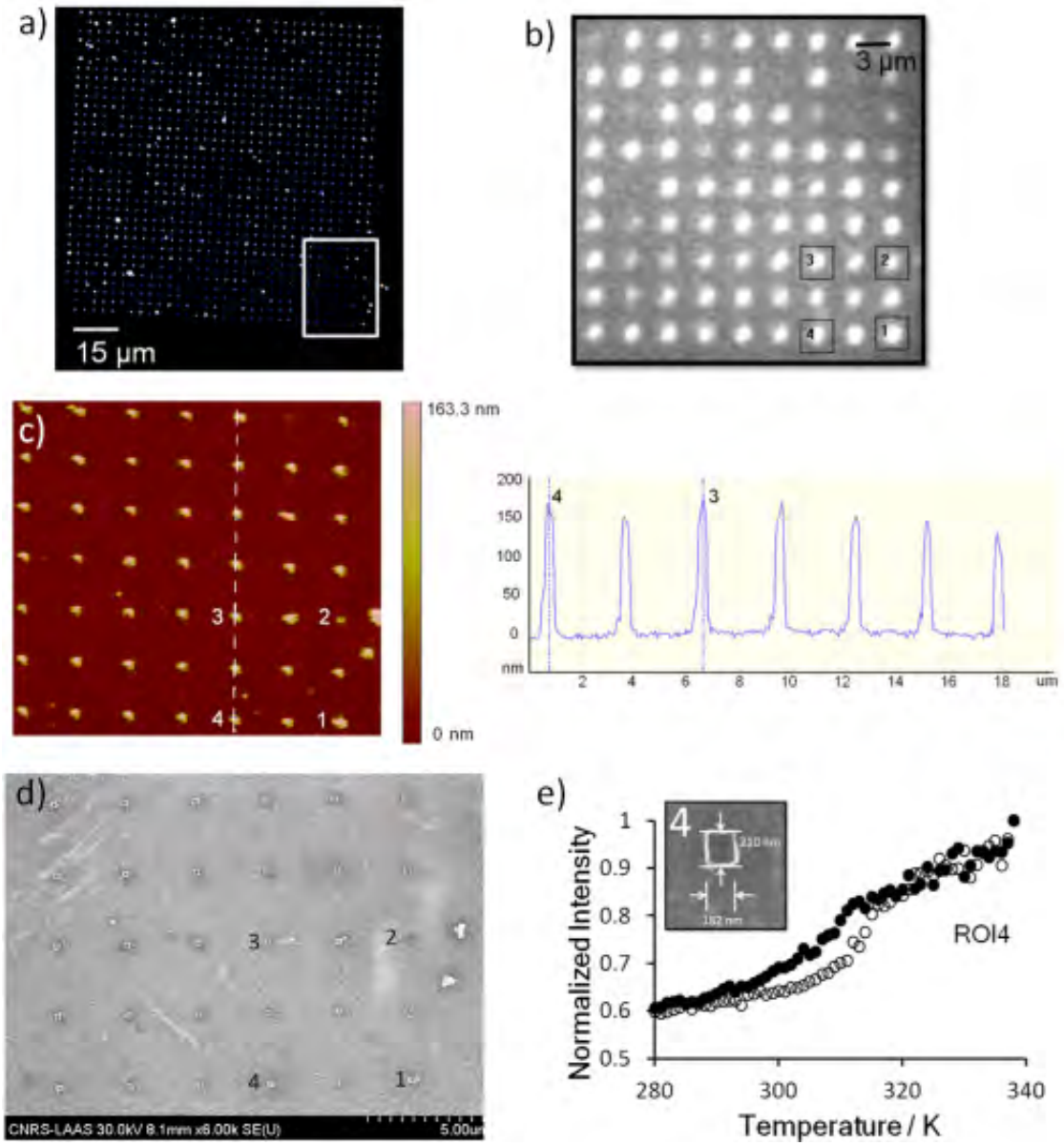

Figure A.19: **a)** Image en champ sombre d'un réseau de nano-plots obtenu avec un motif de 370 nm de taille latérale, un pas de 3 μm et une profondeur nominale de 150 nm. **b)** Image de fluorescence des plots de la zone entourée dans a. **c)** Image AFM (21 x 21 μm^2) et profil de la topographie du réseau de nano-plot observé en b le long de la ligne en pointillés dans la zone en surbrillance dans l'image AFM. **d)** Image MEB de la même zone du réseau de luminescence étudié en **a,b,c**. Des structures avec 200 nm de taille latérale sont typiquement observées. **e)** Variation thermique normalisée de la luminescence à 550 nm pour le nano-plot numéro 4. (Les symboles ouverts et fermés représentent respectivement le chauffage et le refroidissement).

A.4 Microthermométrie

Le développement de capteurs de température continue à être attractif dans divers domaines de science et technologie, tels que le traitement de tumeur par hyperthermie et photothermie, l'ingénierie aérospatiale, les tests de circuits microélectroniques, la recherche de laboratoire sur puce, *etc.* En particulier, avec l'avènement des nano(bio)-technologies, mesurer la température aux échelles micro- et nanométrique devient un enjeu de plus en plus important . Ainsi, non seulement le besoin de développer de nouvelles techniques de nano-caractérisation thermique pour l'utilisation de nouveaux nanomatériaux ont augmentés, mais aussi l'exigence de mesurer et contrôler la température avec une résolution spatiale nanométrique et une haute résolution temporelle est devenue une préoccupation majeure pour de nouveaux développements. En conséquence, il est essentiel d'utiliser une thermométrie précise jusqu'à l'échelle nanométrique où les méthodes classiques ne sont plus performantes. Cependant, le développement d'un thermomètre micro / nanométrique n'est pas seulement une question de taille, mais nécessite aussi des matériaux avec des propriétés physiques nouvelles, ainsi que des techniques de nanocaractérisation adaptées.

Dans ce chapitre, des nanofils métalliques sont utilisés comme éléments à l'échelle sub-micrométrique pour contrôler la température. En raison de leur masse thermique faible, les dispositifs à base de micro et nanofils sont particulièrement intéressants en termes de temps de réponse et aussi en termes de confinement de leurs changements de température, quand ils sont chauffés par effet Joule. La caractérisation thermique de ces éléments chauffants est une étape critique qui peut être réalisé par thermométrie de fluorescence. Pour ce faire, nous avons utilisé nos systèmes hybrides à SCO en tant que sondes de température luminescentes sur des circuits de nanofils d'or chauffés par effet Joule. Notre objectif principal était d'explorer le potentiel des nanomatériaux à SCO luminescents pour réaliser la cartographie de températures de surface à haute résolution spatiale par détection de luminescence.

A.4.1 Méthodes de Thermométrie

Il vaut la peine de survoler l'ensemble des techniques de thermométrie les plus couramment utilisées pour avoir une meilleure compréhension des limites dues aux mesures de micro et nanosystèmes. Une question importante à garder à l'esprit au sujet des méthodes de thermométrie à cette échelle est la suivante : Est-ce que la méthode se fait avec un contact physique?

A.4.1.1 Méthodes avec contact

Certaines des méthodes qui utilisent une approche avec un contact physique sont les suivantes: thermistors, sondes de température à résistance (resistance temperature detector = RTD) et thermocouples. Les deux premiers éléments profitent du fait que la résistance de presque tous les matériaux conducteurs ou semi-conducteurs change en

fonction de plusieurs facteurs et l'un d'entre eux est la température. Les thermistors sont fabriqués en matériaux céramiques ou polymères ; en revanche, les RTD sont fabriquées en métal pur tel que le platine [147]. D'autre part, les thermocouples sont basés sur l'effet Seebeck, également connu comme l'effet thermoélectrique.

Souvent, la meilleure façon de faire une mesure de température est d'utiliser une méthode de contact. Néanmoins, si l'objet à mesurer est de taille réduite, les méthodes de contact ne sont pas la meilleure option. La sonde de mesure peut facilement modifier la température de l'échantillon dès qu'il touche la surface. De cette façon, la sonde induit une perte de chaleur pour le système à analyser et par conséquent, conduit à des erreurs de mesure [94]. En outre, si la masse de la sonde est supérieure à la masse de l'échantillon, deux choses se produisent : les erreurs de lecture sont plus importantes et il faut plus longtemps pour obtenir une mesure stable [149].

Pour les raisons mentionnées ci-dessus, la nécessité de miniaturiser la sonde de mesure est un facteur clé pour obtenir une plus grande résolution spatiale et temporelle. Dans cet esprit, des efforts ont été accomplis grâce au développement de la microscopie thermique à balayage (scanning thermal microscopy = SThM) [150, 151]. Cette technique utilise une pointe pour scanner la surface d'un échantillon et mesurer les caractéristiques thermiques locales de la surface. En conséquence, une carte de température et toute autre information thermique peuvent être tracées après un balayage de l'échantillon entier. Certains mécanismes à l'origine des systèmes de détection de la SThM impliquent les mêmes principes que pour les thermistors, les RTD et les thermocouples [152–155]. Les principales différences sont la taille de la sonde et ses capacités de positionnement précis. Il existe aussi une variante supplémentaire pour la SThM qui utilise une pointe fluorescente - dépendant de la température [156–158]. Cependant, malgré la résolution spatiale exceptionnelle que la SThM peut offrir, elle présente quelques inconvénients, indépendamment du mécanisme de détection utilisé. Tout d'abord, les pointes exigent des procédés de fabrication très complexes. Deuxièmement, ce type de technique fourni un rendu d'image lent. Troisièmement, le transfert de chaleur entre la sonde et la micro - nanostructure n'est pas entièrement compris et la mise en place des facteurs de correction appropriés est une tâche complexe [149].

A.4.1.2 Méthodes sans contact

Les techniques sans contact analysent la lumière émise ou réfléchie par un objet. Le grand avantage de cette approche est que la température qui est mesurée n'est pas influencée par le processus de mesure. Les techniques les plus couramment utilisés sont les suivantes: la thermographie IR, la thermoréflectance, la spectroscopie Raman et la thermométrie de fluorescence.

La thermographie IR analyse le rayonnement émis par un corps et retourne des informations sur sa température. Elle constitue une technique rapide de plein champ puisque les données de chaque point de l'échantillon peuvent être obtenues avec une seule mesure. En outre, la méthode est efficace pour caractériser les changements de température rapides [149]. Cependant, la résolution spatiale est une faiblesse de

la thermographie infrarouge. Puisque l'information de température est portée par un rayonnement de faible énergie, la méthode est limitée par la diffraction limite de quelques micromètres ($\approx 5\ \mu$m) [161–163]. En outre, afin d'avoir une mesure précise, il est nécessaire de connaître l'émissivité de l'échantillon. Ainsi, la mesure se complique s'il y a différents matériaux dans l'échantillon observé car il y a plus d'un coefficient d'émissivité impliqué.

Une autre méthode de plein champ est basée sur la technique de thermoréflectance. Cette procédure analyse les changements induits thermiquement de la réflectivité sur une surface. Habituellement, ces changements sont associés à la dilatation thermique dans la plupart des matériaux ; en particulier, la réflectance des semiconducteurs est également affectée par la modification de la largeur de bande avec les variations de la température [164]. Par conséquent, la lumière réfléchie par n'importe quel matériau présente des informations sur la température de celui-ci, encodée dans son amplitude, sa phase et sa polarisation. Cependant, une connaissance précise des coefficients de réflexion des surfaces est nécessaire pour tirer des conclusions correctes de la lumière collectée. Cette tâche est particulièrement difficile car les coefficients sont fortement dépendants de nombreux facteurs. La microscopie Raman thermique à balayage peut être également utilisée pour effectuer des mesures de température. Les modes (vibrations) Raman sont affectés par les changements de température dus à des changements structurels induits thermiquement du matériau étudié. L'analyse des spectres Raman en termes d'intensité absolue ou relative, de rapport Stokes / antiStokes, de variations de la position et de la largeur des modes de vibration, peut être éventuellement traduits en température. Le Raman offre une résolution spatiale autour du micromètre et une large plage de températures de mesure avec une sensibilité de l'ordre de 10 K [166]. Toutefois, l'un des principaux problèmes du Raman est sa nature invasive due au chauffage laser. En outre, en raison de sa nature d'acquisition de données en série, la thermométrie μRaman a un rendu d'image lent. Enfin, cette technique n'est pertinente que pour des matériaux qui présentent une réponse Raman importante et très sensible aux changements de température [166].

La dernière méthode sans contact considérée dans cette section est la thermométrie de luminescence. Ici, la lumière émise par une sonde fluorescente dépendante de la température est utilisée pour extraire les informations thermiques de l'échantillon. Contrairement à d'autres méthodes sans contact, la thermométrie de luminescence est considérée comme semi-invasive; même si un film mince d'une sonde fluorescente est déposé au-dessus de la région à analyser, l'information est transportée seulement par la lumière émise par la sonde et non par le film lui-même. La résolution spatiale de la thermométrie de luminescence, comme dans le cas de la spectroscopie Raman, est limitée par la diffraction de la lumière. Néanmoins, avec des longueurs d'onde courtes et une optique appropriée, une résolution sub-micrométrique a été rapporté [168, 169].

A.4.1.3 Pourquoi des matériaux à TS luminescents?

En thermométrie de luminescence, il est habituel de détecter les changements de température en suivant l'extinction thermique de la luminescence d'une sonde donnée.

En d'autres termes, le système est composé d'un seul élément qui effectue deux tâches en même temps: la détection de température et la transduction du signal. Néanmoins, il est également possible d'adopter une approche à deux éléments où les deux fonctions sont attribuées à deux entités différentes: ainsi, une flexibilité supplémentaire est obtenue afin de mieux adapter la sonde à des environnements différents en faisant varier les propriétés de chaque composant indépendamment [171]. De ce point de vue, dans le cadre de cette thèse, nous avons conçu un système à deux éléments de thermométrie constitué de nanoparticules à transition de spin, dont la bistabilité et les changements de propriété optique associés modulent l'intensité de la réponse d'un luminophore. Ces systèmes pourraient ainsi être adaptés de façon simple à différents problèmes où l'utilisation de la thermométrie de fluorescence serait bénéfique. Il convient de souligner qu'ici le principal avantage sur la thermométrie par fluorescence classique vient du fait que la plage de température et la sensibilité de détection peuvent être réglées indépendamment de la sonde de fluorescence par des méthodes bien établies, telles que la dilution du métal, l'échange d'anions, l'ingénierie du ligand ou l'ajustement de la taille des particules [5].

A.4.2 Des nanofils à des fins de chauffage

Un nanofil peut être chauffé à l'aide d'un flux de courant électrique. En raison de ses faibles dimensions et de sa capacité thermique faible, les réponses temporelles à les variations de température produites par le passage d'un courant dans un nanofil devraient être rapides. En outre, dans des conditions appropriées d'environnement, il a été montré que les changements de température pouvaient être très localisés [168]. En conséquence, les nanofils comme source de chaleur sont un moyen prometteur pour le développement et l'optimisation du contrôle de température à haute vitesse de systèmes sur puce.

Des dispositifs de chauffage basés sur des nanofils peuvent être utilisés dans de nombreuses applications. Cette approche pourrait être suivie pour élaborer des stratégies de contrôle thermique de systèmes de laboratoire sur puce pour effectuer une analyse complexe et efficace d'échantillons biologiques. De plus, ce concept pourrait être appliqué pour induire des modifications de surface très localisées sur des biocapteurs pour créer des sites de liaison. Une autre application intéressante est la caractérisation de la cinétique moléculaire; en produisant une variation rapide de température (saut de température), le début du pliage ou du dépliage moléculaire peut être déclenché de manière contrôlée.

Le principal avantage d'utiliser ce système de nanofil est sa simplicité; les méthodes actuelles de saut de température emploient des dispositifs à base de laser qui ont tendance à être complexes et coûteux. De plus, les dispositifs de nanofils pourraient être intégrés à des technologies sur puce existantes. Même si les réponses temporelles des nanofils (micro seconde) ne sont pas aussi rapides que les configurations laser (nano seconde), elles sont suffisantes pour caractériser la plupart des événements moléculaires en biologie [149].

A.4.2.1 Processus de fabrication de nanofils d'or

La production des puces qui contiennent les nanofils est divisé en deux procédés, une étape de lithographie par faisceau d'électrons (electron beam lithography = EBL) où les nanofils sont fabriqués sur un substrat de Si et ensuite, un procédé de photolithographie supplémentaire pour fabriquer les électrodes qui connectent les nanofils à un circuit externe (Figure A.20). Ces deux étapes sont nécessaires en raison des différences de taille latérale des objets (nanométrique pour la largeur des nanofils et micrométriques pour les électrodes).

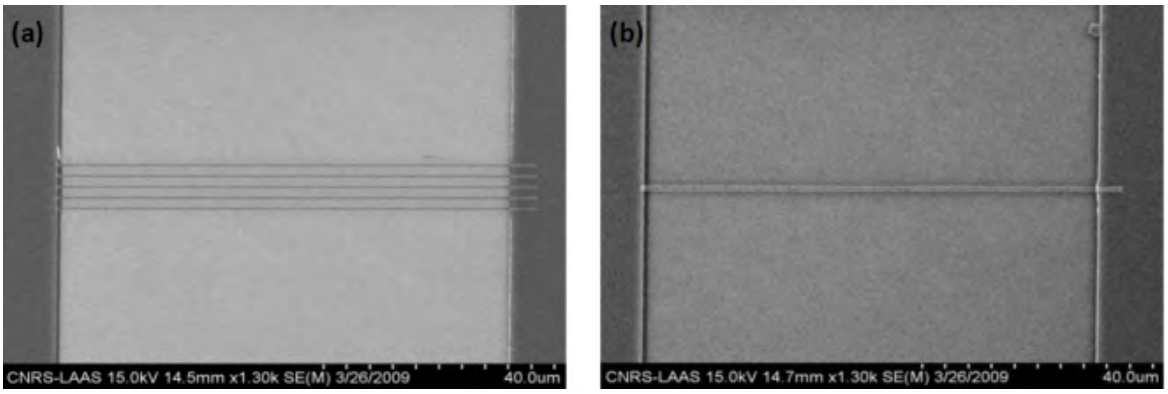

Figure A.20: Images MEB de : **a)** jeu de cinq nanofils d'or de 80 μm x 500 nm x 50 nm, **b)** un nanofil d'or de 80 μm x 1 μm x 50 nm.

A.4.2.2 Caractérisation électrique des nanofils d'or

La caractérisation électrique des nanofils d'or a été réalisée au moyen de deux types d'expériences électriques. Tout d'abord, la variation de la résistance des nanofils a été observée en fonction de la température, chaque nanofil de la puce a été contrôlé avec un ohmmètre quand la température de l'ensemble du circuit variait de 298 K à 353 K. D'autre part, la variation de la résistance des nanofils a été mesurée en fonction du courant électrique appliqué. En supposant que toutes les variations de la résistance mesurée à chaque expérience (ou au moins la plupart d'entre elles) proviennent de la variation de température du nanofil, il est possible de relier la variation de la résistance (ΔR), du courant et de la température (ΔT) pour chaque type de fil (Figure A.21).

A.4.3 Caractérisation thermique des nanofils par microscopie de luminescence

L'idée principale des expériences décrites dans ce chapitre consiste à employer l'un de nos systèmes SCO luminescents comme capteur de température sur la surface d'un circuit nanofil. Une fois qu'une couche de notre matériau est déposée par spin-coating sur la puce, des images du circuit en fluorescence sont prises à différents courants. La section réduite du fil permet un confinement local du chauffage le long de son axe

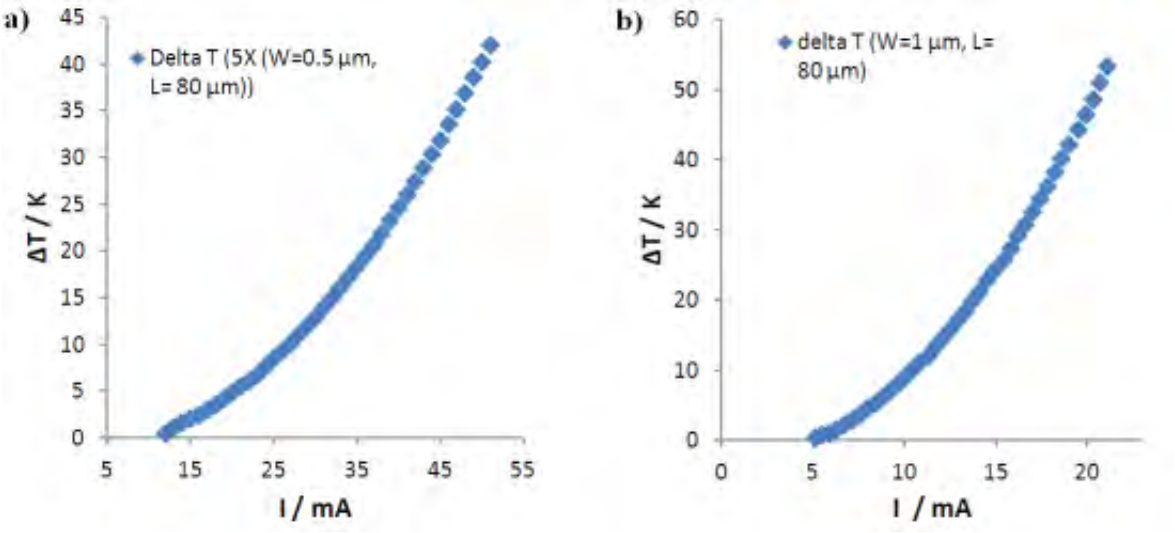

Figure A.21: Variation de la température induite en fonction du courant électrique appliqué aux nanofils d'or: **a)** jeu de 5 nanofils de 80 μm de long, 500 nm de large et **b)** 1 nanofil de 80 μm de long, 1μm de large

lors du passage d'un courant électrique à travers le dispositif (effet Joule) [71, 168]. Lorsque la température augmente, l'état de spin du système va changer localement de LS à HS et, par conséquent, l'intensité de la luminescence de la zone chauffée va augmenter (Figure A.22). Avec une connaissance précise de la relation entre l'intensité de luminescence et la température, une variation donnée de l'intensité peut être convertie en température.

Pour faire ces expériences, le détecteur, la lumière d'excitation et la source de courant du circuit ont été synchronisés afin d'effectuer plusieurs cycles électriques. En outre, pour avoir une analyse fiable de l'information, un protocole de traitement d'image a été créé et programmé dans une boîte à outils de macros et de fonctions développées dans le logiciel ImageJ.

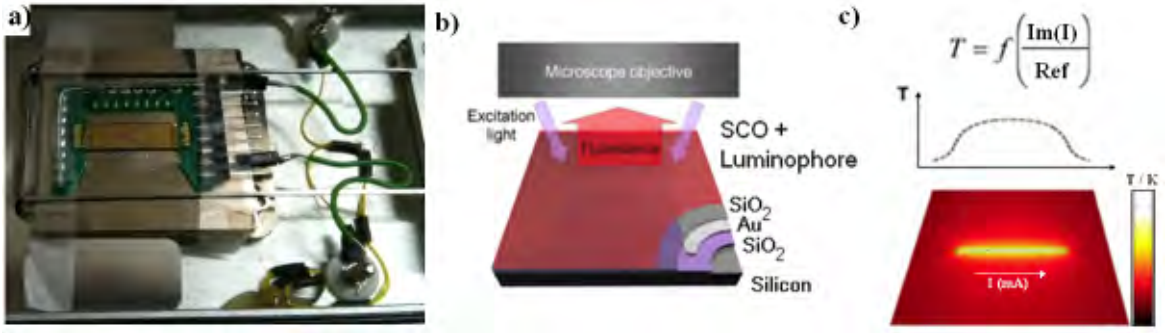

Figure A.22: **a)** Image d'une puce de nanofils avec les connexions électriques dans la chambre d'un Linkam LTS120. **b)** Image schématique de l'agencement d'un nanofil d'Au dans le dispositif de microscopie. **c)** La cartographie thermique de la puce peut être calculée en fonction de l'image de luminescence prise à un courant donné et d'une référence qui correspond à la soustraction d'une image du circuit sans courent à basse température (état LS) d'une autre prise à haute température (état HS).

La Figure A.23 montre une de nos expériences effectuées sur un film de 150 nm du composé $[Fe(hptrz)_3](OTs)_2$ dopé avec la rhodamine 110, déposé sur un nanofil de 1 μm de large, pendant le premier des deux cycles électriques consécutifs entre 0 et 15 mA (signal escalier). L'image inférieure de la Figure A.23a montre la fluorescence autour du fil (image traitée) quand aucun courant n'est appliqué. Les cases du milieu et supérieure montrent la même mesure, mais pour des courants augmentant à 9 mA et 15 mA. Le fort confinement de l'augmentation de température au voisinage du fil est nettement perceptible. Comme on l'observe sur la Figure A.23b, le profil de distribution de température mesurée le long du fil (sens X) est relativement plat, avec une augmentation abrupte de la température au niveau des extrémités du fil et une valeur relativement constante entre les extrémités. De plus, la figure A.23c montre les profils à travers le fil (direction Y) qui permet de mieux illustrer le fort confinement du chauffage sur le nanofil à différents courants. La forme de ces profils est en bon accord avec ceux précédemment rapportés dans la littérature par Löw *et al.* pour des conditions expérimentales similaires [149, 168].

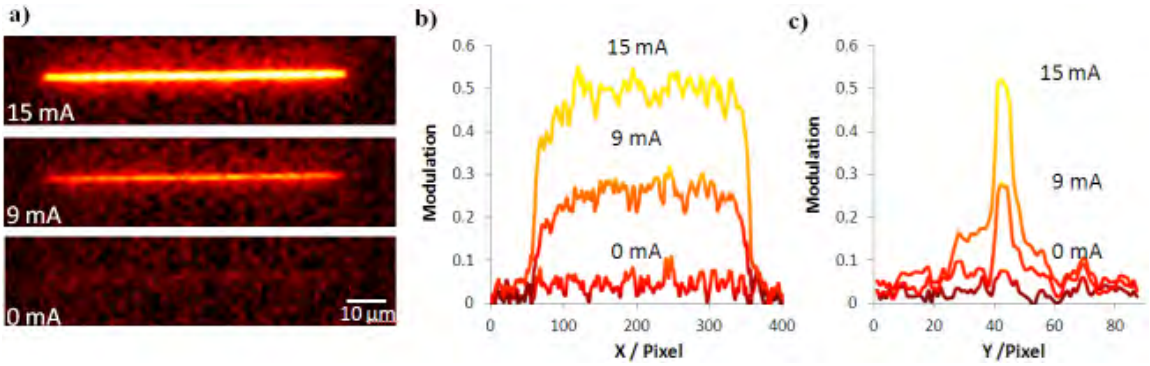

Figure A.23: **a)** Images de microscopie de fluorescence traitées (excitation à 450 nm, émission à 550 nm, objectif X50) d'un nanofil d'or (80 μm de long, 1 μm de large, 50 nm d'épaisseur) recouvert d'une couche mince du composé à transition de spin $[Fe(hptrz)_3](OTs)_2$ dopé avec de rhodamine 110. Pendant les mesures de fluorescence les nanofils ont été chauffés par effet Joule : l'intensité du courant est indiquée pour chaque image. Profils des images de fluorescence **b)** à travers l'axe (direction X) et **c)** à travers le nanofil (direction Y).

Nous avons exploré pour la première fois l'utilisation de nouveaux systèmes à deux éléments composés de nanoparticules à transition de spin et de luminophores organiques à de fins de thermométrie et d'imagerie à haute résolution spatiales. Contrairement à d'autres approches de luminescence, notre système augmente sa réponse de luminescence quand la température augmente. En outre, la versatilité obtenue avec ces sondes à base de nanoparticules à SCO offre la possibilité non seulement d'obtenir le comportement inverse en travaillant avec un chevauchement de la bande d'absorption dans le proche infrarouge, mais aussi de concevoir une stratégie de mesure à deux couleurs en utilisant deux longueurs d'onde en même temps (visible et proche infrarouge). Cette dernière approche est très efficace pour éviter les problèmes de dérive du signal.

Le grand avantage de notre système repose sur le fait que la gamme de température où la transition de spin des particules a lieu peuvent être réglées par des méthodes bien connues de synthèse chimique et sans nécessairement modifier l'agent luminescent.

Cela peut se traduire par une conception flexible quand il s'agit de la sensibilité et de la plage de fonctionnement de la sonde, à une longueur d'onde fixée. De plus, des particules ayant une transition progressive peuvent être utilisées pour une thermométrie en temps réel, alors que d'autres présentant une boucle d'hystérésis thermique (effet mémoire) peuvent être utilisées pour détecter ex-situ le dépassement d'un certain seuil de température, quand des mesures en temps réel ne peut pas être effectuées.

Cependant, nos expériences ont révélé certains problèmes quant à l'étalonnage de la sonde pour déduire avec succès une valeur de température d'une mesure de luminescence. Malgré ces défis, des perspectives passionnantes peuvent être imaginés pour étudier ces films à SCO luminescents avec la plateforme de nanofil. La caractérisation de la dynamique de réponse de chauffage des micro / nanofils d'or en utilisant une installation résolue en temps équipée d'une caméra CCD et l'utilisation d'un microscope optique à champ proche (near field scanning optical microscope = NSOM) peuvent nous permettre d'employer la détection en luminescence de la dissipation de puissance dans la plateforme de nanofil avec une résolution temporelle et spatiale sans précédent.

Appendix B

Image Registration Routine

The following lines present the code developed in MATLAB in order to perform the automatic alignment of stack of images.

```
close all;
clear all;

%File Input:
%File_name receives the name of the file to analyze and then it its
%concatenated to its .tif extention in File_name_1. The variable ...
    num_images
%stores the number of images in File_name_1.
file_name= input('Enter file name .tif (without extention): ', 's');
file_name_1=strcat(file_name,'.tif');
num_images = imfinfo(file_name_1);
num_images = numel(num_images);

%References:
%- IM_base stores the first image of File_name_1. All the stack ...
    will be
%aligned with respect to IM_base.
%
%- im_ROI receives the "feature" to track in the whole stack ...
    during the
%alignment process. The feature is a rectangular ROI selected  by ...
    the user
%from IM_base with the function imadjust; once the area is ...
    selected, a
%double click on the enclosed area closes the window.
%
%- rect_ROI receives a four element position vector composed by
%[xmin ymin width height] parameters of the ROI selected by the user.
%NOTE: xmin ymin are the coordinates of the upper left corner of ...
    the ROI.
IM_base = imread(file_name_1,1);
IM_base_ADJ=imadjust(IM_base);
[im_ROI,rect_ROI] = imcrop(IM_base_ADJ);
im_ROI=imcrop(IM_base,rect_ROI);
```

```
close;

%Fine tuning base points:
%In this step, the function cpselect is employed for receiving ... from the
%user at least three reference points present in all images of the ... stack.
%Here, the function is employed in an unconventional manner. It ... will charge
%and display twice IM_base in its window. The user should choose ... on the
%left image (taged with IMbase) with a click at least three reference
%points (it could be more). However, in order to assure a proper ... execution
%of the routine, an equal number of dummie reference points on the ... right
%image (taged with input_image) should be also given selected. ... These dummie
%points will not be employed at any moment in the alignment process.
%- base_pts stores the coordinates of the reference points ... selected by the
%user.
%- The processed stack of images will be stored in a file with the ... name:
%file_name_Aligned.tif
[input_pts, base_pts]=cpselect(IM_base_ADJ,IM_base_ADJ,'Wait',true);
file_name_2=strcat(file_name,'_Aligned.tif');
imwrite(IM_base,file_name_2,'Compression','none','WriteMode','overwrite');

for i=2:num_images,
%- IM_nonr is a temporal variable that stores the image of the ... stack to be
%aligned with IM_base.
%- c is a temporal variable that receives the resulting matrix of the
%normalized 2D crosscorrelation performed with the function normxcorr2
%between im_ROI and IM_nonr.
%%%%%%%%%%
    IM_nonr = imread(file_name_1,i);
    c = normxcorr2(im_ROI,IM_nonr);

%- max_c stores the maximum value of c.
%- imax receives the linear index that corresponds to max_c in c.
%- ypeak and xpeak stores the subscript equivalents of imax, i.e. ... the Y,X
%coordinates of the correlation maximum, respectively.
%- corr_im_ROI is a vector that receives the X, Y coordinates of ... the upper
%left corner of im_ROI when superposed to IM_nonr at the correlation
%maximum
    [max_c, imax] = max(abs(c(:)));
    [ypeak, xpeak] = ind2sub(size(c),imax(1));
    corr_im_ROI = [(xpeak-size(im_ROI,2))
                   (ypeak-size(im_ROI,1))];

%diff_offset saves the calculated offset between the coordinates ...
```

```
      of the
72 %upper left corner of im_ROI superposed with IM_nonr at the ...
      maximum of
73 %correlation and im_ROI in IM_base.
74     diff_offset=[round((corr_im_ROI(1)-rect_ROI(1)+1)) ...
          round((corr_im_ROI(2)-rect_ROI(2)+1))];
75
76 %- size_pts receives the number of points given by the user in ...
      order to
77 %perform the fine tunning.
78 %
79 %A set of input points is calculated from the offset found previously
80 %between IM_base and IM_nonr. These calculations are done under the
81 %assumption that the new location of the reference points are in the
82 %nearbounds of the original reference points displaced.
83     size_pts=size(base_pts,1);
84     input_pts(:,1)=base_pts(:,1)+diff_offset(1)*ones(size_pts,1);
85     input_pts(:,2)=base_pts(:,2)+diff_offset(2)*ones(size_pts,1);
86
87 %input_pts_adj receives a recalculated set of input points by ...
      performing a
88 %"punctual" crosscorrelation in the boundaries of each input ...
      point. Thus,
89 %the real location of the reference points in IM_nonr is stablished.
90 %By employing the function cp2tform, a spatial transformation for ...
      IM_nonr
91 %is calculated to match IM_base and it is stored in mytform.
92 %IM_reg receives the transformed version of IM_nonr and then it is ...
      stored
93 %in file_name_2.
94     input_pts_adj=cpcorr(input_pts, base_pts, IM_nonr, IM_base);
95     mytform = cp2tform(input_pts_adj, base_pts, 'similarity');
96     IM_reg = imtransform(IM_nonr, mytform, 'XData', [1 ...
          size(IM_base,2)],'YData', [1 size(IM_base,1)]);
97     imwrite(IM_reg,file_name_2,'Compression','none','WriteMode','append');
98
99 end
```

Appendix C

Image J Macros and Functions

The following lines present the different codes of the macros and functions developed in ImageJ to perform the analysis of the images of nanowire images from Chapter IV.

```
////////////////////////////////////////////////////////////
macro "Stack Treatment [q]"{

// Shortcut key: q
// This macro treats the raw stack of images. It receives the
// length (r, in pixels) of the median filter that will be
// employed on the stack, the image numbers for the low (LT)
// and high (HT) temperature reference.
      Dialog.create("Stack Treatment");
      Dialog.addNumber("MedianFilter (r):", 3);
      Dialog.addNumber("Low Temp Reference (LT):",1);
      nPics=nSlices;
      Dialog.addNumber("High Temp Reference (HT):",nPics);
      Dialog.show();
      rNum=Dialog.getNumber();
      ansNorm=Dialog.getChoice();
      LT=Dialog.getNumber();
      HT=Dialog.getNumber();

      Original=getTitle();
      FilterMedian_R3();

// The data type of the stack of images is transformed to 32
// bits float in order to perform divisions between images
// without loosing information of the fractions. The new stack
// is stored in the global variable IM32bits.
      Turn32bits();
      IM32bits=getTitle();
```

```
      selectWindow(Original);
      close();

// The DeltaF() function calculates HT-LT and leaves it open
// in a window named Delta.tif
      selectWindow(IM32bits);
      DeltaF();

// The function StacksubsbyLTimage() substracts LT from each
// image of the stack under analysis. The name of the window
// with the resulting stack is stored in the global variable
// SubLT.
      selectWindow(IM32bits);
      StacksubsbyLTimage();
      SubLT=getTitle();
       //saveAs(".tif");

//The function Ratio() divides the Stack SubLT by (HT-LT)
       Ratio();
       //RecordProfile();
       //run("Dynamic Profiler");
}

//%%%%%%%%%%%%%%%%%%%%%%%%%%%%%%%%%%%%%%%%%%%%%%%%
//Functions of the macro "Stack Treatment"
//%%%%%%%%%%%%%%%%%%%%%%%%%%%%%%%%%%%%%%%%%%%%%%%%

//Median Filter to the stack under analysis
function FilterMedian_R3(){
     run("Median...", "radius="+rNum+" stack");
     //run("Gaussian Blur...", "sigma=1 stack");
}

//Transformation of the stack to 32-bit float data type
function Turn32bits(){
T=getInfo("image.filename");
run("Duplicate...", "title=[Copy_1.tif]");
imageCalculator("Divide create 32-bit stack",
"Copy_1.tif","Copy_1.tif");
selectWindow("Copy_1.tif");
close();
imageCalculator("Divide create 32-bit stack",

T,"Result of Copy_1.tif");
IM32bits=getTitle();
```

```
selectWindow("Result of Copy_1.tif");
close();
            selectWindow(IM32bits);
}

//Calculation of the reference HT-LT
function DeltaF(){
setSlice(LT);
run("Duplicate...", "title=[LT.tif]");
            selectWindow(IM32bits);
setSlice(HT);
run("Duplicate...", "title=[HT.tif]");

            imageCalculator("Subtract create 32-bit
 stack","HT.tif","LT.tif");
TT=getTitle();
run("Duplicate...", "title=[Delta.tif]");
            selectWindow(TT);
close();

selectWindow("HT.tif");
close();
selectWindow("LT.tif");
close();
}

//Substraction of LT from each image of the stack under study
function StacksubsbyLTimage(){
setSlice(LT);
run("Duplicate...", "title=[LT.tif]");
imageCalculator("Substract create 32-bit

stack",IM32bits,"LT.tif");
SubLT=getTitle();
setSlice(LT+1);
run("Enhance Contrast", "saturated=0.35");
            selectWindow(SubLT);
}

//Calculation of SubLT/(HT-LT)
function Ratio(){
imageCalculator("Divide create 32-bit

stack",SubLT,"Delta.tif");
setSlice(LT+1);
```

```
run("Enhance Contrast", "saturated=0.35");
}

////////////////////////////////////////////////////////////
macro "NW Profiles [p]"{

// Shortcut key: p
// This macro receives a ROI predifined by the user in the
// form of a line and returns a table with the the values of
// each pixel along the line for each image of the stack. The
// information contained in the table is also copied in order
// to be pasted directly on another program (Excel, Matlab,
// etc).
// NOTE: Before running this macro it is imperative to define
// in the ROI manager the line of the ROI.

      Dialog.create("NW Treatment");
      Dialog.addNumber("Roi number:", 1);
      Dialog.show();
      ROI_NUM=Dialog.getNumber();

      RecordProfile();
 }

//%%%%%%%%%%%%%%%%%%%%%%%%%%%%%%%%%%%%
//Functions of the macro "NW Profiles"
//%%%%%%%%%%%%%%%%%%%%%%%%%%%%%%%%%%%%

function RecordProfile(){
   count=0;
   setOption("Show All", true);

   for (n=1; n<=nSlices; n++) {
setSlice(n);
       ROI_N=ROI_NUM-1;
roiManager("select", ROI_N);
            roiManager("Remove Slice Info");

roiManager("select", ROI_N);
            profile = getProfile();

count++;

        for (i=0; i<profile.length; i++){
             setResult("d"+count, i, profile[i]);
```

```
            }
   }

 updateResults();
 String.resetBuffer;
 String.copyResults;
 roiManager("deselect");
 setOption("Show All", false);
 roiManager("select",0);
 setSlice(1);
 }

////////////////////////////////////////////////////////////
macro "ROI_Cycle [c]"{

// Shortcut key: c
// This macro receives the number of pictures per cycle
// (NumStep), the initial value in mA applied to the nanowire

// (InValue), step size employed in the cycle (StepSize),
// quantity of cycles contained in the stack under analysis
// (NumCycle) and a ROI number (already defined in the ROI
// manager) (NumRoi). Then, it returns a table with the
// information organized as a function of applied current and
// cycle number ready to be pasted on a different software
// (Excel, Matlab, etc).

Dialog.create("ROI Cycle");
Dialog.addNumber("Size of Cycle:", 0);
Dialog.addNumber("Initial Value (mA):", 0);
Dialog.addNumber("Step Size (mA):", 0.5);
Dialog.addNumber("Quantity of Cycles:", 1);
Dialog.addNumber("ROI to use:", 4);
Dialog.show();
NumStep=Dialog.getNumber();
InValue=Dialog.getNumber();
StepSize=Dialog.getNumber();
NumCycle=Dialog.getNumber();
NumRoi=Dialog.getNumber();
ROI_N=NumRoi-1;

Calc_Roi();
}

//%%%%%%%%%%%%%%%%%%%%%%%%%%%%%%%%%%%%
```

```
//Functions of the macro "ROI_Cycle"
//%%%%%%%%%%%%%%%%%%%%%%%%%%%%%%%%%%%%

function Calc_Roi(){

for (n=0; n<=NumStep-1; n++){
             setResult("i (mA)", n, n*StepSize);
         }

for (k=1; k<=NumCycle; k++) {
for (n=1; n<=NumStep; n++) {
setSlice(n+(k-1)*NumStep);
roiManager("select", ROI_N);
getRawStatistics(area,mean,std);
setResult("Cycle"+k, n-1, mean);
//setResult("Cycle"+k, n-1, std);

}
}

updateResults();
String.resetBuffer;
String.copyResults;
roiManager("deselect");
setOption("Show All", false);
roiManager("select",0);
}

////////////////////////////////////////////////////////////
//ROI managment macros
//These two macros were writen to facilitate the storage and
//charge of a particular set of ROIs

macro "Save ROIs [r]"{
//Shortcut key:r
     for (n=0; n<roiManager("count"); n++){
       roiManager("select", n);
       roiManager("Remove Slice Info");
       }
     roiManager("Save", "");
 }
////////////////////////////////////////////////////////////
macro "Open ROI [o]"{
//Shortcut key: o
     if(roiManager("count")!=0){
```

```
            roiManager("deselect");
            roiManager("Delete");
            }
    roiManager("Open", "");
    roiManager("Show all with labels");
 }
////////////////////////////////////////////////////////////////
```

Bibliography

[1] A. Bousseksou, G. Molnár, L. Salmon, and W. Nicolazzi, "Molecular spin crossover phenomenon: recent achievements and prospects," *Chemical Society Reviews*, vol. 40, no. 6, pp. 3313–35, 2011.

[2] G. Blasse and B. C. Grabmaier, *Luminescent materials*. Berlin, Germany: Springer-Verlag, 1994.

[3] A. S. Marfunin, *Mineralogy, Spectroscopy Luminescence and Radiation Centers in Minerals*. Berlin, Germany: Springer-Verlag, 1979.

[4] M. Gaft, R. Reisfeld, and G. Panczer, *Modern luminescence spectroscopy of minerals and materials*. Berlin, Germany: Springer, 2005.

[5] P. Gütlich and H. A. Goodwin, *Spin Crossover in Transition Metal Compounds I-III*, vol. 233-235 of *Top. Curr. Chem.* Berlin - Heidelberg, Germany: Springer, 2004.

[6] J. R. Lakowicz, *Principles of fluorescence spectroscopy*. New York, USA: Springer, 2006.

[7] R. C. Powel and G. Blasse, "Energy transfer in concentrated systems," in *Luminescence and Energy Transfer*, vol. 42 of *Structure and Bonding*, pp. 43 – 96, Berlin, Germany: Springer - Verlag, 1980.

[8] B. Valeur, *Molecular fluorescence: principles and applications*. Weinheim, Germany: Wiley VCH, 2002.

[9] S. E. Braslavsky, "Glossary of terms used in photochemistry, 3rd edition (IUPAC Recommendations 2006)," *Pure and Applied Chemistry*, vol. 79, no. 3, pp. 293–465, 2007.

[10] B. N. Figgis, *Introduction to ligand fields*. New York, USA: Wiley-Interscience, 1964.

[11] R. M. Clegg, "Chapter 1 Förster resonance energy transfer-FRET what is it, why do it, and how it's done," in *Laboratory Techniques in Biochemistry and Molecular Biology* (T. W. J. Gadella, ed.), vol. 33, pp. 1–57, Elsevier, 2009.

[12] W. E. Moerner and D. P. Fromm, "Methods of single-molecule fluorescence spectroscopy and microscopy," *Review of Scientific Instruments*, vol. 74, no. 8, p. 3597, 2003.

[13] T. Förster, "Energiewanderung und Fluoreszenz," *Naturwissenshaften*, vol. 6, pp. 166 – 175, 1946.

[14] T. Förster, "Zwischenmolekulare Energiewanderung und Fluoreszenz," *Ann. Phys.*, vol. 2, pp. 55 – 75, 1948.

[15] T. Förster, "Intermolecular energy migration and fluorescence," in *Biological physics* (E. V. Mielczarek, E. Greenbaum, and R. S. Knox, eds.), pp. 148–160, New York, USA: American Institute of Physics, 1993.

[16] D. L. Dexter, "A Theory of Sensitized Luminescence in Solids," *The Journal of Chemical Physics*, vol. 21, no. 5, p. 836, 1953.

[17] D. L. Dexter and R. S. Knox, *Excitons*. New York, USA: Interscience, 1965.

[18] P. Gütlich and H. A. Goodwin, "Spin Crossover-An Overall Perspective," in *Spin Crossover in Transition Metal Compounds I*, vol. 233 of *Top. Curr. Chem.*, pp. 1–47, Berlin - Heidelberg, Germany: Springer, 2004.

[19] L. Cambi, L. Szego, and A. Cagnasso *Atti accad Lincei*, vol. 13, p. 168, 1931.

[20] H. A. Bethe, "Splitting of Terms in Crystals," *Ann. Physik*, vol. 3, pp. 133–206, 1929.

[21] A. Bousseksou, G. Molnár, P. Demont, and J. Menegotto, "Observation of a thermal hysteresis loop in the dielectric constant of spin crossover complexes: towards molecular memory devices," *Journal of Materials Chemistry*, vol. 13, no. 9, pp. 2069–2071, 2003.

[22] A. Rotaru, I. A. Gural'skiy, G. Molnár, L. Salmon, P. Demont, and A. Bousseksou, "Spin state dependence of electrical conductivity of spin crossover materials," *Chem Commun (Camb)*, vol. 48, no. 35, pp. 4163–5, 2012.

[23] A. Hauser, "Ligand Field Theoretical Considerations," in *Spin Crossover in Transition Metal Compounds I*, vol. 233 of *Topics in Current Chemistry*, pp. 49–58, Berlin - Heidelberg, Germany: Springer, 2004.

[24] Y. Tanabe and S. Sugano, "On the Absorption Spectra of Complex Ions. I," *Journal of the Physical Society of Japan*, vol. 9, no. 5, pp. 753–766, 1954.

[25] Y. Tanabe and S. Sugano, "On the Absorption Spectra of Complex Ions II," *Journal of the Physical Society of Japan*, vol. 9, no. 5, pp. 766–779, 1954.

[26] P. Gütlich, "Spin crossover in iron(II)-complexes," in *Structure and Bonding* (M. Complexes, ed.), vol. 44 of *Structure and Bonding*, pp. 83–195, Springer Berlin / Heidelberg, 1981.

[27] L. F. Lindoy and S. E. Livingstone, "Complexes of iron(II),cobalt(II) and nickel(II) with α-diimines and related bidentate ligands," *Coordination Chemistry Reviews*, vol. 2, no. 2, pp. 173–193, 1967.

[28] E. König, G. Ritter, and S. K. Kulshreshtha, "The Nature of Spin-State Transitions in Solid Complexes of Iron(II) and the Interpretation of Some Associated Phenomena," *Chemical Reviews*, vol. 85, no. 3, pp. 219–234, 1985.

[29] M. Sorai and S. Seki, "Magnetic Heat Capacity Due to Cooperative Low-Spin $^1A_1 \rightleftharpoons$High-Spin $^5T_2$ Transition in $Fe(phen)_2(NCS)_2$ Crystal," *Journal of the Physical Society of Japan*, vol. 33, p. 575, 1972.

[30] H. Spiering, E. Meissner, H. Köppen, E. Müller, and P. Gütlich, "The effect of the lattice expansion on high spin $\rightleftharpoons$ low spin transitions," *Chemical Physics*, vol. 68, no. 1-2, pp. 65–71, 1982.

[31] C. P. Slichter and H. G. Drickamer, "Pressure-induced electronic changes in compounds of iron," *The Journal of Chemical Physics*, vol. 56, no. 5, pp. 2142–2160, 1972.

[32] S. Bedoui, G. Molnár, S. Bonnet, C. Quintero, H. J. Shepherd, W. Nicolazzi, L. Salmon, and A. Bousseksou, "Raman spectroscopic and optical imaging of high spin/low spin domains in a spin crossover complex," *Chemical Physics Letters*, vol. 499, no. 1-3, pp. 94–99, 2010.

[33] Y. Garcia, O. Kahn, L. Rabardel, B. Chansou, L. Salmon, and J. P. Tuchagues, "Two-Step Spin Conversion for the Three-Dimensional Compound Tris(4,4'-bis-1,2,4-triazole)iron(II) Diperchlorate," *Inorganic Chemistry*, vol. 38, no. 21, pp. 4663–4670, 1999.

[34] J. A. Real, H. Bolvin, A. Bousseksou, A. Dworkin, O. Kahn, F. Varret, and J. Zarembowitch, "Two-step spin crossover in the new dinuclear compound $[Fe(bt)(NCS)_2]_2$bpym, with bt = 2,2'-bi-2-thiazoline and bpym = 2,2'-bipyrimidine: experimental investigation and theoretical approach," *Journal of the American Chemical Society*, vol. 114, no. 12, pp. 4650–4658, 1992.

[35] S. Bonnet, M. A. Siegler, J. S. Costa, G. Molnar, A. Bousseksou, A. L. Spek, P. Gamez, and J. Reedijk, "A two-step spin crossover mononuclear iron(II) complex with a [HS-LS-LS] intermediate phase," *Chemical Communications*, pp. 5619–5621, 2008.

[36] A. Bousseksou, J. Nasser, J. Linares, K. Boukheddaden, and F. Varret, "Ising-Like Model for the 2-Step Spin-Crossover," *Journal de Physique I*, vol. 2, no. 7, pp. 1381–1403, 1992.

[37] I. Krivokapic, C. Enachescu, R. Bronisz, and A. Hauser, "The interaction between the spin transition and a crystallographic phase transition in the spin-crossover compound $[Fe(bbtr)_3](ClO_4)_2$: Nucleation, formation of domains and fluctuations," *Inorganica Chimica Acta*, vol. 361, pp. 3616–3622, 2008.

[38] A. Akou, I. A. Gural'skiy, L. Salmon, C. Bartual-Murgui, C. Thibault, C. Vieu, G. Molnár, and A. Bousseksou, "Soft lithographic patterning of spin crossover complexes. Part 2: stimuli-responsive diffraction grating properties," *Journal of Materials Chemistry*, vol. 22, no. 9, pp. 3752–3757, 2012.

[39] G. Aromí, L. A. Barrios, O. Roubeau, and P. Gamez, "Triazoles and tetrazoles: Prime ligands to generate remarkable coordination materials," *Coordination Chemistry Reviews*, vol. 255, no. 5-6, pp. 485–546, 2011.

[40] A. Grosjean, N. Daro, B. Kauffmann, A. Kaiba, J. F. Létard, and P. Guionneau, "The 1-D polymeric structure of the $[Fe(NH_2trz)_3](NO_3)_2{\cdot}nH_2O$ (with n = 2) spin crossover compound proven by single crystal investigations," *Chemical Communications*, vol. 47, no. 45, pp. 12382–4, 2011.

[41] O. Roubeau, J. M. Alcazar Gomez, E. Balskus, J. J. A. Kolnaar, J. G. Haasnoot, and J. Reedijk, "Spin-transition behaviour in chains of FeII bridged by 4-substituted 1,2,4-triazoles carrying alkyl tails," *New Journal of Chemistry*, vol. 25, no. 1, pp. 144–150, 2001.

[42] Y. Garcia, V. Niel, M. C. Muñoz, and J. A. Real, "Spin Crossover in 1D, 2D and 3D Polymeric Fe(II) Networks," in *Spin Crossover in Transition Metal Compounds I*, vol. 233 of *Topics in Current Chemistry*, pp. 229–257, Berlin - Heidelberg, Germany: Springer, 2004.

[43] P. J. Koningsbruggen, "Special Classes of Iron(II) Azole Spin Crossover Compounds," in *Spin Crossover in Transition Metal Compounds I*, vol. 233 of *Topics in Current Chemistry*, pp. 123–149, Berlin - Heidelberg, Germany: Springer, 2004.

[44] Y. Garcia, P. J. van Koningsbruggen, R. Lapouyade, L. Rabardel, O. Kahn, M. Wieczorek, R. Bronisz, Z. Ciunik, and M. F. Rudolf, "Synthesis and spin-crossover characteristics of polynuclear 4-(2 '-hydroxy-ethyl)-1,2,4-triazole Fe(II) molecular materials," *Comptes Rendus De L Academie Des Sciences Serie II Fascicule C-Chimie*, vol. 1, no. 8, pp. 523–532, 1998.

[45] O. Kahn, "Spin-Transition Polymers: From Molecular Materials Toward Memory Devices," *Science*, vol. 279, no. 5347, pp. 44–48, 1998.

[46] A. Urakawa, W. Van Beek, M. Monrabal-Capilla, J. R. Galan-Mascaros, L. Palin, and M. Milanesio, "Combined, Modulation Enhanced X-ray Powder Diffraction and Raman Spectroscopic Study of Structural Transitions in the Spin Crossover Material $[Fe(Htrz)_2(trz)](BF_4)$," *Journal of Physical Chemistry C*, vol. 115, no. 4, pp. 1323–1329, 2011.

[47] T. Kitazawa, Y. Gomi, M. Takahashi, M. Takeda, M. Enomoto, A. Miyazaki, and T. Enoki, "Spin-crossover behaviour of the coordination polymer $Fe(II)(C_5H_5N)_2Ni(II)(CN)_4$," *Journal of Materials Chemistry*, vol. 6, pp. 119–121, 1996.

[48] V. Niel, J. M. Martinez-Agudo, M. C. Muñoz, A. B. Gaspar, and J. A. Real, "Cooperative Spin Crossover Behavior in Cyanide-Bridged Fe(II)-M(II) Bimetallic 3D Hofmann-like Networks (M = Ni, Pd, and Pt)," *Inorganic Chemistry*, vol. 40, no. 16, pp. 3838–3839, 2001.

[49] C. Bartual-Murgui, N. A. Ortega-Villar, H. J. Shepherd, M. C. Munoz, L. Salmon, G. Molnár, A. Bousseksou, and J. A. Real, "Enhanced porosity in a new 3D Hofmann-like network exhibiting humidity sensitive cooperative spin transitions at room temperature," *Journal of Materials Chemistry*, vol. 21, no. 20, pp. 7217–7222, 2011.

[50] C. Bartual-Murgui, L. Salmon, A. Akou, N. A. Ortega-Villar, H. J. Shepherd, M. C. Munoz, G. Molnár, J. A. Real, and A. Bousseksou, "Synergetic effect of host-guest chemistry and spin crossover in 3D Hofmann-like metal-organic frameworks [Fe(bpac)M(CN)$_4$] (M=Pt, Pd, Ni)," *Chemistry - A European Journal*, vol. 18, no. 2, pp. 507–16, 2012.

[51] G. Agusti, R. Ohtani, K. Yoneda, A. B. Gaspar, M. Ohba, J. F. Sanchez-Royo, M. C. Munoz, S. Kitagawa, and J. A. Real, "Oxidative addition of halogens on open metal sites in a microporous spin-crossover coordination polymer," *Angewandte Chemie International Edition*, vol. 48, no. 47, pp. 8944–7, 2009.

[52] M. Ohba, K. Yoneda, G. Agusti, M. C. Munoz, A. B. Gaspar, J. A. Real, M. Yamasaki, H. Ando, Y. Nakao, S. Sakaki, and S. Kitagawa, "Bidirectional Chemo-Switching of Spin State in a Microporous Framework," *Angewandte Chemie International Edition*, vol. 48, no. 26, pp. 4767–4771, 2009.

[53] P. D. Southon, L. Liu, E. A. Fellows, D. J. Price, G. J. Halder, K. W. Chapman, B. Moubaraki, K. S. Murray, J. F. Létard, and C. J. Kepert, "Dynamic Interplay between Spin-Crossover and Host-Guest Function in a Nanoporous Metal-Organic Framework Material," *Journal of the American Chemical Society*, vol. 131, no. 31, pp. 10998–11009, 2009.

[54] G. Félix, K. Abdul-Kader, T. Mahfoud, I. A. Gural'skiy, W. Nicolazzi, L. Salmon, G. Molnár, and A. Bousseksou, "Surface plasmons reveal spin crossover in nanometric layers," *Journal of the American Chemical Society*, vol. 133, no. 39, pp. 15342–5, 2011.

[55] M. S. Alam, M. Stocker, K. Gieb, P. Müller, M. Haryono, K. Student, and A. Grohmann, "Spin-State Patterns in Surface-Grafted Beads of Iron(II) Complexes," *Angewandte Chemie International Edition*, vol. 49, no. 6, pp. 1159–1163, 2010.

[56] V. Meded, A. Bagrets, K. Fink, R. Chandrasekar, M. Ruben, F. Evers, A. Bernand-Mantel, J. S. Seldenthuis, A. Beukman, and H. S. J. van der Zant, "Electrical control over the Fe(II) spin crossover in a single molecule: Theory and experiment," *Phys. Rev. B*, vol. 83, p. 245415, Jun 2011.

[57] F. Prins, M. Monrabal-Capilla, E. A. Osorio, E. Coronado, and H. S. J. van der Zant, "Room-Temperature Electrical Addressing of a Bistable Spin-Crossover Molecular System," *Advanced Materials*, vol. 23, no. 13, pp. 1545–1549, 2011.

[58] Aravena, Daniel and Ruiz, Eliseo, "Coherent Transport through Spin-Crossover Single Molecules," *Journal of the American Chemical Society*, vol. 134, no. 2, pp. 777–779, 2012.

[59] M. Engeser, L. Fabbrizzi, M. Licchelli, and D. Sacchi, "A fluorescent molecular thermometer based on the nickel(II) high-spin/low-spin interconversion," *Chemical Communications*, pp. 1191–1192, 1999.

[60] Y. Garcia, F. Robert, A. D. Naik, G. Zhou, B. Tinant, K. Robeyns, S. Michotte, and L. Piraux, "Spin transition charted in a fluorophore-tagged thermochromic dinuclear iron(II) complex," *Journal of the American Chemical Society*, vol. 133, no. 40, pp. 15850–3, 2011.

[61] R. Gonzalez-Prieto, B. Fleury, F. Schramm, G. Zoppellaro, R. Chandrasekar, O. Fuhr, S. Lebedkin, M. Kappes, and M. Ruben, "Tuning the spin-transition properties of pyrene-decorated 2,6-bispyrazolylpyridine based Fe(II) complexes," *Dalton Transactions*, vol. 40, no. 29, pp. 7564–70, 2011.

[62] M. Hasegawa, F. Renz, T. Hara, Y. Kikuchi, Y. Fukuda, J. Okubo, T. Hoshi, and W. Linert, "Fluorescence spectra of Fe(II) spin crossover complexes with 2,6-bis(benzimidazole-2'-yl)pyridine," *Chemical Physics*, vol. 277, no. 1, pp. 21–30, 2002.

[63] C. Edder, C. Piguet, J.-C. G. Bünzli, and G. Hopfgartner, "High-Spin Iron(II) as a Semitransparent Partner for Tuning Europium(III) Luminescence in Heterodimetallic d-f Complexes," *Chemistry - A European Journal*, vol. 7, no. 14, pp. 3014–3024, 2001.

[64] H. Matsukizono, K. Kuroiwa, and N. Kimizuka, "Self-assembly-directed Spin Conversion of Iron(II) 1,2,4-Triazole Complexes in Solution and Their Effect on Photorelaxation Processes of Fluorescent Counter Ions," *Chemistry Letters*, vol. 37, no. 4, pp. 446–447, 2008.

[65] C. Piguet, E. Rivara-Minten, G. Hopfgartner, and J.-C. G. Bünzli, "Molecular Magnetism and Iron(II) Spin-State Equilibrium as Structural Probes in Heterodinuclear d-f Complexes," *Helvetica Chimica Acta*, vol. 78, no. 7, pp. 1651–1672, 1995.

[66] C. Piguet, E. Rivara-Minten, G. Bernardinelli, J.-C. G. Bünzli, and G. Hopfgartner, "Non-covalent lanthanide podates with predetermined physicochemical properties: iron(II) spin-state equilibria in self-assembled heterodinuclear d-f supramolecular complexes," *Journal of the Chemical Society, Dalton Transactions*, no. 3, pp. 421–434, 1997.

[67] C. A. Tovee, C. A. Kilner, J. A. Thomas, and M. A. Halcrow, "Co-crystallising two functional complex molecules in a terpyridine embrace lattice," *CrystEngComm*, vol. 11, no. 10, p. 2069, 2009.

[68] S. Titos-Padilla, J. M. Herrera, X. W. Chen, J. J. Delgado, and E. Colacio, "Bifunctional hybrid SiO2 nanoparticles showing synergy between core spin crossover and shell luminescence properties," *Angewandte Chemie International Edition*, vol. 50, no. 14, pp. 3290–3, 2011.

[69] M. Matsuda, H. Isozaki, and H. Tajima, "Electroluminescence Quenching Caused by a Spin-crossover Transition," *Chemistry Letters*, vol. 37, no. 3, pp. 374–375, 2008.

[70] M. Matsuda, H. Isozaki, and H. Tajima, "Reproducible on-off switching of the light emission from the electroluminescent device containing a spin crossover complex," *Thin Solid Films*, vol. 517, no. 4, pp. 1465–1467, 2008.

[71] L. Salmon, G. Molnár, D. Zitouni, C. Quintero, C. Bergaud, J. C. Micheau, and A. Bousseksou, "A novel approach for fluorescent thermometry and thermal imaging purposes using spin crossover nanoparticles," *Journal of Materials Chemistry*, vol. 20, no. 26, pp. 5499–5503, 2010.

[72] C. Quintero, G. Molnár, L. Salmon, A. Tokarev, C. Bergaud, and A. Bousseksou, "Design of fluorescent spin-crossover nanoparticles for thermometry applications," in *Thermal Investigations of ICs and Systems (THERMINIC), 2010 16th International Workshop on*, pp. 1–5, 2010.

[73] C. M. Quintero, I. A. Gural'skiy, L. Salmon, G. Molnár, C. Bergaud, and A. Bousseksou, "Soft lithographic patterning of spin crossover complexes. Part 1: fluorescent detection of the spin transition in single nano-objects," *Journal of Materials Chemistry*, vol. 22, no. 9, pp. 3745–3751, 2012.

[74] I. A. Gural'skiy, C. Quintero, K. Abdul-Kader, M. Lopes, C. Bartual-Murgui, L. Salmon, Z. Pengxiang, G. Molnár, D. Astruc, and A. Bousseksou, "Detection of molecular spin-state changes in ultra-thin films by photonic methods," *Journal of Nanophotonics*, 2012. In press.

[75] I. A. Gural'skiy, C. M. Quintero, G. Molnar, I. O. Fritsky, L. Salmon, and A. Bousseksou, "Synthesis of Spin-Crossover Nano- and Micro-objects in Homogeneous Media," *Chemistry - A European Journal*, 2012. In press.

[76] J.-F. Létard, P. Guionneau, and L. Goux-Capes, "Towards Spin Crossover Applications," in *Spin Crossover in Transition Metal Compounds III*, vol. 235 of *Top. Curr. Chem.*, pp. 221–249, Berlin - Heidelberg, Germany: Springer, 2004.

[77] E. Coronado, J. R. Galan-Mascaros, M. Monrabal-Capilla, J. Garcia-Martinez, and P. Pardo-Ibanez, "Bistable spin-crossover nanoparticles showing magnetic thermal hysteresis near room temperature," *Advanced Materials*, vol. 19, no. 10, p. 1359, 2007.

[78] T. Forestier, S. Mornet, N. Daro, T. Nishihara, S. Mouri, K. Tanaka, O. Fouche, E. Freysz, and J. F. Létard, "Nanoparticles of iron(II) spin-crossover," *Chemical Communications*, no. 36, pp. 4327–9, 2008.

[79] C. Arnaud, T. Forestier, N. Daro, E. Freysz, J.-F. Létard, G. Pauliat, and G. Roosen, "Observation of an asymmetry in the thermal hysteresis loop at the scale of a single spin-crossover particle," *Chemical Physics Letters*, vol. 470, no. 1-3, pp. 131–135, 2009.

[80] T. Forestier, A. Kaiba, S. Pechev, D. Denux, P. Guionneau, C. Etrillard, N. Daro, E. Freysz, and J. F. Létard, "Nanoparticles of $[Fe(NH_2\text{-}trz)_3)]Br_2 \cdot 3H_2O$ (NH_2-trz=2-Amino-1,2,4-triazole) Prepared by the Reverse Micelle Technique: Influence of Particle and Coherent Domain Sizes on Spin-Crossover Properties," *Chemistry-a European Journal*, vol. 15, no. 25, pp. 6122–6130, 2009.

[81] J. R. Galan-Mascaros, E. Coronado, A. Forment-Aliaga, M. Monrabal-Capilla, E. Pinilla-Cienfuegos, and M. Ceolin, "Tuning Size and Thermal Hysteresis in Bistable Spin Crossover Nanoparticles," *Inorganic Chemistry*, vol. 49, no. 12, pp. 5706–5714, 2010.

[82] V. Martinez, I. Boldog, A. B. Gaspar, V. Ksenofontov, A. Bhattacharjee, P. Gutlich, and J. A. Real, "Spin Crossover Phenomenon in Nanocrystals and Nanoparticles of Fe(3-Fpy)(2)M(CN)(4) (M-II = Ni, Pd, Pt) Two-Dimensional Coordination Polymers," *Chemistry of Materials*, vol. 22, no. 14, pp. 4271–4281, 2010.

[83] S. M. Neville, C. Etrillard, S. Asthana, and J. F. Létard, "Light-Induced Stored Information in Nanoparticles," *European Journal of Inorganic Chemistry*, no. 2, pp. 282–288, 2010.

[84] A. Tissot, J. F. Bardeau, E. Riviere, F. Brisset, and M. L. Boillot, "Thermo- and photoswitchable spin-crossover nanoparticles of an iron(II) complex trapped in transparent silica thin films," *Dalton Transactions*, vol. 39, no. 33, pp. 7806–12, 2010.

[85] A. Tokarev, L. Salmon, Y. Guari, W. Nicolazzi, G. Molnár, and A. Bousseksou, "Cooperative spin crossover phenomena in $[Fe(NH_2trz)_3](tosylate)_2$ nanoparticles," *Chemical Communications*, vol. 46, no. 42, pp. 8011–8013, 2010.

[86] Y. Raza, F. Volatron, S. Moldovan, O. Ersen, V. Huc, C. Martini, F. Brisset, A. Gloter, O. Stephan, A. Bousseksou, L. Catala, and T. Mallah, "Matrix-dependent cooperativity in spin crossover $Fe(pyrazine)Pt(CN)_4$ nanoparticles," *Chemical Communications*, vol. 47, no. 41, pp. 11501–11503, 2011.

[87] I. A. Gural'skiy, G. Molnár, I. O. Fritsky, L. Salmon, and A. Bousseksou, "Synthesis of $[Fe(hptrz)_3](OTs)_2$ spin crossover nanoparticles in microemulsion," *Polyhedron*, vol. 38, no. 1, pp. 245–250, 2012.

[88] I. Boldog, A. B. Gaspar, V. Martinez, P. Pardo-Ibanez, V. Ksenofontov, A. Bhattacharjee, P. Gutlich, and J. A. Real, "Spin-crossover nanocrystals with magnetic, optical, and structural bistability near room temperature," *Angewandte Chemie International Edition*, vol. 47, no. 34, pp. 6433–6437, 2008.

[89] F. Volatron, L. Catala, E. Riviere, A. Gloter, O. Stephan, and T. Mallah, "Spin-crossover coordination nanoparticles," *Inorganic Chemistry*, vol. 47, no. 15, pp. 6584–6586, 2008.

[90] E. Codjovi, L. Sommier, O. Kahn, and C. Jay, "A spin transition molecular material with an exceptionally large thermal hysteresis loop at room temperature," *New Journal of Chemistry*, vol. 20, no. 5, pp. 503–505, 1996.

[91] J. Sakakibara and R. J. Adrian, "Whole field measurement of temperature in water using two-color laser induced fluorescence," *Experiments in Fluids*, vol. 26, no. 1, pp. 7–15, 1999.

[92] G. B. Dutt, "Fluorescence anisotropy of ionic probes in AOT reverse micelles: Influence of water droplet size and electrostatic interactions on probe dynamics," *Journal of Physical Chemistry B*, vol. 112, no. 24, pp. 7220–7226, 2008.

[93] K. R. Fewings, P. C. Junk, D. Georganopoulou, P. D. Prince, and J. W. Steed, "Supramolecular interactions in metal tosylate complexes," *Polyhedron*, vol. 20, no. 7-8, pp. 643–649, 2001.

[94] J. Stehr, J. M. Lupton, M. Reufer, G. Raschke, T. A. Klar, and J. Feldmann, "Sub-microsecond molecular thermometry using thermal spin flips," *Advanced Materials*, vol. 16, no. 23-24, pp. 2170–+, 2004.

[95] C. C. Blanco, A. M. G. Campaña, F. A. Barrero, and M. R. Ceba, "Micellar medium for the analysis of complex mixtures of molybdenum and tungsten by derivative synchronous spectrofluorimetry in steels," *Talanta*, vol. 42, no. 8, pp. 1037–1044, 1995.

[96] H. Kunkely and A. Vogler, "Fluorescence of alizarin complexone and its metal complexes," *Inorganic Chemistry Communications*, vol. 10, no. 3, pp. 355–357, 2007.

[97] J. A. Muñoz, A. M. G. Campaña, and F. A. Barrero, "Effect of cationic micelles on the formation of the complex oxalate-Alizarin Red S-Zr(IV): Application to the sensitive fluorescence determination of oxalate ion," *Talanta*, vol. 47, no. 2, pp. 387–399, 1998.

[98] R. Sai Sathish, M. Ravi Kumar, G. Nageswara Rao, K. Anil Kumar, and C. Janardhana, "A water-soluble fluorescent fluoride ion probe based on Alizarin Red S-Al(III) complex," *Spectrochimica Acta Part A Molecular and Biomolecular Spectroscopy*, vol. 66, no. 2, pp. 457–61, 2007.

[99] L. Shao-Qin, L. Xuan, H. Shi-Rong, Z. Li-Qing, W. Yan, C. Li, L. Jia-Ming, and L. Long-Di, "Determination of trace aluminum by fluorescence quenching method based on catalysis of potassium chlorate oxidizing alizarin red," *Spectrochimica Acta Part A Molecular and Biomolecular Spectroscopy*, vol. 62, no. 1-3, pp. 637–40, 2005.

[100] J. Chen, F. Zeng, and S. Wu, "Construction of energy transfer systems within nanosized polymer micelles and their fluorescence modulation properties," *A European Journal of Chemical Physics and Physical Chemistry*, vol. 11, no. 5, pp. 1036–43, 2010.

[101] K. Kuroiwa, H. Kikuchi, and N. Kimizuka, "Spin crossover characteristics of nanofibrous Fe-II-1,2,4-triazole complexes in liquid crystals," *Chemical Communications*, vol. 46, no. 8, pp. 1229–1231, 2010.

[102] L. Catala, A. Gloter, O. Stephan, G. Rogez, and T. Mallah, "Superparamagnetic bimetallic cyanide-bridged coordination nanoparticles with TB = 9 K," *Chemical Communications*, no. 9, pp. 1018–1020, 2006.

[103] T. Uemura and S. Kitagawa, "Prussian blue nanoparticles protected by poly(vinylpyrrolidone)," *Journal of the American Chemical Society*, vol. 125, no. 26, pp. 7814–7815, 2003.

[104] D. Brinzei, L. Catala, N. Louvain, G. Rogez, O. Stephan, A. Gloter, and T. Mallah, "Spontaneous stabilization and isolation of dispersible bimetallic coordination nanoparticles of $Cs_xNi[Cr(CN)_6]_y$," *Journal of Materials Chemistry*, vol. 16, no. 26, pp. 2593–2599, 2006.

[105] V. Vo, M. N. Van, H. I. Lee, J. M. Kim, Y. Kim, and S. J. Kim, "A new route for obtaining Prussian blue nanoparticles," *Materials Chemistry and Physics*, vol. 107, no. 1, pp. 6–8, 2008.

[106] H. O. Bayer, R. S. Cook, and W. C. von Mayer. US Pat. 1974, 3, 821 376-10.

[107] D. Coucouvanis in *Inorganic Syntheses*, vol. 33, pp. 98–99, John Wiley & Sons, 2002.

[108] G. Molnár, S. Cobo, J. Real, F. Carcenac, E. Daran, C. Vieu, and A. Bousseksou, "A Combined Top-Down/Bottom-Up Approach for the Nanoscale Patterning of Spin-Crossover Coordination Polymers," *Advanced Materials*, vol. 19, no. 16, pp. 2163–2167, 2007.

[109] H. Soyer, C. Mingotaud, M.-L. Boillot, and P. Delhaès, "Spin Crossover of a Langmuir-Blodgett Film Based on an Amphiphilic Iron(II) Complex," *Langmuir*, vol. 14, no. 20, pp. 5890–5895, 1998.

[110] H. Soyer, E. Dupart, C. J. Gómez-García, C. Mingotaud, and P. Delhaès, "First Magnetic Observation of a Spin Crossover in a Langmuir-Blodgett Film," *Advanced Materials*, vol. 11, no. 5, pp. 382–384, 1999.

[111] J.-F. Létard, O. Nguyen, H. Soyer, C. Mingotaud, P. Delhaès, and O. Kahn, "First Evidence of the LIESST Effect in a Langmuir-Blodgett Film," *Inorganic Chemistry*, vol. 38, no. 13, pp. 3020–3021, 1999.

[112] H. Soyer, E. Dupart, C. Mingotaud, C. Gomez-Garcia, and P. Delhaès, "Spin crossover phenomenon of a semi-fluorinated iron (ii) complex organized in a langmuir-blodgett film," *Colloids and Surfaces A: Physicochemical and Engineering Aspects*, vol. 171, no. 1, pp. 275–282, 2000.

[113] Y. Bodenthin, U. Pietsch, H. Möhwald, and D. G. Kurth, "Inducing Spin Crossover in Metallo-supramolecular Polyelectrolytes through an Amphiphilic Phase Transition," *Journal of the American Chemical Society*, vol. 127, no. 9, pp. 3110–3114, 2005.

[114] A. Nakamoto, Y. Ono, N. Kojima, D. Matsumura, and T. Yokoyama, "Spin Crossover Complex Film, [Fe^{II}(H-trz)$_3$]-Nafion, with a Spin Transition around Room Temperature," *Chemistry Letters*, vol. 32, no. 4, pp. 336–337, 2003.

[115] A. Nakamoto, Y. Ono, N. Kojima, D. Matsumura, and T. Yokoyama, "Spin Crossover Complex Film, [Fe^{II}(H-trz)$_3$]-Nafion,with a Spin Transition around Room Temperature," *Chemistry Letters*, vol. 32, no. 4, p. 476, 2003.

[116] S.-W. Lee, J.-W. Lee, S.-H. Jeong, I.-W. Park, Y.-M. Kim, and J.-I. Jin, "Processable magnetic plastics composites-spin crossover of pmma/fe(ii)-complexes composites," *Synthetic Metals*, vol. 142, no. 1-3, pp. 243–249, 2004.

[117] M.-L. Boillot, S. Pillet, A. Tissot, E. Rivière, N. Claiser, and C. Lecomte, "Ligand-Driven Light-Induced Spin Change Activity and Bidirectional Photomagnetism of Styrylpyridine Iron(II) Complexes in Polymeric Media," *Inorganic Chemistry*, vol. 48, no. 11, pp. 4729–4736, 2009.

[118] A. Jaiswal, S. Floquet, M.-L. Boillot, and P. Delhaès, "A Comparative Investigation of Spin Crossover in Bulk Materials, Lamellar CdPS3 Layers, and Polyelectrolytes in a Series of Ferric Complexes: [FeIII((X-sal)2trien)]Y," *A European Journal of Chemical Physics and Physical Chemistry*, vol. 3, no. 12, pp. 1045–1049, 2002.

[119] T. Mahfoud, G. Molnár, S. Cobo, L. Salmon, C. Thibault, C. Vieu, P. Demont, and A. Bousseksou, "Electrical properties and non-volatile memory effect of the [Fe(HB(pz)$_3$)$_2$] spin crossover complex integrated in a microelectrode device," *Applied Physics Letters*, vol. 99, no. 5, 2011.

[120] M. Seredyuk, A. B. Gaspar, V. Ksenofontov, S. Reiman, Y. Galyametdinov, W. Haase, E. Rentschler, and P. Gütlich, "Room Temperature Operational Thermochromic Liquid Crystals," *Chemistry of Materials*, vol. 18, no. 10, pp. 2513–2519, 2006.

[121] M. Ruben, J. Rojo, F. J. Romero-Salguero, L. H. Uppadine, and J.-M. Lehn, "Grid-Type Metal Ion Architectures: Functional Metallosupramolecular Arrays," *Angewandte Chemie International Edition*, vol. 43, no. 28, pp. 3644–3662, 2004.

[122] S. Cobo, G. Molnár, J. A. Real, and A. Bousseksou, "Multilayer Sequential Assembly of Thin Films That Display Room-Temperature Spin Crossover with Hysteresis," *Angewandte Chemie International Edition*, vol. 45, no. 35, pp. 5786–5789, 2006.

[123] G. Agustí, S. Cobo, A. B. Gaspar, G. Molnár, N. O. Moussa, P. . Szilágyi, V. Pálfi, C. Vieu, M. Carmen Muñoz, J. A. Real, and A. Bousseksou, "Thermal and Light-Induced Spin Crossover Phenomena in New 3D Hofmann-Like Microporous Metalorganic Frameworks Produced As Bulk Materials and Nanopatterned Thin Films," *Chemistry of Materials*, vol. 20, no. 21, pp. 6721–6732, 2008.

[124] C. Bartual-Murgui, A. Akou, L. Salmon, G. Molnár, C. Thibault, J. A. Real, and A. Bousseksou, "Guest effect on nanopatterned spin-crossover thin films," *Small*, vol. 7, no. 23, pp. 3385–3391, 2011.

[125] C. Bartual-Murgui, L. Salmon, A. Akou, C. Thibault, G. Molnár, T. Mahfoud, Z. Sekkat, J. A. Real, and A. Bousseksou, "High quality nano-patterned thin films of the coordination compound Fe(pyrazine)[Pt(CN)$_4$] deposited layer-by-layer," *New Journal of Chemistry*, vol. 35, pp. 2089–2094, 2011.

[126] G. Decher, "Fuzzy Nanoassemblies: Toward Layered Polymeric Multicomposites," *Science*, vol. 277, no. 5330, pp. 1232–1237, 1997.

[127] P. Hammond, "Form and Function in Multilayer Assembly: New Applications at the Nanoscale," *Advanced Materials*, vol. 16, no. 15, pp. 1271–1293, 2004.

[128] S. Srivastava and N. A. Kotov, "Composite Layer-by-Layer (LBL) Assembly with Inorganic Nanoparticles and Nanowires," *Accounts of Chemical Research*, vol. 41, no. 12, pp. 1831–1841, 2008.

[129] M. Cavallini, I. Bergenti, S. Milita, G. Ruani, I. Salitros, Z.-R. Qu, R. Chandrasekar, and M. Ruben, "Micro- and Nanopatterning of Spin-Transition Compounds into Logical Structures," *Angewandte Chemie International Edition*, vol. 47, no. 45, pp. 8596–8600, 2008.

[130] M. Cavallini, I. Bergenti, S. Milita, J. C. Kengne, D. Gentili, G. Ruani, I. Salitros, V. Meded, and M. Ruben, "Thin Deposits and Patterning of Room-Temperature-Switchable One-Dimensional Spin-Crossover Compounds," *Langmuir*, vol. 27, no. 7, pp. 4076–4081, 2011.

[131] C. Thibault, G. Molnár, L. Salmon, A. Bousseksou, and C. Vieu, "Soft Lithographic Patterning of Spin Crossover Nanoparticles," *Langmuir*, vol. 26, no. 3, pp. 1557–1560, 2010. PMID: 19950983.

[132] S. P. Leytus, L. L. Melhado, and W. F. Mangel, "Rhodamine-based compounds as fluorogenic substrates for serine proteinases.," *Biochem. J.*, vol. 209, no. 2, pp. 299–0, 1983.

[133] Y. Kubota and R. F. Steiner, "Fluorescence decay and quantum yield characteristics of acridine orange and proflavine bound to DNA," *Biophysical Chemistry*, vol. 6, no. 3, pp. 279–289, 1977.

[134] "Andor Technology." http://www.andor.com.

[135] R. M. Haralick and L. G. Shapiro, *Computer and Robot Vision*, vol. II, pp. 316–317. Addision-Wesley, 1992.

[136] J. P. Lewis, "Fast Normalized Cross-Correlation," tech. rep., Industrial Light & Magic, 1995-2011. www.idiom.com/ zilla/Papers/nvisionInterface/nip.html.

[137] A. Cerf, *Assemblage dirigé de nano-objets*. PhD thesis, Toulouse University, 2010.

[138] A. Cerf and C. Vieu, "Transfer printing of sub-100 nm nanoparticles by soft lithography with solvent mediation," *Colloids and Surfaces A: Physicochemical and Engineering Aspects*, vol. 342, no. 1-3, pp. 136–140, 2009.

[139] J. Lee, C. Park, and G. M. Whitesides, "Solvent Compatibility of Poly(dimethylsiloxane)-Based Microfluidic Devices," *Analytical Chemistry*, vol. 75, no. 23, pp. 6544–6554, 2003.

[140] Y. Xia and G. M. Whitesides, "Soft Lithography," *Annual Review of Materials Science*, vol. 28, no. 1, pp. 153–184, 1998.

[141] J. Lee and N. A. Kotov, "Thermometer design at the nanoscale," *Nano Today*, vol. 2, no. 1, pp. 48 – 51, 2007.

[142] J. Pomeroy, M. Kuball, D. Wallis, A. Keir, K. Hilton, R. Balmer, M. Uren, T. Martin, and P. Heard, "Thermal mapping of defects in AlGaN/GaN heterostructure field-effect transistors using micro-Raman spectroscopy," *Applied Physics Letters*, vol. 87, no. 10, 2005.

[143] P. K. L. Chan, K. P. Pipe, G. Qin, and Z. Ma, "Thermoreflectance imaging of current dynamics in high power SiGe heterojunction bipolar transistors," *Applied Physics Letters*, vol. 89, no. 23, 2006.

[144] B. Schuler, E. Lipman, and W. Eaton, "Probing the free-energy surface for protein folding with single-molecule fluorescence spectroscopy," *Nature*, vol. 421, no. 6918, p. 94, 2003.

[145] C. Dobson, "Protein folding and misfolding," *Nature*, vol. 426, no. 6968, pp. 884–890, 2003.

[146] J. He, H. F. VanBrocklin, B. L. Franc, Y. Seo, and E. F. Jones, "Nanoprobes for medical diagnosis: Current status of nanotechnology in molecular imaging," *Current Nanoscience*, vol. 4, no. 1, pp. 17–29, 2008.

[147] P. Childs, J. Greenwood, and C. Long, "Review of temperature measurement," *Review of Scientific Instruments*, vol. 71, no. 8, pp. 2959–2978, 2000.

[148] J. Yoo, "Recent studies on fluid flow and heat transfer in thermal microdevices," *Nanoscale and Microscale Thermophysical Engineering*, vol. 10, no. 1, pp. 67–81, 2006.

[149] P. Löw, *High Spatial Resolution Fluorescent Thermometry: Thermal Characterization of Submicrometer Structures in Dry and Liquid Conditions*. PhD thesis, Toulouse University, 2008.

[150] L. Shi, S. Plyasunov, A. Bachtold, P. McEuen, and A. Majumdar, "Scanning thermal microscopy of carbon nanotubes using batch-fabricated probes," *Applied Physics Letters*, vol. 77, pp. 4295–4297, DEC 25 2000.

[151] L. Shi and A. Majumdar, "Recent developments in micro and nanoscale thermometry," *Microscale Thermophysical Engineering*, vol. 5, no. 4, pp. 251–265, 2001.

[152] A. Majumdar, J. Carrejo, and J. Lai, "Thermal Imaging using the Atomic Force Microscope," *Applied Physics Letters*, vol. 62, no. 20, pp. 2501–2503, 1993.

[153] A. Majumdar, J. Lai, M. Chandrachood, O. Nakabeppu, Y. Wu, and Z. Shi, "Thermal Imaging by Atomic-Force Microscopy using Thermocouple Cantilever Probes," *Review of Scientific Instruments*, vol. 66, no. 6, pp. 3584–3592, 1995.

[154] J. Small, L. Shi, and P. Kim, "Mesoscopic thermal and thermoelectric measurements of individual carbon nanotubes," *Solid State Communications*, vol. 127, no. 2, pp. 181–186, 2003.

[155] L. Lopez, S. Grauby, S. Dilhaire, M. Salhi, W. Claeys, S. Lefevre, and S. Volz, "Characterization of the thermal behavior of PN thermoelectric couples by scanning thermal microscope," *Microelectronics Journal*, vol. 35, no. 10, pp. 797–803, 2004.

[156] L. Aigouy, Y. De Wilde, M. Mortier, J. Gierak, and E. Bourhis, "Fabrication and characterization of fluorescent rare-earth-doped glass-particle-based tips for near-field optical imaging applications," *Applied Optics*, vol. 43, no. 19, pp. 3829–3837, 2004.

[157] L. Aigouy, G. Tessier, M. Mortier, and B. Charlot, "Scanning thermal imaging of microelectronic circuits with a fluorescent nanoprobe," *Applied Physics Letters*, vol. 87, no. 18, 2005.

[158] B. Samson, L. Aigouy, R. Latempa, G. Tessier, M. Aprili, M. Mortier, J. Lesueur, and D. Fournier, "Scanning thermal imaging of an electrically excited aluminum microstripe," *Journal of Applied Physics*, vol. 102, no. 2, 2007.

[159] E. S. Schlegel, "Apparatus for Determining Temperature Profiles in Microstructures," *Review of Scientific Instruments*, vol. 34, no. 4, pp. 360–361, 1963.

[160] D. D. Griffin, "Infrared techniques for measuring temperature and related phenomena of microcircuits.," *Applied Optics*, vol. 7, no. 9, pp. 1749–56, 1968.

[161] A. Kozlowska, M. Latoszek, J. Tomm, F. Weik, T. Elsaesser, M. Zbroszczyk, M. Bugajski, B. Spellenberg, and M. Bassler, "Analysis of thermal images from diode lasers: Temperature profiling and reliability screening," *Applied Physics Letters*, vol. 86, no. 20, 2005.

[162] A. Kozlowska, P. Wawrzyniak, J. Tomm, F. Weik, and T. Elsaesser, "Deep level emission from high-power diode laser bars detected by multispectral infrared imaging," *Applied Physics Letters*, vol. 87, no. 15, 2005.

[163] S. Jorez, J. Laconte, A. Cornet, and J. Raskin, "Low-cost optical instrumentation for thermal characterization of MEMS," *Measurement Science & Technology*, vol. 16, no. 9, pp. 1833–1840, 2005.

[164] G. Tessier, S. Hole, and D. Fournier, "Quantitative thermal imaging by synchronous thermoreflectance with optimized illumination wavelengths," *Applied Physics Letters*, vol. 78, no. 16, pp. 2267–2269, 2001.

[165] S. Dilhaire, S. Grauby, and W. Claeys, "Calibration procedure for temperature measurements by thermoreflectance under high magnification conditions," *Applied Physics Letters*, vol. 84, no. 5, pp. 822–824, 2004.

[166] D. Jaque and F. Vetrone, "Luminescence nanothermometry," *Nanoscale*, vol. 4, pp. 4301–4326, 2012.

[167] C. D. S. Brites, P. P. Lima, N. J. O. Silva, A. Millan, V. S. Amaral, F. Palacio, and L. D. Carlos, "Thermometry at the nanoscale," *Nanoscale*, vol. 4, pp. 4799–4829, 2012.

[168] P. Löw, B. Kim, N. Takama, and C. Bergaud, "High-spatial-resolution surface-temperature mapping using fluorescent thermometry," *Small*, vol. 4, no. 7, pp. 908–914, 2008.

[169] C. D. S. Brites, P. P. Lima, N. J. O. Silva, A. Millán, V. S. Amaral, F. Palacio, and L. D. Carlos, "A luminescent molecular thermometer for long-term absolute temperature measurements at the nanoscale," *Advanced Materials*, vol. 22, no. 40, pp. 4499–4504, 2010.

[170] M. I. J. Stich, L. H. Fischer, and O. S. Wolfbeis, "Multiple fluorescent chemical sensing and imaging," *Chemical Society Reviews*, vol. 39, pp. 3102–3114, 2010.

[171] K. Iwai, Y. Matsumura, S. Uchiyama, and A. de Silva, "Development of fluorescent microgel thermometers based on thermo responsive polymers and their modulation of sensitivity range," *Journal of Materials Chemistry*, vol. 15, no. 27-28, pp. 2796–2800, 2005.

Liste des Travaux

Chapitre du Livre

1. H. J. Shepherd, **C. M. Quintero**, G. Molnár, L. Salmon and A. Bousseksou, "Luminescent Spin Crossover Materials", in *Spin-Crossover Materials: Properties and Applications*, (ed. M. Halcrow), Wiley, (2012) in press.

Articles

1. L. Salmon, G. Molnar, D. Zitouni, **C. Quintero**, C. Bergaud, J. C. Micheau, and A. Bousseksou, "A novel approach for fluorescent thermometry and thermal imaging purposes using spin crossover nanoparticles", *Journal of Materials Chemistry*, vol. 20, pp. 5499-5503, 2010.

2. S. Bedoui, G. Molnar, S. Bonnet, **C. Quintero**, H. J. Shepherd, W. Nicolazzi, L. Salmon, and A. Bousseksou, "Raman spectroscopic and optical imaging of high spin/low spin domains in a spin crossover complex", *Chemical Physics Letters*, vol. 499, pp. 94-99, Oct 20 2010.

3. **C. M. Quintero**, I. A. Gural'skiy, L. Salmon, G. Molnar, C. Bergaud, and A. Bousseksou, "Soft lithographic patterning of spin crossover complexes. Part 1: fluorescent detection of the spin transition in single nano-objects", *Journal of Materials Chemistry*, vol. 22, pp. 3745-3751, 2012.

4. I. A. Gural'skiy, **C. M. Quintero**, G. Molnár, I. O. Fritsky, L. Salmon, and A. Bousseksou, "Synthesis of Spin Crossover Nano- and Micro-objects in Homogeneous Media, Chemistry - a European Journal, in press. DOI: 10.1002/chem.-201201063.

5. I. A. Gural'skiy, **C. M. Quintero**, K. Abdul-Kader, M. Lopes, C. Bartual-Murgui, L. Salmon, Z. Pengxiang, G. Molnár, D. Astruc, and I. O. Fritsky, , and A. Bousseksou, "Detection of molecular spin-state changes in ultra-thin films by photonic methods, *Journal of Nanophotonics*," in press. DOI: 10.1117/1.JNP.6.-063517.

Proceedings

1. **C. Quintero**, G. Molnár, L. Salmon, A. Tokarev, C. Bergaud, and A. Bousseksou, "Design of fluorescent spin-crossover nanoparticles for thermometry applications", *in Thermal Investigations of ICs and Systems (THERMINIC), 2010 16th International IEEE Workshop on*, 2010, pp. 1-5.

2. G. Molnár, I. A. Gural'skiy, L. Salmon, W. Nicolazzi, **C. Quintero**, A. Akou, K. Abdul-kader, G. Félix, T. Mahfoud, C. Bergaud, C. Bartual, C. Thibault, C.

Vieu, and A. Bousseksou, "Bistable photonic nanostructures based on molecular spin crossover complexes", *Proc. SPIE Photonics Europe, 2012*, vol. 8425, pp. 842513-1 - 842513-7.

Communications Orales

1. "Combining Fluorescence and Spin Crossover for Micro - Thermometry", *4éme reunion annuelle du GdR Magnétisme et Commutation Moléculaire*, July 7-8, 2010, Montpellier, France.

2. "Spin-Crossover Nanoparticles for Thermometry Applications", in *Thermal Investigations of ICs and Systems (THERMINIC), 2010 16th International IEEE Workshop on*, October 6-8, 2010, Barcelona, Spain.

3. "Nanoscale Assembly and Fluorescent Doping of Molecular Spin Crossover Complexes: Towards Nanoscale Switching Devices", *Transpyrenees Action on Advanced Infrastructures for Nanosciences and Nanotechnologies (TRAIN2)*, June 19-20, 2012, Toulouse, France.

Posters

1. "Fluorescent SCO Systems for Micro-Thermometry Applications", *MOLMAT 2010: IVth International Conference on Molecular Materials*, July 5-8, 2010, Montpellier, France.

2. "Fluorescent SCO Systems for Micro-Thermometry Applications", *International School & Sympossium on Multifunctional Molecule-Based Materials*, March 13-18, 2011, Chicago, U.S. Poster Award.

TITRE: Nanomatériaux luminescents à transition de spin : propriétés physiques et applications

L'objectif principal de cette thèse est de fournir un nouveau protocole qui permet la détection de la transition de spin (TS) dans un nano-objet unique. Dans ce but, nous proposons d'utiliser la luminescence comme sonde très sensible qui peut être employée à des échelles où d'autres méthodes conventionnelles ne sont plus efficaces. Nous avons cherché à développer des nano-matériaux à TS avec des propriétés de luminescence dans le but d'isoler ces objets et ensuite sonder leurs propriétés via la détection luminescente. Sur la base de techniques de lithographie douce, plusieurs méthodes allant de l'assemblage aléatoire jusqu'à l'assemblage capillaire dirigé de nanoparticules à TS et également la synthèse *in situ* d'objets isolés luminescents à TS (*ca.* 150 nm) ont été explorées. Dans le même temps, leur étude en microscopie de fluorescence est présentée et les défis expérimentaux que cette tâche a imposée sont discutés. En outre, l'application potentielle de ces matériaux hybrides en microthermométrie est étudiée. Comme preuve de concept, des films minces de systèmes luminescents à TS ont été déposés sus des micro / nanofils chauffés par effet Joule afin de cartographier leur température.

MOTS-CLE : transition de spin, luminescence, nanoparticules, nanomatériaux, lithographie douce, micro-thermométrie.

TITLE: Luminescent Spin Crossover Nanomaterials: Physical Properties and Applications

The main objective of this thesis is to provide a new protocol that permits the detection of the spin crossover (SCO) phenomenon in a single nano-object. To accomplish this, we propose luminescence as a highly sensitive technique that may be employed at scales where other conventional methods are no longer effective. We aimed to develop SCO nano-materials with luminescence properties in order to isolate these objects, address them and then probe their properties via luminescent detection. Methods ranging from random to directed microcappilary assembly of SCO nanoparticles and also *in situ* synthesis of isolated luminescent SCO objects (*ca.* 150 nm) based on softlithographic techniques were explored. At the same time, their investigation characterization in fluorescence microscopy is shown and the experimental challenges that this task imposed are discussed. Also, the potential application of these hybrid materials in microthermometry is studied. As a proof of concept, thin films of luminescent SCO systems were employed to obtain thermal cartographies of gold micro / nanowires heated by Joule effect.

KEYWORDS: spin crossover, luminescence, nanoparticles, nanomaterials, soft-lithography, microthermometry.

Laboratoire de Chimie de Coordination, UPR 8241, 205 Route de Narbonne, 31077 Toulouse Cedex 04, France